Università degli Studi di Torino
Scuola di Dottorato in Scienze della Natura e Tecnologie Innovative

Color centers in diamonds: from quantum metrology to biological applications

Ekaterina Moreva

Università degli Studi di Torino
Scuola di Dottorato in Scienze della Natura e Tecnologie Innovative

---

Indirizzo di Fisica ed Astrofisica - XXXII Ciclo

Color centers in diamonds: from quantum metrology to biological applications

Moreva Ekaterina

Tutor: Prof. Marco Genovese

Chapter 1

Chapter 2

Chapter 3
Nanodiamonds processing and applications

Chapter 4
Quantum sensing

Introduction

The second quantum revolution is based on the possibility to controll individual quantum particles or properties, like state superposition or quantum entanglement, that have no classical analogue. New technical advances allow engineering quantum systems that provide unique possibilities and technologies not available before: quantum cryptography and telecommunications, quantum computing and quantum metrology and sensing.

Many different platforms are being considered for implementatius quantum technologies, among which point defects in diamond play an important role. Among the possible optically active defects, the most studied is the nitrogen – vacancy (NV) center, which possesses remarkable spin properties that make it a valuable candidate for many applications. Thanks to the possibility of single spin optical initialization, read out at room temperature and also its long coherence time, this system offers the possibility to detect very localized and weak electric and magnetic fields or measure temperature with an unprecedented combination of spatial resolution and sensitivity in a wide range of temperatures (from 0 K to well above 300 K), opening up new frontiers in biological and matter research. Thermometry, magnetometry and electrometry, performed with these quantum defects in diamond is one of the topic of this thesis and it is discussed in detail in the next chapters. In short, this is an attractive technology as diamond sensors are capable of operating in an unshielded environment at room temperature. Moreover, the biocompatibility of diamond makes it a suitable material for biosensing applications.

Diamond nanocrystals represent a useful platform to exploit diamond color centers characteristics at the nanoscale. They can be used as a single photon sources(SPS) for the quantum communication and quantum metrology, act as a nanoscale sensors of electromagnetic fields or temperature, allow integration in biological samples, where they can be used as luminescent markers or drug delivery carriers. In this thesis work the luminescent nanodiamonds were employed for the experimental demonstration of a new criterion to investigate the non classicality of aggregates of SPSs. A new non-classicality criterion with respect to the usually adopted second-order autocorrelation function was also investigated in ensembles of luminescent nanodiamonds. Its advantage lies in the resistance to poissonian noise as well as in the possibility of assessing the non-classicality of emitters even in large ensembles. The SPS based on NV center in nanodiamonds was used for the pilot international metrological comparison of the measurement ability at single photon level between INRIM, PTB and NPL. Moreover, luminescent nanodiamonds were internalized in living cells consisting in a network of mouse

hyppocampal neurons. Luminescence and ODMR measurements were performed on nanodiamonds containing NV centers internalized inside living neurons, without affecting their physiological functions.

The above mentioned activities, together with an introduction to the diamond properties and a description of the adopted experimental methods will be reported in the manuscript as follows:

- Chapter 1: introduction to diamond and its defects properties, description of the experimental methods
- Chapter 2: Description of applied techniques, applications of colour centers
- Chapter 3: quantum-optical characterization of diamond nanocrystals, new non-classicality criterion for the characterization of Fock states and the pilot metrological study of the $g^{(2)}(0)$ measurement for a SPS based on NV color centers in nanodiamonds
- Chapter 4: quantum sensing with NV centers in diamond.
- Chapter 5: biosensing with NV centers in diamonds and related challenges.
- Summary and results discussion.

Chapter 1

1.1 Diamond

Diamond has properties which make it precious not just as a fascinating gem, but in many technological fields. It's a hard, optical transparency material over a wide spectral range, biocompatible and chemically inert. Diamond's crystalline structure is based on carbon atom, whose electronic configuration is [He] $2s^2 2p^2$.

Carbon has many different allotropic forms: graphite, diamond, fullerenes, nanotubes or graphene - a single graphite layer with remarkable physical properties. Diamond is a metastable form of carbon. Graphite is only a few electron-volts more stable than diamond, but the activation barrier for conversion requires almost as much energy as destroying the entire lattice and rebuilding it.

Among the above listed allotropic forms of carbon, diamond is the only one in which carbon atoms are bonded through sp^3 hybridized orbitals. In the diamond crystal each carbon atom is surrounded by four neighbours distant 0.154 nm in a tetrahedral configuration with an angle of 109°. The lattice configuration of a diamond is a face-centreed cubic (FCC) lattice with basis in (0,0,0) and $a(\frac{1}{4},\frac{1}{4},\frac{1}{4})$, with lattice parameter a = 0.357 nm (see Fig 1.1.1). The atomic density of diamond is 1.77×10^{23} atoms·cm^{-3} while the mass density is 3.54 g·cm^{-3} [1].

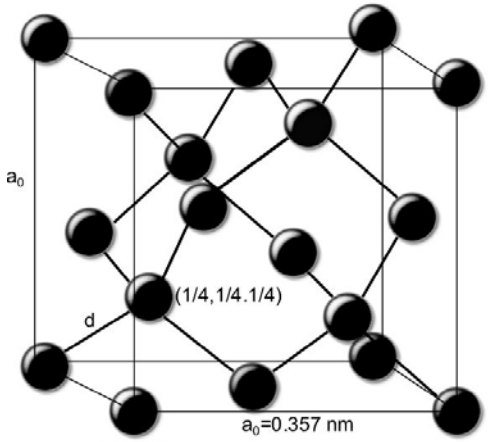

Fig. 1.1.1 The unit cell of diamond, showing the bond lengths and tetrahedral structure.

1.1.1 Physical properties

Diamond is the hardest available natural material, thermally resistant and chemically inert. It has the highest thermal conductivity at room temperature amongst all materials and good electrical

insulation, is transparent over a very wide range of wavelength (see Table 1.1.1). The binding energy between carbon atoms in diamond is 7.62 eV, a high value compared to silicon (4.63 eV) that is the most similar crystal from a structural point of view. For this reason, in such a strongly bonded crystal the Young modulus is extremely high (1220 GPa), as well as the sound velocity (18 $km \cdot s^{-1}$). This property allows one to use diamond in high-end audio components as the membrane operating at high acoustic frequencies. The phonon density of states in diamond shows that a large number of states are available only at high frequencies just below the maximum allowed one (i.e. 16 THz), for this reason the Debye temperature is particularly high (2000 K)[2] .

This property significantly affects the thermal conduction and the carriers mobility: at room temperature the phonon density is low compared to other crystals, this reflects in a small number of collision between phonons and thus in the higher thermal conduction among all solids (25 $W \cdot cm^{-1} \cdot K^{-1}$ [3]). Similarly, the electron mobility is high due to the small amount of phonon scattering. These two important characteristics make diamond a promising material for many technological applications, especially in high-power electronics and miniaturized heat sinks.

Properties	*CVD Diamond*	*Single Crystal Diamond*
Density, g/cm³	*3.51*	*3.515*
Specific heat, C_p, J/mol (at 300K)	*6.195*	*6.195*
Thermal conductivity at 25 °C, W/mK	*2100*	*2200*
Thermal expansion (10^{-6}/°C @ 25–200 °C)	*2.0*	*1.5–4.8*
Index of refraction at 10 µm	*2.34–2.42*	*2.40*
Band-gap, eV	*5.45*	*5.45*
Electrical resistivity, ohm cm	*10^{12}–10^{16}*	*10^{16}*
Young's modulus, GPa	*910–1250*	*1250*
Compression strength, GPa	*8.68–16.53*	*16*
Vickers hardness range, GPa*	*50–100*	*57–100*
Coefficient of friction	*0.05–0.15*	*0.05-0.15*

Tab.1.1.1 Physical properties of single crystalline and CVD diamond

1.1.2 Electronic and Optical properties

As mentioned in the previous paragraph, diamond presents a sp^3 hybridisation. From an electronic point of view, these four orbitals generate eight sub-bands: four of them are bonding states and determine the valence band, while the remaining four are anti-bonding states and form the conduction band. The high value of energy gap makes diamond an insulator or a very high energy gap semiconductor. As in more conventional semiconductors, doping plays an important role in changing the electric features of diamond.

The high value of energy gap gives diamond an optical transparency over a wide spectral range extending from far infrared to near ultraviolet. Optical properties can be changed by the presence of active optical defects in diamond lattice. Due to its extremely rigid lattice and high atomic density, it may contain a limited range of defects, among which boron and nitrogen are most common. Defects can consist of substitutional or interstitial atoms, vacancies, or complex clusters and can be found both in natural and artificial diamond.

The presence of some types of defects can create states in the bandgap. These states can be potentially optically-active transitions and affect the absorption spectra, causing artefacts and features that can be interpreted as lower bandgap than the actual, non-defected value of "pure" diamond. Two different types of transitions can occur: one between “pure” electronic states and one with interaction with phonons. In the former case the luminescence spectrum is consisting of a single sharp line at a specific wavelength, referred as Zero Phonon Line (ZPL). In the latter case the emission is instead characterized by satellite emission peaks with respect to the ZPL, which are referred as “phononic sidebands”. Due to the high transparency of diamond, if the light emitted by the impurities is in the visible range, it can be easily transmitted through the crystal.

Defects with a luminescent emission in the visible range are called color centres. The most evident optical property of diamond due to the presence of these impurities is its color: depending on which defect is inside the crystal lattice, the material appears of different colors. As an example, many diamonds are yellow; in this case the impurity is nitrogen, which is responsible for the introduction of an absorption band in the blue spectral range.

1.1.3 Diamond synthesis

Nowadays artificial diamonds are mainly employed for industrial purposes: manmade diamonds are as good as natural ones for all the applications of interest and can be produced in relatively large crystals with low costs. Moreover, with a scalable and repeatable process the impurity concentration is well known and reproducible. The two main methods used to produce synthetic

diamonds are the High Pressure High Temperature (HPHT) and the Chemical Vapor Deposition (CVD) techniques.

HPHT diamond growth was first announced by the General Electric Company (GE) in 1955, and today most HPHT synthesis has its origins in the temperature gradient method first developed in 1959[4]. In general, HPHT growth proceeds at temperatures and pressures designed to approximate the conditions of natural diamond growth. In HPHT growth, a carbon source such as graphite or diamond powder is placed in the reactor chamber along with other ingredients to facilitate diamond growth atop a diamond seed. A molten metal catalyst (usually containing a mixture of Fe, Ni, Co, or other elements) allows growth to proceed at a lower temperature. This also reduces the technological complexity and some of the expense required to grow diamond under HPHT conditions. HPHT growth occurs at pressures of 5–6 GPa and at temperatures of 1300–1600°C. As with CVD diamond growth, HPHT growth proceeds by creating a temperature gradient in which the carbon source is at a slightly higher temperature than the diamond growth seed. This causes the carbon atoms to diffuse through the molten flux toward the slightly colder section of the chamber to form a synthetic diamond crystal on the seed.

Most early gem-quality HPHT synthetics were color, since color-causing impurities, such as nitrogen (yellow) or boron (blue), were often prevalent within the growth system. Recent progress in growth technology has allowed for better control of impurity contents, resulting in the creation of colorless crystals. HPHT diamonds are mainly used as indenters and cutting instruments. Because of their lower cost and higher crystal quality with respect to CVD method, they are frequently used as substrate for epitaxial CVD growth of high quality (i.e. optical and electronic grade) diamond layers.

CVD refers to the process where solid materials are formed from the gas phase at some suitable temperature and pressure. In CVD diamond synthesis, the process generally takes place below atmospheric pressure, typically between 130 Pa and 26 kPa. The starting materials (called precursors) for diamond synthesis are hydrogen and hydrocarbons such as methane. Only a small amount of hydrocarbon, often between 1% and 5%, is normally present in the gas mix and provides the source of carbon from which the diamond is grown.

Hydrogen plays a key role during the synthesis process because it terminates the dangling carbon bonds of the surface atoms increasing the surface stability and, as radical species, removes the graphite formed on the substrate 1000 times faster with respect to diamond. Precursors are phyrolized on the substrate using hot filament or plasma: the plasma process is faster and allows a better control on the impurities, however hot filament is a cheaper technique and can be used for very large surfaces.

Up to now, the only path to a high quality single crystal growth is homoepitaxy, therefore the substrate material is usually a thin slab of diamond that will be thickened or cut off at the end of the growth process. Chemical composition of pristine vapour phase and contaminations in the reactor are fundamental parameters to control the amount of impurities of diamond that will be obtained: CVD crystals are usually more pure than HPHT ones, even if the main contamination is still nitrogen, but also silicon (coming from the glass windows of the vacuum chamber) is well accommodated in the crystal structure and can be frequently found in CVD samples. The main limitation of this production technique is the growth rate that limits the amount of crystal that can be deposited over the substrate, so CVD diamonds are usually large but thin. A typical dimension for a CVD sample is $3\times3\times0.5$ mm^3. In applications that are mainly based on surface or near-surface functionalization the thickness limitation is not a problem. CVD technique can also yield polycrystalline diamonds, typically with lower costs and less technical difficulties. Moreover, this polycrystalline material can be deposited over a large number of substrates, for example on silicon electronic devices to act as a heat sink. Optical and electric properties of polycrystalline diamond are grain-size dependant and generally worse with respect to single crystal.

1.2 The nitrogen vacancy centre

1.2.1 Structure

The nitrogen vacancy (NV) centre is a point defect in the diamond crystal lattice[5]. The NV centre arises when a vacant lattice site lies nearest-neighbour to a substitutional nitrogen atom in the diamond lattice (Fig. 1.2.1). Two types of such centres have been identified, the neutral NV^0 centre and the singly-charged NV^- centre (commonly referred to as the NV centre). The reason of the strong interest towards the latter is motivated by the S=1 triplet spin state, that can be suitably controlled and optically read out (see Section 1.2.3 for further details). This property discloses wide potential applications in fields such quantum computing and sensing, also thanks to the very long spin coherence time of this system[6]–[10]. The NV centre has six electrons. Five of the electrons are contributed from the dangling bonds of the three neighboring carbon atoms and the nitrogen atom. One extra electron is captured from an electron donor and gives rise to the negative charge state. The axis defined by the line connecting the nitrogen atom and the vacancy is called the NV axis. There are four possible spin orientations for NV centres in single-crystal diamond, leading to four possible NV alignments. The angle between each different pair of the possible orientations is 109.4^o.

The NV centre has the strong coupling to its vibrational levels (so-called quasi-local phonons in the case of point defects in crystals): only 4 % of the photons are emitted in the Zero Phonon Line (ZPL). As a result, the emission spectrum at room temperature is broadened in a spectral range of more than 150 nm for both the charge states making the NV centre unsuitable for single photon emission but still very appealing for its spin structure. In the Fig.1.2.2 the typical PL emission spectra from NV^0 and NV^- centres are shown.

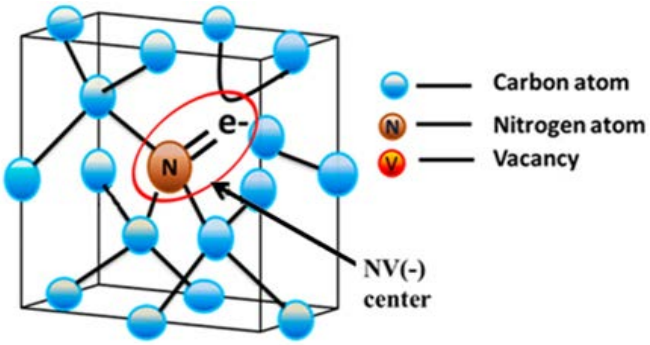

Fig.1.2.1 The diamond structure with nitrogen-vacancy defect

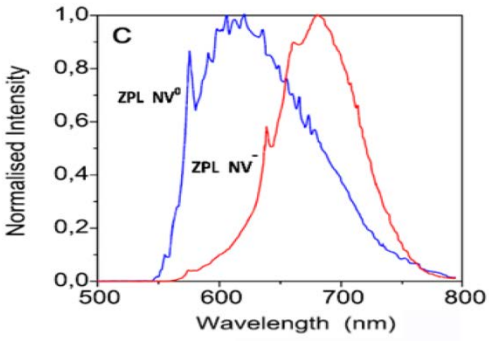

Fig.1.2.2 NV centres emission spectra

1.2.2 Electronic and optical properties

The energy level scheme of NV centre is shown in Figure 1.2.3. The electronic structure of the NV centre is mainly governed by the dangling bonds of the three carbon atoms and the one nitrogen atom surrounding the vacancy [11], [12]. Thus, the overall number of electronic states is eight. For the NV^- centre two of the six electrons are unpaired, therefore they determine the effective spin of S = 1 of the system. Therefore, the energy levels scheme presents a triplet ground state ($^3A_2$) and a triplet excited state (^3E). The notation A and E refers to for the symmetry deduced from the form of orbitals involved in the states which lead to symmetry group considerations[13]. The ground state has 3 electron spin states. The spin states $|m_s = \pm 1\rangle$ are degenerate in absence of an external magnetic field. The energy difference between the $|m_s = \pm 1\rangle$ and $|m_s = 0\rangle$ ground state due to spin-spin interaction is the so-called zero-field splitting and corresponding to D_{gs} = 2.87 GHz. The same splitting in the excited state is instead equal to D_{ex} = 1.42 GHz[14].

The $^3A_2 \rightarrow {}^3E$ transition can be non-resonantly excited with light with wavelength from 450 nm to 637 nm, and one typically uses a 532 nm diode-pumped solid state laser to drive this transition. The fluorescence from the $^3E \rightarrow {}^3A_2$ decays is in the 637 nm to 800 nm wavelength range.

An important feature of the NV centre is that it is possible to optically detect its spin state and optically pump it into the m = 0 sublevel. The mechanism is described as follows. Depending on the electron spin state, two different decaying paths are possible. If the system is in the $|m_s = 0\rangle$ state, then a spin preserving transition occurs with single-photon emission at wavelength λ = 637 nm. If phonon relaxation also presents, the emission sidebands are also observed at wavelengths in a spectral range between 650-800 nm, as shown Figure 1.2.2. This transition is cyclic and one detects high fluorescence intensity when continuously illuminating the NV centre.

The state has a different lifetime at room temperature depending on the host crystal: τ =12 ns is typical for bulk diamonds, while τ =25 ns for nanodiamonds[15]. The higher value in the latter case arises from two different reasons. Firstly, at these scales the Purcell effect becomes relevant[16]; secondly, a different effective refractive index can be considered between two cases. This is due to the fact that in a nanocrystal, due to its sub-wavelength size, the emission of the centre can be seen as in air rather than in a medium with refractive index of n_d= 2.4, as in bulk diamond[15].

If the electron spin state is instead $|m_s = \pm 1\rangle$, two possible decay paths are possible. The first one is again spin-preserving and leads to the previously-described photoluminescence (PL) emission. The second one is non-spin-preserving and the system ends up in spin state $|m_s = 0\rangle$ of the ground level. In this latter case the system relaxes through the two metastable singlet spin states, namely ^{1}A and ^{1}E. These have a transition wavelength in the infrared range, λ = 1046 nm, therefore the transition is considered "non radiative"[17]. In this case spin changes to $|m_s = \pm 1\rangle$, and thus the process is referred as "intersystem-crossing" (ISC). The transition via the metastable state happens with a 30% probability for the $|m_s = \pm 1\rangle$ excited state: this is the reason why $|m_s = \pm 1\rangle$ spin state is less luminescent with respect to $|m_s = 0\rangle$ one. These two states are respectively referred as "dark" and "bright" states. Remarkably, the above explained feature allows the optical read-out of the spin state of the NV centre at room temperature[18]. At room temperature, the decay of the metastable state into the ground state through ISC has a 200 ns lifetime, i.e. a longer value with respect to the triplet state lifetime which was measured to be <1 ns [19]. After several cycles of excitation and relaxation, NV centre accumulates at $|m_s = 0\rangle$ in the ground state with a high probability [20]. This is the procedure which will be referred in the following as "initialization" of the NV system.

The ISC to the metastable state not only allows for spin polarization, but also for optical read-out of the electron spin. Due to the long lifetime of the metastable state, for $|m_s = 0\rangle$ more optical

cycles can be undergone as compared to $|m_s = \pm 1\rangle$, where the NV ends up in the metastable state. Therefore for a gated illumination, the fluorescence signal for the first 200 - 300 ns is significantly different (Fig. 1.2.4). With normalization for the steady state fluorescence (after about 1 μs laser illumination) and an integration window of 200 ns a high fluoresence contrast between $|m_s = 0\rangle$ and $|m_s = \pm 1\rangle$ can be observed. The NV center's ground state spin states exhibit substructure arising from hyperfine coupling to the NV center's nitrogen nuclear spin (I = 1 for ^{14}N and I = 1/2 for ^{15}N) and, for ^{14}N, the nuclear quadrupolar interaction[21], [22].

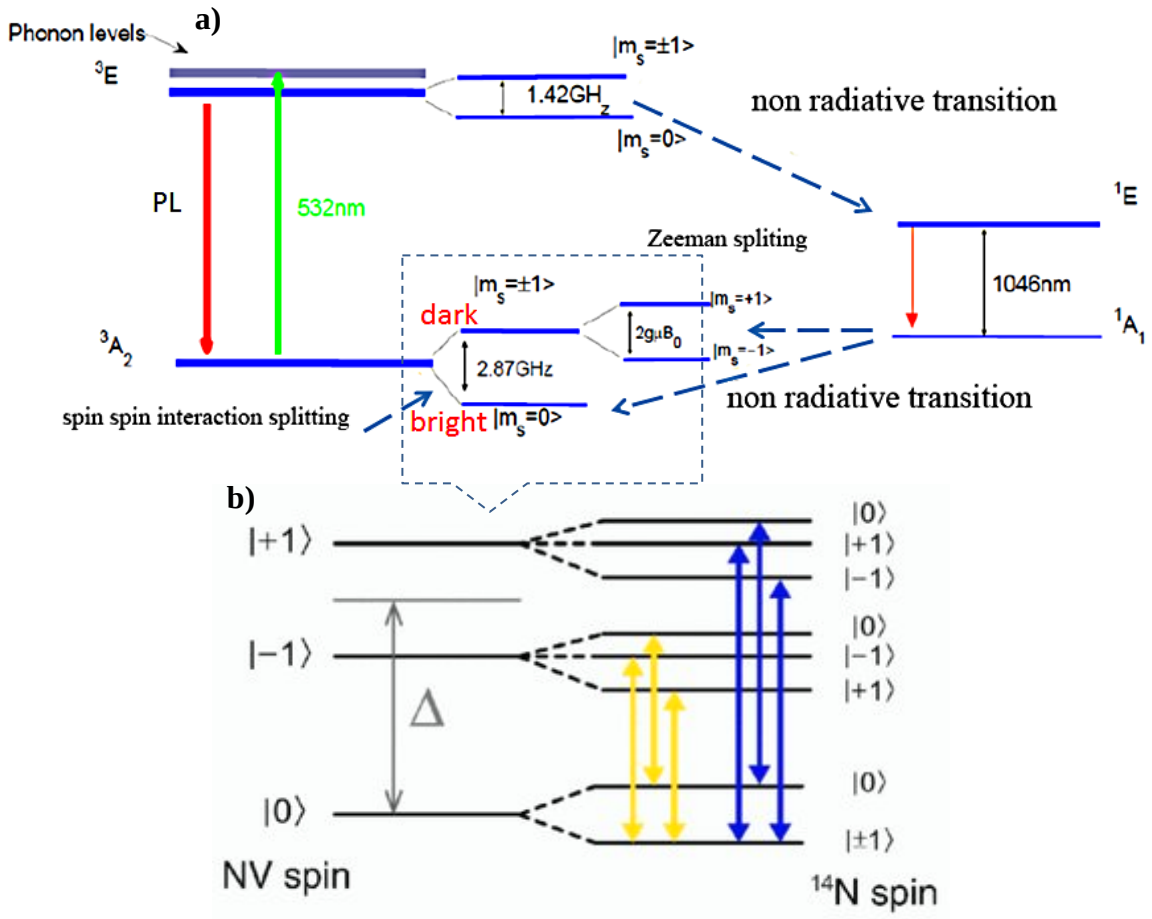

Fig.1.2.3 a)Energy levels of the negatively charged NV center, including the 14N hyperfine splitting(b); Δ is the zero-field splitting.

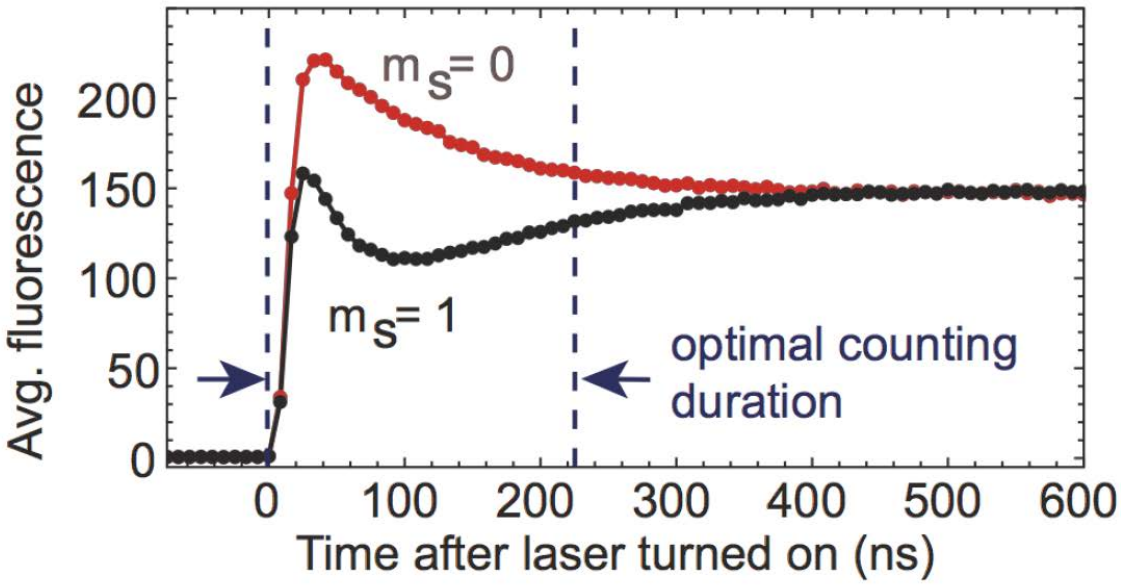

Fig.1.2.4 Photon counts for different spin states: Example fluorescence traces after optical initialization ("ms = 0") and after initialization followed by a π pulse on the 0 → 1 spin transition ("ms = 1") [23]

1.2.3 Spin properties

As pointed out in the previous section the ground state is a spin triplet without spin orbit coupling. Thus, the main influences on the electron spins are spin-spin interaction and electron Zeeman shift [24], [25]. The spin Hamiltonian of NV centres in the presence of an external magnetic field can be formulated in terms of different contributions as:

$$\hat{H} = Dgs(S_z^2 - \frac{1}{3}[S(S+1)]) + F(S_x^2 - S_y^2) + \frac{g\mu_B}{h}\mathbf{B}\cdot\mathbf{S} + S\hat{A}_N\hat{I}_N + \sum_j S\hat{A}_j I_j \qquad (1.2.1)$$

The first term in the Hamiltonian equation (Eq.1.2.1) is the zero-field splitting (ZFS) frequency of the NV centre Dgs = 2.87 GHz. S = (S_x; S_y; S_z) is the electron spin, *F* is the mechanical strain, g is the electronic Landé factor, μ_B is the Bohr magneton, *B* is the external magnetic field. $\hat{A}_N$ and $\hat{A}_j$ are the hyperfine interaction tensors of the nitrogen and the other electrons in the surrounding, $\hat{I}_N$ and $\hat{I}_j$ are nuclear spins of nitrogen atom and of other nuclear spins surrounding the electron spin. The microscopic origin of the ZFS parameter D_{gs} is thought to be spin-spin interactions in the NV's orbital structures, and the amount of splitting depends on the lattice length, which is strongly influenced by the local temperature. When the local temperature increases, for example, the diamond lattice at the NV centre expands, which effectively lowers the spin-spin interaction and reduces the ZFS parameter D. This property can be used for temperature sensing, for further details about temperature measurements see Section 4.2.

The second term represents the contribution of the mechanical strain introduced in the system by the breaking of the C_{3v}. This term depends on the diamond material. In single-crystal samples the mechanical strain field is negligible and not resolved, while in polycrystalline ones a relatively high strain field is induced by growth conditions, which lead to a splitting of the spin state $|m_s = \pm 1\rangle$ even in absence of external magnetic fields. The third term of this equation corresponds to the Zeeman term, which represents the magnitude of the $|m_s = \pm 1\rangle$ levels splitting in the NV ground state.

The NV centre is not sensitive only to magnetic fields or temperature. The sensing of electric field is one from the most prominent effects, even if the coupling with it is much weaker than the interaction with the magnetic field. The electric field Hamiltonian was derived from molecular orbit theory by Doherty et al. in reference [14] and can be rewrite from Eq.1.2.1 as:

$$\hat{H} = (D_{gs} + d_{gs}^{\parallel} \prod_z)(S_z^2 - \frac{1}{3}[S(S+1)]) + \frac{g\mu_B}{h}\mathbf{B}\cdot\mathbf{S} + d_{gs}^{\perp}\left[\prod_x (S_x S_y - S_y S_x) + \prod_y (S_x{}^2 - S_y{}^2)\right] \quad (1.2.2)$$

Where $d_{gs}^{\parallel} = (0.35 \pm 0.02) Hz \cdot cm \cdot V^{-1}$ and $d_{gs}^{\perp} = (17 \pm 3) Hz \cdot cm \cdot V^{-1}$ [26] are respectively the axial and non-axial Stark shift components of the permanent electric dipole moment dgs in the ground triplet state. The frequency shift caused by the electric field is much smaller than the shift produced by the presence of a magnetic field, which is $\frac{\mu_B g}{h} = 28 MHz \cdot mT^{-1}$ [27]. For this reason, in order to reliably measure the Stark shift it is necessary to decouple it from the Zeeman shift. It is important to mention that the $\boldsymbol{\Pi}$ field is actually resulting from the sum of the electric field $\boldsymbol{E}$ and of the strain field $\boldsymbol{F}$ that have the same contribution to the energy levels [28] (see Section 4.1.4 for detailed expressions). The Stark shift is a second order effect for the ground state of the NV centre and for this reason its measurement by means of optical detected magnetic resonance (ODMR) is not straightforward. Nonetheless, it may be very useful to exploit this feature for the self-diagnostics in diamond-based devices in which NV centres are common and where charge trapping with the production of local intense electric fields takes place. For further details about electric field measurements using ODMR see Section 4.1.

1.2.4 Engineering of NV centres

NV centres are usually present in natural diamond samples due to the fact that nitrogen is the most common impurity in diamond. Over the long time of the natural growth, vacancies migrating close to a nitrogen site are energetically favoured to form the NV complex. However,

natural NV centres distribute randomly in diamond, which induces great difficulties to make photon-NV centre coupling on demand. But, as well as it is possible to create artificial diamonds, also NV centres can be artificially created inside diamonds during their production. Especially, to create NV centres at fixed positions is highly required for diamond based nano-photonics and quantum information techniques. The concentration of NV centres also can be controlled on the basis of special purposes and applications.

The main requirement for the production of NV centres consists in the presence of both nitrogen and vacancies during the production, and establishing high temperatures to allow their migration. At temperatures higher than 600 °C vacancies become mobile while nitrogen atoms remain still immobile in the diamond crystal[29]. If high temperatures last several hours, vacancies migrate towards nitrogen atoms forming NV centres. The thermal process is usually referred as annealing and it is intrinsically present during both HPHT and CVD growth. Some techniques are available to control the creation of NV centres some them are: ion irradiation, nitrogen implantation and CVD growth.

One of the most common methods used to create NV centres in diamond is ion irradiation. Diamonds with initially high concentration of NV and native single substitutional nitrogen atoms can be irradiated by ions or other damage-inducing radiation (electrons, neutrons, etc) creating of vacancies inside the crystalline structure. After the irradiation, an annealing at temperatures near 800 °C allows the induced vacancies to diffuse within the sample, reach nitrogen sites and form NV complexes.

Another efficient way to create NV centres in diamonds based on nitrogen ions implantation. In this case nitrogen and vacancies are formed together in the high-purity (i.e. low-nitrogen) sample. Pioneering implantation with a focused nitrogen beam of 2 MeV N+ was realized using a dynamitron tandem accelerator (DTL) in group of J.Meijer at the University of Bochum[30]. The volume and the depth of implantations depend on the ion beam energy. The higher is the ion energy, the deeper they are the implanted and the higher is the number of induced vacancies. Engineering of point defects in diamond with nanometer-size resolution can be realised with focused ion beam (FIB) technology. FIB technique is based on the Liquid Metal Ion Source (LMIS). The high interest to such systems is caused by wide range of applications, as for instance, high energies could be used for the sample milling, by using instead lower ion beam energies (<10 keV), NV centres can be created with high spatial resolution [31].

1.3 Confocal photoluminescence microscopy

In this section a general description of the experimental setups is given. Both setups are based on the same confocal microscopy scheme, but with different orientation: vertical orientation for experiments based on samples characterization or single photon sources characterisation and horizontal orientation for sensing measurements and bio measurements. Sometimes special equipment was used and some parts of the setup are only briefly explained, additional details will presented *in the relevant* chapters.

The basic principle behind fluorescence microscopy consists of the detection of the fluorescence emitted from the sample instead of the transmitted or reflected light, like in traditional optical microscopy. The sample under analysis is hit by an excitation light source, either monochromatic (typically a laser) or characterized by different spectral components. The light is absorbed by the fluorophores and re-emitted with at a longer wavelenght, because a given amount of energy is non-radiatively dissipated in the excitation process (e.g. phonons, heating), so the emitted light can be easily separated from the excitation beam. The standard components of a fluorescence microscope are: the excitation source, a dichroic mirror which acts as a beamsplitter, focusing elements and spectral filters. The detection can be performed in different ways:

Wide field: the fluorescence light is not focused and directly acquired by a matrix of detectors (typically a CCD camera). This allows one to obtain an image of the sample based on the volume stimulated by the excitation beam.

Confocal: the excitation light and the emitted fluorescence are focused respectively at the sample and at the detector, the focal points are optically conjugated and out of focal plane fluorescence does not contribute to the measurement.

These different operation principles have some key differences, and each one has specific advantages depending on the application. Wide field microscopy allows the simultaneous detection of the fluorescence from a whole region of the sample and is useful when measuring fast variations in the fluorescence intensity. The biggest disadvantage of this method is that the fluorescence arises from a volume and not from a specific focal plane, so it is not possible to discriminate fluorophores at different depths. Confocal microscopy on the other hand is much slower if relatively large areas of a sample are to be mapped, because scanning is needed to acquire the fluorescence from each spot; on the other hand, confocal microscopy gives higher optical contrast of the sample under investigation.

1.3.1 The single-photon sensitive confocal microscope

In this thesis we are going to investigate single quantum systems where the one of the way to interrogate them is via laser excitation and subsequent detection of the emitted fluorescence. As the fluorescence count rate is low compared to ambient light for single photon microscopy the use of a confocal configuration setup is preferable since it has a higher depth spatial resolution and allows one to filter out as much as possible the original signal from the background light. To achieve this, the focusing objective should have a very high magnification, and focus the excitation light in a micrometric volume. This is usually achieved using high magnification (i.e. 100×) objectives. A schematic representation of a typical confocal microscopy setup is shown in Fig. 1.3.1. First of all the laser source must provide a beam as close as possible to a plane wave. Then it hits the dichroic beamsplitter and if $\lambda < 570$nm, where λcut is the cutoff wavelength of the dichroic beamsplitter, the light is reflected towards the objective lens, which focuses the light on the sample. The cutoff wavelength λcut is selected to transmit the greater part of the fluorescence from the sample. This light, cleaned from the pump background light is refocused with another objective at the detection pinhole. If the laser light is focused on points in the sample out of the focal plane, the fluorescence is not focused at the detection pinhole and the contribution to the signal of the light emitted from these points is negligible. The combination of the focusing of the laser beam on the sample and on the pinhole greatly reduces the luminescence arising from "out of focus" points, both laterally and in depth. This effect strongly depends from the pinhole dimension, therefore its optimal value must be identified to optimize both the optical sectioning resolution and the signal intensity. In setup based on optical fiber coupling the pinhole corresponds to the diameter of the core of the fiber that brings the fluorescence to the detector. Usually a multi-modal fiber is used because it allows propagation of multiple wavelengths in a given range with minimum losses. The typical value of the core diameter of the fiber is ~50 μm.

The resolution of the confocal microscope can be quantified through the point spread function (PSF) of the imaging system. The point spread function is a measure of the spatial intensity distribution of the beam, and this function varies both laterally, along the beam propagation axis, and radially, in the plane perpendicular to the beam propagation axis, depending on the input.

For the plane wave approximation the radial distribution of the point spread function is given by

$$PSF = P(r) = 2\left[\frac{J_1(ar)}{ar}\right]^2 \tag{1.3.1}$$

where $a = \frac{4\pi NA}{\lambda}$ and the function $J_1(x)$ is the Bessel function of the first order, λ is the wavelength and NA is a numerical amplitude of the objective. In each microscope the image of an object is the convolution of a function representing the object (OBJ) itself and the *PSF*, so:

$$I(x, y, z) = OBJ(x, y, z) \otimes PSF(x, y, z) \tag{1.3.2}$$

For the case of the single NV centre observation in the confocal microscope, OBJ can be approximated as a Dirac delta function, because has size much smaller than dimension of the PSF. In this case the image coincides with the *PSF* of the microscope: The PSF is used to describe the confocal volume and thus the resolution of the microscope.

The difference in resolution between confocal and widefield microscope can be estimate can be estimated as follows. Both excitation (ext) and collection probabilities for a color centre must be taken into account to calculate the PSF of a microscope: in a widefield setup all the color centres in the sample are simultaneously excited using a defocused beam that covers the entire objective's field of view and it can be assumed that the excitation probability is unitary for all emitters. On the other hand, in a confocal microscope only a very small region is investigated at a time, because the excitation beam is now focused. The PSF is the product of both excitation and collection probabilities:

$$PSFwidefield\ (x, y, z) \propto Idet\ (x, y, z) \tag{1.3.3}$$

$$PSFconfocal\ (x, y, z) \propto Idet\ (\ x, y, z) \cdot Iexc\ (x, y, z) \tag{1.3.4}$$

Here I_{det} is the convolution between the theoretical intensity distribution of light close to the object focal plane in paraxial approximation, I_{point}, and a function describing the transmittance of the employed pinhole [32]. The same holds for I_{exc}, but if a single-mode fiber coupled laser is used, the beam can be efficiently focussed into a diffraction-limited pattern.

Since in confocal systems the same objective is used for both excitation and detection, $Idet$ and $Iexc$ are basically equal (apart from the difference in λ which we assume negligible in the first approximation). It follows that:

$$PSFconfocal = (PSFwidefield)^2. \tag{1.3.5}$$

The PSF of a confocal microscope is the square of a comparable wide-field microscope and therefore features a higher resolution apart from the increased SNR. The lateral and axial resolution (Δr, Δz) of a confocal microscope are given by

$$\Delta r = \frac{0.44\lambda}{NA}, \Delta z = \frac{1.5n\lambda}{NA^2} \tag{1.3.6}$$

where NA is the numerical aperture of the microscope objective $NA = n\sin(\theta)$, θ is the half angle of the focused light cone and n is the refractive index (n=1 for air objective or n = 1.517 for the immersion oil used in our microscope).

From Eq. 1.3.6 follows that resolution depends on NA of the objective. For larger values of NA, more light rays will experience an angular deviation by the objective, with respect to the divergence caused by diffraction, resulting into a narrower imaged spot. But the value of θ has both fundamental (α < 90°) and practical limitations: it cannot be larger than ~ 65°. Increasing the refractive index n results into an effective decrease of λ and this effect is used when water or oil objectives are employed, reaching a limiting value of about NA = 1.4 for objectives operating with oil.

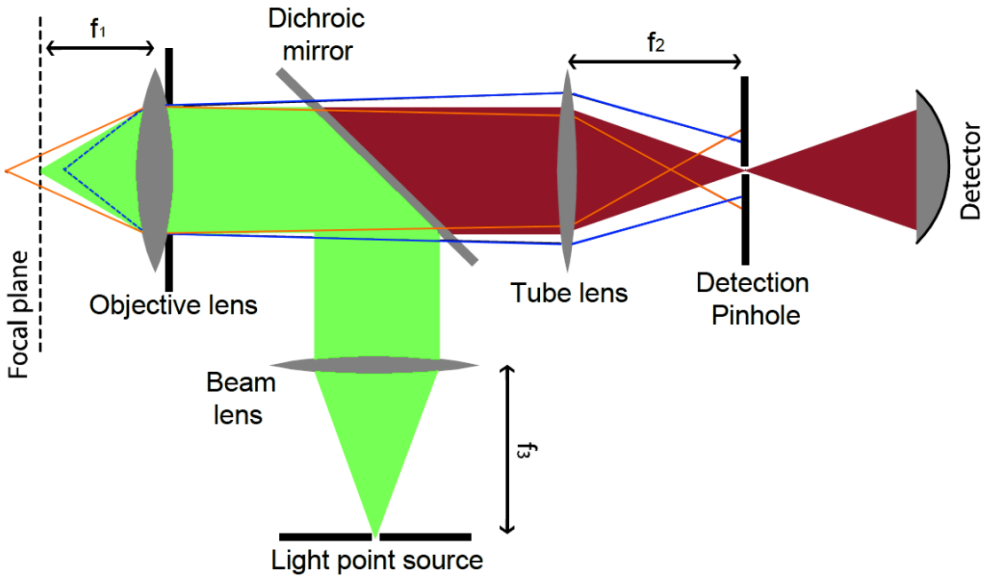

Fig. 1.3.1. Cartoon representation of the confocal microscope. This figure also serves to illustrate the essential features of a confocal microscope. The light from the laser is reflected off the dichroic mirror and focused by high **NA** objective lens. The sample sits at the focus and when excited the fluorescence. This fluorescence is collected by the lens, and passes through the dichroic mirror, because the wavelength of the emitted light is shifted in frequency from the excitation. The pinhole spatially filter the beam from the "out of focus" fluorescence.

1.3.2 Confocal microscopy experimental setup

The “work horse” in all experiments presented in Thesis were two custom-made confocal microscopes, designed and realized by the candidate at the laboratory of the “Quantum Optics” research group of the National Institute of Metrologic Research (INRiM). These systems have the advantage, with respect to commercial ones, to be more versatile, because they are mounted over an optical table and each optical element (lens, dichroic beamsplitter, filters) of the setup can be adopted for a specific sample or addition modules like microware excitation of the sample can be included; moreover the light emitted from color centres can be directly coupled to other optical systems for different quantum optics experiments.

The first experimental setup realized at the INRIM is shown in Fig. 1.3.2. The excitation light emitted by a solid state lasers operating at 532 nm ((Nd-YAG LDH-FA series PicoQuant, repetition rate (2.5-80), 20 mW max output) or is coupled by 20× objective into a singlemode fiber. This procedure allows one to select only one spatial laser mode and have clean beam profile on the output. The laser beam then is expanded by a 4× objective and is sent, through a double-mirrors system, to a dichroic mirror (longpass at 567 nm for the 532 nm excitation, Thorlabs), which reflects the excitation light inside the objective (Olympus 100×, NA = 0.9 in air, or Olympus 100×, NA = 1.3 in oil). The sample is mounted vertically on a closed-loop XYZ piezoelectric stage, remotely controlled via PC, allowing positioning with nanometric resolution and 80×80 μm^2 maximum area. The fluorescence light is collected by the same objective used for excitation and then passes through the dichroic beamsplitter and a set of long-pass filters in order to obtain a suitable attenuation ($>10^{12}$) of the 532nm component. The signal is then focused by a f = 100 mm achromatic doublet and coupled to a 50 μm graded index multimode optical fiber that not only delivers the signal to the detectors, but also acts as a pinhole for the confocal system. The overall magnification of the microscope is then 60x and the back-projected pinhole diameter at the focusing point in the sample is 0.83μm, corresponding at 1.2 times the diameter of the Airy Disk at 532 nm.

The fiber leads to an integrated beam-splitter whose outputs are connected to two Single Photon Avalanche Photo-Diodes (SPADs) (Excelitas model SPCM-AQRH- 13FC), operating in Geiger mode. This configuration reproduces a “Hanbury Brown and Twiss” interferometer (HBT) allowing the detection of a single emitter via the measurement of the second order autocorrelation function $g^{(2)}(t)$ computed from the coincidence counts between the two detectors (see Chapter 1.4).

The setup works in three different configurations:

First: imaging. When the user wants to make imaging of the sample, the electronic signal from one or both detectors is sent to a single photon avalanche detector (SPAD) (Agilent 5313A) and the PC can make the scanning map of the sample using a Labview program that was written for the scope. Scanning resolution is typically 250 nm/pixel and the dwell time is 7 ms for a good signal/noise ratio. The counter that communicates with the PC via data acquisition card (DAC) Nation Instruments, the software is written in Labview and works in asynchronous mode: a start command is sent to the counter that is enabled for a trigger time selected by the user (the dwell time, typically 7 ms, internally triggered). After the number of counts is received, the software reads and display the data on a color-graded map and communicates the new piezo position.

Second: Spectrum collection. A monochromator is also present for recording spectra of the fluorescence: in this configuration the light coming from one of the two arms of the HBT interferometer is sent into the device, while the others serves as monitor for excitation intensity. The monochromator is a single-grating, 1600 grooves/mm, controlled by the pc and the output is again fiber-coupled and sent to another APD. The resolution is around 7 nm and spectra typically needs 10 minutes to be collected.

Third: Second-order correlation measure: In this configuration the signal from one SPAD is sent to a Time to Amplitude Converter (TAC) into the Start input; the second SPAD's signal passes through a delay line and then goes into the Stop input. TAC's output is analyzed by a Multi Channel Analyzer (MCA) that makes a histogram of the delay times for every photon couple (start-stop) (the functions of both the TAC and MCA are integrated in a IDQ800 time-to-digital converter). A single emitter cannot emits two photon at the same time, so the two detectors must never detect a photon within a small (compared to the emitter's lifetime) temporal window. The shape of recorded chronogram can be well described by theory and permits to extract useful information about the emitter's lifetime, the presence of a shelving state and the signal to noise ratio.

The second setup based on confocal geometry, but adopted also for the wide field imaging. It consisted of inverted microscope Olympus IX73 with special module, there optical elements for the confocal part were integrated (Fig.1.3.3(a)). Microscope has few independent output ports and can be used for wide-field imaging with CCD camera or photodiodes, confocal imaging with SPADs and visual observation. The laser beam (532nm, Coherent Prometheus 100NE, 60-80mW)) through the system of aligning mirrors is sent onto the dichroic mirror which reflects the excitation light in vertical direction inside the objective (Olympus 60× UPlanApo, NA = 0.67). The diamond sample was mounted on the microwave planar ring antenna (see Chapter 1.3.2.1). The sample with antenna was situated in the Stage Top Chamber "H301-K-FRAME"

fitted in the moving stage of the microscope and connected to “Okolab Temperature Controller”. The moving stage consists of a stepper motor XY stage with 200x200mm travel range and nanoscan Z (NZ400) with a range 400 micron. The photoluminescence from the diamond sample (PL) was collected, spectrally filtered, and detected with two different acquisition systems. Four percent of the total PL was sent on HBT interferometer with single photon avalanche detectors (SPADs). Major part was collected by NA=0.25 objective (Olympus 10x) and imaged onto a bias photodetector (Thorlabs DET 10A2). (Fig. 1.3.3(b)). An ancillary switchable output was used for the wide-field imaging with CCD camera.

The second setup, unlike the first one was adapted for the magnetometry of bio- objects, where the main goal was measuring of biological currents in tissues of live cells. Therefore, *greater attention* was focused on temperature stabilization, convenience features and integrability. As a field sensitive sensor for these measurements we used bulk diamond crystals with high density ($n=3x10^{19}cm^{-3}$) of the NV centres, so quantum-optical samples characterization (single NV centres, nanodiamonds) was done on the first setup, better-*designed for these purposes.*

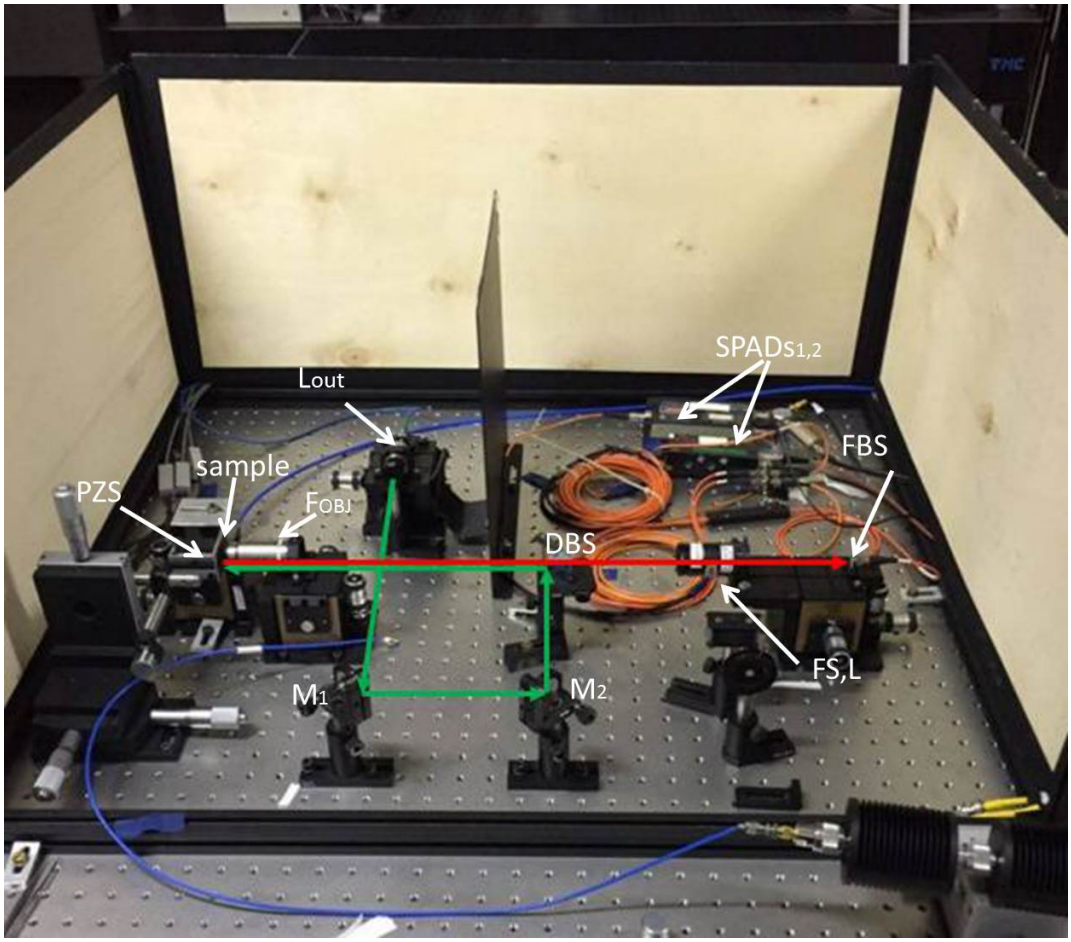

Fig. 1.3.2. Confocal microscope at INRIM. The excitation light from laser is expanded by the first objective (L_{OUT}), then is redirected towards the alignment mirrors M_1 and M_2; it is reflected by the dichroic beamsplitter DBS and focused by the focusing objective F_{OBJ} on the sample, which is mounted over a piezoelectric stage (PZS). The luminescence is transmitted by the dichroic, filtered from the scattered excitation beam by the filters set (FS) and coupled by the tube lens L into a multi-modal fiber with an integrated 50-50% beamsplitter (FBS). The signal is acquired by detectors SPAD1 and SPAD2.

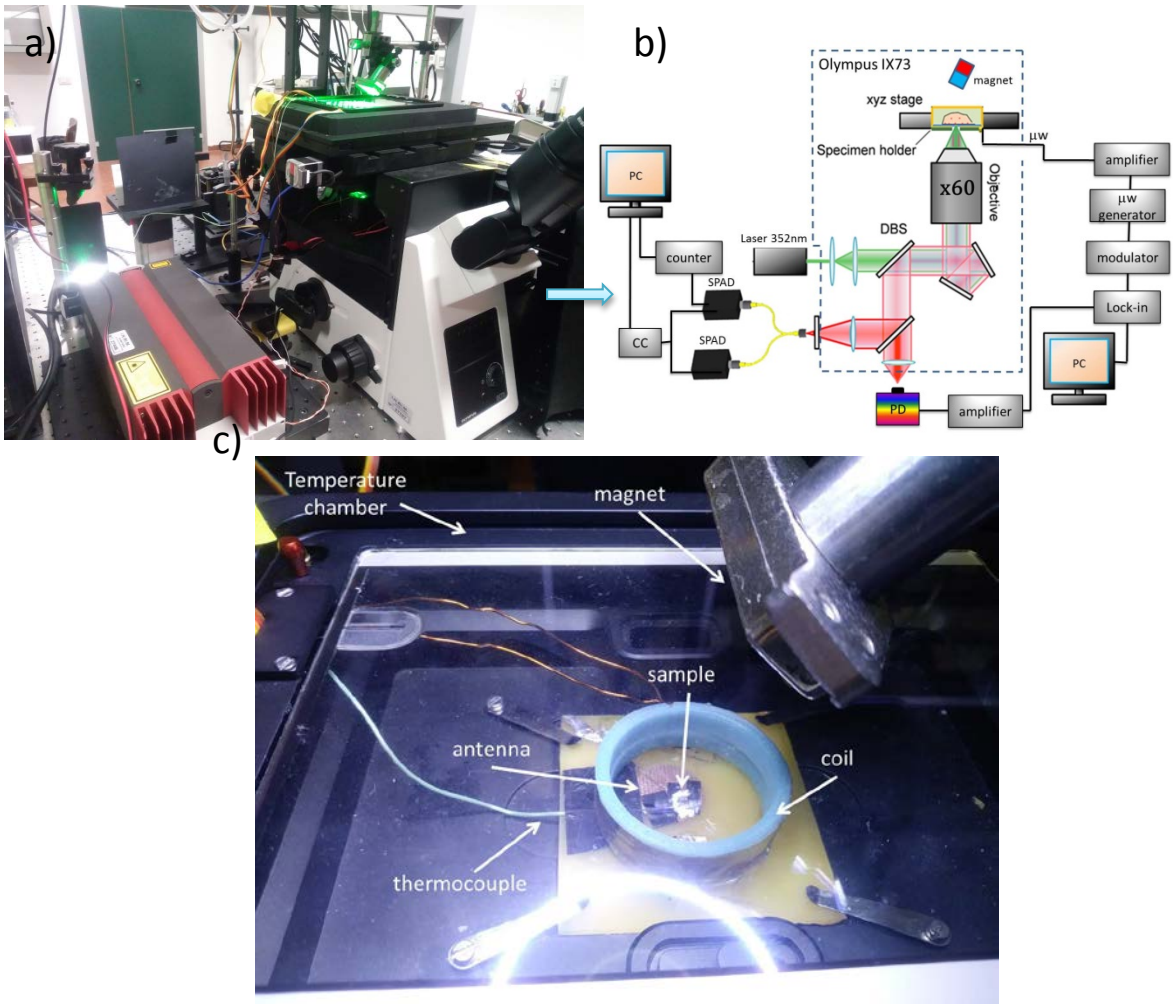

Fig. 1.3.3. Confocal microscope, integrated with widefield microscope for bio-measurements

a) General view of the setup without if the electronics part. b) A schematic of the measurement setup shown in Fig.1.3.3(a). The excitation light from laser is sent to the inverted microscope Olympus IX73; it is reflected by the dichroic beamsplitter DBS and focused by the objective on the sample, situated in the Stage Top Chamber with a temperature control. The photoluminescence from the diamond sample is collected and detected with two different acquisition systems: HBT interferometer with SPADs or bias photodetector. c) Thermostabilized part of the setup with antenna and sample.

1.3.2.1 The magnetic field and microwave equipment

In order to manipulate the electron spin of NV centres, magnetic fields and microwaves are needed and the second part of the setup acts to this scope. The magnetic field is used to separate resonance transitions from NVs centres with different orientation of NV axis. The field must be sufficiently homogeneous because we are observing not only single spins but ensembles with high density. The external magnetic field was applied by magnet with which generates a ~10 mT field. Magnet was fixed on the stage with the possibility to moving it in x, y, z directions and to rotate it for better alignment with the NV axis. For the magnetic field modulation in some experiments we also used a coil, set symmetrically above the diamond sample (Fig.1.3.3(c)).

In order to measure ODMR spectra, a variable-frequency microwave (MW) field must be applied to the NV– system. We used a commercial MW source (Agilent N517172B) operated in the range 9kHz-3GHz. The output MWs signals were amplified (Mini-Circuits ZHL-16W-43+) and then sent to the Bi Directional coupler (WERLATONE C8000-102). The coupled output is sent to a spectrum analyzer (Agilent E4405B) while the transmitted output to the microwave antenna. It is a microwave planar ring antenna specifically designed for optically-detected magnetic resonance (ODMR) of nitrogen-vacancy (NV) centres in diamond (Fig.1.3.4).
In particular, the antenna is characterized by the following characteristics:

(i) It is placed beneath a diamond sample, thereby does not interfere with the objective lens or the specimen.

(ii) It generates a spatially uniform field within an area of about 1 mm^2, which covers large parts of typical diamond samples.

(iii) It has a resonance frequency at around 2.8 GHz and a bandwidth of a ~200 MHz so that multiple resonances can be addressed.

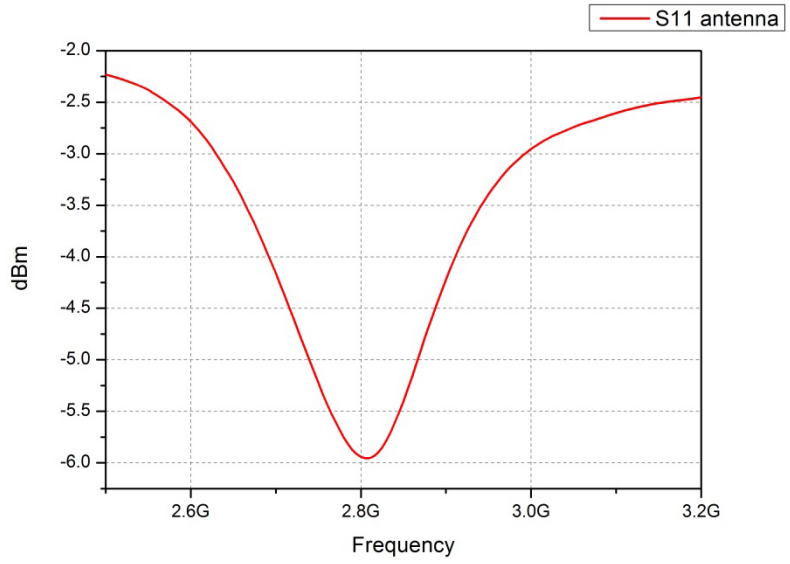

Fig. 1.3.4 Reflection coefficients S_{11} of the antenna measured with a vector network analyzer.

1.4 Second-order autocorrelation function

A criterion for the characterization of the quantum nature of light is necessary in order to determine whether a light emitter is a single photon source. As mentioned before NV centres can be classified as deterministic single-photon emitters. Once excited, the system relaxes by emitting one photon. Before emitting a second photon, the system needs a second transition back

again to the excited state. The time separation between two consecutive photon emissions is determined by the lifetime of the centre and there is no probability for two photons to be emitted at the same time from the same NV. This effect can be formally represented through the definition of the second-order autocorrelation function $g^{(2)}(t)$ which has the following expression for an electromagnetic wave:

$$g^{(2)}(t) = \frac{\langle I(t)I(t+\tau)\rangle}{\langle I(t)\rangle^2} \tag{1.4.1}$$

where $I(t)$ and $I(t+\tau)$ are the electric field intensities of the electromagnetic field respectively at time t and $t+\tau$ [33]. This function can be interpreted as the probability to detect two photons with a time difference of τ. The intensity $I(t) = E^*(t)E(t)$ is directly proportional to the electric field which, in quantum field theory allows to express the $g^{(2)}(t)$ function in terms of creations and annihilation operators $\hat{a}^\dagger, \hat{a}$:

$$g^2(t) = \frac{\langle \hat{a}^\dagger(t)\cdot\hat{a}(t)\cdot\hat{a}^\dagger(t+\tau)\cdot\hat{a}(t+\tau)\rangle}{\langle \hat{a}^\dagger(t)\cdot\hat{a}(t)\rangle^2} \tag{1.4.2}$$

By knowing that the bosonic number operator is: $\hat{n} = \hat{a}^\dagger\cdot\hat{a}$ and $\left[\hat{a}(t), \hat{a}^\dagger(t)\right] = \hat{a}\hat{a}^\dagger - \hat{a}^\dagger\hat{a} = 1$ for $\tau \to 0$ we obtain:

$$\begin{aligned}\lim_{\tau\to 0} g^2(t) \approx g^2(0) = \frac{\langle \hat{a}^\dagger\hat{a}\hat{a}^\dagger\hat{a}\rangle}{\langle \hat{a}^\dagger\hat{a}\rangle^2} = \frac{\langle \hat{a}^\dagger(\hat{a}\hat{a}^\dagger - 1)\hat{a}\rangle}{\langle \hat{a}^\dagger\hat{a}\rangle^2} = \\ = \frac{\langle \hat{a}^\dagger\hat{a}\hat{a}^\dagger\hat{a} - \hat{a}^\dagger\hat{a}\rangle}{\langle \hat{a}^\dagger\hat{a}\rangle^2} = \frac{\langle \hat{n}^2\rangle - \langle\hat{n}\rangle}{\langle\hat{n}\rangle^2}\end{aligned} \tag{1.4.3}$$

Where $\langle\hat{n}\rangle$ is the mean value of the Fock state, referred also as a quantized monochromatic field with an angular frequency ω and n photons. Notably, different types of light can be classified thanks to $g^{(2)}(t)$, or more precisely, they depend on their value of $g^{(2)}(0)$.

Coherent source

The perfectly consistent monochromatic light source, laser, can be defined through the coherent state $|a\rangle = \sum_n c_n |n\rangle$ with photon number distribution associated with Poissonian statistic[33]:

$$p_n = \frac{\mu^n e^{-\mu}}{n!}, \tag{1.4.4}$$

where μ is the average number of photons.

Then from Eq.1.4.3 follows:

$$g^{(2)}(0) = 1 \tag{1.4.5}$$

The main characteristic of a coherent state is that $g^{(2)}(t)\big|_{\forall t} = 1$.

Thermal source

Thermal sources are for example light bulbs or discharge lamps and can be explained through the so-called thermal state. The photon number distribution characteristic of a thermal state is:

$$p_n = \frac{1}{1-\mu}\left(\frac{\mu}{\mu+1}\right)^n \tag{1.4.6}$$

where μ is the mean value. The second-order autocorrelation function, in this case, assumes the value:

$$g^{(2)}(0) = 2 \tag{1.4.7}$$

Quantum source

From Eq. 1.4.3 it is easy to note that for a state single photon state with n = 1, $g^{(2)}(0) = 0$. This obviously represents the ideal case, while in real experimental procedures background noise and dark counts from the detectors are always present. The $g^2(0) = 0$ value is therefore to be regarded as an ideal limit, but typically $g^{(2)}(0) < 0.5$ value can be considering as upper limit to confirm the presence of single photon source. If the value of the autocorrelation function is $g^{(2)}(0) = 0$, there is no bunching between photons: this means that there is a time anti-correlation between two photons of the same source. This effect is called anti-bunching. The characteristic theoretical trend of this effect can be observed in Fig. 1.4.1. On the left, a continuous wave source is shown, while in the right picture of Fig. 1.4.1, a pulsed wave is considered: in both cases at zero-time delay the second order autocorrelation function tends to zero[34].

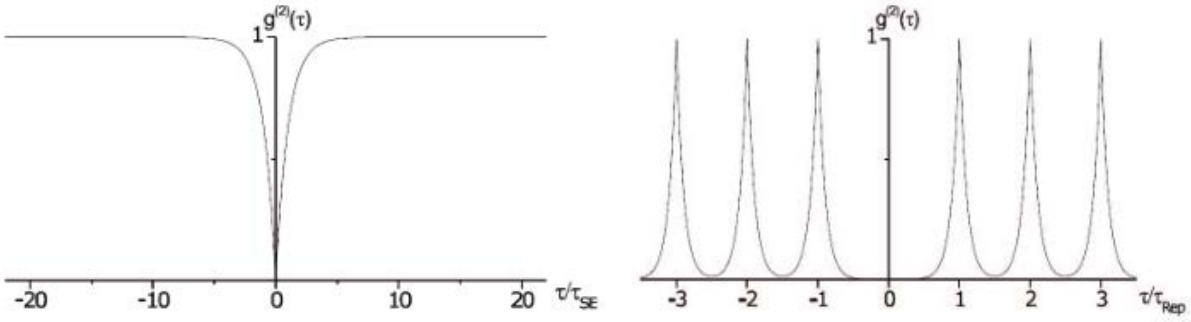

Fig. 1.4.1 Theoretical g^2 function for a continuous wave source (left) and a pulsed wave source (right). In both cases, at zero-time delay the second order autocorrelation function tends to zero: the source under exam is a single-photon source.

1.4.1 NV centre as a single photon source

1.4.1.1 Two level model

A very simple model for estimating the dynamics of a color centre is clearly a two-level system with a ground state, labelled by 1 and the excited state, number 2. When considering a NV centre in diamond, after an excitation, the system evolves from the ground state to one of the available excited states and rapidly relaxes to the lowest excited state in a not radiative way. Finally the system relaxes from 2 to 1 in a radiative way with a rate k_{21}. k_{12} is the excitation rate that depends on the pumping power P, i.e.:

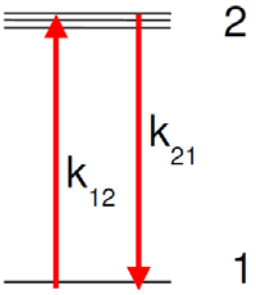

Fig 1.4.2: The two-level model: Transitions with solid lines are radiative, while the one with dotted line is a fast nonradiative transition.

The rate equations for the two-level model are:

$$\begin{pmatrix} \dot{n}_1 \\ \dot{n}_2 \end{pmatrix} = \begin{pmatrix} -k_{12} & k_{21} \\ k_{12} & -k_{21} \end{pmatrix} \bullet \begin{pmatrix} n_1 \\ n_2 \end{pmatrix} \tag{1.4.8}$$

Where k_{12} is clearly proportional to the pumping light power: $k_{12} = \alpha P$ and k_{21} is the sum of radiative and non-radiative (if exists) decay rate. The differential equations system should be solved with the initial condition of the system being prepared in the ground state at $t = 0$, i.e.:

$$\begin{cases} n_1(0) = 0 \\ n_2(0) = 0 \end{cases} \tag{1.4.9}$$

Considering that the electromagnetic field is emitted in photons, emission intensities can be substituted by emission probabilities: thus, let n_1 and n_2 be the probabilities of finding the system on either the ground or excited state, respectively. Then, we can replace in Eq. 1.4.1:

$$(t) = kn_2(\infty) \tag{1.4.10}$$

Eq.(1.4.10) expresses the emission probability for the first photon at a generic time τ with k being the radiative emission rate. Since we assume that the pump light was turned on a long time before τ, the system is in steady state, thus n_2 is to be evaluated at $\tau \to \infty$. i.e:

$$(t+\tau) = kn_2(\tau) \tag{1.4.11}$$

Eq. (1.4.11) expresses the probability of emission for the second photon, after the first was emitted at time t. The term t is thus representing the delay between the two photon emissions. Since the emission of the first photon prepares the color centre on the ground state, the emission probability of the second photon is proportional to $n_2(\tau)$ and, while it does not depends from t.
Note that in Eq. 1.4.1 the time average is performed on t, so the average actually vanishes because it is simply the mean squared intensity, i.e.:

$$\langle I \rangle^2 = I(t)^2 = \left[kn_2(\infty)\right]^2 \tag{1.4.12}$$

Then, from Eq.1.4.1, follows that the second-order autocorrelation function for a single quantum system with one radiative transition from level 2 to 1 can be written as:

$$g^2(t) = \frac{n_2(t)}{n_2(\infty)} = 1 - e^{-\lambda_1|t|} \tag{1.4.13}$$

with $\lambda_1 = k_{12} + k_{21}$.

Measuring the correlation function at different pump powers permits to obtain the k_{21} parameter: $\lambda_1(P) = k_{21} + \alpha P$.

Since the excitation photons have an energy which is larger than the transition gap (i.e. in the excitation process is “off-resonance”), there is no stimulated emission and therefore k_{21} does not depend from the pump power. If a non-radiative decay mode from 2 to 1 with a rate k_{21}^N is to be taken into account, then the total decay rate is: $k_{21} = k_{21}^R + k_{21}^N$.

The quantum efficiency of the emitter is defined as the following ratio:

$$\eta_Q = \frac{k_{12}}{k_{21}^R + k_{21}^N} \quad . \tag{1.4.14}$$

Evaluating $n_2(\tau \rightarrow \infty)$ from the solution of Eq. 1.4.8 system yields:

$$n_2(\infty) = \frac{k_{12}}{k_{12} + k_{21}^N} \tag{1.4.15}$$

and the number of photons detected per second is the probability product of finding the system on the excited state $n_2(\infty)$, have a radiative emission, k_{21}^R and detecting the photon by the system, η_d thus:

$$R = n_2(\infty) k_{21}^R \eta_d = \frac{k_{12}}{k_{12} + k_{21}^N} \eta_d k_{21}^R = \eta_d \eta \frac{k_{21}}{k_{21}/\alpha P + 1}. \tag{1.4.16}$$

Typically, measures of rate *R* versus pump power (*P)* uses this relation to fit experimental data, written in this form:

$$R = I_\infty \frac{P}{P + P_{sat}} \tag{1.4.16}$$

Where I_∞ indicates the maximum count rate when complete saturation of the emitter occurs. If the detection efficiency of the microscope is known, the quantum efficiency can be derived directly. The following relations are straightforward:

$$\begin{cases} I_\infty = \eta_d \eta k_{21} \\ P_{sat} = k_{21} / \alpha \end{cases} \tag{1.4.17}$$

If η_d is known, the quantum efficiency can be directly derived. In practice, the estimation of η_d is difficult because the collection efficiency of the objective is affected by spherical aberrations, depending on several factors, among which the focal depth that varies from one colorcentre to another. Nevertheless, a rough estimation can be done, at least at the order of magnitude level. The parameter α is proportional to the absorption cross-section, considering that the excitation probability is given by the product of the absorption cross section by the incoming photon's flux. Thus:

$$k_{12} = \alpha P = \frac{\sigma I}{h\lambda}, \tag{1.4.18}$$

where $h\nu$ is the photon energy.

This model reliably describes very well only the correlation function of some colorcentres. For a more complete description of several systems a three level model must be developed, with a non-radiative transition occurring through a shelving state, as shown in the Fig. 1.4.2:

1.4.1.2 Three level model

This model was firstly developed for the study of single molecule fluorescence and is based on the assumption that the quantum system under investigation could have both triplet and singlet levels. Typically the singlet has lowest energy and is the ground state (but an important exception is the NV centre, that can be regarded a two bounded hole system instead of six electrons, in which the situation is opposite). The new level in between originates because of the triplet configuration and transitions from the ground state and the excited state, which are singlet configurations, are not allowed by the selection rule of the electric dipole. Nevertheless is possible to have non radiative transitions and the effect is known as “inter system crossing”

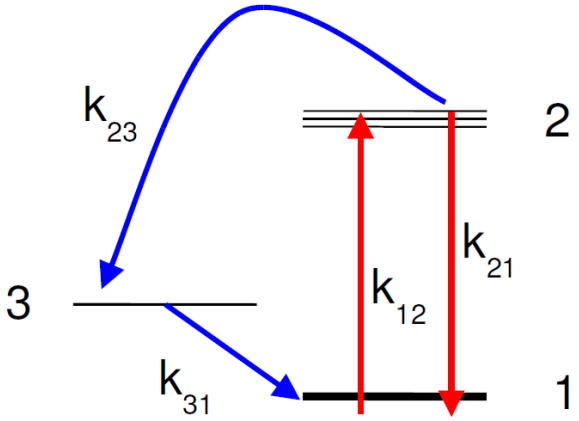

Fig 1.4.3: The three-level model

The system of equations governing the population of this three level system is:

$$\begin{pmatrix} \dot{n}_1 \\ \dot{n}_2 \\ \dot{n}_3 \end{pmatrix} = \begin{pmatrix} -k_{12} & k_{21} & k_{31} \\ k_{12} & -k_{21} - k_{23} & 0 \\ 0 & k_{23} & -k_{31} \end{pmatrix} \bullet \begin{pmatrix} n_1 \\ n_2 \\ n_3 \end{pmatrix} \tag{1.4.19}$$

With the same initial condition of system prepared in the ground state at t=0

$$\begin{cases} n_1(0) = 0 \\ n_2(0) = 0 \\ n_3(0) = 0 \end{cases}. \tag{1.4.20}$$

Under the assumption that $k_{21} \gg k_{23} + k_{31}$ that is reasonable since k_{23} and k_{31} are not electric dipole transitions, the correlation function is:

$$g^2(t) = \frac{n_2(t)}{n_2(\infty)} = 1 - (1+a)e^{-\lambda_1|t|} + ae^{-\lambda_2|t|} \tag{1.4.21}$$

with $\lambda_1 = k_{21} + k_{21}, \lambda_2 = k_{31} + \frac{k_{23}k_{12}}{k_{12} + k_{21}}$

The λ_1 parameter is again the same of the two-level system and is responsible for the dip in the $g^{(2)}$ function: it can be obtained simply by fitting the $g^{(2)}$ in the short interval around the dip. From this parameter is possible to have a measure of the k_{21} rate in the same way as explained for the simpler two-level model. In the same way, the λ_2 parameter can be obtained just by fitting the $g^{(2)}$ function far away from the dip. The presence of a third level makes the $g^{(2)}$ to exceed the value of 1 just before and after the dip: the photons comes out bunched, because sometimes the color centre goes in a "dark" state and stops working, until it decades again into the ground state. The presence of this third state affects then the maximum photon emission rate. The quantity $1 - 1/Max(g^{(2)}(t))$ is an estimation of how many photons in percentage are lost because of the shelving state. So, if a third level must be, the less limiting situation is the one that have a k_{23} (shelving rate) small and a k_{31} (deshelving rate) high. To known shelving and deshelving rates, the same substitutions of $k_{21} \to \alpha P$ is applied and one obtains:

$$\lambda_2 \to k_{31} + \frac{\alpha P k_{23}}{\alpha P + k_{21}} \tag{1.4.22}$$

In the high pumping power limit λ_2 would reaches k_{23}, but experimentally one observes that λ_2 increases almost linearly. This is explained with a new hypothesis: the deshelving transition, identified by k_{31} is pumping power dependent, a fact that is understandable since this transition is not an electric-dipole one and more complicated processes can happen. One can think the deshelving as a two-way process [35]. First way: a pump photon is absorbed and excites the system from the shelving to an excited state (below the conduction band of diamond), then the spin is flipped and finally a decay to the ground state is allowed, with photon emission; second way, the system simply de-excites in non-radiative way from the triplet state, flipping its spin

and going into the ground state. The first way is more and more favoured as the pumping intensity increases and this in some sort attenuates the problem of emission rate reduction due to the presence of the shelving state. To taking into account both decay ways, one will write:

$$k_{31} = k_{31}^{0}(1+\beta P) \tag{1.4.23}$$

The steady state fluorescence rate is in the case of three-level system is:

$$R = \eta_d \eta \frac{k_{21}}{\frac{k_{21}}{\alpha P} + 1 + \frac{k_{21}}{k_{31}}} \tag{1.4.24}$$

A relation very similar to the previous one is obtained for the two-level system, except for the fact that the presence of k_{31}, that is pump depending, can lead to a slight decreasing of counts at high powers. This is observed for example with NV centres in[36], and also in our measurement with a bulk diamond.

1.4.2 Hanbury Brown and Twiss interferometry

The most important measurement for SPS is evaluating the probability of having more than one photon emitted by the source within a prescribed time interval. This is commonly performed with a Hanbury Brown-Twiss (HBT) interferometer operating at single-photon level.

HBT interferometer is usually implemented using two threshold single photon sensitive detectors (click/no-click) detectors ((e.g. SPADs)) placed at the output ports of a 50:50 beam splitter, optical and electric delay and analysing electronics. The optical delay can be introduced with a longer optical fiber or a different optical path in air, while the electronic delay can be increased by connecting one of the detectors with longer cables to the counting device. The detectors convert luminescent signals into electronic ones, and send them to the input channels of an autocorrelator instrument, in our case IDQ800, (it includes 8-channel time-to-digital converter, coincidence counter, and time interval analyser) that records the time interval between detection events on the two SPADs. Whenever a photon is detected at input channel 1 of the autocorrelator, a timer is started and will not be stopped until a photon is detected at the other input channel. The time *t* elapsed between the two signals of the SPADs is measured in this way. By varying the time delay between the detection events in the two detectors and using the data

collected by the electronic acquisition system, the second order correlation function $g^{(2)}(t)$ can be measured.

The HBT setup used for these measurements is shown below in Fig. 1.4.4.

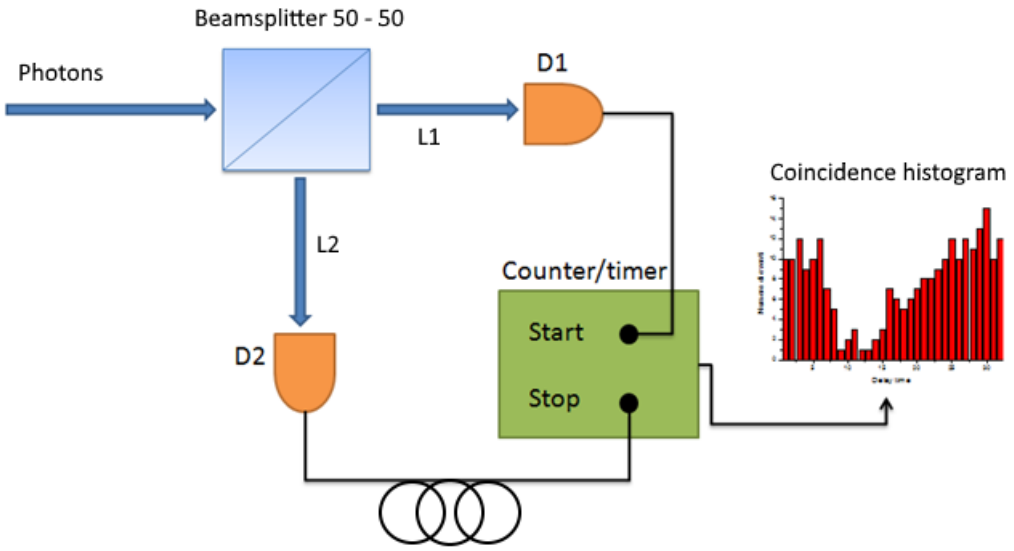

Fig 1.4.4: Schematic representation of a HBT interferometer.

The HBT interferometer is suitable for the estimation of the $g^{(2)}(t)$ function under the assumption that the time interval between two uncorrelated events is much longer than the detection temporal window. Assuming a count rate R of the detectors, it follows that after the arrival of one photon at one detector, the probability of not having a count on the other detector in a time interval Δt is given by:

$$P\Delta t = e^{-\Delta t \cdot R} \tag{1.4.25}$$

This value should be ~ 1. This can be quite strict condition, especially for high count rates and, as it will be show afterwards, a correction is needed.

1.4.3 Experimental estimation of the $g^{(2)}(t)$ function

In order to obtain a normalized and corrected function, from which it is possible to extract the parameters that characterize the emitter under exam, a post-processing of the experimental data acquired from a HBT interferometer is needed. There are four fundamental steps: time-dependent probability distribution corrections, normalization, background corrections, time delay subtraction. Fig. 1.4.5 reports the chronogram of time coincidence detection events from a

quantum emitter. It is evident that the detection probability decreases with increasing delay times. The data refer to an individual NV centre in diamond, and the average count rate is ~100 kcps for both of detectors. The two peaks at lateral positions respect to the anti – bunching dip are called "backflash" peaks. These ghost peaks are typical for fiber-coupled setups, and the physical phenomenon behind their origin is the stimulated emission from the silicon detector of an IR secondary photon and its detection by the other detector. These photons can be emitted by both detectors, for this reason it is possible to observe two different peaks at different delays. The optical path between the two detectors is constant and the events accumulate at a precise delay value.

1.4.3.1 Time-dependent probability distribution correction

The disadvantage of start – stop measurements in HBT interferometry is due to the non-uniform probability distribution for each considered delay time. If we divide the time acquisition window in finite intervals w, the probability distribution is given by:

$$P = (1 - p)^{n-1} \tag{1.4.26}$$

where p depends only on the count rate. This distribution derives from the fact that in order to detect a photon within the n-th channel (that corresponds to a certain delay) no detection should have happened in all the previous $(n - 1)$ channels, since a detection prior to the delay that corresponds to the n-th channel would have stopped the measurement. From this fact derives that at increasing delay times the probability is strongly reduced, especially at high count rates. It is possible to perform a fit of the data with the probability distribution reported in Eq. 1.4.26 to correct the exponential decay of the chronogram, introducing a multiplying constant $k$as free parameter, that takes in account other affecting factors besides the count rate (e.g. beamsplitter asymmetries, unbalanced detection efficiencies). This should be done by excluding significant data such as the anti–bunching dip and the backflash peaks (e.g. delays >400 ns in Fig. 1.4.5) which can affect the result. The data can then be corrected in the normalization process by associating to each interval (n) the obtained probability p.

1.4.3.2 Normalization

The experimentally obtained chronogram at CW excitation in Fig. 1.4.5 represents the $g^{(2)}(t)$ function only in an indirect sense, since it corresponds only to the delay time counts. In order to

reconstruct the correlation function the “normalization” procedure is needed, which can be performed through the following formula:

$$g_{\exp}^{(2)}(t) = \frac{C(t)}{R_1 R_2 T w (1-p)^{n(t)}} \tag{1.4.26}$$

where $R1$ and $R2$ are the count rates of the two detectors, T is the total acquisition time and w is the temporal width of each channel of the IDQ800 (“binning”), p and n are respectively the probability of the detection at a given channel n and the number of the channel discussed in the previous Section. The formula indicates that each data point of the $g^{(2)}(t)$ function is the ratio between the number of “start & stop” pairs that have a defined time delay and the corresponding number of pairs that would have been obtained from a coherent light emitter at the same delay. The chronograms reported in Fig. 1.4.6 consist of the same data reported in Fig. 1.4.5 upon the above-described normalization.

1.4.3.3 Background contribution

To take into account background counts (pump light that leaks into the detection chain, fluorescence arising from surface contaminations and ambient light), and in this way to obtain a correct estimation of the $g^{(2)}(t)$ function, it is necessary to measure the background contributions by collecting the PL signal from a point away from the single centre. The contributions from the background B and the light emitted by the single-centre S to the overall signal Ican be separated as $I = S + B$, then

$$\begin{aligned} g^{(2)}(t) &\equiv \frac{\left\langle \left[S(t_0+t) + B(t_0+t) \right] \right\rangle \cdot \left\langle \left[S(t_0) + B(t_0) \right] \right\rangle}{\left\langle S+B \right\rangle^2} = \\ &= \frac{1}{\left\langle S+B \right\rangle^2} \left[\left\langle S(t_0+t)\cdot S(t_0) \right\rangle + \left\langle S(t_0+t)\cdot B(t_0) \right\rangle + \left\langle B(t_0+t)\cdot S(t_0) \right\rangle + \left\langle B(t_0+t)\cdot B(t_0) \right\rangle \right] \end{aligned} \tag{1.4.27}$$

Since the background is supposed to be uncorrelated light, i.e. $B(t_0+t) = B(t_0)$ for every t, and introducing $\rho = \frac{\langle S \rangle}{\langle S+B \rangle}$, leads to:

$$g^{(2)}(t)=\frac{1}{\langle S+B\rangle^2}\left[\langle S(t_0+t)\cdot S(t_0)\rangle+2\langle S\rangle\langle B\rangle+\langle B\rangle^2\right]=\frac{\langle S(t_0+t)\cdot S(t_0)\rangle}{\langle S+B\rangle^2}+1-\rho^2=$$
$$=\rho^2\frac{\langle S(t_0+t)\cdot S(t_0)\rangle}{\langle S\rangle^2}+1-\rho^2=\rho^2 g^{(2)}_{corr}+1-\rho^2 \qquad (1.4.28)$$

Where $g^{(2)}_{corr}$ is the correlation function corrected from background. Finally,

$$g^{(2)}_{corr}=\frac{g^{(2)}+\rho^2-1}{\rho^2} \qquad (1.4.29)$$

This correction is very relevant when a strong background noise is present: in these cases, a correct estimation of the background light is crucial to determine whether an emitter is a SPS. For example the non-background-subtracted data, reported in Fig. 1.4.6, show a $g^{(2)}(t)$ function which would not be compatible with a single photon emitter, since its value $g^{(2)}(0)\approx 0.6$.

Nonetheless, after the background correction we obtain the graph reported in Fig. 1.4.7, which yields a $g^{(2)}(0)$ value which is fully compatible with a SPS. This example is a bit extreme, since the signal to noise ratio is close to 2, but it often happens due to impurities, low luminescence from SPS, non-efficient coupling.

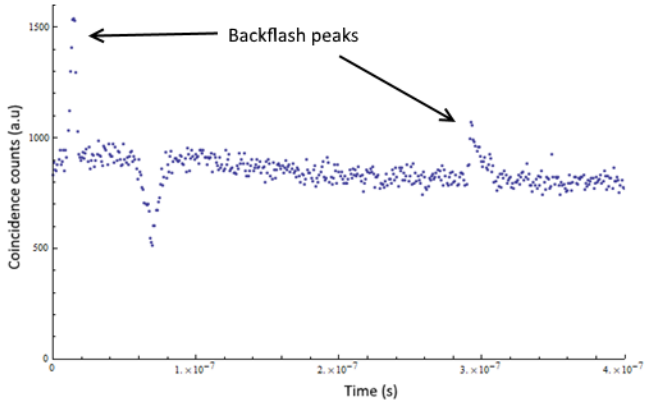

Fig 1.4.5 Raw data chronograms. The data are acquired from an NV– centre

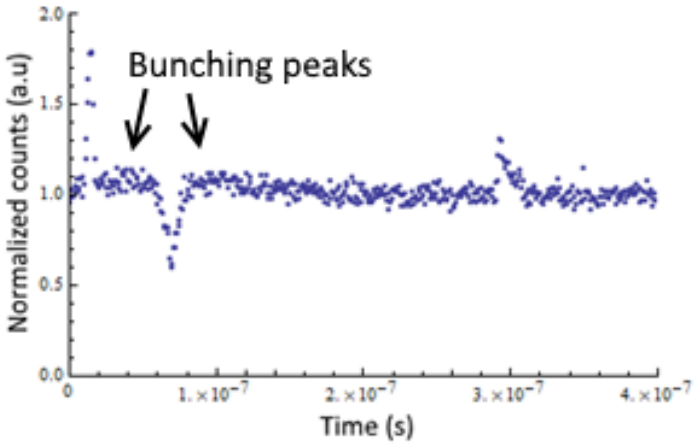

Fig. 1.4.6 Normalized chronograms "bunching" peaks on the histogram give information about the shelving state in electronic structure of the emitter (three-level system).

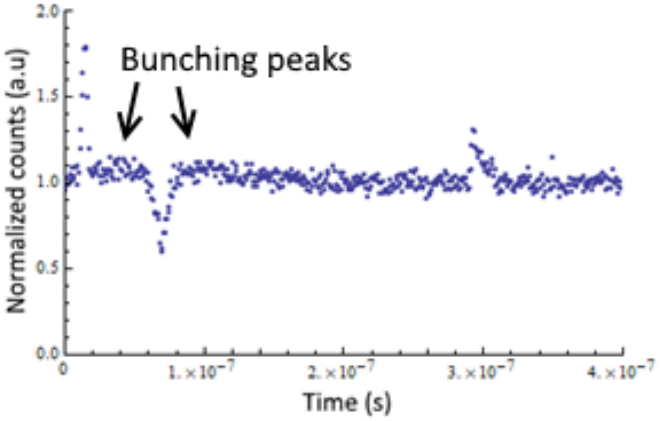

Fig. 1.4.7 Normalized chronograms. "bunching" peaks on the histogram give information about the shelving state in electronic structure of the emitter (three-level system).

1.4.4 Experimental estimation of the $g^{(2)}(t)$ function in pulsed excitation regime

Under pulsed excitation the power is concentrated into small time intervals (in this case, about 70 ps in duration): events of double photon emission within the same pulse are very rare, since they imply for the centre a double cycle of excitation and emission within the 70 ps over which the laser is emitting the pulse. The second-order correlation function represents as a series of peaks which are chronologically separated by the laser's repetition period, in our case 12.5 ns (corresponding to a 80 MHz frequency) (see Fig. 1.4.8).

The normalization of $g^{(2)}(t)$ is performed by considering the counts over a peak, rather than over a bin channel, as performed in CW measurements. Similarly to what is done for the CW

excitation, each peak of the $g^{(2)}(t)$ function represents the ratio between the number of "start &stop" pairs that fall into a single peak located into a defined delay time interval and the corresponding number of pairs that would have been obtained at the same delay interval in the case of a coherent light emitter. The latter quantity is given by the product of $R1$ and $R2$ which are the count rates of the two detectors, the integration time T and the temporal width $w$of one peak (i.e. instead of the temporal width of one time bin). One can take w equal to the repetition period of the laser t_r. The normalized $g^{(2)}(t)$ in this case can be written in this way:

$$g^{(2)}(t) = \frac{C(t)}{R_1 R_2 T t_r} \tag{1.4.30}$$

Then it is possible to calculate the $g^{(2)}(t)$ function as:

$$g^{(2)}(t) = \frac{P(click_{D1}, click_{D2})}{P(click_{D1})P(click_{D2})} \tag{1.4.31}$$

where numerator can be calculated as the area under the peak in coincidence histogram corresponding to time at moment $t = 0$, while denominator is represented be the averaged area of other peaks at time $t \neq 0$. As shown in Fig. 1.4.8, the area of peaks was calculated after the substraction of the background radiation. Green peak corresponds to antibunching, while areas of the three red peaks were averaged in order to have better accuracy and estimate of the uncertainty associated with the measurement. The red baseline in Fig. 1.4.7 shows the level of background.

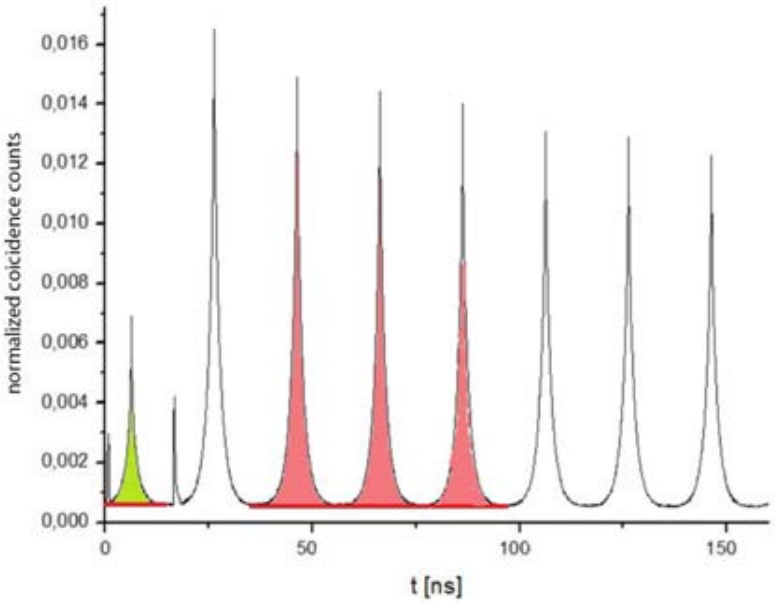

Fig. 1.4.8 Coincidence histogram in pulse excitation regime.

Chapter 2

2.1 Optically detected magnetic resonance

Due to the different photoluminescence (PL) yield of the two spin states $m_s = 0$ and $m_s = \pm 1$, the spin state of the NV center can be optically detected. The experimental technique used for this scope is the Optically Detected Magnetic Resonance (ODMR), which will be described in this section.

Initialization generally is the first step in the ODMR procedure. The NV center is optically pumped by a green laser. After several cycles of excitation and relaxation, the electronic spin of NV center polarises with high probability at $m_s = 0$ ground state and a high level of fluorescence is detected (bright state). Afterwards, by irradiating it continuously with a laser light, microwave (MW) radiation is applied to the NV center. The MW frequency is scanned within a certain range containing the magnetic resonance frequencies. When the MW frequency is on resonance with one of the $m_s = 0 \leftrightarrow m_s = \pm 1$ transitions, the fluorescence level decreases since the MW field transfers the population to the dark state $m_s = \pm 1$ (see Chapter 1 for more details). The associated spectrum showing the fluorescence intensity as a function of MW frequency is called an ODMR spectrum and is plotted in Fig. 2.1.1. The population transfer from the bright state to the dark state is visible as a dip at $D_{gs} \approx 2.87 GHz$ in the ODMR spectrum. An external magnetic field lifts the degeneracy of $m_s = \pm 1$. The splitting is proportional to the applied magnetic field B, increasing at $\Delta\nu \approx 2\gamma_{NV} B_z$ where $\gamma_{NV} = \frac{g\mu_B}{\hbar} \approx 28 MHz/T$ is the gyromagnetic ratio of the NV centre (Fig.2.1.1). The difference in fluorescence intensity between MW on- and off-resonances is called the fluorescence contrast C. For single NV centers, a C = 0.20 contrast is typical. Another important parameter is the linewidth of the magnetic resonance $\Delta\nu_{FWHM}$. For a Lorentzian line shape, the full width at half maximum is related to the inhomogeneously-broadened transverse spin relaxation time $T_2^* = \frac{1}{\pi \Delta\nu_{FWHM}}$, which is ~100 ns for NV centers in diamond with high concentration of nitrogen and tens of μs for NV centers in pure diamonds. In order to measure the transition frequencies and thereby the magnetic field accurately, it is advantageous to have a large contrast and a narrow linewidth.

NV sensing schemes are usually based on either continuous-wave optically detected magnetic resonance (CW-ODMR) or pulsed ODMR, both which are used to determine small shifts of the resonance frequency around a fixed offset. CW ODMR suffers from MW and optical power broadening, degrading contrast *C* and linewidth Δ of the resonance dip. In order to mitigate this

power broadening, a pulsed ODMR protocol uses a temporally separated laser initialization, a MW control π pulse, and a laser readout pulse as demonstrated in Fig. 2.1.2(a). This leads to the decreased linewidths shown in Fig. 2.1.2(b) as compared to CW ODMR. Alteration of the MW power changes the necessary duration of a π pulse, and must be optimized to balance linewidth and contrast of ODMR resonance features. In this thesis we used only CW ODMR measurement, therefore we describe this method in details.

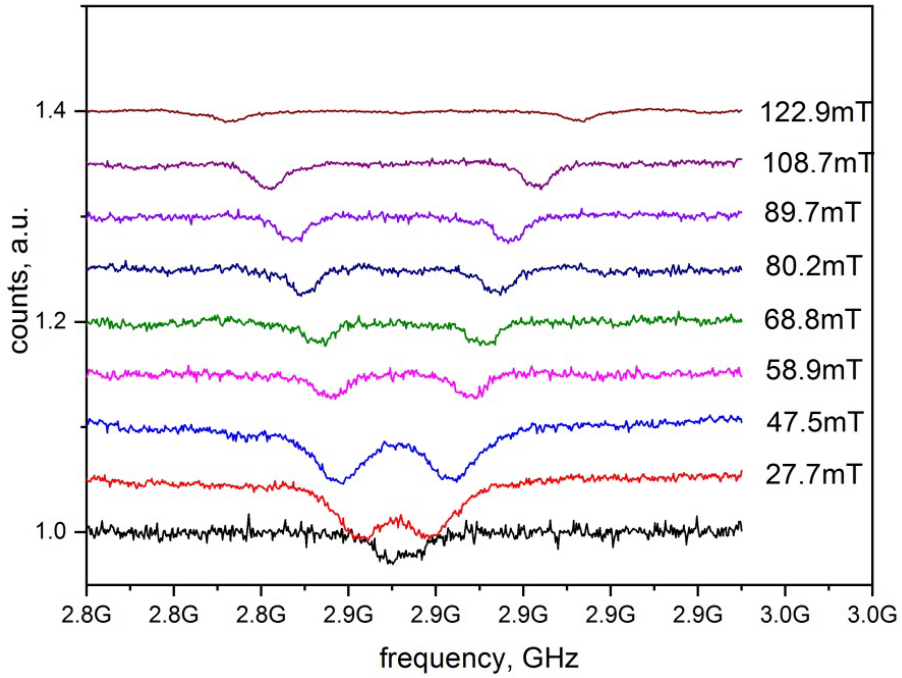

Fig.2.1.1 ODMR spectra in the absence of a magnetic field (black line) and in the presence of an external magnetic field (other colors).

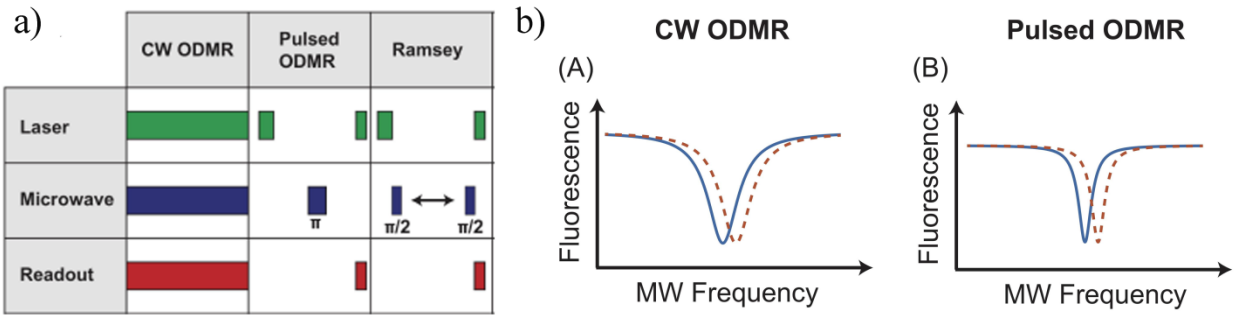

Fig.2.1.2: a) NV Measurement Protocols. Schematic of timing and duration of laser pulses, MW pulses, and readout sequences relative to the field being sensed for common NV diamond protocols. b) DC Magnetometry Protocols. (A) Example CW ODMR lineshape before (blue) and after (red) change in magnetic field. (B) Example pulsed ODMR lineshape before (blue) and after (red) change in magnetic field.

CW-ODMR schemes is more technically convenient for the low frequency fields (< 1 kHz) or spatial field variations over macroscopic areas because avoids the difficulty facing pulsed schemes. The efficiency in this case is based on how large a change in fluorescence can be generated and how small a change can be detected, for incremental resonance shifts induced by an external magnetic/electric field of a temperature. The challenge is thus generating the narrowest spectral linewidth during cw-driving while ensuring that the fluorescence contrast is as high as possible.

The sensitivity of an NV magnetometer employing CW-ODMR is defined as:

$$\eta_B(T/\sqrt{Hz}) \approx \frac{\hbar}{g\mu_B} \frac{1}{C\sqrt{\varepsilon n_{NV} T_2^*}} \tag{2.1}$$

where n_{NV} is the number of NV centers in sensing volume, C – contrast, ε - coupling efficiency. Operating with a single spin has a sensitivity limited to ~100nT/ Hz1/2 but provide nano-scale sensor resolution. The sensitivity can be drastically improved by collecting photons from many NV centers simultaneously (ensemble magnetometry) at the expense of losing the exquisite nanoscale resolution provided by single defects. However number of active NV centers has direct implications on the apparatus used. For single NV spins, the amount of generated light is ~0.05 pW range, which correspond to the working limits of single photon avalanche photodiodes (SPAD). SPADs usually give excellent signal-to-noise ratios due to their low intrinsic noise levels, and do not require additional lock-in detection provided that the noise in the driving fields or environment does not exceed the shot-noise level. Dense ensembles (> 1 ppm NV) prepared through conventional irradiation and annealing techniques promise high sensitivity but display a degraded collective ODMR linewidth due to inhomogeneous broadening. The generated light from an ensemble is beyond the working limits of conventional SPADs, and the use of pin-type photodiodes is necessary which are noisier. In the low-density case (<< 1 ppm NV), an enhanced fluorescence rate can be achieved without too much degradation of the collective coherence/linewidth. However, the inherent cw-ODMR contrast for an ensemble of NVs of a single crystallographic orientation is usually around 1-3% [37], so the working signal-to-noise ratio needs to exceed this limit. The variation in ODMR signal is hardly sufficient in intensity to observe a change in the dynamic. However, the detection sensitivity can be greatly improved using a lock-in method.

2.2 Lock-in technique

The lock-in (or phase-sensitive) technique provides the possibility to detect small signal amplitudes even in the presence of strong noise. The working principle of a lock-in amplifier (LIA) can be explained in this way.

Consider a single ODMR dip with Lorentzian lineshape, linewidth Δ, contrast C and angular frequency ω_0 (Fig. 2.1.3(a)). The detected fluorescence can be written as:

$$I\ (\omega) = I_0\left(1 - C\frac{(\Delta/2)^2}{(\Delta/2)^2 + (\omega-\omega_0)}\right), \tag{2.2}$$

where I_0 is the fluorescence in the absence of MW

Consider a sinusoidal MW input signal, $\omega_{MW}(t) = \omega_c + \omega_{dev}\sin(2\pi f_{\mathrm{mod}} t)$, where f_{mod} – is modulation frequency, ω_c – the central frequency and ω_{dev} – the frequency deviation. The collected fluorescence is then ($\omega_{\mu\omega}$). Suppose that we also have available a reference signal $V^{ref}(t) = V_0^{ref}\sin(2\pi f_{\mathrm{mod}} t)$ at the same modulation frequency (Fig.2.1.4). After integration over the period *T* all oscillating components vanished and only DC output in form of dispersion-type signal with a zero-crossing at ω_0 remains:

$$\begin{aligned} V_{LIA}(\omega_c, \omega_{dev}) &\propto \frac{I(\omega_c+\omega_{dev}) - I(\omega_c-\omega_{dev})}{2} = \\ &= \frac{V_0 C}{2}\left(\frac{(\Delta/2)^2}{(\Delta/2)^2 + \left((\omega_c+\omega_{dev})-\omega_0\right)^2} + \frac{(\Delta/2)^2}{(\Delta/2)^2 + \left((\omega_c-\omega_{dev})-\omega_0\right)^2}\right) \end{aligned} \tag{2.3}$$

V_0 is a voltage determined by F_0 and the output settings of the LIA (Fig 2.1.3(left)). Setting $\omega_{dev} = \frac{\Delta}{2\sqrt{3}}$ maximizes the amplitude of the LIA signal and *consequently the signal-to-noise ratio of the* measured signal. A time-varying field, for example magnetic *B(t),* is sensed by setting $\omega_c = \omega_0$ and detecting resonance frequency shifts $\omega_0(t) = \omega_0 + \delta\omega(t)$, where $\delta\omega(t) = \frac{g_e \mu_B}{\hbar} B(t)$ as:

$$V_{LIA}(t) \approx -\frac{3\sqrt{3}}{4}\frac{V_0 C}{\Delta}\frac{g_e \mu_B}{\hbar} B(t) \tag{2.4}$$

The demodulated signal is linear in the magnetic field and therefore provides a good measure for B(t). Lock-in detection is ideal for very noisy signals and allows one to achieve optimally driving a low-density ensemble, maintaining a linewidth that closely resembles those obtained from single NV defects.

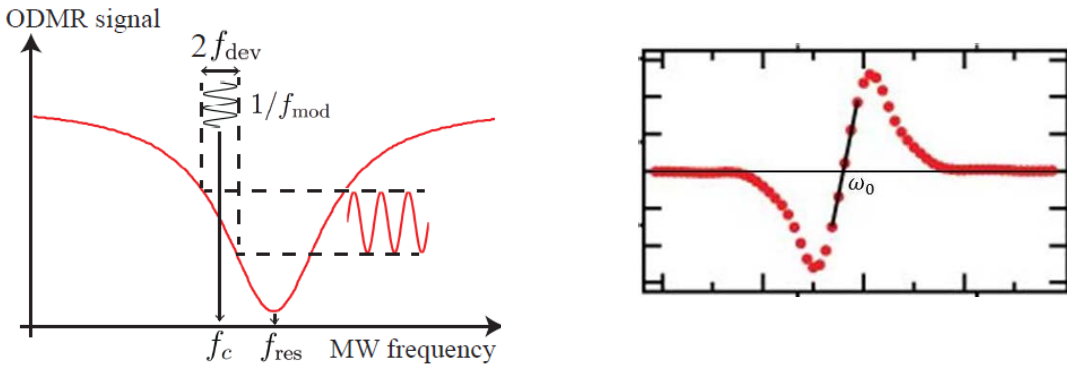

Fig. 2.1.3. (Left) Optically detected magnetic resonance signal. The MW frequency is modulated at the frequency f_{mod} around the central value f_c with a certain frequency deviation f_{dev}. Right: The demodulated signal has a dispersive lineshape when sweeping the central frequency.

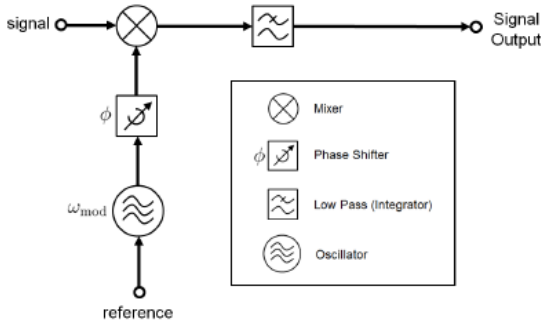

Fig. 2.1.4: Block diagram of a lock-in amplifier.

2.3 Color centers applications

Due to its outstanding properties crystal defects in diamond have emerged as unique objects for a variety of applications, like quantum metrology[38], quantum cryptography and quantum computation[39]. In form of nanocrystals, they can serve, for example, as robust single-photon sources or as fluorescent photostable and nontoxic biomarkers[40]. The most fascinating aspect, however, is the ability of some crystal defects, like the NV center, to locally detect and measure

a number of physical quantities, such as magnetic and electric fields or temperature. In this Section we will summarize these applications[41].

2.3.1 Single photon sources

Not all of the defects in diamonds are optically active and only few of them represent promising single photon sources. To be used as a single photon source (SPS), a color center needs two primary characteristics: a high quantum efficiency and ashort emission lifetime. Also shelving states and/or metastable levels should be avoided because these decay channels usually are characterized by lifetimes 100 – 1000 times larger than the optical decays. These constraints limit the possible SPS candidates.
An ideal single photon source should have some primary characteristics:

- **On – demand**: for each excitation cycle, only single photon should be emitted, multiphotonic emission should be avoided; the source should be deterministic i.e. a single photon should be emitted at any arbitrary time defined by the user.
- **Monochromatic**: the photon emission should be ideally monochromatic, in order to optimize the optical transport and detection protocols. Moreover for some application there is a quantum advantage if the single photons are indistinguishable in all their degrees of freedom.
- **Bright**: high emission rate, that corresponds to short lifetime and high quantum efficiency.

There are different ways to realize single photon sources:

- **Attenuated laser pulses (or "faint lasers"):** The easiest way to approximate a SPS is to use highly attenuated laser pulses: their operation principle is based on applying neutral optical filters until the statistically at the mean 0.1 photon per pulse is emitted: it leads to a probability of 90% for zero photons, 9% for one photon and 1% for more than one photon. Although such a source can be used for certain applications, it suffers from not being truly quantum in the sense that it has second-order correlation function equal to one (does not have antibunching).
- **Heralded single photons:** A widely used alternative is parametric down-conversion, where a non-linear crystal is pumped by UV laser. With a certain probability, a photon of the pump is down-converted to a highly correlated photon pair of a half frequency. The detection of the first photon heralds the presence of the second one with a high accuracy. It is a random process, and no on-demand single-photon generation can be achieved.
- **Semiconductor quantum dots**: "Artificial" atoms, or quantum dots, constitute one of the most promising on demand single photon sources. Quantum dots are tiny semiconductor particles or

nanocrystals, typically operated also at cryogenic temperatures, but newest prototypes can operate at room temperature.[42]

•**Point defects in solid state**: Another up-and-coming, promising quantum technology is based on color centers in diamond. Unfortunately the very broad emission of NV is a major limitation to its use as a single photon source. For this reason, there is a considerable effort being undertaken in exploring other centers with improved photophysical properties. There are a number of candidates, including nickel-, silicon- and chromium-related centers, which also show single-photon emission, but have narrower spectral widths and often shorter lifetimes than NV.

2.3.2 Quantum radiometry

An interesting application of single-photon sources is the one for quantum radiometry - in particular, an attempt to define the candela unit in terms of single photon counts. This idea has been explored in a project involving seven European national metrology institutes, and founded by the European commission[43]. The Quantum Candela project is aimed both at re-defining the unit base in terms of photon number rather than optical power and at developing standards for photon metrology ranging from radiometric standards (10^{13}-10^{14} photons s^{-1}, 10 - 100μW) down to single photons. The present realisation of candela is achieved by calibrating the optical power of a light source against an equivalent electric heater. A potentially more accurate way of realizing the candela is to use a deterministic single-photon source. In perspective, the absorbed photon flux could be determined with greater accuracy than for conventional sources due to reduced uncertainty in the number of emitted photons. As each photon carries a well-defined energy and the photon's flux is known, photon counting becomes a very precise power measurement technique that could bridge the gap between conventional and quantum radiometry.

2.3.3 Sensing with NV– centers

Color centers in diamonds, especially the NV color center, is a promising system for various quantum sensing applications. There have been several studies regarding the use of NV centers to sense magnetic fields[41], [44], electric fields[28], [45], pressure[46], and temperature [47]–[49] at high sensitivities, spatial resolutions and under ambient conditions. Furthermore, NV centers have found applications in the fields of neuroscience and cellular biology[50]–[52] due to the unlimited photostability and low cytotoxicity.

The optical detected magnetic resonance (ODMR) effect makes it possible to modulate the fluorescence intensity, which depends on the magnetic interactions of a single electron spin. This feature formed the basis of several recent proposals aimed at using the NV center to measure magnetic fields and other physical quantities with high sensitivity and nanoscale spatial resolution[10]. To understand how different perturbations affect the spin electron levels, one needs to examine the NV center spin Hamiltonian (see Chapter 1 for more details).

$$\hat{H} = \underbrace{D_{gs}(S_z^2 - \frac{2}{3})}_{ZFS} + \underbrace{\frac{g\mu_B}{\hbar}\mathbf{B}\cdot\mathbf{S}}_{magnetic} + \underbrace{\zeta_{\perp}(S_z^2 - \frac{2}{3}) + \zeta_{\parallel}\left\{P_x(S_xS_y + S_yS_x) + P_y(S_x^2 + S_y^2)\right\}}_{electric} \qquad (2.5)$$

Here D_{gs} is the zero-field splitting (ZFS), $\mathbf{B}$ is a vector of magnetic field, $\zeta_{\perp}, \zeta_{\parallel}$ are coupling constants. It is important to mention that the $\boldsymbol{P}$ field is actually resulting from the sum of the electric field $\boldsymbol{E}$ and of the strain field $\boldsymbol{F}$ that have the same contribution to the energy levels ($\boldsymbol{P}$ =$\boldsymbol{\sigma}$+$\boldsymbol{E}$). The Hamiltonian (2.5) neglects a number of interactions that are not important here, namely hyperfine interactions to the nitrogen and to nearby carbon nuclear spins. It can be analysed in terms of external perturbations and coupling parameters (Table 2). Magnetic and electric fields directly act on the spin through the magnetic and electric terms in the Hamiltonian (2.5). The magnetic interaction, caused by the Zeeman effect, is far stronger than the electric interaction, caused indirectly by the Stark effect and spin-orbit coupling[28]. Electronic energy levels of the NV center can be also perturbed by a number of other physical quantities via the ZFS parameter D_{gs}. The zero-field splitting is a consequence of the confinement of the electronic wave function and sensitively responds to crystal compression and expansion, as well as to the vibrational motion of surrounding atoms. Examples of quantities affecting D_{gs} are pressure, strain, and temperature. Several coupling constants and best sensitivities have been theoretically or experimentally determined and are collected in Table 1[40].

Property	Coupling coefficient		best sensitivity
Magnetic field	$\frac{g\mu_B}{\hbar}$	28GHz/T	15pT/Hz$^{-1/2}$
Electric field	$\zeta_{\perp}$ $\zeta_{\parallel}$	0.17Hz/(V/m) 3.5*10^{-3} Hz/(V/m)	5.8kV/Hz$^{-1/2}$ 280kV/Hz$^{-1/2}$
Temperature	$\partial D_{gs} / \partial T$	-74kHz/K	430μK/Hz$^{-1/2}$
Strain	F	10^{11}Hz/(Δl/l)	10^{-7}/Hz$^{-1/2}$
Pressure	$\partial D_{gs} / \partial P$	0.015Hz/Pa	6.8*10^{5}Pa/Hz$^{-1/2}$

Table 1: Coupling coefficients and sensitivities for DC ODMR detection

2.3.3.1 Magnetic field sensing

High sensitivity magnetometry has been mainly spurred on by advances in superconductivity and atomic magneto-optics[53], where fT/Hz$^{-1/2}$ sensitivities have been achieved for a ~0.3cm^3 sampling volume in both pulsed and continuous-wave operating regimes[54], [55]. However, there has been a recent surge of interest in exploring diamond-based magnetometry using ensembles of nitrogen-vacancy (NV) defects, due to the relatively simple technical operation under ambient conditions, their small potential sampling volume and their chemical inertness which allows for direct physical contact with the biological systems[40], [50].

NV sensing schemes are usually based on either continuous-wave optically detected magnetic resonance (cw-ODMR) or pulsed ODMR. The magnetic field sensitivity directly follows from the Hamiltonian (Eq. 2.5), where the Zeeman interaction with the NV electron spin can be write as:

$$\hat{H}_m = D_{gs}(S_z^2 - \frac{2}{3}) + \frac{g\mu_B}{\hbar}\mathbf{B}\cdot\mathbf{S} \tag{2.6}$$

As was noted in chapter 2.1 the ODMR spectrum of a single NV center contains two resonance dips separated by $\Delta\nu \approx 2\frac{g\mu_B}{h}B_z$ if an external magnetic field is applied. (Fig.2.1.5(b)). If instead of a single NV center, one has an ensemble of NV centers in the confocal volume, there may be in total eight magnetic resonance dips due to the four possible orientation of the NV axis. The angle between each different pair is 109.4^0. For certain directions of the magnetic field, some resonances can be degenerated. Figure 7 shows an example ODMR spectrum with a bias magnetic field along an arbitrary direction. One option for NV magnetometry is to select one NV alignment by applying a bias field along the NV axis so that changes in the magnetic field projection along this axis affect the resonance frequencies approximately linearly. Another option is to use all four NV alignments; although the eight ODMR frequencies have more complicated dependence on B, this option yields information about the direction of magnetic field. (Fig.2.1.5(c)).

a) b)

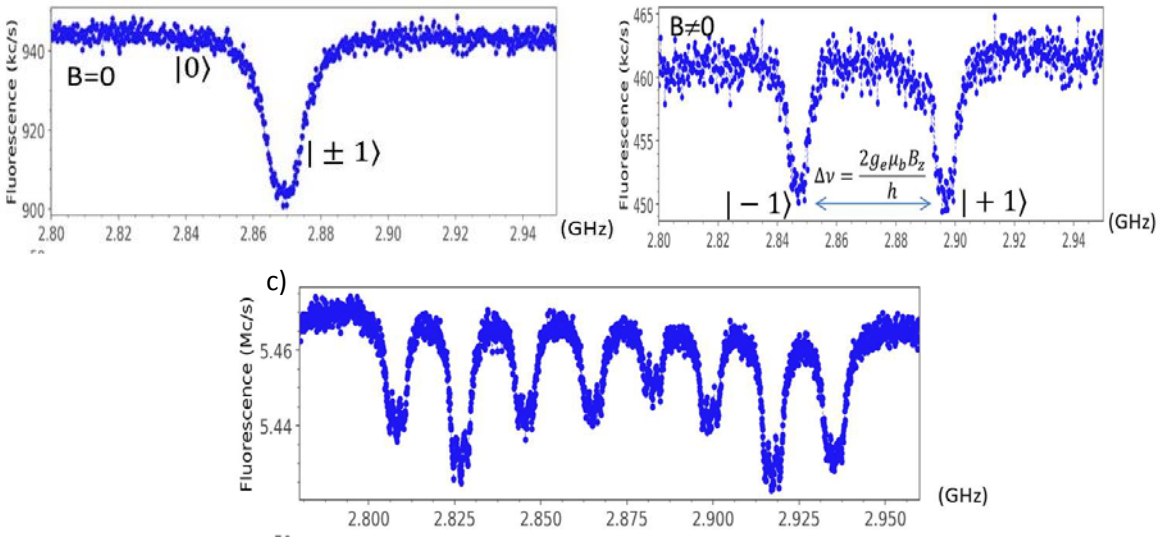

Fig.2.1.5 ODMR spectra (a) in the absence of a magnetic field and (b) in the presence of an external magnetic field. The magnetic field lifts the degeneracy of the ms = ±1 states and results in two separate dips in the ODMR spectrum. c) An example ODMR spectrum (excited at 532 nm) with a magnetic field in an arbitrary direction for an ensemble NV centers in CVD diamond. Each of the four NV alignments has a different magnetic field projection along its quantization axis, leading to eight ODMR peaks (two for each NV alignment). The asymmetry between the two peaks arising from the same alignment is due to differences in the applied microwave field. For each dip a coupling with the nuclear spin of the N^{14} atom generates additional three hyperfine levels.

2.3.3.2 Comparison NV magnetometers with existing technologies

Understanding magnetic properties at the microscale level is a topic of crucial importance in basic science, material sciences and life sciences due to its wealth of applications. For example, for massive data storage in modern information technologies, the recording and reading of information should be implemented using magnetic bits of nanometer size [1]. The progress in nanotechnology require sensing techniques with nanoscale resolution for the investigation and further development of materials. However, the most notable application of magnetic field sensors has been in the area of biosensing, that is, the detection of the weak magnetic fields produced by the human brain, heart and other organs. For example, measurements of the magnetic field produced by the neurons can be used to diagnose epilepsy or understanding of neurodegenerative diseases (such as Alzheimers disease and other forms of dementia).

Superconducting quantum interference device (SQUID) sensors, which dominate of the above-mentioned applications, have reached sensitivity levels of (0.9–1.4) $fT/Hz^{1/2}$ with a pick-up coil area of the order of 1 cm^2. However, SQUIDs require cryogenic cooling, which implies significant cost and maintenance complexity.

Recently, magnetometers based on the precession of atomic spins have demonstrated sensitivities of 0.2fT/Hz$^{1/2}$. These instruments consist of a glass cell containing a vapor of alkali-metal atoms (such as rubidium or cesium) with volumes of several thousand cubic millimeters. In the case of Chip-scale atomic magnetometers (CSAMs), significantly better spatial resolution is possible[56]. CSAMs are based on microfabricated alkali vapor cells integrated with small optical components such as diode lasers and fiber optics. These devices have reached sensitivities below 5 fT/Hz$^{1/2}$ at sensor volume 8 mm^3. However, in spite of exceptional sensitivity, the minimum working distance between sensor and magnetic source for CSAM or SQUIDS remains about few mm, that makes them incapable of monitoring individual neural signalling.

Recently, a new technique for measuring weak magnetic fields at the nanosize scale based on optical detection of electron spin resonances of nitrogen-vacancy (NV) centers in diamond has been developed. NV-diamond sensors operate at wide range of temperatures and doesn't require cryogenics, vacuum systems or strong bias magnetic field. Furthermore, its chemical inertness allows a direct physical contact with delicate biological samples. The use of NV center as a magnetic field sensor firstly was proposed in [10], [57] and demonstrated with single NVs[44], [58] and NV ensembles[59] in 2008.

A comparison of different magnetic field measurement techniques (Fig. 2.1.9) shows that NVs as magnetic sensors potentially reach unprecedented sensitivity over a large spatial resolution range. There is a clear trade-off between sensitivity and resolution determined by how much sensing material can be placed in a given volume so that statistical errors are minimized.

New generation of NV center based sensors is a promising candidate to realize the goal of highly sensitive sensing with nanometer-scale resolution, and even if measurement of single cell activity seems very challenging task, the tissues slice activity will be possible.

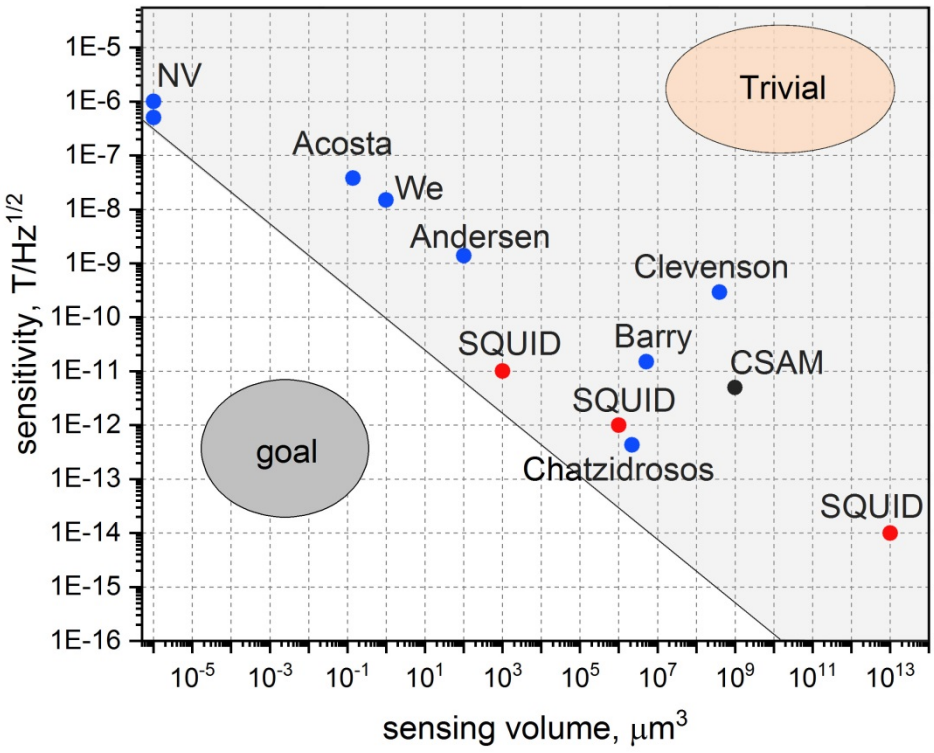

Fig.2.1.9 Comparison of various magnetometers in terms of spatial resolution and magnetic field sensitivity. The data are adopted from; SQUID[60]–[62](red points), CSAM[56] ; NV-magnetometers[44], [50], [63]–[65](blue points).

2.3.3.3 Electric field sensing

Detecting electric fields with a nanoscale probe yield a broad field of potential applications. Existing methods, like single-electron transistors, capacity based scanning probes, scanning tunnelling microscopy are limited to low temperatures. The NV center is a unique system, allowing for multidimensional sensing with nanoscale resolution and at ambient conditions not only of magnetic fields but also electric fields.

Hamiltonian that describes the interaction with the electric field is the following:

$$\hat{H}_e = \zeta_{\perp}(S_z^2 - \frac{2}{3}) + \zeta_{\parallel}\left\{P_x(S_xS_y + S_yS_x) + P_y(S_x^2 + S_y^2)\right\} \quad (2.7)$$

Where $\zeta_{\parallel}$ = (0.35 ± 0.02) $Hz\ cm\ V^{-1}$ and $\zeta_{\perp}$ = (17 ± 3) $Hz\ cm\ V^{-1}$ are respectively the coupling constant for electric field parallel to the NV symmetry axis and for the orthogonal one. The frequency shift caused by the electric field is much smaller than the shift produced by the presence of a magnetic field, which is 28GHz/T[27]. For this reason, in order to reliably measure the Stark shift it is necessary to decouple it from the Zeeman shift.

For electric field detection, the nonaxial Stark effect is preferable to the axial, due to the stronger coupling constant ($\zeta_\perp / \zeta_\parallel \approx 50$). Considering fixed strain fields and magnetic aligned along the NV axis ($B_z = 0$), the change in the Larmor frequency $\delta\nu$ due to a small change of the electric field $\boldsymbol{E}$ is given by perturbation theory:

$$\delta\nu_\pm = \zeta_\parallel E_z \pm \left[f(\mathbf{B},\mathbf{E},\boldsymbol{\sigma}) - f(\mathbf{B},\mathbf{0},\boldsymbol{\sigma}) \right], \tag{2.8}$$

where $f(\mathbf{B},\mathbf{E},\boldsymbol{\sigma}) = \left[(g\mu_B B_z)^2 + (\zeta_\perp P_\perp)^2 \right]^{\frac{1}{2}}$.

From Eq. (2.8) follows, that a reasonable line shift due to electric fields is detectable only if the effective electric field interaction is larger than the axial magnetic field interaction. Therefore, B_z should be precisely controlled in order to have the maximal Stark effect. *However,* for high strain NV centers, for example in nanodiamonds, the magnetic field compensation becomes less imperative, since the effective field is responsible for the suppression of B_z. With high strain, the electric field is projected on the strain axis allowing only detection electric fields along this axis. Nonetheless, it may be very useful to exploit this feature for the selfdiagnostics in diamond-based devices in which NV– centers are common and where charge trapping with the production of local intense electric fields takes place. For further details about electric field measurements using ODMR see Section 4.1.

2.3.3.4 Temperature sensing

Many promising approaches are currently being explored for local temperature sensing. These include scanning probe microscopy[66], [67], Raman spectroscopy[68], and fluorescence-based measurements using nanoparticles[69], [70] and organic dyes[71]. Fluorescent polymers and green fluorescent proteins have recently been used for temperature mapping within a living cell. However, many of these existing methods are limited by drawbacks such as low temporal/spatial resolution, poor signal-to-noise ratio, fluctuations in the fluorescence rate and unsuitability for long term recording.

Nitrogen vacancy (NV) centers in diamond attracted increasing attention thanks to its unique sensing capabilities. Sensing techniques based on NV sensors in diamond can be implemented at room temperature (or 37 °C), and have already been applied inside living cells[51], that makes them ideal sensors for nanoscale bio-applications. By taking advantage absence of biotoxicity [72], cell/neurons can be grown directly on its surface[73]. Thanks to the tiny dimension of

nanodiamonds, mapping temperature fluctuations up to sensitivity of 9mK/Hz$^{1/2}$ and length scales as short as 200 nanometres is possible when being integrated with optical microscopic imaging techniques[52].

The operating concept of the NV sensor is based on the temperature dependence of zero-field splitting frequency (ZFS) and optical readout of NV centres in diamond.

As seen in Fig. 2.1.6, the degenerated $m_s = \pm 1$ spin states in the absence of the external magnetic field are separated from the $m_s = 0$ state by ZFS D_{gd}~2.87 GHz at room temperature. The microscopic origin of the zero-field splitting is thought to be spin-spin interactions in the NV's orbital structures, and the amount of splitting depends on the lattice length, which is strongly influenced by the local temperature. When the local temperature increases, for example, the diamond lattice at the NV center expands which effectively lowers the spin-spin interaction and reduces the ZFS parameter D. Under ambient conditions the temperature dependence is $c_\tau = dD / dT \approx -74kHz / K$ [74]. The ZFS parameter D nonlinearly depends on temperature and is getting larger with temperature decreasing. Sensing temperature using the NV color center in diamond has been well-studied[8], [74], [75]. In the paper[75] a magnetic resonance and fluorescence spectra of NV color centers ensemble in high purity diamond sample were measured, with temperature ranging from 5.6 K to 295 K (Fig. 2.1.7). Both resonant frequencies, one measured with ODMR method (ZFS) and another (zero phonon line) with spectrum analyser show similar temperature dependent shifts. They are nonlinear with temperature and tend to be stable with decreasing temperature.

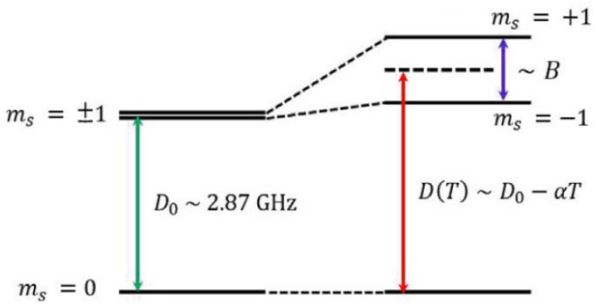

Fig.2.1.6 Energy diagram of the NV center's ground spin states. The zero-field splitting, $D0 \sim 2.87$ GHz, at room temperature varies depending on temperature; $D(T) \sim D0 + \alpha T$, where $\alpha \sim -74.2$ kHz/K.

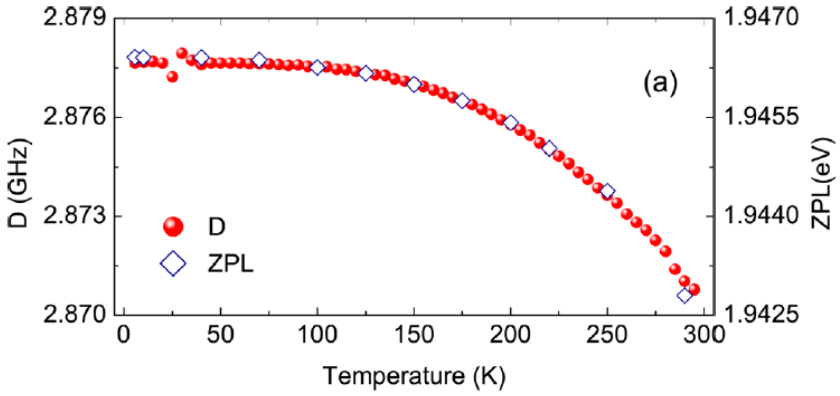

Fig.2.1.7 Zero-field splitting parameter D(red spots) and zero phonon line(blue squares) of NV^- center versus temperature.

For a sensor containing N color centers, the temperature sensitivity is given by

$$\eta = \frac{1}{dD/dT}\frac{1}{C\sqrt{T_{coh}NR}} \tag{2.9}$$

where T_{coh} is the NV spin coherence time, C is the contrast of the resonance dip and R is a photon detection rate. Assuming T_{coh} on the order of few milliseconds and C ~ 0.03, a single NV can potentially exhibit a sensitivity better than 1 mK/ $Hz^{-1/2}$.

The Fig. 2.1.8 demonstrates state-of-the-art NV based quantum thermometers and other reported techniques with comparable sensing volume. Beyond high sensitivity, NV-based thermometry offers several distinct advantages over existing methods in biological and chemical temperature sensing. First, owing to diamond's chemical inertness, it is generally robust to changes in the local chemical environment. Second, sensors based of NV center can be applied over a wide range of temperatures.

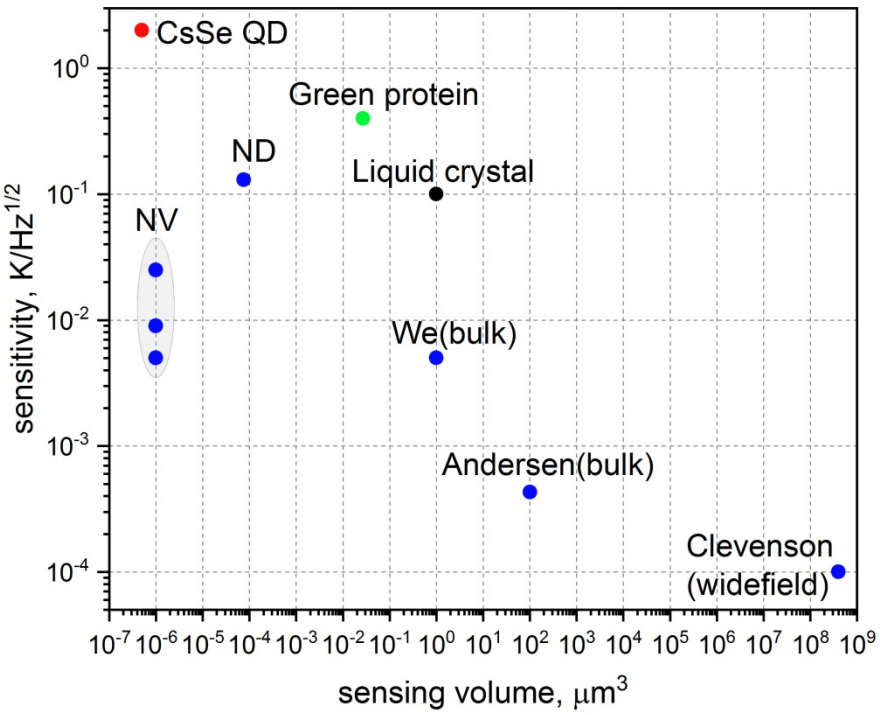

Fig. 2.1.8 Comparison of temperature sensitivity versus sensing volume for NV based sensors (blue points) and quantum dot(red), liquid crystals (black), green proteins (green).

To measure the temperature with the NV center via the ODMR spectra, either the degenerated resonance dips of $m_s = \pm 1$ spin states without an applied magnetic field or a normal dips structure (nondegenerated) with an applied magnetic field are suitable. Generally in the experimental demonstrations or degenerated regime of ODMR spectra or only one from $m_s = 1/m_s = +1$ spin states is used. Degenerated resonance dips in absence of the magnetic field usually gives lower resolution due to the larger FWHM of the resonance line introduced by earth's magnetic field, strain (Fig.2.1.5(a)). Applied bias magnetic field makes resonance dips well defined however in this case shift of the resonance frequency at temperature changing is indistinguishable from fluctuations in an external magnetic field and thus pose an important challenge to accurate sensing operation. Indeed, even a change of only 30 nT would mimic a change of 10 mK in temperature. However this problem can be resolved by simultaneous driving of two transitions $m_s = -1/m_s = +1$ using CW, frequency- or amplitude-modulated MW fields with either the same or the opposite phase of modulation(Fig. 2.1.9). Depending on the choice of electronic transitions and modulation phases (polarity of each contribution), the output signal may contain information about the temperature, the magnetic field or both. Such protocol of the measurement was suggested in paper[47] where a temperature sensitivity of $430\mu K/Hz^{-1/2}$ was achieved.

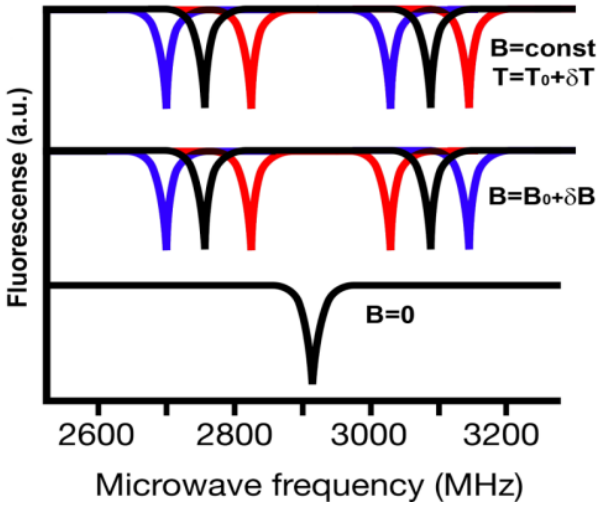

Fig 2.1.9 Example of magnetic and thermal shifts of the spin resonance in spectra ODMR. Dips with equal colors correspond to paired resonances.

In this thesis we describe a novel all-optical method for nanothermometry based on NV- centers in diamonds. Specifically, we explore a sensing regime at a strong transverse bias magnetic. This special regime can be advantageous for the temperature sensing on two grounds. First, due to the degenerated hyperfine structure the resonance transitions of the ODMR spectrum have higher contrast and narrow linewidth respect to common cw ODMR spectra. Second, the NV spin is non-sensitive to the magnetic field fluctuation, because the contribution of the magnetic component enters only in the second order in the Hamiltonian. It allows one protect the measurements from the magnetic field noise. We will discuss details of the experiment in Chapter 4.2.

2.3.4 Nanodiamonds as fluorescent bio-markers

A technology that allows scientists to directly display biological processes has started a revolution in our understanding of biology at the cellular and subcellular levels. The efforts were focused on the development of fluorescent nanoparticles for the sensing(e.g. temperature, voltage, ions currents) as well as for tracking and localization of individual drugs, proteins, nucleic acids and small molecules[76]–[80].

Ideal marker for biological applications should exhibit most, if not all, of the following features:

-small temporal and spatial resolution

-high sensitivity, down to the single molecule level

-biocompatibility and low cytotoxicity

-absence of photo bleaching

Furthermore, a suitable fluorescent marker should be conveniently excitable with easy separated spectra of absorption and excitation. Unfortunately, most fluorescent markers do not possess all of these features.

Commonly used fluorophores suffer from photobleaching and blinking—which limits their effectiveness. Other biolabels, such as quantum dots, are toxic and require encapsulation. Voltage sensitive dyes can be used for readout of the neuron membrane potential, but have poor signal-to-noise ratio and are toxic. Voltage sensitive fluorescent proteins are promising, but also limited in temporal and spatial resolution.

Fluorescent nanodiamonds (FNDs), owing to their unique optical and chemical properties, are proposed to be the best alternative probes that can meet the ideal fluorescent marker's criteria. FNDs are very bright and photostable and can cover a wide range of the VIS to NIR spectrum, depending on the active defect in diamond lattice. For example N3 center has blue emission, nitrogen-vacancy(NV), silicon-vacancy (SiV), germanium-vacancy (GeV) centers have emission in the red-NIR range[30], [81]. Some of the color centers are narrowband and can be used for multi- color labelling[82].

The NV center is the most extensively studied type of fluorescent diamond centers and has been well characterized for its photophysics. NDs incorporating NV^- centers provide a stable luminescent label suitable for different types of bio-imaging and bio-sensing applications [76]–[80], [82]–[91](Fig.2.1.10). A significant advantage of fluorescent nanodiamond (FNDs) is related to their photostability, resistance to bleaching or quenching phenomena[88], that allows their monitoring along neuronal branches with high spatio-temporal resolution, as well as to perform long-term cell tracking[80], [89]. More specifically, the peculiar structure of the spin-dependent radiative transitions of the NV centers allows the optical detection of weak electro-magnetic fields and small temperature variations within the biological samples under exams, by means of Optically Detected Magnetic Resonance (ODMR), thus disclosing a range of new perspectives in cell sensing with unprecedented spatial resolution and sensitivity[50]–[52], [92], [93]. For example, NV-magnetometry with a bulk diamond substrate was successfully demonstrated for detection of action potentials in the giant axon of a marine worm[50]. The thermal variation of the NV center electron spin resonance frequency allows the measurement of temperature changes with a noise as small as 10 $mK/Hz^{1/2}$ [52], [71], and in a range of temperatures from 5.6 K to 295K[75]. The nanoscale resolution in the range of a few tens of nanometers makes FND well suited for sensing temperature fluctuations at the subcellular resolution in living cells.

FNDs exhibit unique optical and chemical properties, as well as exceptional biocompatibility as discussed above. However, there are still challenges that can limit short and long-term

interaction of nanodiamonds with living organisms. These include colloidal stability, maximal allowed concentration, effect on the intercellular processes. In chapter 5 will focus more detailed on magnetic measurements for neuroscience application and related challenges. The effect of FNDs on the electrophysiological properties of single hippocampal neurons and the whole network development will be investigated.

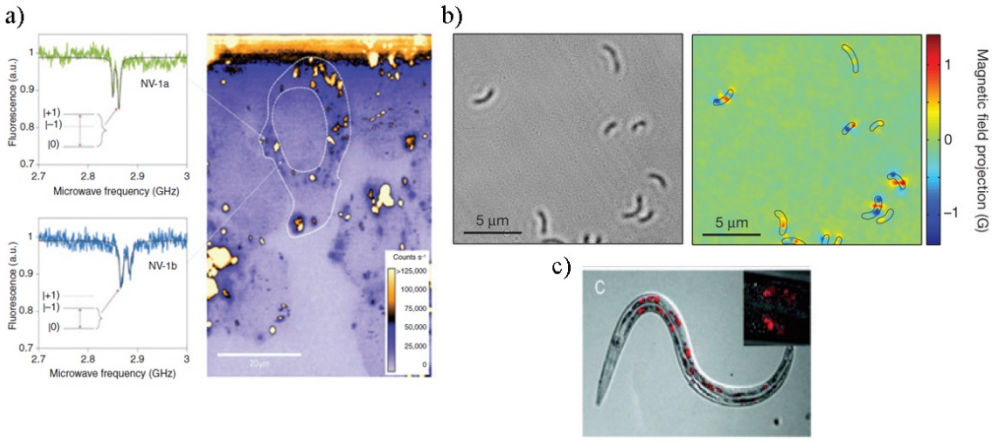

Fig 2.1.10 Examples of the FND applications for bio-sensing and imaging: a)ODMR spectra of NV-1a and NV-1b showing the different strain splitting between the two NV color centers in HeLa cells.[51] b)Optical and magnetic image of bacterial cells[84], c)NV center fluorescence of 100 nm inside a worm. Red spots are the NV luminescence in the optical image [94]

Chapter 3

Nanodiamonds processing and applications

Deterministic single-photon sources (SPSs) are a fundamental tool for several emerging applications in quantum sensing and quantum metrology[95], [96], quantum key distribution[97] and optical quantum computing. In these fields, the exploitation of individual quantum systems could significantly improve the current measuring capabilities[47], [98], define a new generation of standard measure units. In addition, the availability of nanoscale-sized single-photon emitters is also of considerable interest, as it enables a further integration with external structures or biological samples [99], [100] and imaging[51], [101], [102].

As discussed in this thesis, NV centers in nanodiamonds (NDs) are the subject of intense investigation for their unique physical and chemical properties. Due to nanoscale size, optical transparency and biocompatibility, NDs find applications not only as fundamental building block for integrated quantum photonics, but also as ideal candidate for a wide range of nanoscale optical sensors. The first application does not use most of its unique properties, but only NV's bright room-temperature fluorescence and single-center fabrication: ND can be used as a practical and robust single-photon source.

In this Chapter we will talk about nanodiamonds processing and applications. The fabrication and optical characterization of nanodiamond samples, as well as the study of single photon emission from the NVs contained in the nanodiamonds will be reported in Section 3.1. The recently proposed criterion addressed to detect nonclassical behavior in the fluorescence emission of ensembles of single-photon emitters will be demonstrated in Section 3.2. A pilot study on the characterization of a pulsed-pumped test SPS based on a NV centre in nanodiamonds, performed by INRIM, NPL and PTB, will be reported in Section 3.3.

3.1 Fabrication and optical characterization of nanodiamond samples

In this Section the fabrication by MeV ion irradiation and subsequent quantum-optical characterization of SPSs based on single NV centers will be discussed. The processing includes chemical processing, ion beam irradiation and thermal annealing. The optical characterization as well as the study of single photon emission from the NVs contained in the nanodiamonds will then be reported.

3.1.1 Sample fabrication

The material used in this work is a batch of synthetic nanodiamonds (NDs) produced by ElementSix by disaggregation of High Pressure High Temperature (HPHT) synthetic diamond. The nominal size of individual NDs is comprised between 10 nm and 250 nm, with a median size of d=(80 ± 2) nm, as determined by X-ray Diffraction (XRD) analysis of a powder sample (data not reported here). The NDs are classified as type Ib, their nominal substitutional N concentration being 100 ppm. Complementarily, the NDs are characterized by a low concentration of native vacancy defects, resulting in a low concentration of native NV centers. Therefore, the introduction of irradiation-induced vacancies and a subsequent thermal treatment were exploited for the formation of NV centers in NDs. Firstly, ND powders were exposed to an acid bath (H_2SO_4:HNO_3=9:1 solution) for 72 hours at 100 °C before irradiation, with the purpose of removing possible surface organic contaminations and graphitic phases[103]. After filtering, the acid solution with the ND dispersion was neutralized in NH3. The chemical reaction led to the formation of (NH_4)+NH_3^-, which were removed by diluting the samples with distilled water. The diluted solution was exposed to a sonic bath for 30 min, in order to obtain a homogeneous suspension. A centrifugation at 10,000 rpm for 15 min finally removed the remaining residuals of the chemical processing. The afore-mentioned chemical treatment was repeated three times for each NDs batch. The processed NDs were deposited and pressed on a silicon substrate to form a∼10 μm film for the subsequent ion irradiation process. The irradiation was performed at the AN2000 accelerator of the INFN – National Laboratories of Legnaro (Italy), where several beamlines are available for the fabrication and characterization of materials[104], [105]. The samples were irradiated with a 2 MeV proton broad beam over a 7×7mm^2 area, with a 5 nA ion current. In a statistical approach, the irradiation fluence was chosen to maximize the production of individual NV centers in each ND. The substitutional nitrogen concentration was assumed to be equal to ρ_N=1.77×10^{19} cm^{-3} (corresponding to 100 ppm, according to the supplier specifications). The median volume of a ND with a 80 nm diameter (V_{ND}=2.7×10−16 cm^3) was considered. The linear vacancy density λ_v value was assumed to be constant within the whole depth of the deposited ND layer, as the penetration depth of protons in diamond is (24.3 ± 0.5) μm, and therefore the layer thickness does not overlap the Bragg's peak (Fig. 3.1.1(a)). The average volumetric vacancy density ρ_V across the irradiated volume (Fig. 3.1.1(b)) was then evaluated by multiplying the ion fluence F with a corresponding average linear vacancy density of λ_v=103 cm^{-1} ion^{-1}. The latter value was estimated with the SRIM 2013.00 Monte Carlo code[106] in "Detailed damage calculation" mode, after having set the diamond displacement energy to 50 eV[107] and an average mass density of 3.52 g cm^{-3} for the diamond film. The

fluence value was determined by the need of statistically introducing a single vacancy in each nanodiamond, i.e. $F=\lambda_v^{-1}\times V_{ND}^{-1}=5\times10^{12}$ cm^{-2}. However, a 10% NV centers creation yield needs to be taken into account[108], therefore the fluence value was rounded to $F=5\times10^{13}$ cm^{-2}. After ion irradiation, the samples were annealed at 800°C for 1 h in a 800 hPa controlled N_2 atmosphere, to induce the formation of the NV centers. Subsequently, an additional cleaning step (30 min sonic bath in H_2SO_4, followed by a cleaning in "Piranha" solution (mixture of H_2SO_4 and H_2O_2)) ensured the effective removal of organic residuals, metal oxides and carbonate deposits from the samples. The ND powders were finally dispersed on a cover-slip silica glass substrate (Sample #1) for their optical characterization. The deposition was performed at T > 340 °C (i.e. the sulfuric acid boiling point) to allow the liquid to evaporate, thus leaving a homogeneous ND dispersion over the substrates. An optical image of Sample #1 is displayed in Fig. 3.1.1c. A typical optical micrograph of the dispersed NDs with a 100× air objective is reported in Fig. 3.1.1d. In order to assess the role of ion irradiation and of chemical processing, two additional samples were investigated. Sample#2 did not experience proton irradiation, but still underwent the same chemical and thermal treatment performed on Sample #1 prior and after ion irradiation. Likewise, Sample #3 underwent the chemical processing only, i.e. without experiencing neither irradiation nor thermal annealing.

3.1.2 Experimental setup

The photoluminescence (PL) characterization of samples was performed with a single-photon-sensitive confocal microscopy setup (described in Section 2), with a custom acquisition software[109]. The excitation radiation was provided by a solid state Nd:YAG pulsed laser at 532 nm by PicoQuant (10 MHz repetition rate,<100 ps pulse width), a 100× oil-immersion objective (1.3 N.A.) was used for excitation of NDs and PL collection. PL spectra were acquired with a Princeton Instrument Acton SP-2150 monochromator, with a 1200 grooves mm−1 grating and a spectral resolution of ∼2 nm.

3.1.3 Results and discussion

3.1.3.1 Single-photon emission

A typical 80×80 μm^2 PL intensity map acquired from a ND dispersion of Sample #1 is reported in Fig. 3.1.2. All the different probed regions exhibited similar features, consisting of several isolated luminescent spots (∼30 kcps emission intensity) with sub-micrometer size surrounded by a low background emission from the silica substrate. By means of HBT interferometry, the spots could be identified as individual NDs containing single color centers, while several larger

and significantly brighter (up to ~Mcps intensity) regions revealed the presence of NDs clusters due to their aggregation during the deposition process. The distribution in size and density of individual NDs and ND clusters was observed to be homogeneous on all the samples investigated in this work. The magnification of the confocal PL map in Fig. 3.1.2(b) (taken from the region highlighted by the black square in Fig. 3.1.2(a)) exhibits the presence of several individual NDs, which displayed a stable photon emission rate over time. The analysis of the PL emission from a typical ND SPS is shown for the spot highlighted by the crossbar in Fig. 3.1.2(b). Its PL spectrum (Fig. 3.1.2(c)) revealed the typical emission of the negative charge (NV^-) state of the nitrogen-vacancy complex, with a pronounced zero phonon line at 638 nm and its phonon replica at higher wavelengths[5].

Second-order autocorrelation function measurements (see Section 2…) (Fig. 3.1.2(d)) were performed to determine the non-classical features of the PL emission. The spacing between the peaks observed in the coincidences chronogram corresponds to the period of the pulsed excitation. The observation of a smaller peak at zero delay time indicates the presence of nonclassical emission, i.e. the impossibility for the point source under analysis of emitting two photons at the same time[110]. The two narrow peaks, called "backflash", at t~55 ns and t~−95 ns are associated with the photons, emitted during the charge carriers avalanche of the detecting SPADs pair[111], [112]. In order to quantify the non-classicality of the emitter, the data were normalized according to the procedure described in Ref.[113]. The $g^{(2)}(t=0)=0.101\pm0.005$ value was finally determined, as the ratio between the area underlying the zero-delay peak ($\Delta t=0$) and the corresponding value associated with the next pulse repetition (i.e. the one centered at $\Delta t=100$ ns delay). The emission lifetime of the SPS was directly estimated by a fit of the single exponential decays in correspondence of the $g^{(2)}(t)$ coincidence peaks at $t\neq0$, the pulse width being shorter than the expected lifetime.

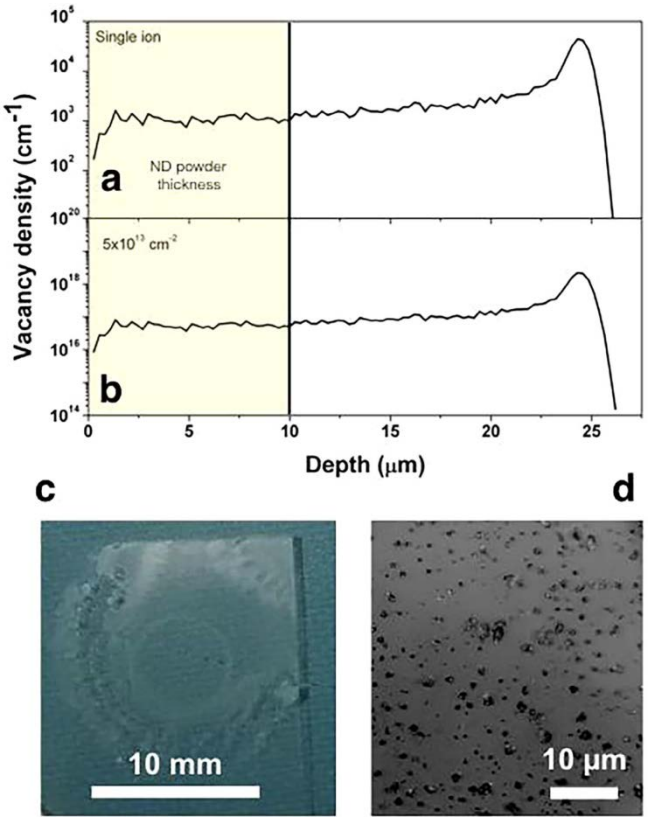

Fig. 3.1.1. Vacancy densities (ρV) versus penetration depth in diamond, as evaluated by SRIM 2013 Monte Carlo code: (a) linear density for a single implanted proton; (b) volumetric density corresponding to a 5×1013 cm−2 fluence. The thickness of the ND layer is superimposed for clarity. (c) Optical image of the silica cover-glass with dispersed nanodiamonds. (d) Optical micrograph of the dispersed NDs distribution.

3.1.3.2 Single-photon emission properties

The distributions of the $g^{(2)}(0)$ and emission lifetime values measured on a sample of 46 single-photon-emitting NV centers embedded in individual NDs in Sample #1 are displayed in Fig. 3.1.3(a,b), respectively. Second-order autocorrelation values exhibited a wide variability in the (0.05–0.5) range, typically depending on the local enviroment such as background luminescence, scattered light from surrounding nanocrystals and substrate surface inhomogeneities. Nevertheless, $g^{(2)}(0) < 0.15$ values such as the one reported in Fig. 3.1.2(d), were not uncommon. Remarkably, NV centers with $g^{(2)}(0)$ values as low as < 0.04 were measured on Sample #1. Similarly, the emission lifetime distribution (Fig. 3.1.3(b)) also exhibits a wide variability in the (13–31) ns range, spanning from the typical values of NV centers in bulk diamond (~12 ns[114]) to those of ND-embedded emitters (i.e.~19–25 ns[114], [115]). This last effect was attributed in previous works, demonstrating that the surface of the nanocrystal will have different optical properties than the true centers of NV due to the modification of local symmetry[15]. The dispersion in the emission lifetime may be attributed to the position of the NV center relative to the ND/silica interface, as well as to the randomness of the dipole orientation.

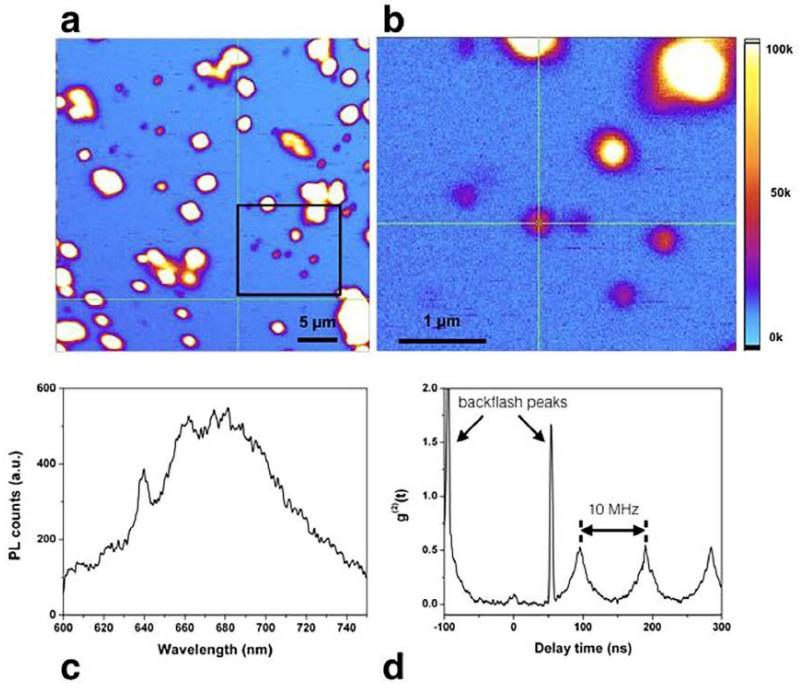

Fig. 3.1.2. Confocal PL microscopy characterization of single-photon emitting NDs. (a) Typical 2-dimensional 80×80 μm^2 PL map acquired from Sample #1. (b) Magnification of the region highlighted by the black square in (a). (c) PL spectrum of the single-photon emitting ND with the typical features of the NV− emission. d) Typical background-subtracted second-order autocorrelation chronogram $g^{(2)}(t)$ of the coincidence events at the two outputs of the HBT interferometer, acquired from the single-photon emitting ND highlighted by the crossbar in (b). Measurements were acquired under 10 MHz pulsed 532 nm laser excitation. The spacing between the peaks of the $g^{(2)}(t)$ function corresponds to the period of the pulsed excitation.

3.1.3.3 The role of ion implantation

A systematic PL mapping of Samples #1–3 enabled to assess the role of the ion irradiation and of the chemical and thermal treatments on the formation of SPS based on NV centers in NDs. In Fig. 3.1.3(c) the density of SPSs (i.e. the density of NDs containing individual NV centers) per unit area is reported. This density was estimated under the assumption of a homogeneous ND dispersion in all the samples under investigation, consistently with the procedure adopted for their deposition on the silica substrate. The control Sample #3, which was chemically processed but neither irradiated nor annealed, exhibited a negligible density of single-photon emitters. Conversely, the density of single-photon-emitting NDs in Sample #1 was estimated as~4.0×10^{3}mm^{-2}, i.e. significantly higher than that (~1.5×103mm^{-2}) of unirradiated NDs which underwent both chemical and thermal processing (Sample #2). On the other hand, it is worth noting that, in line with previous reports in the scientific literature[116], the thermal treatment alone resulted in the formation of a non-negligible amount of NV centers, which is however boosted by the vacancy introduction provided by the ion irradiation process.

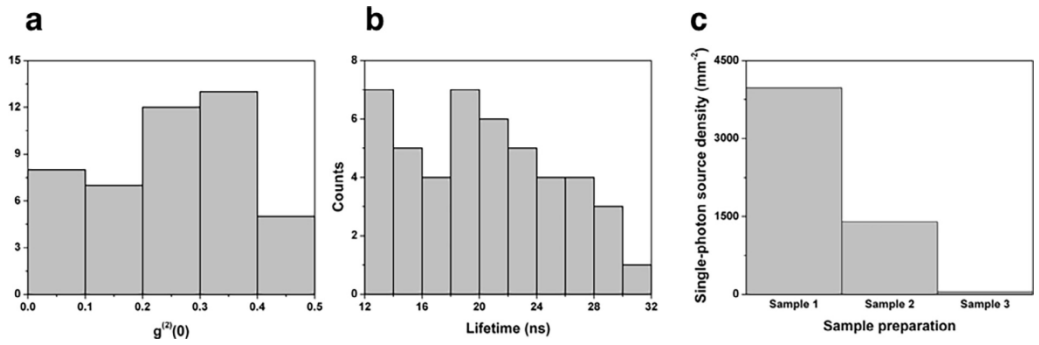

Fig. 3.1.3. (a) Distribution of $g^{(2)}(t=0)$ over a population of 46 single-photon emitting NV centers embedded in individual NDs from Sample #1. (b) Distribution of the emission lifetime of the same set of NV centers. (c) Estimated density of single-photon sources per square millimeter in Sample #1 (irradiated, chemically and thermally processed), Sample #2 (chemically and thermally processed) and Sample #3 (chemically processed).

3.2 Direct observation of nonclassicality in ensembles of single-photon emitters

One of the most debated issues in quantum mechanics is related to understanding the boundary separating the counterintuitive behavior of the systems governed by the quantum laws from the classical, familiar properties of the macroscopical systems. This transition also manifests itself in the realm of optics [180] where, even if undoubtedly the radiation emitted by any possible source of light is indeed composed by an ensemble of individual photons, the properties of classical sources differ consistently from those of nonclassical ones. In particular, single-photon sources (SPSs) have found many experimental and reliable realizations in systems such as heralded sources based on parametric down-conversion[96], [117]–[120], quantum dots[121], [122], trapped ions[123], molecules[124], and color centers in diamond. Since nonclassical optical states have now become a fundamental resource for quantum technology[125], the determination of nonclassicality[126] for a state is not only important for studies concerning boundaries from quantum to classical world, but also represents an important tool for quantifying such resources. Vast literature exists on the characterization of SPSs. Most of the techniques rely on the sampling of the second-order autocorrelation function (or Glauber function) (reported in Section 1.3.1).

$$g^{(2)}(\tau=0)=\frac{\langle I(t)I(t+\tau)\rangle}{\langle I(t)\rangle\langle I(t+\tau)\rangle}\Big|_{\tau=0} \tag{3.2.1}$$

whose value is never smaller than 1 for classical light, while it is lower than 1 for sub-Poissonian light, and in particular vanishes for single-photon states, where $g^{(2)}(\tau=0)=0$ is expected in the ideal case of a single photon source (see Section 1.3.1.2). This quantity has been shown to be substantially equivalent to the parameter $\alpha^{(2)}$ introduced by Grangier et al.[127] It experimentally measured as the ratio between the coincidence probability at the output of a Hanbury Brown and Twiss (HBT) interferometer[128], typically implemented by a 50:50 beam-splitter connected to two non photon-number-resolving detectors, and the product of the click probabilities at the two detectors, i.e.:

$$g^{(2)}\approx\alpha=\frac{P_C}{P_A P_B} \tag{3.2.2}$$

where P_C, P_A, P_B are, respectively, the coincidence and click probabilities at the outputs *A*, *B* of an HBT interferometer. This identity holds strictly for very low value of the click probabilities P_A and P_B (namely much less than 0.1), i.e. for very faint SPSs, while it is only approximately

verified for brighter sources. Due to the equivalence between $g^{(2)}(0)$ and α in the regime typical of quantum optics experiments, all experimental measurements of $g^{(2)}(0)$ in the relevant literature are actually measurements of α, since the two parameters are used substantially without distinction in this community. The parameter α can be generalized to account for the statistical properties of N-fold coincidence events at the outputs of detector-tree apparatuses and several techniques for the reconstruction of optical states as well as quantum enhanced imaging techniques are allowed by the experimental sampling of $g^{(N)}$ functions[129]–[132]. Unfortunately, the amount of background light can affect the measurement, leading to a camouflage of the quantum characteristics due to noise. More specifically, in practical cases, when sampling $g^{(2)}(0)$ to characterize single possible to distinguish between the true quantum signal and background light contribution and, in extreme cases, one is not able to detect a single emitter drowned in dominant noise bath. Recently a novel criterion allowing one to reveal non-classical light from large numbers of independent SPSs has been proposed[133]. According to the theoretical predictions, an experimental implementation of this criterion would be extremely advantageous not only because it would allow one to spot nonclassical signatures in the emission of clusters of emitters, but also because it can be shown that this technique is extremely robust in the presence of Poissonian noise, the parameter under test being absolutely independent from this kind of noise contribution (even when it is dominant).

In this work we experimentally apply the criterion[133] to directly detect nonclassical emission from ensembles of SPSs based on NV color centers in nanodiamonds observed by means of a confocal microscope coupled to four non-PNR single-photon detectors in a detector-tree configuration. Although the reported methodology can be generally extended to a broad range of different physical systems, NV color centers in diamond have been elected to benchmark this new criterion. This choice is motivated by the high relevance of this physical system in quantum optics due to its appealing spin-dependent transition structure, as widely demonstrated by a broad range of works on the subject in recent years. Moreover, the choice is motivated by the fact that generally the quantum-optical characterization of individual photon emitters in solid-state systems (such as NV and other color centers in diamond) is significantly affected by complex issues in the correct assessment of sources of background luminescence in confocal microscopy, such as nearby defects, scattered light, diffused fluorescence from extended defects, ambient light, etc., which are not always easily manageable, or duly taken into account.

3.2.1 Theory

In general, the system considered here is an ensemble of M single-photon-emitters, each coupled by the detection system with an efficiency η_α (α = 1,...,M) detected by N non-PNR detectors connected by a generalized *N*-dimensional beam-splitter (BS). Each detection channel has an overall efficiency (due to BS unbalance and detector efficiency) ξ_i (i = 1,...,N).

Generally, *n* incoming photons entering in the detector tree are distributed in the *N* channels following the multinomial probability $\frac{n!}{\prod_{i=1}^{N} k_i!}\left(\frac{1}{N}\right)^n$ corresponding to k_i photons in the *i*th channel (satisfying $\sum_i k_i = n$). In each channel of the detector tree, the probability of observing a *no-click* event given k_i photons is $(1-\xi_i)^{k_i}$, thus the *click* probability is $1-(1-\xi_i)^{k_i}$, since the positive operator-valued measurements (POVM) of a non-PNR single-photon detector at the end of each channel of the detector tree are

$$\hat{Q}_{click} = \sum_{n=0}^{+\infty}\left[1-(1-\xi_i)^n\right]\left|n\right\rangle\left\langle n\right|, \tag{3.2.3}$$

$$\hat{Q}_{no-click} = \sum_{n=0}^{+\infty}\left[(1-\xi_i)^n\right]\left|n\right\rangle\left\langle n\right| \tag{3.2.4}$$

Starting from this, it is possible to define the POVM of the single detection of the detector tree as

$$\hat{Q}_{[i]}^{[\mathrm{Single}]}(0) = \sum_{n=0}^{+\infty}\hat{Q}_{[i]}^{[\mathrm{Single}]}(0|n)\left|n\right\rangle\left\langle n\right| \ , \tag{3.2.5}$$

$$\hat{Q}_{[i]}^{[\mathrm{Single}]}(1) = \hat{I} - \hat{Q}_{[i]}^{[\mathrm{Single}]}(0), \tag{3.2.6}$$

Where $\hat{Q}_{[i]}^{[\mathrm{Single}]}(0|n) = (1-\xi_i/N)^n$ is the probability that 0 out of *n* incoming photons are detected per excitation pulse. Since the measurement is phase insensitive, the operators have diagonal form in the Fock basis and, due to the nature of non-PNR detectors (able only to distinguish between dark and light) the possible outcomes are “0” (the detector does not click) and “1” (the detector clicks).

Analogously, one can obtain the POVM associated to the no-click in all the outputs of the detector tree as

$$\hat{Q}^{[\otimes N]}(0) = \sum_{n=0}^{+\infty}\hat{Q}^{[\otimes N]}(0|n)\left|n\right\rangle\left\langle n\right| \tag{3.2.7}$$

where $\hat{Q}^{[\otimes N]}(0|n) = \left(1 - \frac{\sum_{i=1}^{N} \xi_i}{N}\right)^n$.

Finally, the POVM of *N*-fold coincidence results is

$$\hat{Q}^{[\otimes N]}(N) = \sum_{n=0}^{+\infty} \hat{Q}^{[\otimes N]}(N|n)|n\rangle\langle n| \tag{3.2.8}$$

where $\hat{Q}^{[\otimes N]}(N|n)$ has in general a nontrivial form, but under the hypothesis that the detection system is a tree of perfectly balanced identical detectors $(\xi_i = \xi, \forall_i)$, it reduces to

$$\hat{Q}^{[\otimes N]}(N|n) = \sum_{r=0}^{N} (-1)^r \frac{N!}{r!(N-r)!}\left(1 - \frac{r\xi}{N}\right)^n \tag{3.2.9}$$

The latter assumption of perfectly balanced detector- tree does not limit the general validity of the discussion because it can be shown that also without this hypothesis the technique preserves its noise-resilience properties.

The generalized $g^{(N)}(0)$ function is expressed in terms of detection probabilities as:

$$g^{(N)}(0) = \frac{P_{click^{\otimes N}}}{\prod_{i=1}^{N} P_{click[i]}} \tag{3.2.10}$$

where $P_{click^{\otimes N}} = tr\left[\hat{\rho}\hat{Q}^{[\otimes N]}(N)\right]$ is the probability of N-fold coincidence at the output of the detector-tree, and $P_{click[i]} = tr\left[\hat{\rho}\hat{Q}_i^{[\text{Single}]}(1)\right]$ is the probability for the *i*-th detector to fire, $\hat{\rho}$ being the density matrix describing the quantum state of the ensemble of emitters. As stated above, the condition $g^{(N)}(0) = 1$ can be adopted to discriminate between classical and nonclassical states, while ideally $g^{(N)}(0) = 0$ for any order of N for single-photon states. Instead, the nonclassicality criterion under study[133] is expressed by the fact that for any classical system the following proposition is verified:

$$\theta^{(N)}(0) = \frac{P_{0^{\otimes N}}}{\prod_{i=1}^{N} P_{0[i]}} > 1, \tag{3.2.11}$$

where, $P_{0[i]} = tr\left[\hat{\rho}\hat{Q}_i^{[\text{Single}]}(0)\right]$ is the no-click probability at the *i*-th detector and $P_{0^{\otimes N}} = tr\left[\hat{\rho}\hat{Q}^{[\otimes N]}(0)\right]$ is the probability that all the N detectors of the detector-tree do not click in correspondence of an excitation event .

3.2.2 Calculation of $\theta^{(N)}$ and $g^{(N)}$ in the presence of Poissonian noise

the probability $P_{0^{\otimes N}}$ in Eq. (3.2.11) can be expressed in the form

$$P_{0^{\otimes N}} = \sum_{n=0}^{\infty} \sigma^n p_n \tag{3.2.12}$$

Where $p_n = \langle n | \hat{\rho} | n \rangle$ is the probability distribution of the photons and σ_n is equal to $(1-\xi)^n \left[\left(1 - \frac{\xi}{N} \right)^n \right]$. We study the case of single emitters' fluorescence in the presence of Poissonian noise. The photon-number probability distribution in this case is

$$p_n = \sum_{m=0}^{M} \sum_{k=0}^{\infty} \delta_{n,m+k} P_{SPS}(m) P_{\lambda}(k), \tag{3.2.13}$$

where, assuming that all the emitters in the ensemble are coupled with the same efficiency $(\eta_\alpha = \eta, \forall_\alpha)$, $P_{SPS}(m) = \frac{M!}{m!(M-m)!} \eta^n (1-\eta)^{M-m}$ is the distribution of the photons of the emitters, $P_{\lambda}(k) = \frac{\lambda^k e^{-\lambda}}{k!}$ is the distibution of the Poissonian light, and $\delta_{x,y}$ is the Kronecker delta. By substituting the suitable value for σ in Eq. (3.2.12), one gets

$$P_{0^{\otimes N}} = (1-\eta\xi)^M e^{-\lambda\xi} \tag{3.2.14}$$

$$P_{0[i]} = P_0 = 1\left(-\frac{\eta\xi}{N} \right)^M e^{-\lambda\xi/N} \tag{3.2.15}$$

Finally, substituting Eqs. (3.2.14, 3.2.15) in Eq. (3.2.11), the λ-dependent terms appear as equal factors both in the numerator and in the denominator of the ratio and are simplified, resulting in

$$\theta^{(N)}(0) = \frac{\left(1-\eta\xi\right)^M}{\left(1-\frac{\eta\xi}{N}\right)^{MN}} \tag{3.2.15}$$

Thus, under our assumptions, the parameter $\theta^{(N)}$ estimation is independent from the Poissonian contribution at any order N (at variance with $g^{(N)}$).

This parameter must be compared with the $g^{(N)}$ function that is expressed according to Eq. (3.2.10). In order to calculate it in analogy with the expression of $\theta^{(N)}$), we must first of all write the probability of N-fold coincidence:

$$P_{click^{\otimes N}} = tr\left[\hat{\rho}\hat{Q}^{[\otimes N]}(N)\right] = \sum_{n=0}^{\infty}\hat{Q}^{[\otimes N]}(N|n)p_n = \sum_{r=0}^{N}(-1)^r\frac{N!}{r!(N-r)!}\left(1-\frac{\eta r\xi}{N}\right)^M e^{-\lambda e\xi/N},$$

leading to

$$g^{(N)}(0) = \frac{P_{click^{\otimes N}}}{\left(P_{click}\right)^N} = \frac{\sum_{r=0}^{N}(-1)^r\frac{N!}{r!(N-r)!}\left(1-\frac{\eta r\xi}{N}\right)^M e^{-\lambda e\xi/N}}{\left[1-\left(1-\frac{\eta\xi}{N}\right)^M e^{-\lambda e\xi/N}\right]^N},$$

where, in accordance with Eq. (3.2.15) we used $P(click) = 1 - P_0$. It is clear that, in opposition with the $\theta^{(N)}$ case, the contribution of the Poissonian terms to $g^{(N)}$ cannot be eliminated.

3.2.3 Calculation of $\theta^{(N)}$ for unbalanced multiport HBT interferometer in presence of Poissonian noise

In the case of a nonideal (unbalanced) multiport HBT interferometer, the disproportion of the single-photon detections at each output port of the interferometer can be due either to the nonideal splitting ratio of the beam splitters of the detector tree at the heart of the multiport HBT or to the different value of quantum efficiency of each detector. To simplify the calculation we consider the situation in which the beam splitters are ideal (thus, for an N-port HBT interferometer, the probability of finding a single photon in each port is $1/N$) and the whole unbalancement is summarized in the quantum efficiency ξ_i of each detector. Starting from Eqs. (3.2.3)–(3.2.8), and carrying on the calculation, in complete analogy with Section 3.2.2 but without the assumption of identical detectors, we obtain

$$P_{0^{\otimes N}} = \left(1-\eta\frac{\sum_{i=1}^{N}\xi_i}{N}\right)^M e^{-\lambda\left(\sum_{i=1}^{N}\xi_i/N\right)} \qquad (3.2.17)$$

Thus, also in the case of an unbalanced HBT interferometer, $\theta^{(N)}(0)$ is independent from the Poissonian noise. There is essentially a trade-off between $\theta^{(N)}$ and $g^{(N)}$ measurements. While $g^{(N)}$ values are independent from inefficiencies and losses, and obviously from HBT interfermeter unbalancement, they are strongly affected by Poissonian noise. On the contrary,

$\theta^{(N)}$ values strongly depend on inefficiencies and losses, but they are completely unaffected by the Poissonian noise irrespective of the level of unbalancement of the HBT interferometer.

3.2.4 Experimental setup

We performed the comparison of the behaviors of $g^{(N)}$ and $\theta^{(N)}$ exploiting different ensembles of single-photon emitters with different levels of background Poissonian noise in synthetic Ib nanodiamond (ND) powders produced by ElementSix by fragmentation of high-pressure-high-temperature (HPHT) synthetic diamond (see Section 3). The sample is observed via a single-photon-sensitive confocal microscope, described in Section 2.2.3, with pulsed laser as a pump. The repetition rate for the excitation source was chosen as 5 MHz with 50 ps FWHM in this case. The difference from the above-mentioned experiments lays in the detection part. In this case the signal is collected by a detector-tree configuration realized by means of three integrated 50:50 beam splitters in cascade connecting to four single photon avalanche photodiodes operating in Geiger mode (Fig.3.2.1). This configuration, reproducing six nonmutually independent HBT interferometers (or equivalently two completely independent HBT interferometers) [193], allows the detection of all the twofold coincidences among the detection channels and to obtain six estimates of the second-order autocorrelation functions $g^{(2)}$. The pulses (60 ps FWHM) of the laser simulating the Poissonian noise (PICOQUANT LDH-D-C-690), emitting at 685 nm, inside the detection window, were electronically synchronized with the excitation laser emission. This laser was directly coupled to the pinhole of the detection system.

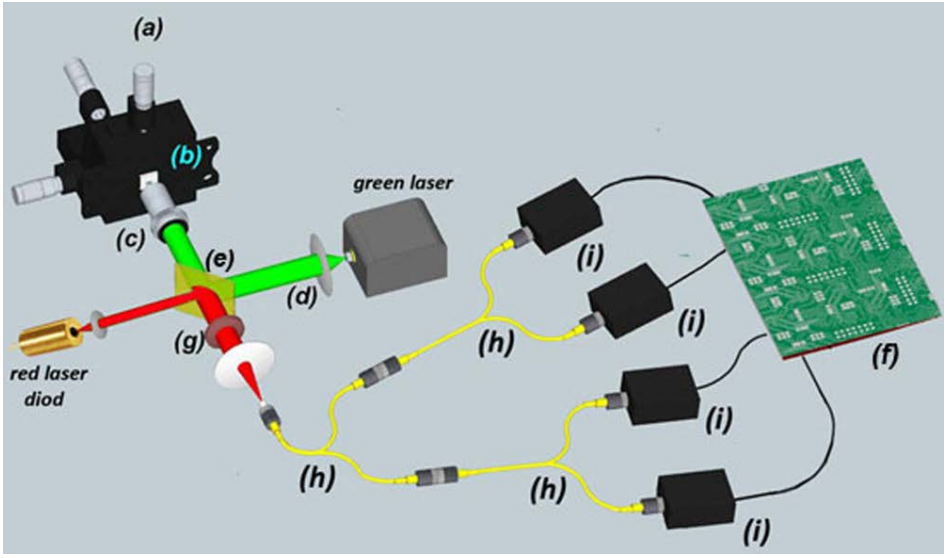

Fig.3.2.1 Experimental setup: (a) XYZ piezoelectric stage, (b) sample, (c) oil immersion objective, (d) excitation light, (e) dichroic mirror, (f) coincidence electronics, (g) long-pass filters, (h) 50:50 beam splitter, and (i) single-photon detectors

3.2.5 Experimental results

We implemented the measurement of $g^{(2)}$ and $\theta^{(2)}$ by the characterization of three fluorescent objects in a nanodiamond sample (see Fig. 3.2.2). To perform this study, the width of the time window (40 ns) was chosen to be compatible with the lifetime of the centers (around 25 ns). The objects under study (see Fig. 3.2.2) are dubbed Item-1, Item-2, and Item-3. Item-1 is not far from a single-photon emitter having $g(2)$ value below 0.5 [$g_{I_1}^{(2)}(0) = 0.407 \pm 0.012$] if no artificial noise is added, while Item-2 and Item-3 are clusters of unknown quantities of single-photon emitters [respectively, $g_{I_2}^{(2)}(0) = 0.832 \pm 0.004$ and $g_{I_3}^{(2)}(0) = 0.832 \pm 0.004$, always without noise]. The overall efficiency of the system has been estimated as (1.582 ±0.002)% (calculated as the ratio between the emission rate of Item-1 and the excitation rate). In order to simulate Poissonian noise, a laser source at a wavelength falling in the detection spectral window was reflected directly in the coupling pinhole of the microscope. To analyze the robustness of the two parameters against noise, measurements on each sample were performed in the absence of noise and in the presence of two different values of intensity of the noise source. These two noise levels, estimated in terms of counts/s observed by the HBT system as a whole, in the absence of single-photon source emissions are 10 000 counts/s and 25 000 counts/s. For testing the stability of the experimental system, the measurement without Poissonian noise was repeated after the measurement including noise and the g and θ parameters are found to be consistent with the first measurements (Fig. 3.2.3). As an example, this measurement in the case of Item-1 is shown as a red dot. Also, to test the capability of our setup to detect nonclassical behavior, we performed the measurement of $g^{(2)}$ and $\theta^{(2)}$ parameters on the light reflected by a nonfluorescent nanodiamond present in the sample (Item-4 in see Fig. 3.2.2). This kind of object is not distinguishable from the emitters in a confocal map but does not produce antibunching (being produced by coherent light) and can be recongnized only from its spectral features. As expected, this object showed clear signatures of classical emission [$g_{I_4}^{(2)}(0) = 1 - g^{(2)}(0) = 0.004 \pm 0.005$, $\theta_{I_4}^{(2)}(0) = 1 - \theta^{(2)}(0) = (-4 \pm 2) \cdot 10^{-8}$].

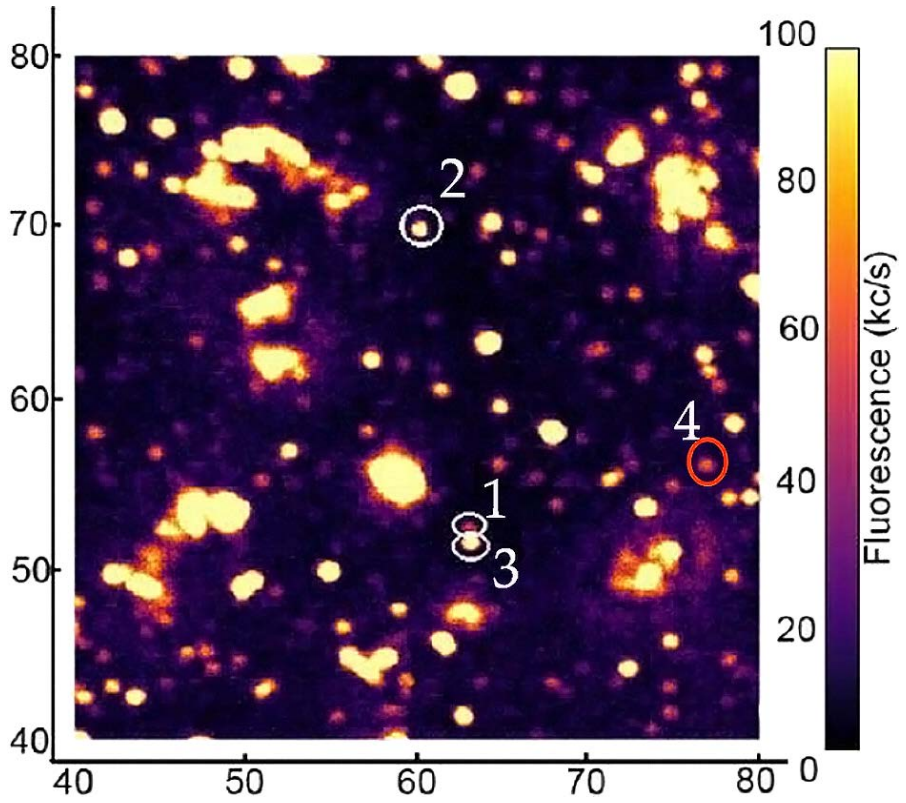

FIG. 3.2.2. Fluorescence map of the selected area of the sample obtained with the single-photon-sensitive confocal microscope. The three highlighted by white spots correspond to the fluorescent nanodiamonds under study. Red spot is a nonfluorescent nanodiamond.

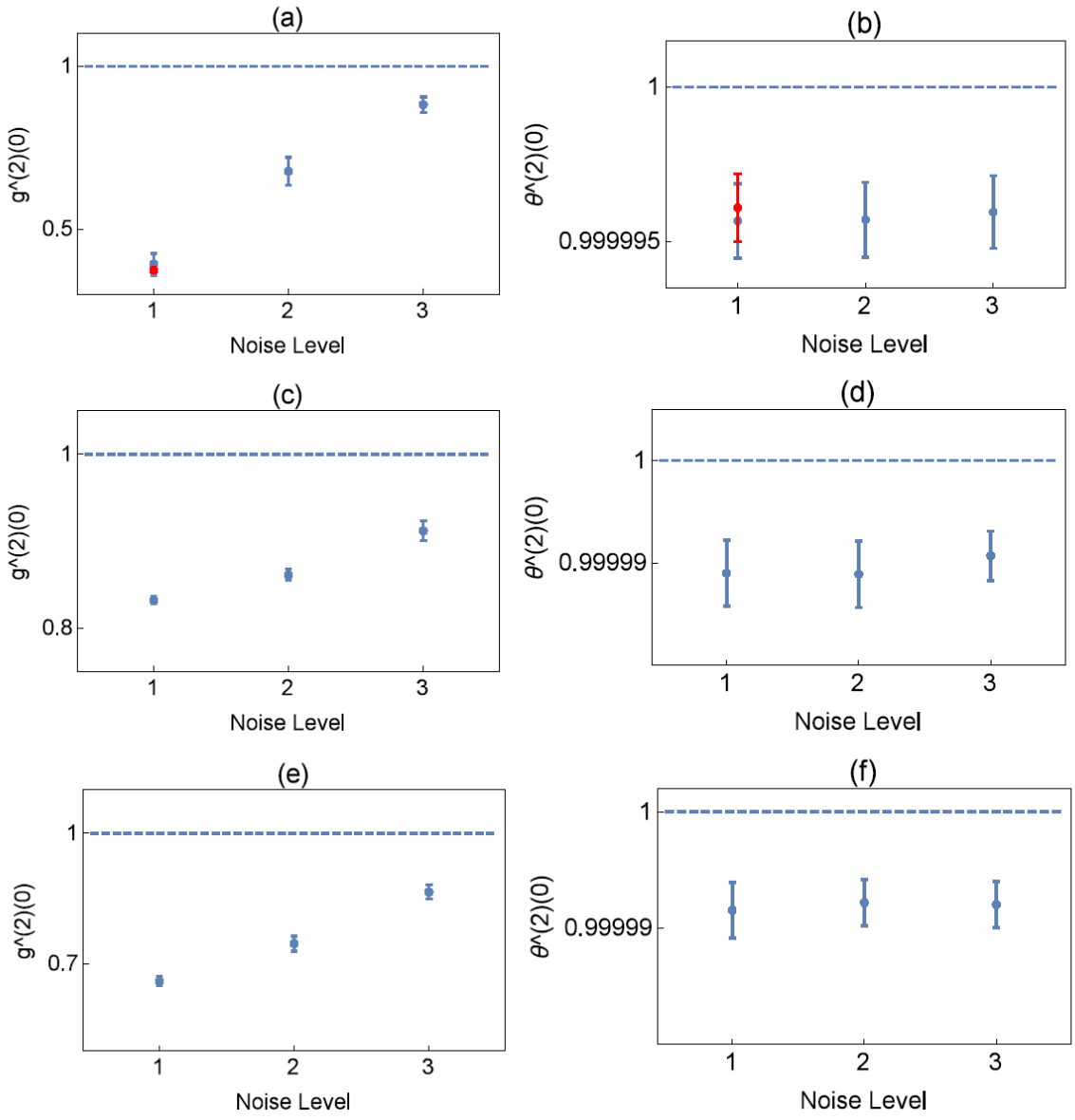

FIG. 3.2.3. (a) Plot of $g^{(2)}_{I_1}$. (b) Plot $\theta^{(2)}_{I_1}$. (c) Plot of $g^{(2)}_{I_2}$. (d) Plot of $\theta^{(2)}_{I_2}$. (e) Plot of $g^{(2)}_{I_3}$. (f) Plot of $\theta^{(2)}_{I_3}$. All values were measured for three different levels of Poissonian noise (1: noise off; 2: $1\text{x}10^4$counts/s due to noise; 3: $25\text{x}10^4$ counts/s due to noise). Each measure is the average of ten runs, coincidences registered in every twofold combination of the detector-tree branches, of 200 s. Excitation rate is 5 MHz. The red dot in (a) and (b) corresponds to a successive repetition of the first measurement to test the stability of the apparatus.

As expected from the analysis in Ref. [133], the experimental data (Fig. 3.2.3) clearly demonstrate the advantages of the nonclassicality criterion based on $\theta^{(2)}$ with respect to $g^{(2)}$: firstly, the parameter estimation is more robust against Poissonian noise since the three $\theta^{(2)}$ values for each object are perfectly compatible, while $g^{(2)}$ values differ considerably for different noise contributions; secondly, the deviation from classicality is even stronger when the object under study is not a single emitter but instead an ensemble of them. This is supported by two observations: (i) the deviation from the classical value in terms of $\theta^{(2)}$ is larger for clusters

characterized by a greater $g^{(2)}$ value with respect to the others (measured in the same conditions); (ii) the raw data regarding the two-, three- and fourfold coincidence events (not reported here) show significantly different multiphoton coincidence behavior for the three objects. Those events are rare for Item-1, they are significantly occurring for Item-3, and they are definitely more frequent for Item-2, justifying the conclusion that the number of centers in each cluster increases accordingly. For this reason this method allows detecting nonclassical behavior of quantum emitters without the necessity of isolating a single one. On the other hand, the $\theta^{(2)}$ function presents some disadvantages, since its value depends strongly on the efficiency of the channel ξ (see the Section 3.2.2) as opposed to $g^{(2)}$ which is independent from the balance of the branches of the detector tree. This can be observed in the plots in Fig. 3.2.4, where respectively, the click probabilities of the single channels [inset (a)], the twofold coincidence probabilities [inset (b)], and the experimental $g^{(2)}$ [inset (c)] and $\theta^{(2)}$ [inset (d)] values in the characterization of Item-3 are shown. It results that the unbalance of the detector tree in terms of detection efficiency which is observable in Fig. 3.2.4(a), is compensated when sampling $g^{(2)}$ [Fig. 3.2.4(c)], delivering six fairly consistent estimates, while the values of $\theta^{(2)}$ obtained for different pairs of channels are not consistent [Fig. 3.2.4(d)]. This results in a rather large uncertainty (calculated as the standard deviation of the six sampled quantities) in the mean $\theta^{(2)}$ values plotted in Figs. 3.2.3(b), (d) and (e). One must be reminded anyway that the average of the latter values is below the classical limit within a 3σ confidence level [as can be observed in Fig. 3.2.3(f)] thus this inconsistency does not affect the observation of nonclassical behavior. See Tables I and II for data collected by a single beam splitter (showing smaller uncertainty). In our experiment we limited the analysis to the second order of correlation of θ and g functions. Since the family of nonclassicality criteria under test is defined for any arbitrary order, it is reasonable to investigate the possible advantages/disadvantages of experimentally sampling three and fourfold coincidences as well. The calculations on the behavior of the $\theta^{(N)}$ functions clearly reveal the independence of the value of the parameter with respect to the noise level for all the orders of correlation, exactly as we observed in the second-order case and at variance with the behavior of g functions. Even if our detection apparatus is capable of detecting up to fourfold coincidences, for the three objects under study the three- and fourfold coincidence rates were extremely low (respectively, 10^{-7} and 10^{-9}; less than the associated statistical uncertainty for the brightest object, Item-2), so that no significant consideration on high-order behavior could be extracted in our experimental conditions.

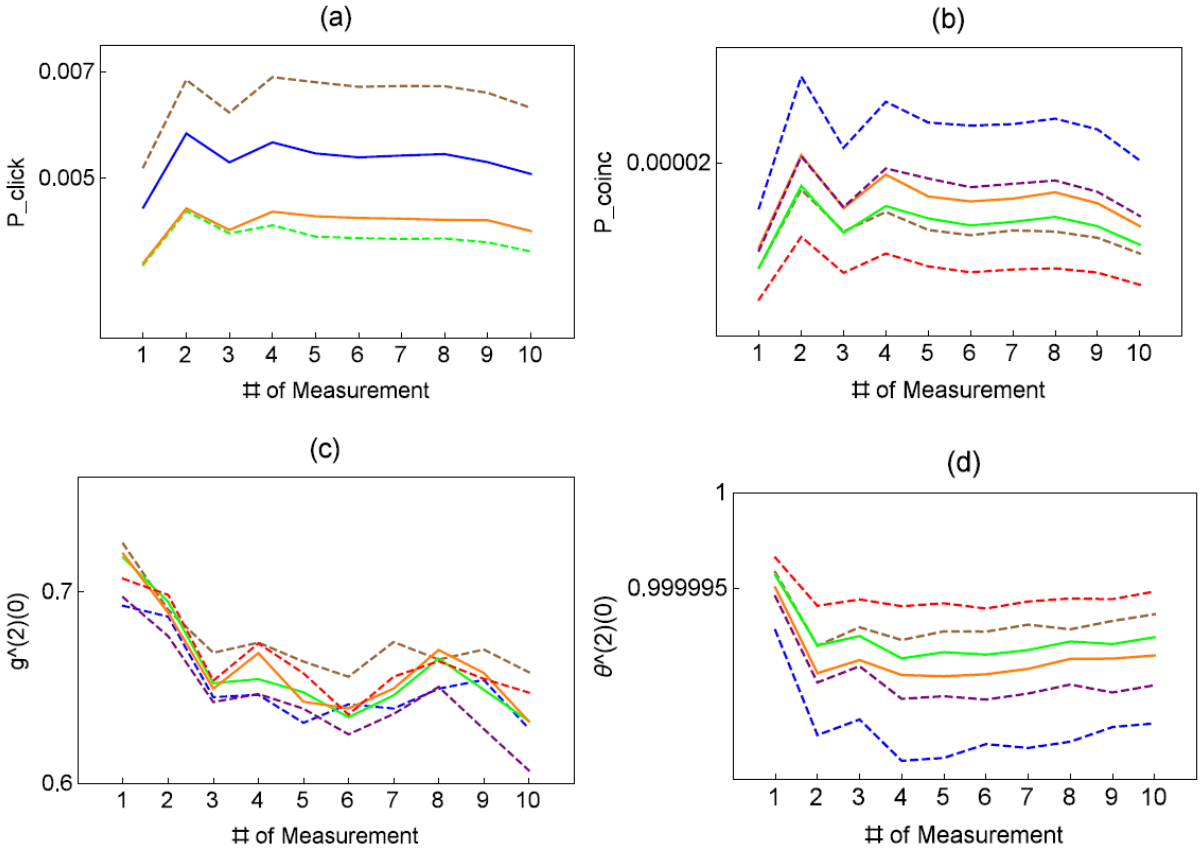

FIG. 3.2.4. (a) Click probabilities at the four outputs of the detector-tree while observing Item-3. The style of the line (continuous/dashed) distinguishes between the outputs of the two independent BS constituting the detector-tree. (c) and (d) values, respectively, of $g^{(2)}(0)$ and $\theta^{(2)}(0)$ measured for each twofold combination among the four outputs of the detector-tree while observing Item-3. Same measurement settings as Fig. 3.2.3. In (b)–(d) the continuous lines mark the two independent twofold coincidences.

$1-g^2(0)$	Noise level 1	Noise level 2	Noise level 3
Item-1	0.615 ± 0.009	0.345 ± 0.011	0.130 ± 0.008
Item-2	0.166 ± 0.003	0.141 ± 0.005	0.0966 ± 0.0004
Item-3	0.34 ± 0.03	0.260 ± 0.007	0.144 ± 0.004

TABLE I. Table of the experimental deviations of $g(2)(0)$ from the classical limit.

$1-\theta^2(0)$	Noise level 1	Noise level 2	Noise level 3
Item-1	$(40 \pm 3) \cdot 10^{-7}$	$(41 \pm 2) \cdot 10^{-7}$	$(39 \pm 3) \cdot 10^{-7}$
Item-2	$(100 \pm 7) \cdot 10^{-7}$	$(103 \pm 9) \cdot 10^{-7}$	$(92 \pm 7) \cdot 10^{-7}$
Item-3	$(77 \pm 1) \cdot 10^{-7}$	$(73 \pm 3) \cdot 10^{-7}$	$(75 \pm 5) \cdot 10^{-7}$

TABLE II. Table of the experimental deviations of $g(2)(0)$ from the classical limit as sampled by a single beam splitter of the detector tree.

3.3 Towards standardization of single-photon sources measurements

3.3.1 Introduction

Single-photon sources (SPSs)[95], [96], [125], i.e. sources that are able to produce single photons on demand, are key elements for the development of quantum optical technologies as well as for radiometry and photometry at the single-photon level. This requires developing a metrological support for the development and commercialisation of these technologies. The current development of quantum technologies is already mature enough to establish standard techniques in single-photon metrology. Measurement of the $g^{(2)}(0)$ parameter plays a vital role in characterising and understanding single-photon emission.

This section presents a systematic study of the $g^{(2)}(0)$ measurement for a SPS based on NV color centers in nanodiamonds (ND) (see Section 3.1) in the pulsed regime, with the purpose of developing a measurement procedure and an analysis of the uncertainty to provide an unbiased value of the measurand which is independent of the experimental apparatus used, ultimately producing an estimate unaffected by the non-ideal behavior of the physical systems. Consensus on such a procedure would produce great benefits for the metrology community, enabling the development of SPS characterization techniques that are robust enough for practical measurement services. The results reported in this work were obtained during a pilot study performed by INRIM, NPL and PTB. This is a precursor to organising an international comparison on the $g^{(2)}(0)$ measurement, which would pave the way for the realization of a mutual recognition agreement on the calibration of key elements for forthcoming optical quantum technologies, such as SPSs and single-photon detectors.

3.3.2 Methods

The typical parameter employed to test the properties of a SPS is the second order correlation function (or Glauber function), reported in Section 1, defined as

$$g^{(2)}(\tau = 0) = \frac{\langle I(t)I(t+\tau)\rangle}{\langle I(t)\rangle\langle I(t+\tau)\rangle}\Big|_{\tau=0}, \tag{3.3.1}$$

where $I(t)$ is the intensity of the optical field. In the regime of low photon flux, this parameter, how has been shown in Chapter 3.2, to be substantially equivalent to the Grangier parameter α. With regards to Eq.3.2.2, probabilities P_C, P_A, P_B in this experiment were estimated as the ratio

between the total number of the corresponding events versus the number of excitation pulses during the experiment, i.e. $P_x = N_x/(Rt_{acq})(x = C, A, B)$, where R is the excitation rate and t_{acq} is the total acquisition time. The value of the measurand is independent from the total efficiencies (η_A, η_B) of individual channels (including detection and coupling efficiency), optical losses and splitting ratio so we can write

$$\alpha = \frac{P_C}{P_A P_B} = \frac{\eta_A \eta_B P_C}{\eta_A P_A \eta_B P_B} \tag{3.3.2}$$

The value of the parameter from the experimental data, corrected for the contribution of the background coincidences (due, for example, to stray light or residual excitation light), can be estimated as follows:

$$\alpha = \frac{P_C - P_{Cbg}}{(P_A - P_{Abg})(P_B - P_{Bbg})} \tag{3.3.3}$$

Where P_{Cbg}, P_{Abg}, P_{Bbg} are, respectively, the coincidence and click probabilities of background photons, calculated analogously to their counterparts P_C, P_A, P_B.

Figure 3.3.1 shows the typical chronogram of the behaviour of a pulsed SPS obtained by sampling the coincidence events at the two outputs of an HBT interferometer. The coincidence probability has been estimated as the ratio between the total number of events in the chronogram falling in a fixed temporal window *w* around the central peak (showing antibunching, i.e. the 'b' interval in Fig. 3.3.1) and the total number of excitation pulses occurring in the acquisition time. The product $P_A P_B$, corresponding to the probability of accidental coincidences, has been evaluated by integrating the events occurring in an equal interval around the subsequent peak ('c' interval in Fig. 3.3.1) not showing antibunching (always divided by the number of pulses). In fact, those coincidence events (amounting to N_ξ) are related to independent events (coincidences between single photons emitted after two subsequent laser pulses and detected by detector A and detector B respectively) and thus $P_\xi - P_{bg} = (N_\xi - N_{bg})/(R * t_{acq})$. The parameter to be estimated is thus:

$$\alpha_{\exp} = \frac{N_C - N_{Cbg}}{N_\xi - N_{bg}} \tag{3.3.4}$$

where (Ni being the coincidence events sampled in the ith channel)

$$N_C = \sum_{i=-k_w/2}^{k_w/2} N_i \,, \tag{3.3.5}$$

$$N_{\xi} = \sum_{i=T-k_w/2}^{T+k_w/2} N_i \tag{3.3.6}$$

k_w is the number of bins corresponding to the chosen coincidence window w, N_{bg} is the estimated background due to spurious coincidences (the number of events in the 'a' interval in Fig. 3.3.1) and T is the excitation period (expressed in bins). In Fig. 3.3.1 two backflash peaks[111], [112] can be observed on either side of the central peak. These are due to secondary photon emission that arises from the avalanche of charge carriers that occurs in one of the two detectors in the HBT interferometer as a photon is absorbed and that are afterwards detected from the other detectors. To avoid overestimating α, these peaks must not be included in the coincidence window.

The presence of the backflash peaks prevented us to estimate P_A, P_B directly from the counts of the two detectors, since we were forced to consider a coincidence window smaller than the NV-center emission time window (of the order of tens of nanoseconds, i.e. at least three NV lifetimes). For this reason we estimated P_A P_B consistently with the coincidences measured at time 0. The probability of observing a coincidence in the autocorrelation window around the peak at 400 ns can be underestimated by the presence of the coincidence counts between 0 and 400 ns, because of detectors and electronics dead-time. Due to the extremely low level of counts in this interval, we have estimated that this correction is negligible within the declared probability uncertainty.

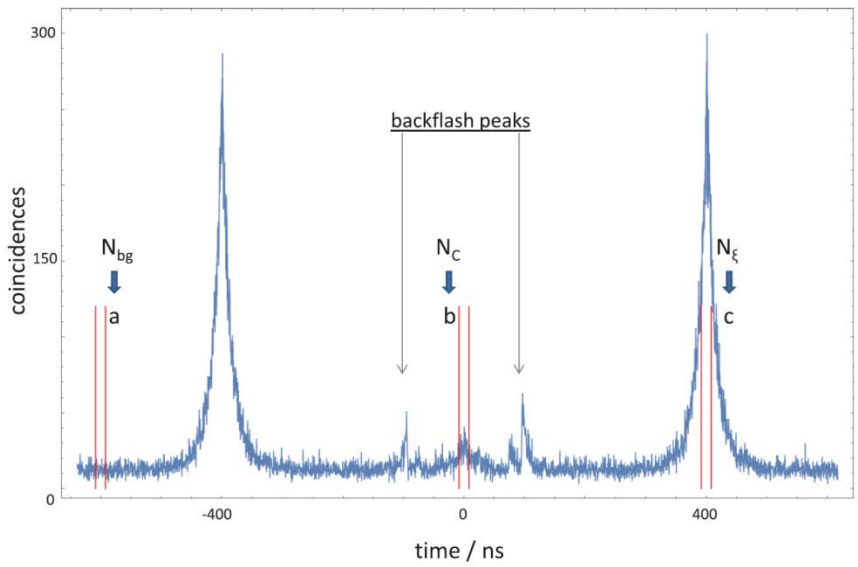

Fig.3.3.1. Typical chronogram of the coincidence events registered with an HBT interferometer. The three identical highlighted time intervals are used to estimate, respectively, background coincidences (a), true coincidences (b) and accidental coincidences (c).

3.3.3 Measurement facility

We used a laser-scanning confocal microscope described in Chapter 2 whose output signal was split by a 50:50 beamsplitter and connected to two measurement devices, i.e. two single-photon sensitive HBT interferometers (see Fig.3.3.2).

Note that, according to the model described in Chapter 3.3.1, the value of α measured by the two HBT interferometers is independent of optical losses and splitting ratio at the beam-splitter. The excitation light, produced by a pulsed laser (48 ps FWHM, 560 pJ per pulse) emitting at 532 nm with a repetition rate R = 2.5 MHz was focused by a 100× oil-immersion objective on the ND sample hosting an SPS based on a single NV center of negative charge, with emission in a broad spectral band starting approximately at 630 nm and ending at 750 nm (_ZPL = 638 nm). The preparation of sample is described in Section 3.1. The optical filters used here were a notch filter at 532 nm and two long-pass filters (FEL600 and FEL650). The photoluminescence signal (PL), thus occurring in a 650 nm–750 nm spectral range, was collected by a multimode fibre and split by a 50:50 beam-splitter (BS). As stated above, each end of the BS was connected to a separate HBT setup used for the joint measurement. In particular:

• The INRiM facility was composed of a fused 50:50 fibrebeam-splitter connected to two Excelitas SPCM-AQR-14-FC single-photon avalanche detectors (SPADs). Single and coincidence counts were sampled via ID Quantique ID800 time-to-digital converter (60 ps time resolution).

• The NPL facility was composed of a fused 50:50 fibre beam-splitter connected to two Perkin-Elmer SPCMAQR-14-FC single-photon avalanche detectors (SPADs). Coincidence counts were sampled via PicoQuant HydraHarp 400 multichannel picosecond event timer (1 ps time resolution).

• The PTB facility was composed of a fused 50:50 fibre beam-splitter connected to two Excelitas SPCM-AQR-14-FC single-photon avalanche detectors (SPADs). Single and coincidence counts were sampled via PicoQuant HydraHarp 300 multichannel picosecond event timer (4 ps time resolution).

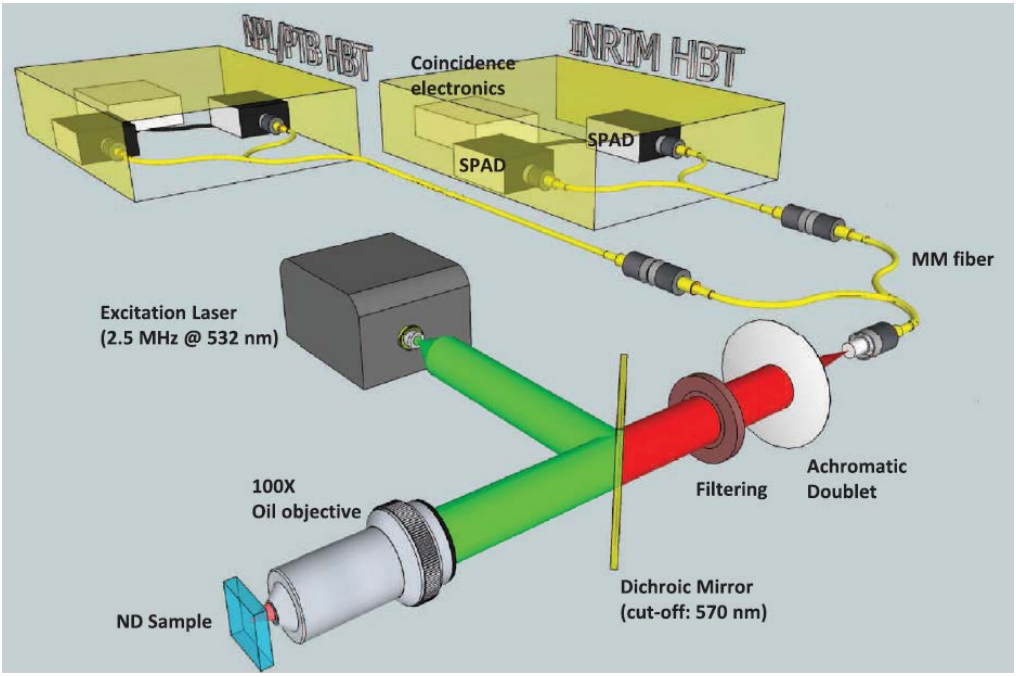

Fig. 3.3.2. Scheme of the experimental setup: the output of a laser-scanning confocal microscope is split by a 50:50 beam-splitter and directed to two independent HBTs measurement systems performing the comparison. One of the measurement devices is held by the host institution (INRIM) while the other one is used, in turn, by the other two partners (NPL, PTB).

3.3.4. Results

Each measurement consisted of 10 runs each of 500 s acquisition time. The total coupling rate, accounting for limited SPS quantum efficiency, collection angle, optical losses and detection efficiency (excluding the splitting ratio of the detector-tree), has been estimated as the ratio between the counting rate of the detectors (summing over all four of them) and the excitation rate, yielding η_{TOT} = (1.76 ± 0.01)%. The coincidence window w considered for evaluating the reported α was w = 16 ns. By repeating the analysis for different temporal widths w it was observed that the results were consistent as long as the backflash peaks were not included in the coincidence window (see Fig 3.3.5). Figures 3.3.3 and 3.3.4 show the distributions of the α_{exp} values measured by each partner; the continuous line indicates the mean value and the dashed lines draw a 1-σ confidency band around the mean value. Tables I– IV report the uncertainty budgets associated with the measurements. The summary of the results of the joint measurement is presented in Table V. We observe that individual measurement sessions (INRIM/NPL and INRIM/PTB) yield results that are extremely consistent. Mechanical instability in the coupling of the source may be the reason why the two sessions are not perfectly in agreement and the results of the INRIM/PTB joint measurements yield a slightly higher α value (as well as greater associated uncertainty) with respect to the INRIM/ NPL ones. In fact, the agreement in the INRIM/NPL measurements is better than indicated by Fig. 3.3.4 and the calculations, since the

NPL measurements took longer than the INRIM measurements, the last two NPL measurements being performed after INRIM had completed its measurements. However, all values are compatible within the uncertainty (k = 2). The uncertainties on the results of the measurements have been calculated as combined standard uncertainties for correlated input parameters N_x (x = C, ξ, bg) according to the formula[134]:

$$u_C(\alpha_{\exp}) = \sqrt{\sum_x \left(\frac{\partial a_{\exp}}{\partial N_x}\right)^2 u(N_x)^2 + 2\sum_{x,y} \rho_{xy} \left(\frac{\partial a_{\exp}}{\partial N_x}\right)\left(\frac{\partial a_{\exp}}{\partial N_y}\right) u(N_x)u(N_y)} \qquad (3.3.7)$$

where the correlation coefficient ρ_{xy} is defined as

$$\rho_{xy} = \frac{\langle N_x N_y \rangle - \langle N_x \rangle \langle N_y \rangle}{u(N_x)u(N_y)}. \qquad (3.3.8)$$

3.3.5. Dependence α on the coincidence window

To prove that the estimation of α is independent of the choice of the time interval of integration, we performed an analysis of the values of the measurand obtained by varying the coincidence window w. The results are shown in Fig. 3.3.5, demonstrating that, as long as the backflash peaks are not included in the integration, the estimate is consistent independently of w.

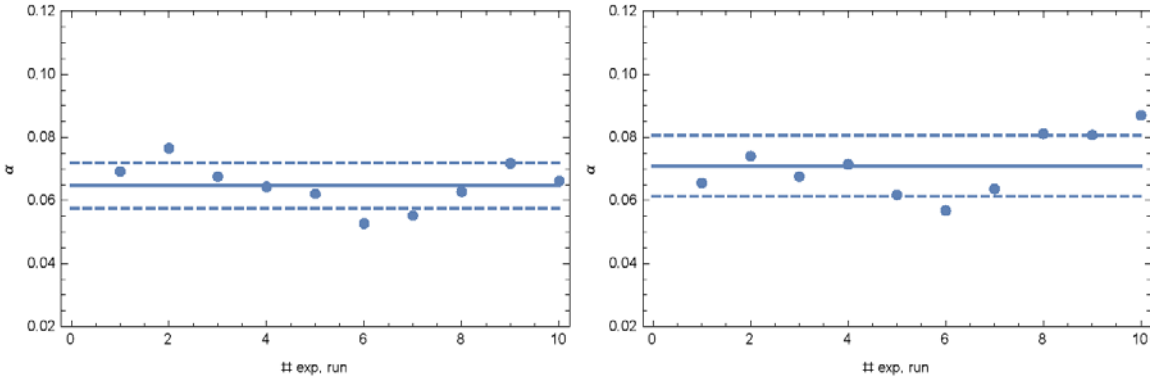

Fig. 3.3.3. Distribution of the individual measurements performed by INRIM (left) and PTB (right) in joint measurement.

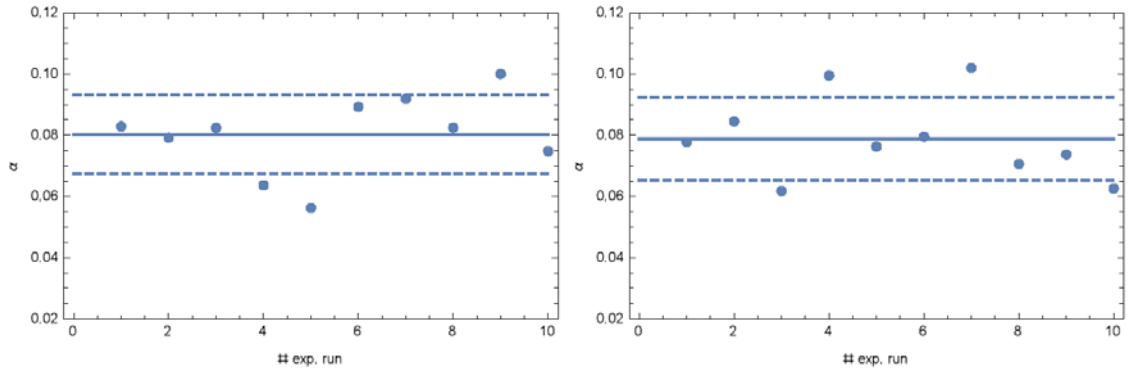

Fig. 3.3.4. Distribution of the individual measurements performed by INRIM (left) and NPL (right) in joint measurement.

Quantity	Value	Standard unc.	Sens. coeff.	Unc. contribution
N_C	1000	70	1.5×10^{-4}	1×10^{-2}
N_ξ	7400	900	-9×10^{-6}	-1×10^{-2}
N_{BG}	560	30	-1.4×10^{-4}	-3×10^{-3}
α_{exp}	0.065			0.005

Tab. I. Uncertainty Budget (k = 2) associated with INRIM (in joint measurement with NPL).

Quantity	Value	Standard unc.	Sens. coeff.	Unc. contribution
N_C	900	200	2×10^{-4}	2×10^{-2}
N_ξ	6000	2000	-1×10^{-5}	-2×10^{-2}
N_{BG}	540	50	-2×10^{-4}	-7×10^{-3}
α_{exp}	0.068			0.005

Tab. II. Uncertainty Budget (k = 2) associated with NPL measurement (in joint measurement with INRIM).

Quantity	Value	Standard unc.	Sens. coeff.	Unc. contribution
N_C	800	100	2×10^{-4}	3×10^{-2}
N_ξ	5000	1000	-2×10^{-5}	-2×10^{-2}
N_{BG}	380	30	-2×10^{-4}	-6×10^{-3}
α_{exp}	0.079			0.009

Tab. III. Uncertainty Budget (k = 2) associated with INRIM measurement (in joint measurement with PTB).

3.3.6 Lifetime estimation

The mean lifetime associated with the source has been estimated by numerically fitting the coincidence histograms (as in Fig.3.3.1) via the single-exponential function[135]

$$f(\tau) = ab \sum_{n=-\infty}^{+\infty} \left(1 - \frac{\delta_{0n}}{c}\right) e^{-\frac{|\tau - n\Delta t|}{d}} \tag{3.3.9}$$

Quantity	Value	Standard unc.	Sens. coeff.	Unc. contribution
N_C	900	70	2×10^{-4}	2×10^{-2}
N_ξ	5300	900	-2×10^{-5}	-2×10^{-2}
N_{BG}	530	40	-2×10^{-4}	-6×10^{-3}
α_{exp}	0.076			0.007

Tab. IV. Uncertainty Budget (k = 2) associated with PTB measurement (in joint measurement with INRIM).

	INRIM	PTB
α_{exp}	0.079 ± 0.009	0.076 ± 0.007
	INRIM	NPL
α_{exp}	0.065 ± 0.005	0.068 ± 0.005

Tab.V. Summary of the results of the joint measurements performed by INRIM, NPL and PTB (k = 2).

where a corresponds to the number of background coincidences, b is a normalization factor, δ_{0n} is the Dirac Delta, c is the number of excited emitters, n is the excitation pulse number, Δt is the excitation period and, finally, d accounts for the lifetime (convoluted with the detectors' jitter) of the center. Figure 3.3.3 shows the results of the lifetime estimation independently performed by the partners. Each value in the plot represents the mean of the results of 10 fits (one for each experimental run performed by one partner). Averaging the results, it is obtained the value t_{LIFE} = (15.34 ± 0.08) ns, what corresponds to characterisation of the ND sample done in Section 3.2.

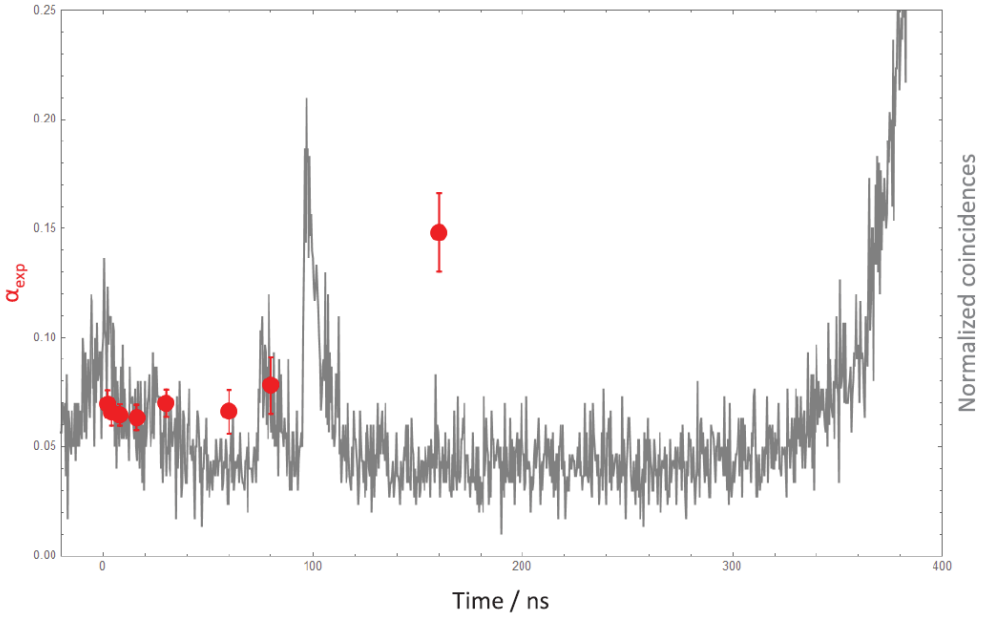

Fig. 3.3.5. Value of α_{exp} as a function the coincidence window w (k = 1). For the sake of clarity, the data (i.e. the red dots) are compared to the normalized chronogram of the coincidences (without background subtraction), shown in gray.

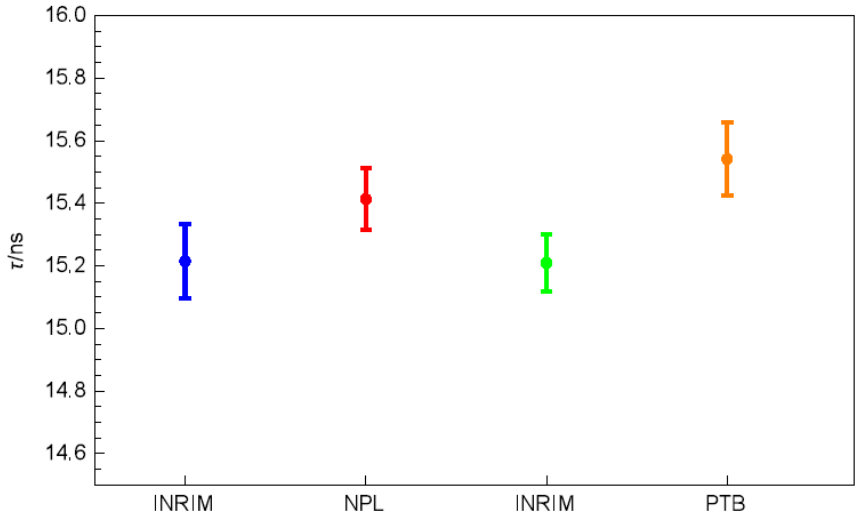

Fig. 3.3.5. Results of the emitter's lifetime _ (k = 1) joint measurement respectively performed by: INRIM (blue dot) and NPL (red dot), INRIM (green dot) and PTB (orange dot)

Conclusions

In this Chapter the fabrication process of fluorescent nanodiamonds and the optical characterization of the NV centers fabricated in these nanoparticles by means of ion beam implantation was reported. The produced NDs samples were used as ensembles of single-photon emitters for the experimental demonstration of a new non-classicality criterion. The most important advantage of nonclassicality criteria based on $\theta^{(N)}$ is the resilience to Poissonian noise affecting the source. Another important behaviour of $\theta^{(N)}$ measurement is that its value gets more nonclassical for increasing number of emitters, while $g^{(N)}$ approaches classicality in this cases. The technique is of high interest in quantum technology because, in principle, the information gained by its implementation can be used together with other multicoincidence techniques[113], [134]–[141], leading to an improvement of the latter applications. Finally, for more complex cases (not only single emitters and Poissonian noise but also thermal modes are present), $\theta^{(N)}$ and $g^{(N)}$ measurements can be possibly combined as in the algorithm described in Ref.[129] to obtain a rigorous and reliable reconstruction of the modal structure of the fields.

The $\theta^{(N)}$ measurement technique has also one drawback: the $\theta^{(N)}$ value depends on the experimental conditions (optical and coupling losses, detection efficiency, detector-tree splitting ratio). On the other hand, if the measurement apparatus is previously characterized, one could identify the number of single-photon emitters in the ensemble and then optimization can be carried on to remove the noise source.

The pilot study of the $g^{(2)}(0)$ measurement for a SPS based on NV color centers in nanodiamonds performed by INRIM, NPL and PTB was presented. Consensus on such a procedure would produce great benefits for the metrology community and pave the way for the realization of a

mutual recognition agreement on the calibration of key elements for forthcoming optical quantum technologies, such as SPSs and single-photon detectors.

Chapter 4

Quantum Sensing

4.1 Electrical characterization of a graphite-diamond-graphite junction

The detection of weak electric signals and elementary charges is important for a broad field of potential applications. One of them is development of innovative devices based on diamond: high-power and fast electronics[142]–[144], detectors[145], [146], biosensors[147]–[149] and integrated platforms for quantum technologies[109], [147], [148], [150]–[152]. The main hindrance at the step of optimizing devices performance are lattice defects with deep levels in the diamond energy gap, which act as charge carrier traps.

In the previous works carrier traps have been investigated by ion, electron x-ray and visible beam-induced charge microscopies[153]–[156], but these technics cannot reconstruct the local electric-field distribution in the defective material.

In this work we demonstrate that N-*V* ensembles can be successfully exploited as a nanoscale sensors to perform direct local mapping of the internal electric-field distribution of a graphite-diamond-graphite junction exhibiting electrical properties dominated by trap- and space-charge related conduction mechanisms. In this novel "self-diagnostic" approach, NV centers represent not only the source of detrimental spatial charge but also a unique tool for their direct investigation.

4.1.1 Device fabrication

The investigated graphite-diamond-graphite junction was fabricated by means of ion beam implantation on an optical grade type-IIa diamond substrate from "Element Six Ltd", cut along <100> and with nominal concentrations of substitutional nitrogen and boron respectively <1 ppm and <0.05 ppm. The structure consisted of two microelectrodes with a width 15μm and length 100μm, separated by 9μm gap, as shown in Fig.4.

The sample was fabricated on a planar geometry by raster-scanning a focused 6 MeV C3+ beam with ~ 5 μm diameter. A power of ion beam (~ 4×10^{16} cm^{-2}) was chosen to overcome the graphitization threshold[157] at a depth of ~ 2.7 mm below the diamond surface, as shown in Fig.4.1.1a. To convert the amorphized layer to a graphitic phase the sample was annealed at 950 °C in vacuum for 2 hours. This thermal process induced the formation of high-density ensembles of NV centers in the gap region between the graphitic channels, due to the aggregation of native nitrogen atoms and the vacancies created by ions during in the fabrication process.

Subsequently, by mean of focused Ion Beam (FIB) milling the endpoints of graphite microchannels were expose and 70 nm thick Ag contacts through a stencil mask were deposited. Electrical contact with the graphitic channels was implemented by two electrical microprobes two controlled by micrometric manipulators.

The ion microbeam fabrication also resulted in the implantation of a halo of stray ions surrounding the graphitized layers [Fig. 4.1.1(d)] and located mainly on a plane at the same depth as that of the graphitic electrodes. The concentration of induced NV centers in this region can be approximately estimated in this way. The concentration of native nitrogen atoms of the order of 10^{17} cm^{-3} was taken from the manufacturer specifications. The density of vacancies due to the ion implantation process is estimated as ~1×10^{22} cm^{-3} (Fig.4.1.a). Such a value is below the graphitization threshold for subsuperficial ion implantations but high enough to promote the formation of a high concentration of N-*V* centers upon thermal annealing[158], as well as to introduce other types of defects and carrier traps, such as the *B*-band and interstitial-related defects[157].

The N-*V* concentration is estimated to be proportional to the density of vacancies introduced in the diamond lattice. The efficiency of conversion "V + N → NV" is about 1-10 % range [114], thus, the NV concentration could be estimated in the range of 10^{3}-10^{4} centers/μm^{-3} at the end of the ion range in diamond[157].

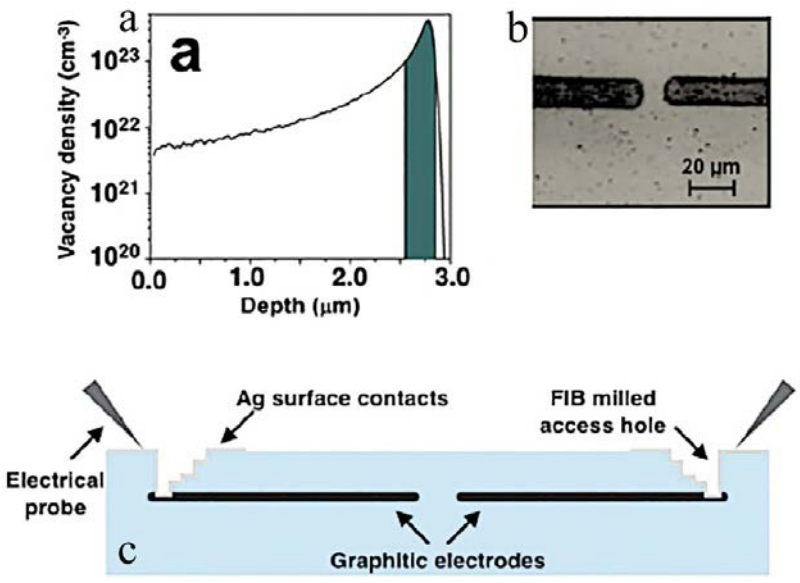

Fig 4.1.1. a) SRIM simulation of depth profile of induced vacancies in diamond by the implantation of 6 MeV C3+ ions. The green area represents the depth range where the vacancy density exceeds the graphitization treshold **b)** Optical micrograph of the fabricated graphitic electrodes in the diamond substrate. **c)** Schematic representation of the final device (cross-sectional view), the FIB milled holes are exposed to the Ag contacts deposition.

4.1.2 Experimental setup

Measurements were performed using a confocal fluorescence microscope (see Section 1.3) equipped with cw 515-nm laser excitation and microwave (MW) generator set on the resonant frequency for the ODMR measurements (see Section 2.1).

The employed components are reported in the following:
- MW Generator: EXGX -Series RF Vector Signal Generator
- Amplifier (ZHL-16W-S+) +40 dBm
- Bi Directional coupler (WERLATONE C8000-102)
- Attenuator: Bird 25-6T-MN
- Spectrum analyzer: N1996A Agilent CSA Spectrum Analyzer
- Magnet: Eclipse 20mm Alnico Deep Pot Magnet

The MW generator operates in a 9 kHz – 3.2 GHz frequency range. The relative power output (with respect to a maximum value of 39.8 mW) ranges between -144 dBm and +16 dBm. In order to increase the MW output, a power amplifier was added to the system, which increments the input signal by 40 dBm. The output of amplifier was connected to Bi directional coupler, one outer port of which was used by the spectrum analyser for the measurement of reflected signal from the sample and the frequency of the microwaves in order to allow for a real-time control of the system. The cables used to bring the signal to the sample are Type N coaxial type, which allows transmission at frequencies up to 11 GHz. In order to avoid reflections in the circuit a 50 Ω attenuator was added after the sample holder. An external magnetic field was applied by cilidric magnet which generates a ~ 10 mT field. The magnet was fixed on the stage with the possibility to moving it in x, y, z directions and to rotate it for better alignment with the NV axis. CW microwave excitation was sourced by a Cu wire with diameter 30 μm placed on the diamond surface and soldered at both sides of the sample holder in way of having it stretched over the diamond without any gap between them. The distance between the wire and active zone was ~ 25 μm (see Fig.4.1.2a). The contrast of ODMR spectrum depends mostly on the distance between the antenna and the NV center, so the MW power was optimized to achieve the best contrast. The microwave generation and acquisition of ODMR spectra were controlled by a program in LabView that allows one to set the following parameters:
- Microwave power
- Frequency interval of scanning
- step of microwave frequency

- Acquisition time
- Total acquisition time

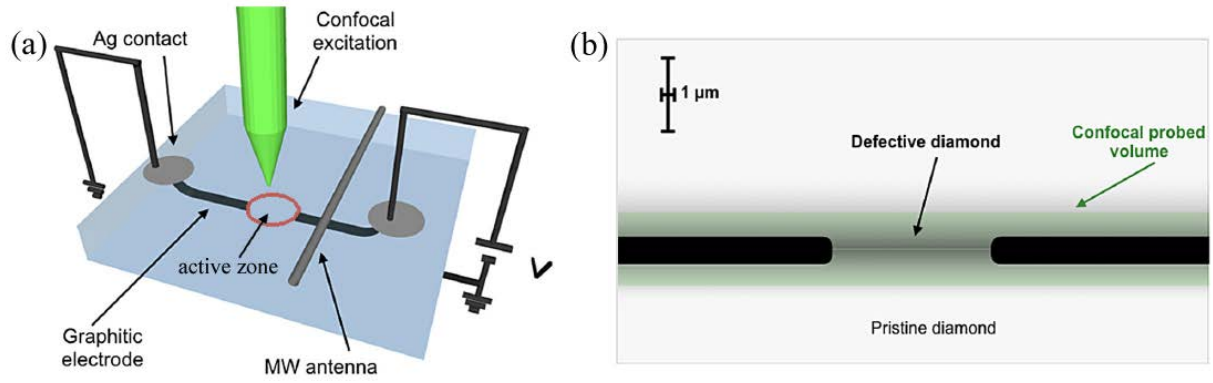

Fig. 4.1.2: (a) Schematic representation (not to scale) of the graphite-diamond-graphite junction with MW antenna under confocal excitation. (b) Schematic representation (to scale) of the cross section of the device, highlighting the depth and thickness of the graphitic electrodes and the presence of a defective region in the active region. The region highlighted in green indicates the ~ 1µm thick focal plane probed by the confocal microscope.

The experimental procedure needed to perform an ODMR measurement in dc mode can be summarized in 3 steps: PL map acquisition, focusing on the desired coordinate (e.g. corresponding to a single NV center) and then the application of a MW sweep at a certain power. Photoluminescence and ODMR measurements were performed by mapping the graphite-diamond-graphite junction across a plane parallel to the sample surface. The focal plane was set to coincide with the end of the 6-MeV C^{3+} range, i.e., where the concentration of radiation-induced defects and NV- centers is maximal. The measured signal was therefore averaged along a focal depth of ~1 µm, i.e., comparable with the thickness of the graphitic electrodes (see Fig. 4.1.2b).

4.1.3 Results and discussion

4.1.3.1 Electrical characterization

The room-temperature current-voltage characteristics of the junction are presented in Fig. 4.1.3 in the same voltage ranges as explored in the ODMR measurements[157], [159] . The curve exhibits an Ohmic trend up to a voltage threshold (V_T~+250 V), at which the space-charge density starts affecting the conduction mechanism and a deviation from the linear trend is observed. In accordance with the SCLC model[157], [160], this deviation is associated with the progressive filling of traps by the electrons injected in the active region[161] and leads to the transition to a high-current regime (>10 μA) at voltages larger than a critical value V_C (~+330

V). At higher bias voltages, the superlinear dependence of the current on the applied bias is compatible with the Poole-Frenkel conduction model[162].

According to the SCLC model, the current is limited at biases in the $V_T < V < V_C$ range by a counter-field built by the progressive filling of traps by carriers injected in the active region of the junction[163]. Such an interpretation is based on a unipolar conduction mechanism[164] and is consistent with several experimental features observed in other works[109], [157], [159] over repeated measurement cycles, i.e., different slopes in the current-voltage curves under polarity reversal (Fig. 4.1.3), a progressive conversion of the NV centers to a negative charge state at increasing currents, a decrease in the critical voltage at increasing temperatures, a marginal variability of a few volts in the value of V_C from different experimental runs, and a pronounced current-voltage hysteresis at decreasing bias voltages.

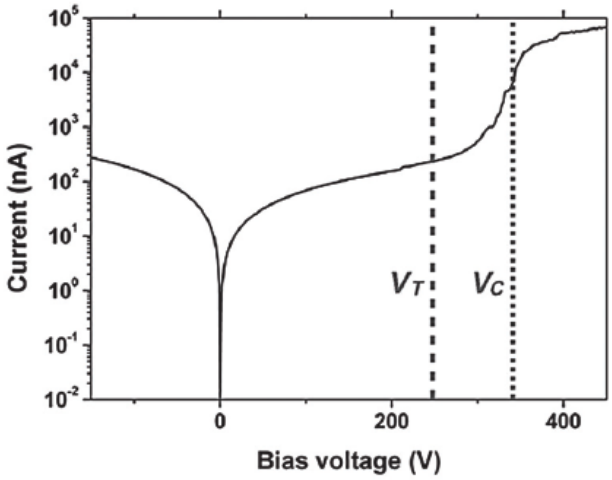

FIG. 4.1.3. Current-voltage characteristic of the junction; the threshold and critical bias voltages (V_T and V_C, respectively) are marked by dashed vertical lines.

4.1.3.2 ODMR spectra at variable applied bias voltage

The PL mapping at zero bias voltage of the regions located above the electrodes (Fig 4.1.4a) exhibits an intense emission from the regions directly above the electrodes, which is determined by negative NV centers and other optically active radiation-induced defects located between the sample surface and the graphitic layer. Conversely, the PL emission from the active region is largely dominated by NV– ensembles[157]. The peculiar spin properties of the NV– center were exploited to obtain a direct measurement of the local electric field in the active region of the device by means of ODMR.

Before the ODMR measurements, the junction underwent multiple voltage sweeps in the 0 to +200 V range, resulting in the buildup of a space charge in the active region. In Fig 4.1.4e, the label [C] identifies the initial “charged” state of the junction at zero bias voltage. Subsequently,

ODMR spectra were acquired at increasing bias voltages from 0 to +350 V at the fixed position labelled by the green spot in Fig. 4.1.4a: this first voltage sweep is indicated in Fig. 4.1.4e by the arrow labeled as (1). A second bias-voltage sweep from 0 to −105 V (labeled as (3)) was subsequently acquired from the same spot after the bias voltage had reverted to zero (label (2)). Each ODMR spectrum displays two dips at the characteristic resonance frequencies for NV– centers, with a splitting value that is systematically dependent on the strength of the local electric field, as clearly visible in Fig. 4.1.4b, which reports in color scale (encoding the normalized PL intensity) the series of acquired ODMR spectra as a function of the bias voltage. The black dashed line indicates the bias voltages V_T corresponding the current-voltage characteristic deviates from the linear trend. The black dotted line indicates the bias voltage V_C corresponding to the transition to the high-current regime (see Fig. 4.1.4(b,c)). The observation of two resonances in the recorded ODMR spectra is consistent with the geometry of the junction, since the electric field within the active region is mainly parallel to the axis joining the graphitic electrodes, i.e., the <100> crystal direction (Fig 4.1.4a). It is worth noting that the ODMR spectra were acquired from a ∼ 1 μm thick focal plane centered at the electrode depth. For this reason, the ODMR measurement results from an average of the electric field sensed by an ensemble of NV– centers over the above-mentioned depth.

In order to interpret the ODMR spectra according to the Hamiltonian discussed in Section 2.3.3.3, as well as to provide an assessment of the electric field outside of the central region, an ODMR scan was subsequently acquired at −50 V applied bias (label (4) in Fig. 4.1.4e) along a 15 μm – long horizontal line (highlighted by the red dashedline in Fig. 4.1.4a) bisecting the active area of the junction. The relevant fitted values of the ODMR resonances are reported in Fig. 4.1.4c. The dashed black line indicates the evaluated D frequency. The electric-field profile extracted from the experimental data (bottom, black circles) is reported together with its numerical simulations based on a two-dimensional FEM model in the presence of a local space charge (section 3.3.3). The blue line indicates the simulated profile obtained assuming a spacecharge extension ($V = -50\ V$) = 2.5 μm, in agreement with the data in Fig. 3.16a. The blue dotted line represents the simulated profile obtained including an additional space-charge effect due to diamond polarization, i.e., assuming $u(V = -50\ V)$ = 3 μm.

The ODMR resonances were analyzed to estimate the amplitude of the electric field according to the Hamiltonian reported in Chapter 2.3.3.3. It is worth remarking that, as discussed above, the ODMR resonance frequencies depend from both the amplitude of the electric field and other additional effects, such as background magnetic fields, due to the fact that the experimental setup was not fully shielded, local temperature variations related to the injected current in the device,

local strain fields due to the mechanical distortion of the diamond substrate related to the previous ion implantation. These contributions will be considered in next section.

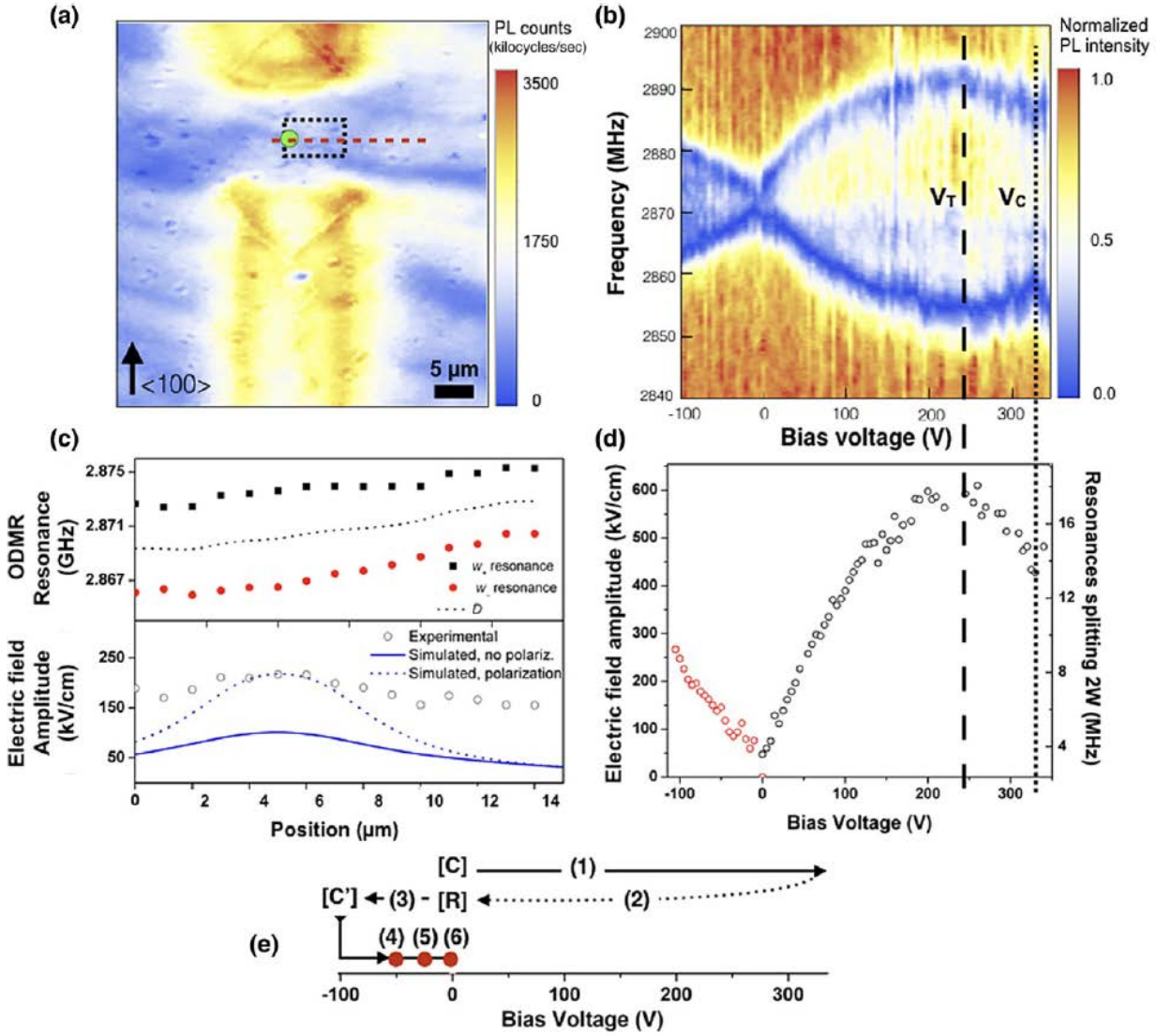

FIG. 4.1.4. (a) PL map of the unbiased junction; the rectangular region highlighted by the dashed black line indicates the region where the electric-field maps displayed in Fig 3.1.7 were acquired; the green spot indicates the point where the ODMR spectra under applied voltage displayed in (b) and (d) were acquired; the dashed red line indicates the scan along which the electric-field profile displayed in (c) was measured. (b) Intensity-color-encoded and normalized ODMR spectra acquired during a voltage sweep from the position highlighted by the green spot in (a). (c) ODMR resonances (top, black, and red data points) acquired along the red dashed line highlighted in (a) at a bias voltage of −50 V. (d) Electric-field amplitude vs the applied bias voltage, as evaluated from the ODMR splitting measured at the point highlighted in green in (a). (e) Layout of the voltage bias cycles performed on the junction. The arrows indicate the temporal sequence of the operations.

4.1.4 Electric- field sensing by the ODMR technique

The Hamiltonian of the ground state of the NV system, describing the energy levels of the electronic spin states due to the spin (*S*) interaction with the static magnetic (*B*), electric (*E*), and strain **(***F*) fields, can be written in terms of the natural spin-triplet basis {|*ms* =0> , |*ms*=+1>, |*ms*=−1> } in the following matrix form[28]:

$$\frac{\hat{Hs}}{h}=\begin{pmatrix} 0 & -\mu g\frac{B_x-iB_y}{\sqrt{2}} & -\mu g\frac{B_x+iB_y}{\sqrt{2}} \\ -\mu g\frac{B_x+iB_y}{\sqrt{2}} & D+\mu gB_{\|} & -d_{\perp}(P_x-iP_y) \\ -\mu g\frac{B_x-iB_y}{\sqrt{2}} & -d_{\perp}(P_x+iP_y) & D-\mu gB_{\|} \end{pmatrix} \tag{4.1.1}$$

where $D=D_o+d_{\|}P_{\|}$ describes the frequency shift of the resonance lines resulting from the zero-field splitting and from the Stark effect associated with the component of the **P=E+F** vector parallel to the NV axis, with coupling constant $d_{\|}$ =0.35 HzV^{-1} [28]. The $\mu gB_{\|}$ term on the matrix diagonal describes the Zeeman splitting of the ODMR resonances (μ is the Bohr magneton and *g* is the ground-state electronic *g* factor[5]), and indicates that the natural-spin basis vectors are eigenstates of the Hamiltonian in the sole presence of the magnetic field aligned with the NV axis.

The presence of additional transverse (i.e., lying in the *x-y* plane in the current notation) strain- and electric-field components $P_{\perp}$ (with coupling constant $d_{\perp}$ =17 HzV^{-1} cm) modifies the ground-state hyperfine structure. The Hamiltonian assumes a quasidiagonal form considering a new spin basis {|0>, |+>, |−>}, obtained by a field-dependent mixing of the |+1> and |−1> spin states according to the following unitary operator:

$$\hat{U}=\begin{pmatrix} 1 & 0 & 0 \\ 0 & e^{i\phi/2}\sin(\frac{\theta}{2}) & e^{-i\phi/2}\sin(\frac{\theta}{2}) \\ 0 & e^{i\phi/2}\cos(\frac{\theta}{2}) & -e^{-i\phi/2}\sin(\frac{\theta}{2}) \end{pmatrix} \tag{4.1.2}$$

where $\tan(\varphi) = P_y / P_x$ and $\tan(\theta) = d_\perp P_\perp / \mu g B_\parallel$ are the field-dependent phases defining the spin state mixing. With further consideration of the quantity *W*,

$$W = \left[\left(\mu g B_\parallel \right)^2 + \left(d_\perp P_\perp \right)^2 \right]^{1/2}, \tag{4.1.3}$$

Defined by imposing $\mu g B_\parallel = W \cos(\theta)$, $d_\perp P_\perp = W \sin(\theta)$, the Hamiltonian in Eq.(4.1) takes the following form in the {|0> , |+1>, |−1>} basis:

$$\frac{\hat{H}_d}{h} = \frac{1}{h} \hat{U} \hat{H}_s \hat{U}^\dagger = \begin{pmatrix} 0 & c_1 \mu g B_\perp & c_2 \mu g B_\perp \\ c_1^* \mu g B_\perp & D+W & 0 \\ c_2^* \mu g B_\perp & 0 & D-W \end{pmatrix}, \tag{4.1.4}$$

where c_1 and c_2 describe the relative phase of the matrix elements and $B_\perp$ is the transverse component of the magnetic field with respect to the axis of the NV center. If an ensemble of NV centers, distributed according to all the four possible orientations in the diamond lattice, is considered, we can assume that $B_\perp \sim B_\parallel$ and $B_\perp^2 / (DW) \ll 1$, i.e., the nondiagonal terms can be neglected and the Hamiltonian in Eq.(4.1.1) can be regarded as diagonal in the basis $\{|0\rangle, |+\rangle, |-\rangle\}$[14]. It is worth noting that, since only the m_s=±1 states are involved in the spin-state mixing of $|0\rangle$, $|+\rangle$ and $|-\rangle$ in Eq.(4.1.2), their resonant microwave-induced transitions with the $|0\rangle$ state still result in a detectable PL contrast, thus ensuring the suitability of the ODMR technique for electric- and strain-field sensing. Therefore, the energy difference between the between the $|0\rangle$ and the $|\pm\rangle$ states is given by $h(D \pm W)$, and the observed ODMR resonances are separated by a $2W$ frequency splitting [Fig. 4.1.5b], which is determined by the strengths of the magnetic, electric, and strain fields, as well as their orientations with respect to the axes of the NV center, according to Eq.4.1.3.

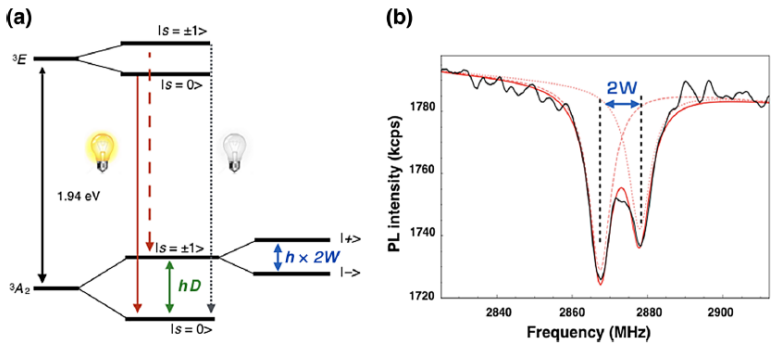

FIG. 4.1.5. (a) Schematic representation of the relevant energy levels of the negatively charged NV center. (b) typical ODMR spectrum acquired at +25 V bias voltage (black line). The fitting curve (solid red) is superimposed, together with the two corresponding Lorentzian peaks.

The transverse component of the electric field can be derived from the ODMR spectra through the Eq.4.1.3 as

$$d_{\perp}E_{\perp} = -k_{\perp}F_{\perp} + \left[W^2 - \left(\mu g B_{\parallel}\right)^2\right]^{1/2}, \tag{4.1.5}$$

This operation relied on preliminary knowledge of the $B_{\parallel}$ and strain fields $F_{\perp}$ to ODMR spectrum, whose analysis and quantification are discussed in detail in the following subsections.

4.1.4.1 Magnetic field contribution

The coupling of the NV center spin with the environmental magnetic field results in the Zeeman splitting term $\left[W_1 = \mu_B g B_{\parallel}\right]$which does not contribute to the resonance shift of zero-field splitting frequency *D*. The resonance splitting was evaluated from the ODMR spectrum acquired at 0 V bias before the voltage sweep at negative polarity [label [R] in Fig. 4.1.4e], from the probed spot at the center of the active region [green spot in Fig. 4.1.4a]. In the absence of the external electric field, the relevant energy-splitting term reduces to the sole contribution of the strain vector field **P=F**, and Eq.4.5 reduces to $\mu g B_{\parallel} = \left[W^2 - \left(d_{\perp}F_{\perp}\right)^2\right]^{1/2}$. A 0.46-MHz increment in the zero-field splitting term *W* associated with the local radiation-induced strain field (corresponding to a ~0.24 GPa stress along the <100> crystallographic axis) was derived, as discussed in more detail in the next subsection, leading to an estimation of the $\mu g B_{\parallel}$ value of 1.09 MHz, which in turn corresponds to a 39 μT magnetic field. Due to the absence of a magnetic screening of the experimental setup, this value is ascribed to the earth and environmental magnetic field and is assumed to be constant in the whole region investigated in this work. This

assumption is supported by the fact that any ferromagnetic component of the confocal microscopy setup was left at a fixed position for the whole duration of the measurements. It is also worth noting that the magnetic field associated with the current flowing in the active region of the device is negligible, as it is well below the sensitivity of the experimental setup operating in cw mode. Indeed, even under the unrealistic assumption that a current of 10 μA (i.e., at V=V_C; see Fig. 4.1.3) is entirely flowing within a 1-μm distance (i.e., the focal point size) from the sensed position, the induced magnetic field would be <200 nT, according to the Biot-Savart law.

4.1.4.2 Evaluation of the internal stress

The mechanical stresses associated with the presence of radiation-induced lattice damage[165] within the active region of the junction are included in Eqs.(4.1,4.3) in the effective electric-field vector **P**. The component of such a vector parallel to the NV center axis (i.e., $P_{||}$) induces a shift in the ODMR resonances. This term can be rewritten as $d_{||}P_{||} = d_{||}(F + E_{||}) = k_{||}\Sigma + d_{||}E_{||}$, where Σ is the strength of the stress field associated with the parallel lattice strain and $k_{||}$=14.6 MHz GPa^{-1} is the experimental value of the coupling constant along the NV axis[46]. The electric-field coupling constant $d_{||}$=0.35 HzcmV^{-1} is negligible with respect to $k_{||}$, resulting in the approximated expression $D \cong D_0 + k_{||}\Sigma$.

In order to experimentally assess the value of D_0 (i.e., the D value in absence of mechanical stresses), we estimated the D value from the ODMR spectrum acquired corresponding to the largest distance probed from the central axis of the active region, i.e., $x_0 \cong 12$ μm across the linescan reported in Figs.4.1.4a,c. Indeed, according to the results of three-dimensional FEM simulations of the stress-field strength[166], such a distance is sufficient to probe a region with a negligible stress field. The zero-field splitting was therefore evaluated as $D_0 = D(x = x_0) = (2872.9 \pm 0.2)$ MHz. The local stress-induced shift was then derived for the whole linescan as $\Sigma(x) = \left[D_0 - D(x)\right] / k_{||}$, and resulted in a <0.25 GPa tensile stress at the central position of the active region [Fig. 4.1.4c].

The mechanical stresses building up in the active region are due to two effects, i.e., (i) the constrained volume expansion of the graphitic microelectrodes with respect to the surrounding diamond matrix, and (ii) the volumetric expansion of the defective region surrounding the same microelectrodes. These two mechanisms induce, respectively, a compressive and a tensile stress in the active region of the device, and their concurrent effect was numerically modelled by performing three-dimensional finite element simulations, as described in Ref.[166]. The simulated volume is shown in Fig.4.1.6. The following mechanical parameters were adopted for

diamond and amorphous carbon, respectively: mass densities ρ_d =3515 kg m^{-3} and ρ_{aC} =2060 kgm^{-3}, Young's moduli E_d =1220 GPa and E_{aC} =21.38 GPa. The defective diamond region between the electrodes shown in Fig. 4.1.2b is assumed, in a first approximation, to contain a vacancy density of λ=10^{19} cm^{-3} (i.e., a reduction of three orders of magnitudes with respect to the graphitization threshold) due to irradiation with stray ions, as well as vacancy diffusion resulting from an incomplete recovery of the crystal structure after annealing. The vacancy density decreases along the *x* direction, until it becomes negligible at a significant (i.e., ~10 μm, corresponding to roughly twice the size of the ion microbeam) distance from the nominally irradiated region where the graphitic electrodes are formed. The local mass density and Young's modulus of the defective region of interest can thus be described by a semiempirical model taking into account damage saturation effects[166]:

$$\rho(x) = \rho_d - (\rho_d - \rho_{aC})\left(1 - \exp\left[-\frac{\lambda(x)}{\gamma(1-\rho_d/\rho_{aC})}\right]\right), \tag{4.1.6}$$

where γ =1.77×10^{23} cm^{-3} is the atomic density of diamond, $\lambda(x)$ is the vacancy density, and

$$E(x) = E_d\left(1 - k\left[-\frac{\rho(x)}{\rho_d}\right]\right) \tag{4.1.7}$$

where κ is an empirical constant. The density decrease due to irradiation generates a constrained expansion of the implanted volume, which is only partially counterbalanced by the expansion of the surrounding graphitic electrodes, resulting in residual strains in the *i* = *x,y,z* directions given by

$$\varepsilon_i(x) = \sqrt[3]{\frac{\rho_d}{\rho(x)}} - 1 \tag{4.1.8}$$

Fig.4.1.6(a) shows a color-encoded map of the corresponding FEM-calculated internal volumetric stress $\sigma_V = (\sigma_x^2 + \sigma_y^2 + \sigma_z^2)^{1/2}$ in the material. The stresses reach relatively high compressive values (~5 GPa) close (i.e., at <1 μm) to the electrodes, where the largest density mismatch occurs, and smaller (<1 GPa) tensile values at the center of the active region of the device. The estimated vacancy-density distribution along the dotted white line in Fig. 4.1.7(a) is shown in Fig. 4.1.7b, and the corresponding stresses are shown in Fig. 4.1.7(c) (the curve labeled as FEM). In particular, the calculated tensile stresses along the dotted line are in satisfactory agreement (at least from an order-of-magnitude point of view) with those that were

experimentally derived from the $D(x)$ frequency shift along the linescan reported in Fig.4.1.4c (Exp in the plot), confirming the validity of the assumed vacancy distribution.

The contribution of the stress field to the resonance splitting was then experimentally determined as $d_{\perp}F_{\perp}(x) = k_{\perp}\Sigma(x)$, as described in the following. The coupling constant $k_{\perp}$ =1.93MHzGPa^{-1} was derived from the experimental data reported in [46], where the ODMR splitting as a function of the applied stress field is evaluated in a sample that has the same crystallographic orientation as the substrate investigated in this work. The fitting of the data reported in [46] was performed after suitable removal of the environmental magnetic field (which was assumed to cause the resonance splitting at the minimum stress value of 0.1 MPa), according to Eq.(4.1.3). Such estimation of the coupling constant $k_{\perp}$ enabled the local evaluation of the stress contribution to W, while the stress field $\Sigma(x)$ was determined by the measured resonance shift $D(x)$. Therefore, it was possible to subtract this contribution from the experimental ODMR data according to Eq.4.1.5, as well as to identify the background magnetic field at the central position of the junction, having set $E_{\perp}$ =0.

Figures 4.1.6(a,b) display the maps of the zero-field splitting D evaluated from the ODMR resonances under an external applied bias voltage of 0 and −25 V, respectively. The difference between the zero-field splitting values D acquired in the two maps shown in Figs.4.1.6c indicates values close to zero within the limits determined by the ~2MHz FWHM of the ODMR dips. As the shift is sensitive only to electric and stress fields [see Eq. 4.1.1], the observation that the D parameter is insensitive to changes in the applied bias voltages indicates that the spatial distribution of its shift values is primarily determined by the internal stress fields. Thus, the same procedure adopted for the analysis of the voltage-dependent ODMR spectra allowed the mapping of the internal tensile stresses (Fig.4.1.6d), with typical values in the (0.2–0.3)GPa range, in satisfactory agreement with the results obtained from FEM simulations of the mechanical deformations of the sample.

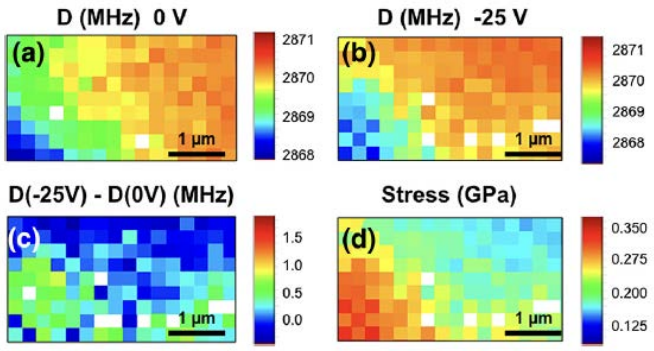

Fig.4.1.6 (a),(b) Maps of the D parameter from the (5 × 2)µm2 region highlighted in Fig. 3.13(a), as evaluated from the ODMR spectra on a pixel-by-pixel basis, under an applied bias voltage of −25 and 0 V, respectively. (c) Difference in the D value between the maps acquired at −25 and 0 V. (d) Corresponding value of the local stress evaluated from the map acquired at −25 V applied bias

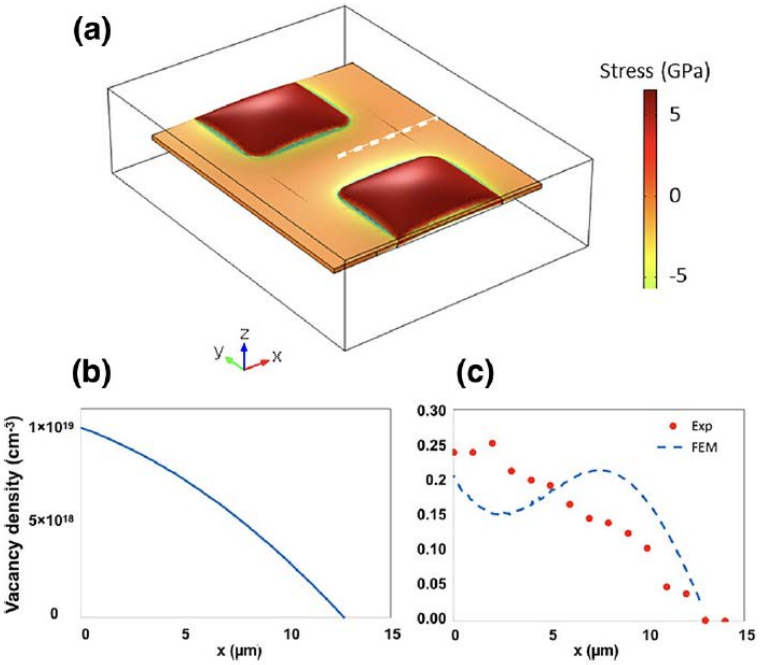

Fig.4.1.7. (a) Color map of the volumetric stresses in the region under study, due to volume expansion of the ion-implanted areas. (b) Vacancy-density distribution along the dotted line in (a). (c) Corresponding stress distribution (dashed blue line) to be compared with experimental results deriving from the ODMR measurements (red dots).

4.1.4.3 Temperature effects

Temperature variations affect the fine structure of the NV center through the thermal expansion of the lattice constant, resulting in the creation of an additional stress field besides that associated with induced structural damage[8]. While the ODMR experiments were performed at room temperature, the Joule heating associated with the current flow in the active region could, in principle, induce a local temperature increase. To test this hypothesis, the D - $D0$ shift (i.e., the contribution to the resonances shift resulting from mechanical stresses) was investigated in the ODMR spectra acquired during the 0–350-V voltage sweep reported in Fig. 4.1.4b. Since this data set was acquired at a fixed position, any voltage-dependent trend in the ODMR resonances shift would not be affected by damage-induced stress contributions. None of the D values displayed any significant dependence on the applied bias voltage, i.e., on the current injected into the junction, since they ranged within ~2MHz around the 2872.1GHz value. This variability imposes an upper limit on the temperature variation of ~30 K.

4.1.5 Data discussion and numerical simulations

This section reports on the interpretation of the obtained results of electric-field distribution free from the external fields discussed in the previous chapter.

4.1.5.1 Voltage-dependent electric field at the center of the active region

The transverse component of the electric field at the probed spot was evaluated from the ODMR spectra according to the procedure discussed in Chapter 4.1.4, upon the deconvolution of concurrent effects of background magnetic fields and local temperature or stress variations. Considering that the electric field is oriented along the <100> crystallographic direction, the four possible orientations of the N-*V* defects form a α =54.75° angle with the electric field, and thus a fourfold degeneracy in the respective spin resonances is expected. This observation is in line with the presence of only two resonances in the ODMR spectra in Fig. 4.1.4(b), indicating the degeneracy in the projection of the electric-field vector on all the NV center orientations. The amplitude of the electric-field vector has therefore been calculated as $|E|=E_{\perp}/\sin(\alpha)$.

The evaluated values of the electric-field amplitude are reported in Fig. 4.1.4(c) for the horizontal profile along the symmetry axis of the junction, and in Fig. Fig. 4.1.4(d), for the voltage-dependent measurements acquired from the probed spot at the center of the active region. The same evaluation procedure has also been adopted to define the electric-field maps discussed in the last section of this chapter. Figure 4.1.4(d), reports the electric-field amplitude at the point highlighted in green in Fig. 4.1.4(a), as a function of the applied bias voltage. The scale on the right-hand vertical axis indicates the evaluated resonance splitting $2W_E = 2\left(-k_{\perp}P + \left[W^2 - \left(\mu g B_{\parallel}\right)^2\right]^{1/2}\right)$ associated with the nonaxial electric-field contribution, upon the deconvolution of magnetic and stress fields. For applied bias voltages below V_T, the electric field linearly increases with the applied bias voltage at both polarities, although starting from a nonzero value at the zero bias voltage in the [C] configuration of the device [see Fig. 4.1.4(e)]. However, its trend is not symmetric under polarity reversal, in accordance with the nonsymmetrical behavior of the current-voltage characteristics shown in Fig.4.1.1(a).

After a progressive deviation from the linear behaviour observed in the (+125–245)V range, the estimated local electric field reaches a maximum value at positive bias voltages ranging between $V_{d/2}$ ~200 V and V_T ~245 V. At higher bias voltages, the electric field steadily decreases up to $V \sim V_C$. While the few data points acquired at bias voltages higher than V_C suggest a new increase [Figs.4.1.4(b,d). the voltage dependence of the electric field could not be adequately assessed in

this conduction regime, due to the concurrent electroluminescent emission occurring from neutrally charged NV^0 centers[157], which significantly decreased the ODMR contrast.

The overall nonmonotonic trend provides a direct insight into the conduction mechanism occurring in the active region[162]. In order to gain a deeper insight into the operation of the junction, the experimental data acquired at the central position of the active region [i.e., from the point highlighted in green in Fig. 4.1.4(a)] were compared in Fig. 4.1.4(a) (black circles) to the results of a one-dimensional finite-element-method (FEM) simulation (black line) based on the solution of Laplace's equation. This numerical result was obtained by assuming the absence of internal space charge and was performed assuming a relative dielectric constant ε_r =7.6 for thedefective substrate, as estimated in a previous electrical characterization of the same device[159].

The electric-field estimation at positive bias voltages (i.e., the first voltage sweep) differs significantly from the FEM numerical predictions, suggesting that the preliminary voltage sweeps carried on the sample before this measurement produced a space-charge buildup near the cathode, resulting in a significant increase of the internal electric field under positive polarity. The contribution of the space charge to the electric field [Fig. 4.1.4(a), green circles], estimated as the difference between the electricfield amplitude evaluated from ODMR measurements and the corresponding FEM-simulated value, has the same nonmonotonic trend at increasing bias voltage, with a maximum centered at $V \sim V_{d/2}$. This trend was interpreted according to the simple model of the space-charge buildup schematically represented in Fig. 4.1.8(b). While the absence of local charge buildup is schematically represented in Fig. 4.1.8(b,I), according to this model the extension of the space charge $u(V)$ increases with the bias voltage from the cathode to the anode due to the progressive trapping of electrons injected in the defective diamond. At low bias voltages (i.e., at $V<V_{d/2}$), $u(V)$ is smaller than $d/2$, which corresponds to the distance between the probed spot and the cathode, d being the interelectrode distance [Fig. 4.1.8(b,II)]. As a consequence, the associated negative space charge density ρ_1 produces an incremental electric field $E(\rho_1)$ adding up to that generated by the bias voltage. Conversely, when the extension of the space charge $u(V)$ is larger than $d/2$ [Fig. 4.1.8(b,III)], the internal electric field is both incremented by the contribution $E(\rho_1)$ generated by the fully charged region at x<d/2 and screened by the term $E(\rho_2)$ related to the negative charge ρ_2 progressively extending between the probed spot ($x = d/2$) and the anode ($x > d/2$).

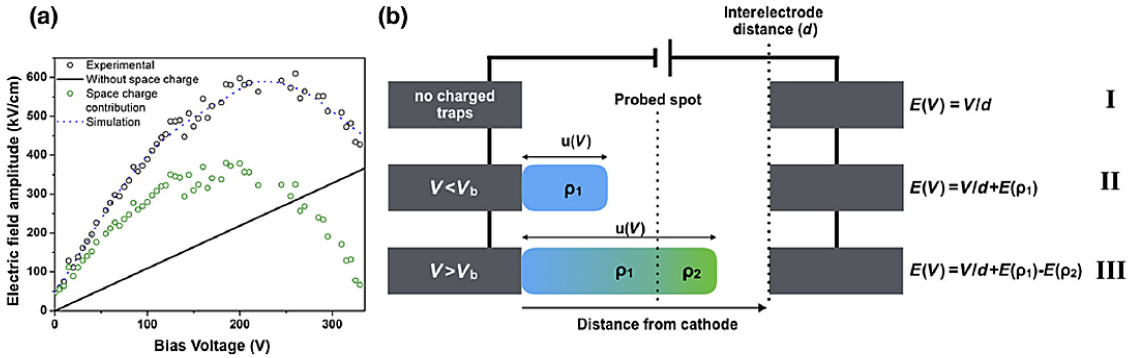

FIG. 4.1.8. (a) Voltage-dependent electric-field amplitude as estimated from: (i) the ODMR spectra reported in Fig. 4.1.4(b) [black circles, same data as in Fig. 4.1.4 (d)] and (ii) a one-dimensional FEM numerical simulation in the absence of an internal space charge (black line). The difference between the two trends (green circles) represents the electric field associated with the presence of an internal space charge. The residual nonzero value of the electric field at zero bias voltage [configuration labeled as [C] in Fig. 4.1.4 (e)] is a consequence of previous biasing cycles performed on the junction. The dashed blue line represents the trend of the electric field as evaluated by finite-element-method simulations. (b) Simplified model describing the contribution of a voltage-dependent internal space charge on the electric field measured at the probed spot [green spot in Fig. 4.1.4 (a)]. The presence of a space-charge distribution ρ_1 between the cathode and the probed spot boosts the internal electric field (II) with respect to the uncharged junction (I). An additional space charge ρ_2 between the probed spot and the anode (III) results in a partial screening of the electric field generated by the bias voltage and the space charge ρ_1 between the cathode and the probed spot.

4.1.5.2 Space-charge modelling

The suitability of the above-described model to provide an adequate description of the ODMR data acquired at positive bias voltages was assessed by including a space-charge distribution in the FEM simulations. The source term ρ of the relevant Poisson's equation was defined assuming, for simplicity, that the space-charge buildup results in the complete electron filling of a uniform distribution of traps N_T, with a gradually increasing extension $u(V)$ from the cathode [Fig. 4.1.8(b)]. The $u(V)$ extension was therefore modeled with a step function $\Theta(x)$, and assumed to monotonically increase with the applied bias to progressively fill the active region:

$$\nabla \bullet \boldsymbol{E} = \rho(x)/(\varepsilon_r \varepsilon_0) = -qN_T\theta(u(V)-x)/(\varepsilon_r \varepsilon_0) \qquad (4.1.9)$$

The value of N_T was first determined by matching the value of the simulated electric field with the experimental data, under the constraint that the space-charge extension reaches the probed spot $x = d/2$ at the bias voltage $V=V_{d/2}$. This led to an estimation of the trap density of $N_T = 1.67\times10^{16}$ cm^{-3}, roughly an order of magnitude higher that what was determined by a previous electrical characterization of the junction under the assumption of SCLC conduction[162], [163].

After the determination of N_T, by matching the simulated and experimental values of the electric-field amplitude [the dashed blue line in Fig. 4.1.8(a) represents the simulated data], it was possible to derive the voltage dependence of the space-charge extension, as shown in Fig. 4.1.9(a) (black circles). The curve highlights a significant residual space-charge extension from the unbiased device [$u(V=0) \cong 2$ μm], which is ascribed to the prior biasing of the junction. Indeed, the permanent polarization due to the formation of persistent regions of high-density space charge upon previous biasing is a well-known effect in several types of diamond-based devices[153], [167], [168].

4.1.5.3 Bias polarity reversal

The same approach was subsequently adopted to investigate the voltage-dependent space-charge buildup at negative bias voltages. The red data points in Fig. 4.1.9(a) correspond to the negative-voltage sweep labeled as (3) in Fig. 4.1.4(e). Differently from the positive-voltage sweep, the analysis yielded a negligible extension of the space-charge region for the unbiased junction, as supported by the less pronounced increase of the electric amplitude at increasing applied bias. This result indicates that the operation of the junction at $V_{\text{bias}} > +V_C$ in the PF conduction regime in the previous voltage sweep resulted in a reset [label [R] in Fig. 4.1.4(e)] of the electron traps in the active region. This interpretation is in agreement with the observation of a strong electroluminescent emission at $V_{\text{bias}} > +V_C$ from neutral NV^0 centers, which is typically interpreted as the consequence of electron-hole-pair recombination at the defect sites[109], [169], [170]. In this context, the concurrent injection of both carrier species in the high-current regime is interpreted as the cause of a progressive trap-neutralization process in the active region.

The $u(V)$ dependence reported in Fig. 4.1.9(a) was also exploited to carry a two-dimensional FEM simulation of the horizontal profile of the electric-field amplitude acquired at −50 V bias voltage after the (0–105)-V sweep [label [4] in Fig. 4.1.4(e)]. A 5-μm lateral width of the space-charge distribution [Fig. 4.1.9(b)] was assumed to achieve an optimal agreement with the shape of the electric-field map measurements discussed in the following. While a 5-μm width could be somewhat counterintuitive, this value was determined by analyzing the extension of the region of the junction that displayed an intense emission in electroluminescence (EL) regime. Indeed, the comparison of confocal maps acquired under PL and EL excitation [Figs. 4.1.9 (c),(d)] provides a strong indication that the carriers' injection and subsequent trapping is prominently localized in a relatively small section of the junction, where a ∼10 μA current is achieved at +450 V applied bias voltage. It is therefore reasonable to expect that the space charge is concentrated in the same

volume where the trapping of carriers occurs. The simulated profile is superimposed to the experimental data in Fig. 4.1.4(c) (blue line). In consideration of the adopted approximations and assumptions, the simulated profile is in satisfactory agreement with the experimental results, although with a systematic negative offset of ~60 kV cm^{-1}, which is to be ascribed to the formation of a new space-charge extension under increasing device bias at negative voltages [label [C'] in Fig. 4.1.4(e)]. The proposed explanation is in line with the observation of a residual space-charge-induced field during the first voltage sweep at increasing positive bias voltages [Fig. 4.1.4(d)]. To better appreciate this point, an additional simulation of the electric-field amplitude profile along the horizontal linescan is reported Fig. 4.1.4(c) (blue dotted line) under the assumption that the space-charge extension *u* maintains the maximum value achieved at the end of the negativebias- voltage sweep [configuration [C'] in Fig. 4.1.4(e)], i.e., u=3 μm. The good agreement of the simulated electric field strength at the center of the active region indicates that the space charge progressively formed upon an increase of the applied voltage persists when the bias reverts to zero. Furthermore, the profile along the symmetry axis of the junction highlights the smooth variation in the electric field across the active region. In this case, the absence of abrupt gradients in the electric-field profile suggests that the peculiar voltage-dependent trend reported in Fig. 4.1.4(d) is determined by a high density of carrier traps associated with the flow of a high current density through a ~(1×5)-μm^2 section of the junction.

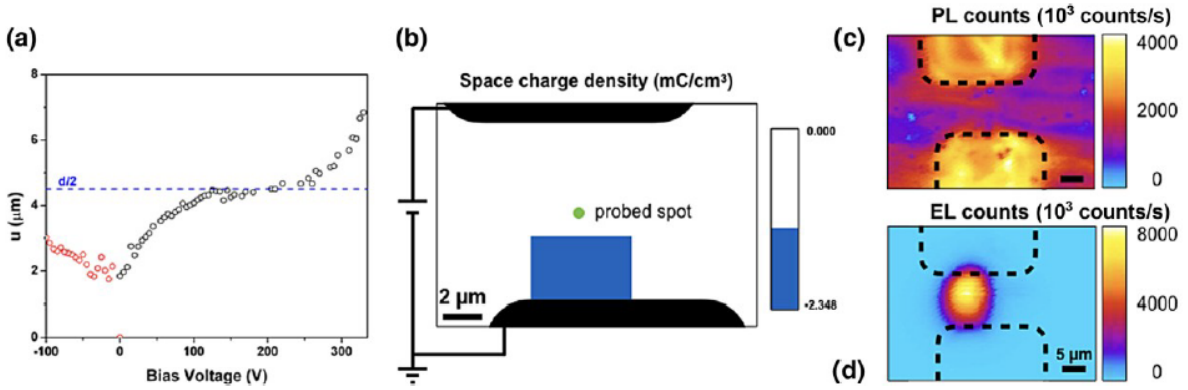

Fig. 4.1.9(a) Extension from the cathode of the space-charge region as a function of the positive (black circles) and negative (red circles) applied bias voltage. (b) Map of the space-charge distribution assumed as the source term for the two-dimensional FEM simulation of the electrostatics of the junction at the bias voltage of −50 V. The green circle corresponds to the probed spot highlighted in Fig. 4.1.4a. (c) PL map of the junction. The dashed lines highlight the edges of the graphitic electrodes. (d) EL map acquired from the same scan area under an applied bias voltage of +450 V.

4.1.6 Electric-field mapping

In order to evaluate the spatial distribution of the electric field in within the active region, ODMR maps were acquired by raster-scanning the sample position over the 5×2 μm^2 area

highlighted by the black square in Fig. 4.1.4(a). The measurements were carried after the second voltage sweep, i.e., after having polarized the junction at V_{bias}=−105 V. To investigate possible polarization effects, a first map at V_{bias}=−25 V [label (5) in Fig. 4.1.4(e)] was followed by a second one at V_{bias}=0 V [label (6)]. The local strength of the electric-field amplitude was evaluated on a pixel-by-pixel basis at both bias-voltage configurations according to Eq. (4.1.7). The resulting electric-field maps are displayed in Figs. 4.1.10(a),(b), and are to be compared with the result of a FEM simulation [Figs. 4.1.10 (c),(d)] performed according to the model in Sec. III C [see Fig. 4.1.9 (b)], where a u(−25 V)=u(0 V)=3 μm extension of the space-charge distribution was considered to describe the effects of the residual polarization in the active region of the device.

The agreement between the experimental and simulated electric-field maps is satisfactory, considering the adopted approximations and assumptions. In particular, the electric-field strength displays a significant increase with increasing proximity to the space-charged region. Indeed, the experimental data acquired at V_{bias}=−25 V [Fig. 4.1.10(a), median map value (165±14) kV cm^{-1}] are in line with the simulated electric-field strength and distribution [Figs. 4.1.10 (c),(d)], under the assumption that the same space charge observed during the negativevoltage sweep at a bias of V=−105 V [Fig. 4.1.9(a)] is still contributing to the electrostatic configuration of the junction.

This effect represents a strong indication that the residual polarization originates from the negative-bias-voltage sweep [labeled as [3] in Fig. 4.1.4(e)], which follows the erasing [label (2)] of the internal space charge formed at large positive bias voltages. In a consistent manner, this interpretation is further strengthened by the significant residual electric field observed at 0 V bias voltage [Fig. 4.1.10(b), median map value (153±11) kV cm−1], which supports the initial assumption that a progressive charging of the active region occurs upon each electric bias cycle.

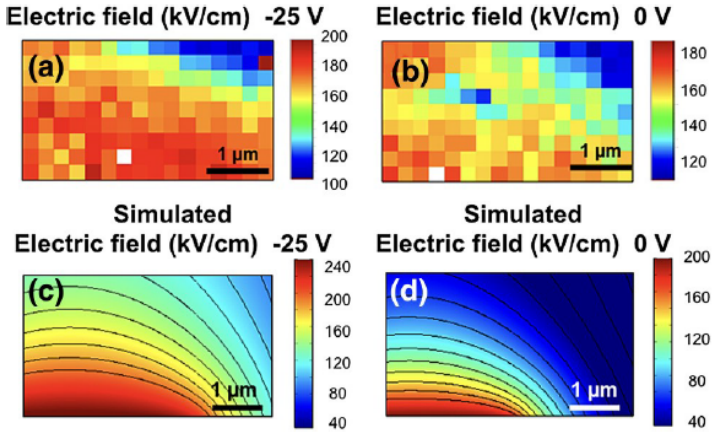

Fig. 4.1.10 (a),(b) Electric-field maps from the same region (dashed black line in Fig 4.1.4) under −25 V and 0 V applied bias voltages, respectively. Two-dimensional FEM simulation of the electric-field amplitude distribution (c) at V_{bias} = −25 V and (d) at V_{bias} = 0 V assuming a space-charge extension u 0 V = 3µm. The black lines represent the isofield lines.

4.2 Thermometers based on NV centers in diamond

4.2.1 Introduction

NV centre-based probes, now established as robust sensors to image the magnetic field, also offer the potential for extraordinarily precise resolution of temperature. In this Chapter we described a novel all-optical method for thermometry based on NV- centres in diamonds. Specifically, we explore the advantages of using a transverse bias magnetic field for temperature measurements. In this regime, a narrower linewidth and an enhanced ODMR appears due to the degeneracy of hyperfine transitions, this allow achieving a temperature noise floor of 5mK/Hz$^{1/2}$. The method described here provides benefits in terms of its simple experimental setup and also better magnetic field noise protection.

4.2.2 Theory for perpendicular field

In general case the Hamiltonian of the ground state of the NV system can be written as (see Chapter 1.2 for more details):

$$\hat{H} = hD_{gs}(S_z^2 - \frac{1}{3}[S(S+1)]) + hF(S_x^2 - S_y^2) + g\mu_B \mathbf{B}\cdot\mathbf{S} + S\hat{A}_N\hat{I}_N + \sum_j S\hat{A}_j I_j \qquad (4.10)$$

For the bulk diamond crystal, as in our case, we can neglect the contribution of the strain fields F and expand the Hamiltonian described by Eq.4.10 in basis of $B_\perp$, $B_\parallel$:

$$\hat{H} = \overbrace{hD_{gs}S_z^2 + g\mu_B B_\parallel S_z}^{H_\parallel} + \overbrace{g\mu_B(B_x S_z + B_y S_y)}^{H_\perp} + \sum_j S\hat{A}_j I_j \ , \qquad (4.11)$$

where $B_\perp = \sqrt{B_x^2 + B_y^2}$.

First, let's focus on weak magnetic field amplitudes and $H_\perp \ll H_\parallel$. The ODMR frequencies are given by well-known equation

$$\nu_{\pm} = D_{gs} \pm \frac{g\mu_B}{h} B_{\parallel} \tag{4.12}$$

The formula 4.12 is relevant for field amplitudes transverse component of the magnetic field $B_{\perp} \ll hD / g\mu_B \approx 100mT$. An accurate calculation, performed in [37], sets a boundary value smaller than 5mT (Fig.4.2.1). Thereby, for a small non-axial magnetic field B⊥, the axial magnetic field is given by $B_{\parallel} = \frac{h\Delta\nu}{g\mu_B}$, where $\Delta\nu$ is the observed frequency difference between the $|m_s = 0\rangle \rightarrow |m_s = +1\rangle$ and $|m_s = 0\rangle \rightarrow |m_s = -1\rangle$ transitions. Since the hyperfine interaction creates a threefold of these transitions one has to consider the frequency difference between the lines that observe the same frequency shift due to the hyperfine interaction (e.g. $|m_s = +1\rangle|m_i = +1\rangle$ and $|m_s = -1\rangle|m_i = -1\rangle$. For zero $B_{\parallel}$ these transitions should overlap perfectly. The minimal detectable magnetic field is here determined by the line width of the observed transition.

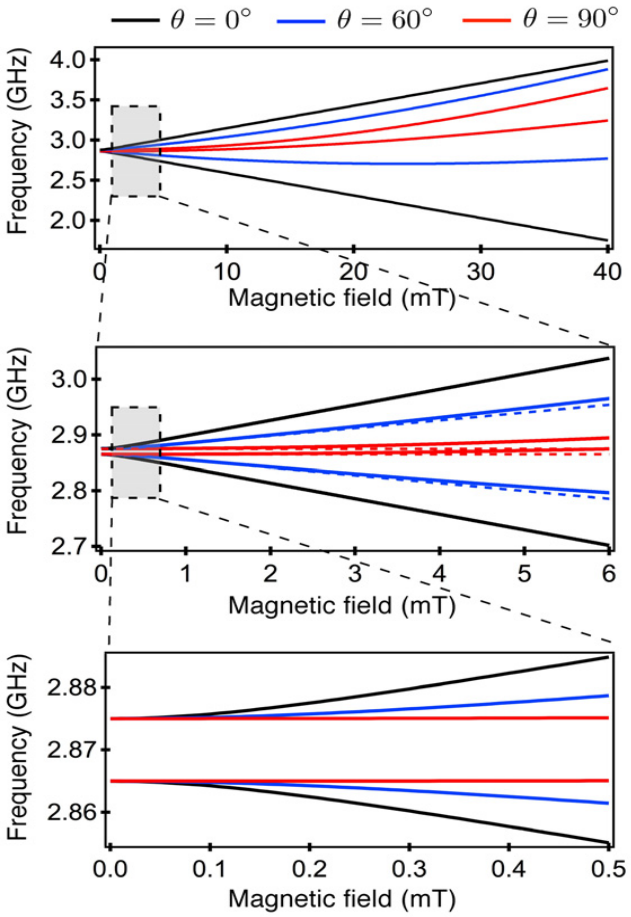

Fig.4.2.1 ODMR frequencies $\nu_{\pm}$ as a function of the magnetic field amplitude |B| at different angles θ with reference to NV axis. The solid lines are obtained by diagonalizing the full Hamiltonian described

by Eq. 4.10, while using D_{gs} = 2.87 GHz and E = 5 MHz. (*c*),(*d*) Weak magnetic field regime. In (*c*), the dotted lines correspond to the approximation given by equation (4.12). (Data from article [37])

For stronger magnetic field amplitudes, when the condition $H_{\perp} \ll H_{\parallel}$ is not fulfilled, the ODMR frequencies $\nu_{\pm}$ strongly depend on the orientation of the magnetic field with respect to the NV defect axes (Fig. 4.2.1). For example, in an ensemble of NV centres, defects with NV axis orthogonal to magnetic field will take strong modifications of spin dynamics, more specifically in hyperfine splitting, while for the NV defects oriented non orthogonal to the magnetic field the common dynamic remains as described above. The effect of a magnetic field aligned orthogonal to NV axis will be considered below.

4.2.2.1 Calculation of perturbed eigenvalues and eigenstates.

For the unperturbed Hamiltonian of a single NV centre, in the absence of external fields, $\hat{H}_0 = D_{gs} S_z^2$ the eigenvectors and eigenvalues can be writing as:

$$\begin{aligned} |0\rangle &= |S_z = 0\rangle, 0 \\ |+\rangle &= \frac{1}{\sqrt{2}}\left(|S_z = +1\rangle + |S_z = -1\rangle\right), D \\ |-\rangle &= \frac{1}{\sqrt{2}}\left(|S_z = +1\rangle - |S_z = -1\rangle\right), D \end{aligned} \tag{4.13}$$

If an orthogonal magnetic field, for example along the x axis, $B_{\perp}$ is applied, the Hamiltonian of the NV centre is:

$$\hat{H} = \hat{H}_0 + \hat{H}_{pert} = D_{gs} S_z^2 + \frac{g\mu_B}{h} B_x S_x \tag{4.14}$$

The Hamiltonian (4.14) can be written in terms of the basis (4.13) in the following matrix form:

$$H_{pert} = \begin{pmatrix} 0 & 0 & \frac{g\mu_B}{h} \\ 0 & D_{gs} & 0 \\ \frac{g\mu_B}{h} & 0 & D_{gs} \end{pmatrix} \tag{4.15}$$

If $\frac{g\mu_B B_\perp}{h} \ll D_{gs}$ we can consider $\hat{H}_{pert}$ as a perturbation λV with: $\lambda = B_\perp, V = \frac{g\mu_B}{h} S_x$.

Then, the eigenvalues and eigenstates, corrected to second order, are:

$$\begin{aligned} E_1 &= 0 + \lambda E_1^{(1)} + \lambda^2 E_1^{(2)} \\ E_2 &= D_{gs} + \lambda E_1^{(1)} + \lambda^2 E_1^{(2)} \\ E_3 &= D_{gs} + \lambda E_1^{(1)} + \lambda^2 E_1^{(2)} \end{aligned} \tag{4.16}$$

$$\begin{aligned} |1\rangle &= c_{11}|0\rangle + (\lambda c_{12}^{(1)} + \lambda^2 c_{12}^{(2)})|+\rangle + (\lambda c_{13}^{(1)} + \lambda^2 c_{13}^{(2)})|-\rangle \\ |2\rangle &= (\lambda c_{21}^{(1)} + \lambda^2 c_{21}^{(2)})|0\rangle + c_{22}|-\rangle + c_{23}|+\rangle \\ |3\rangle &= (\lambda c_{31}^{(1)} + \lambda^2 c_{31}^{(2)})|0\rangle + c_{32}|-\rangle + c_{33}|+\rangle \end{aligned} \quad , \tag{4.17}$$

where $c_{ij}, i, j = 1,2,3$ are coefficients.

The first-order contributions to eigenvalues is null because the perturbation does not have diagonal terms, see Eq.4.15. The second order contribution to eigenvalues s:

$$\begin{aligned} E_1^{(2)} &= -\frac{g^2\mu_B^2}{hD_{gs}} \\ E_2^{(2)} &= 0 \\ E_3^{(2)} &= \frac{g^2\mu_B^2}{hD_{gs}} \end{aligned} \quad , \tag{4.18}$$

so from Eq. (4.16) we get eigenvalues:

$$\begin{aligned} E_1 &= -\frac{g^2\mu_B^2 B_\perp^2}{hD_{gs}} \\ E_2 &= D \\ E_3 &= D + \frac{g^2\mu_B^2 B_\perp^2}{hD_{gs}} \end{aligned} \quad . \tag{4.19}$$

The corresponding eigenstates are:

$$
\begin{aligned}
|1\rangle &= \frac{1}{\sqrt{1+\frac{g^2\mu_B^2 B_\perp^2}{h^2 D_{gs}^2}}}\left(|0\rangle - \frac{g\mu_B B_\perp}{h\ D_{gs}}|+\rangle\right) \\
|2\rangle &= |-\rangle \\
|3\rangle &= \frac{1}{\sqrt{1+\frac{g^2\mu_B^2 B_\perp^2}{h^2 D_{gs}^2}}}\left(|0\rangle + \frac{g\mu_B B_\perp}{h\ D_{gs}}|+\rangle\right)
\end{aligned}
\tag{4.21}
$$

From Eq.4.16 the resonance frequencies $\nu_\pm$, corresponding to $|m_s=0\rangle \rightarrow |m_s=+1\rangle$ and $|m_s=0\rangle \rightarrow |m_s=-1\rangle$ transitions at orthogonal magnetic field $B_\perp$, and the distance $\Delta\nu = \nu_+ - \nu_-$ can be calculated as:

$$
\begin{aligned}
\nu_+ &= D_{gs} + \frac{2g^2\mu_B^2 B_\perp^2}{h^2 D_{gs}} \\
\nu_- &= D_{gs} + \frac{g^2\mu_B^2 B_\perp^2}{h^2 D_{gs}} \\
\Delta\nu &= \frac{g^2\mu_B^2 B_\perp^2}{h^2 D_{gs}}
\end{aligned}
\tag{4.22}
$$

The Eqs.(4.22) explain why the frequencies $\nu_\pm$ shift in one direction, and the distance between them grows (red solid line in Fig.4.2.1), even if the magnetic field along the NV axis is equal a zero.

4.2.2.2 Suppression of hyperfine splitting

The nuclear contribution can be expressed as:

$$
\hat{H}_{nucl} = \hat{H}_{quad} + \hat{H}_{hyper} = QI_z^2 + S_z A_\parallel I_z + S_x A_\perp I_x + S_y A_\perp I_y \tag{4.23}
$$

We will consider the case of $B_\perp$ along *x* and calculate the contribution of the nuclear terms to perturbed eigenstates (Eq. 4.21) as the expectation value of the Hamiltonian (4.23) on these

states. It can be shown that quadrupolar contribution acts only on nuclear degree of freedom creating a gap between states with I_z=0 and I_z=±1.

For the expectation values of the hyperfine terms are:

$$\begin{aligned}
&\langle 1|\langle I_z=\pm 1|H_{hyper}|I_z=\pm 1\rangle|1\rangle=0\\
&\langle 1|\langle I_z=0|H_{hyper}|I_z=0\rangle|1\rangle=0\\
&\langle 2|\langle I_z=\pm 1|H_{hyper}|I_z=\pm 1\rangle|2\rangle=0\\
&\langle 2|\langle I_z=0|H_{hyper}|I_z=0\rangle|2\rangle=0\\
&\langle 3|\langle I_z=\pm 1|H_{hyper}|I_z=\pm 1\rangle|3\rangle=0\\
&\langle 3|\langle I_z=0|H_{hyper}|I_z=0\rangle|3\rangle=0
\end{aligned} \qquad (4.24)$$

From (Eq.4.24) follows that the transitions $|1\rangle\rightarrow|2\rangle$ and $|1\rangle\rightarrow|3\rangle$ are not split by the hyperfine interaction. The main point is that the quadrupole interaction aligns nuclear spins along NV axis, but perturbed electronic spins are different from zero only in a direction orthogonal to NV axis. The *illustrative* diagram in Fig.4.2.2 shows how energetic levels shift for the parallel and orthogonal orientation of the bias magnetic field.

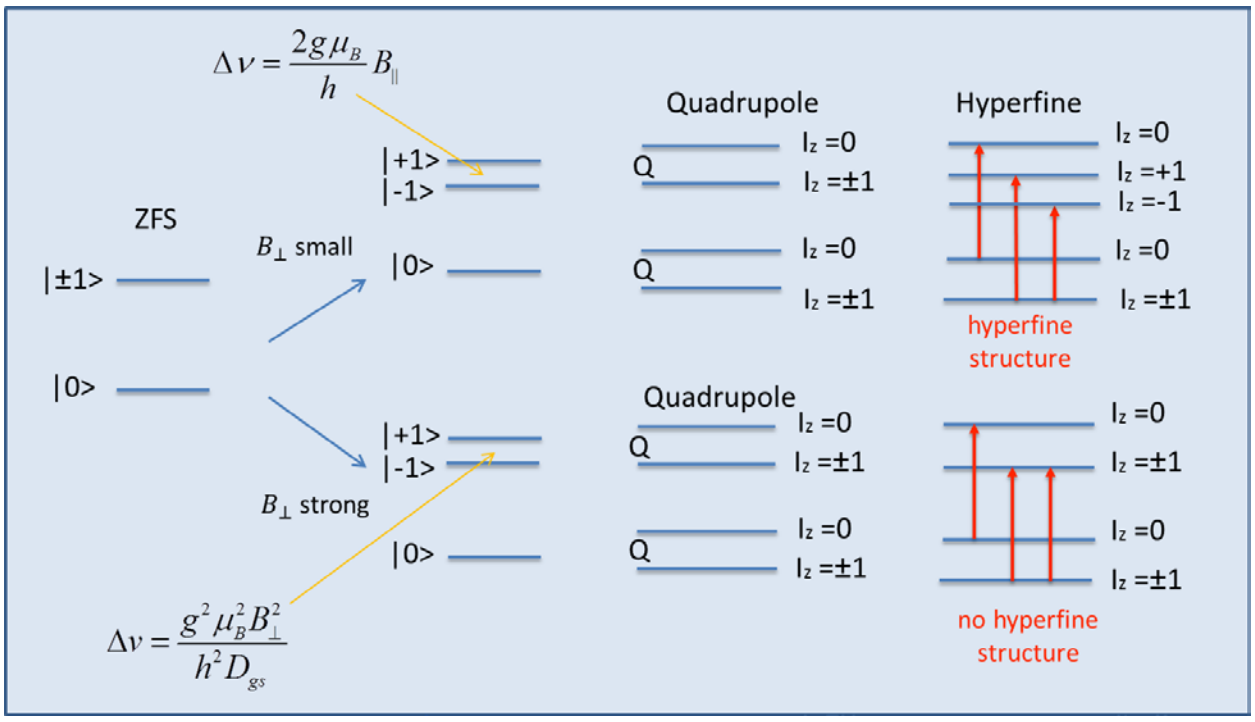

Fig 4.2.2. Energy levels of the negatively charged NV center, including the 14N hyperfine in the presence of a magnetic field in parallel (top of the diagram) and orthogonal(floor of the diagram) directions.

4.1.3 Experimental setup

The setup consisted of an inverted microscope Olimpus IX73, adopted to confocal measurements with single-photon sensitivity (see Chapter 1.3). A high purity bulk diamond (Element Six, size 3mm×3mmx0.3mm), cut to the <100> crystal axis, was used to demonstrate temperature sensing. The diamond was overgrown in a chemical vapor deposition (CVD) process with an 10nm thin, isotopically purified ([^{12}C] > 99.99%) layer, doped with ^{14}N and concentration of NV $n_{NV}=3x10^{19}$ cm^{-3}. The diamond sample was mounted on the microwave planar ring antenna specifically designed for ODMR measurements at frequency around 2.87 GHz with the bandwidth of 400 MHz[171]. The sample with antenna was situated in the Stage Top Chamber "H301-K-FRAME" fitted in the piezo stage of the microscope and connected to "Okolab Temperature Controller". The chamber allows one to set the temperature in the range (293 – 318K) with accuracy ± 0.1 K. More precise measurement of the temperature with accuracy 10^{-4} K was realized by a micro-sensor based on a thermocouple fixed on the top of the diamond *through* thermo-conductive glue (Fig. 4.2.3).

Light from a CW 532 nm laser with high power stability (Coherent Prometheus 100NE , 60-80mW) was focused on the bottom side of the diamond sample through an air objective Olympus UPLANFL with NA=0.67. The photoluminescence (PL) was collected, spectrally filtered with long-pass filter 650nm, and detected with two different acquisition systems. Four percent of the total PL was sent on single photon avalanche detectors (SPAD). The signal from SPAD was used for the ODMR spectrum acquisition. Major part of the emitted PL was collected by a NA=0.25 objective (Olympus 10x) and imaged onto a bias photodetector (Thorlabs DET 10A2). An external magnetic field was applied to the diamond sample using a neodymium magnet fixed on the translation stage with the possibility to micrometric moving it in x, y, z directions and manual rotation. The minimum magnet-sample distance achievable with our apparatus was 4 cm and limited by the thickness of the chamber. At this distance, the magnetic field was approximately 6 mT. For the magnetic field modulation we also used a coil, set symmetrically above the diamond sample (Fig.4.2.3).

The electronic part of the setup included a commercial MW source (Keysight N5172B) outputted a single near-resonant frequency, modulated by internal square-wave oscillator with frequency deviation ω_{dev} = 0.6MHz (half of the FWHW resonance dip) and at frequency f_{mod} = 1009 Hz. The MW then mixed via a double balanced mixer (RELCOM M1G) with a ~10 MHz sinusoid waveform (Stanford Research Systems DS345) to create two simultaneous driving modulated frequencies near the resonance transitions. The output MWs signals were amplified (Mini-Circuits ZHL-16W-43+) and then sent to the Bi Directional coupler (WERLATONE C8000-

102). The coupled output was sent to a spectrum analyzer (Agilent E4405B), while the transmitted output to the microwave antenna.

The photodiode Thorlabs DET 10A2 (PD) was powered by a 12V battery and connected to the current input of a lock-in amplifier (Stanford SR860) which provides phase-sensitive demodulation of the fluorescent signal. Siglent SDG1010 Arbitrary Function Generator was used as a reference signal for the lock-in amplifier and for the synchronisation with acquisition scheme National Instruments USB-6343. All data have been recorded with a 1 kHz sine-wave modulation and lock-in time constants of 100 *m*s.

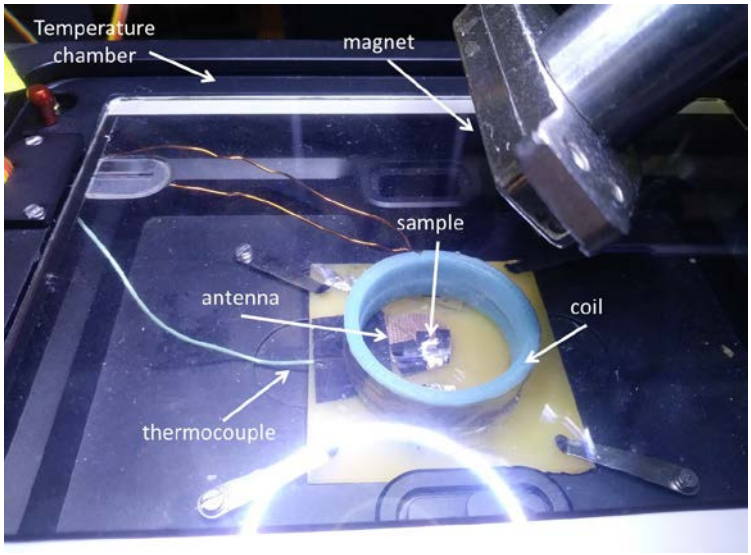

Fig.4.2.3 Thermostabilized part of the setup with a microwave antenna and a sample.

4.1.4 Experimental results and discussion

The special regime of transverse bias magnetic field can be advantageous for the temperature sensing on two grounds. First, due to the degenerated hyperfine structure the resonance transitions of the ODMR spectrum have higher contrast and narrow linewidth respect to common cw ODMR spectra. Second, the NV spin is non-sensitive to the magnetic field component B_z, because according the Eq.4.2 the contribution of magnetic field enters only in the second order to the Hamiltonian. This allows protecting the measurements from the magnetic field noise, which represent an significant advantage of our new measurement scheme respect to previous ones[48], [49], [52], [75].

We started from aligning the external bias magnetic field, that was achieved by scanning the MW frequency in wide range (2.7-2.99) GHz and varying simultaneously the orientation of the

magnet approximately roughly perpendicular to the NV axis. Where the two symmetrical ODMR branches are closest to central frequency D_{gs}, the magnetic field is perpendicular to the NV axis and higher contrast and a narrower linewidth is observed. (see Fig.4.2, red square).

The degeneration of the hyperfine structure can be clearly observed only if the perpendicular component the magnetic field $B_{\perp}$ is strong enough to separate a couple of symmetric dips on a distance larger the hyperfine splitting. From Eq. 4.22 we get:

$$B_{\perp} = \frac{h}{g\mu_B}\sqrt{\Delta\nu_{hyper}\ D_{gs}}\ , \tag{4.25}$$

there $\Delta\nu_{hyper} = 2.15MHz$ is the transition due to the hyperfine interaction with the ^{14}N nuclear spin and $D_{gs} = 2.87GHz$ is a zero field splitting. Thereby, the boundary condition is $B_{\perp} > 2.80mT$. In Fig.4.2.4 the ODMR spectra for magnetic fields strengths 6.2mT and 2.1mT are presented. For smaller magnetic field strengths the effect of degenerated hyperfine structure and higher contrast of ODMR transition cannot be observed. All photoluminescence spectra on this stage were measured by a SPAD.

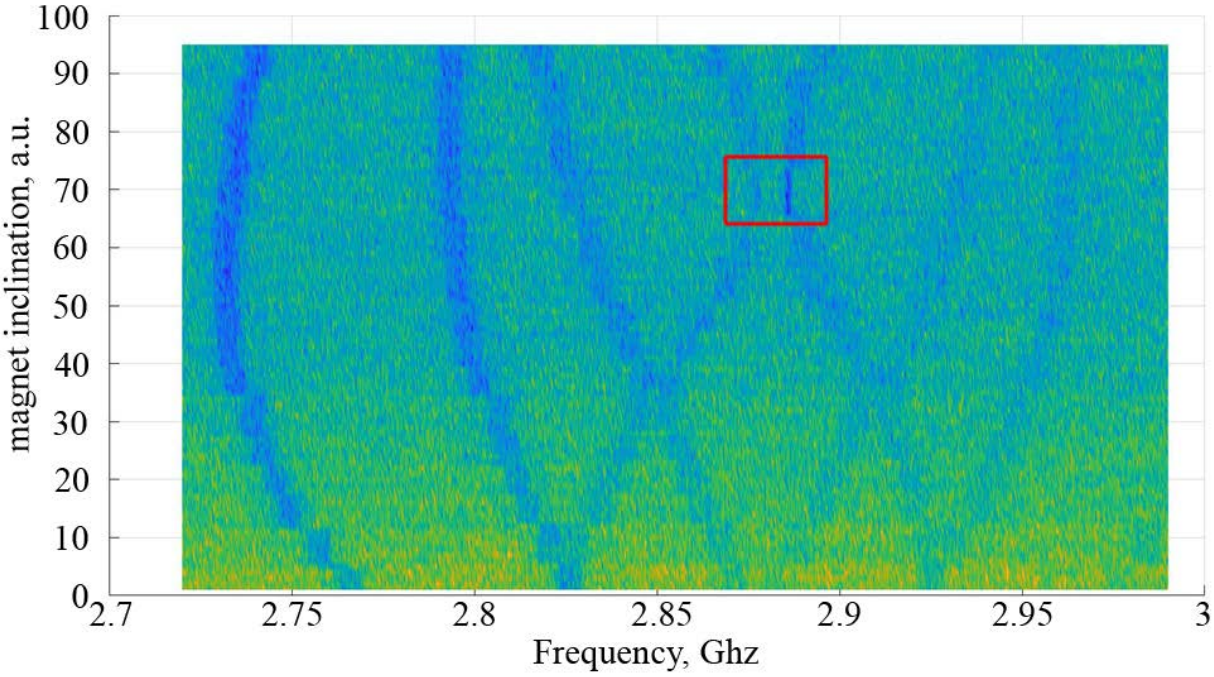

Fig.4.2.4 ODMR spectra map for various magnetic field angles. Where the two ODMR branches are closest the magnetic field is perpendicular to the NV axis (red square)

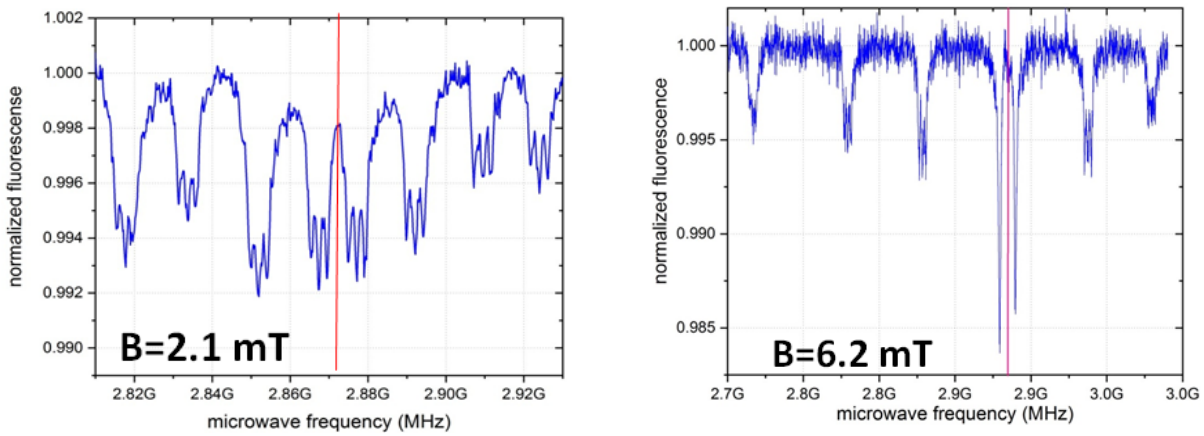

Fig.4.2.5 An example of ODMR spectra plotted for different magnetic fields magnitude, orthogonal to the one of the NV axis. (b) The magnitude of magnetic field is quite enough to see the effect of degenerated hyperfine structure. The different contrast between the symmetrical peaks is due to random polarization of the applied microwave field. Red line shows the frequency of the symmetry D(T).

The second step was the calibration of the NV based diamond temperature probe. To determine the parameter D(T) as a function of temperature, the frequency f_c was modulated at f_{mod} = 1009Hz and deviation f_{dev} = 0.25MHz and was scanned around one of the symmetric degenerated ODMR transitions.

For the each scan at fixed temperature T of the chamber, the lock-in spectrum was plotted and the central frequency $f_i(T)$ of the dip was found. The example of the lock-in spectra at different temperatures and corresponding frequency points are presented in Fig.4.2.6. We repeated the measurement over a wide range of temperatures from 27^o to 33^o , between two consecutive measurements a pause of 15min was used for thermostabilization. Additionally, for temperature control, we used thermocouple readings. The obtained data were approximated with a linear fit (the frequency shift over temperature change, dD/dT is almost linear in this temperature range[48], [49], [172]) the coupling coefficient $k_T=dD/dT$ = (−74.2±0.6) kHz/K of the diamond sensor was evaluated with a good agreement with previous works[48], [74].

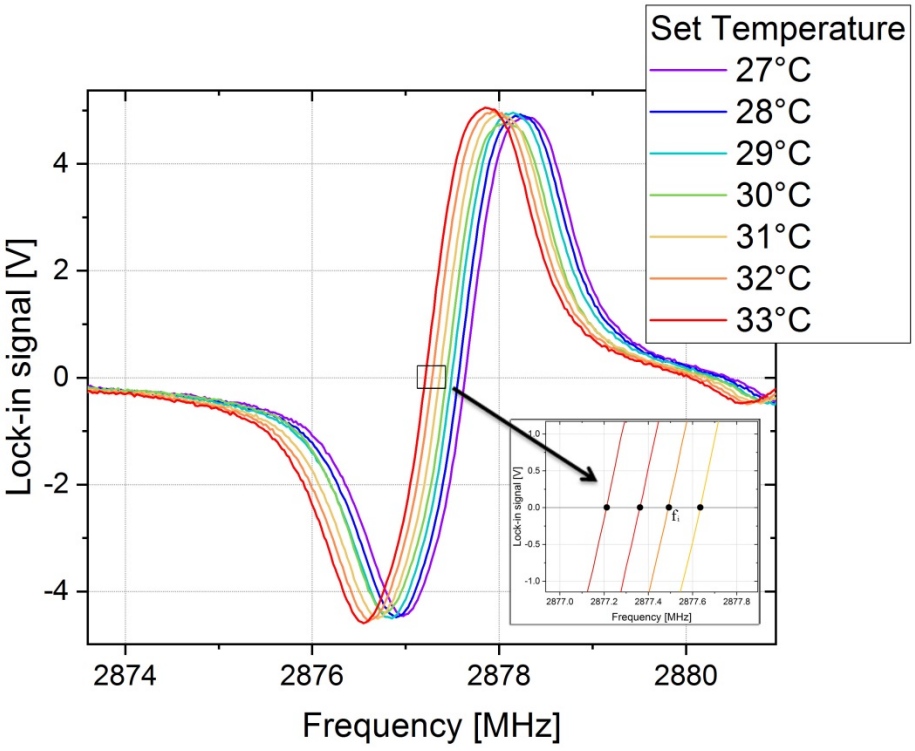

Fig.4.2.6. Experimental lock-in spectra at different temperatures of the diamond sensor. Set of frequencies at zero lock-in signal (insert graph) were used for the calibration of diamond sensor.

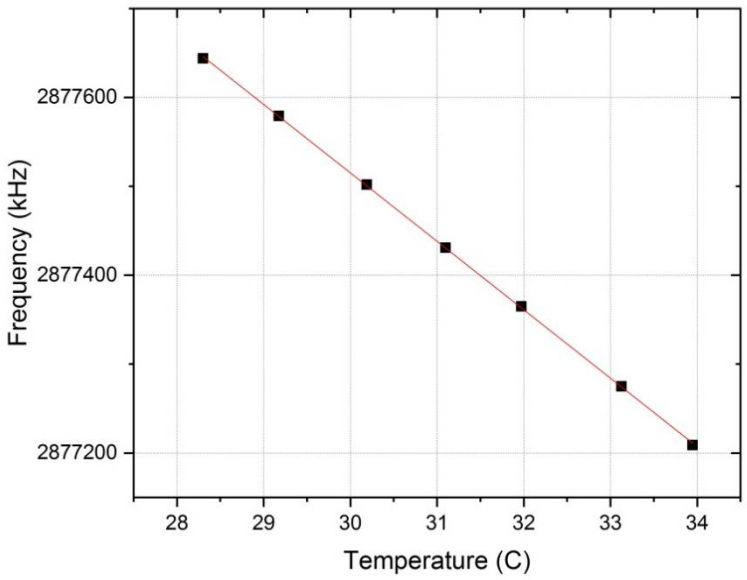

Fig.4.2.5 Calibration graph of the diamond sensor: shift of the resonance frequency as a function of the temperature. Uncertainties of experimental data are too small for being visible with the present scale.

In order to demonstrate the advantages of transverse bias magnetic field () thermometry, we compared two types of measurements. In the first case we used regime of orthogonal magnetic field and enhanced ODMR transition with degenerated hyperfine structure for the measurement of a temperature cycle, defined by thermostabilization chamber. As an independent temperature

control the data from thermocouple, fixed directly on the diamond, were used. The amplitude of the temperature cycle was 1K and the period 15 min. Quite a long period of one step in temperature was defined by passive control cooling of the chamber. The data from sensor were received each 1s. Figure 4.2.7(a) report the measurements in this case.

In the second case we used a the method suggested in articles[49], [52], [65], [173], in the following hyperfine driving(HfD), based on the frequency shift of the resonance ODMR transition at nondegenerate regime of hyperfine structure, where a special alignment is not required. For these purposes, one of the peaks with hyperfine structure in Fig. 4.2.5 was used.
The simultaneous driving of all three transitions was suggested in [174]. This type of resonance tuning usually is used for a better sensitivity, because the presence of the hyperfine transitions, and their considerable overlap, allows one to increase the contrast due to the simultaneous exciting of all of them[174]. The regime of simultaneous hyperfine driving of all three transitions we will call as (SHfD).
We repeated the measurements of temperature cycle only for the SHfD regime, because a better sensitivity is expected for it. The results are plotted in Fig. 4.2.7(b). Comparingthe two different measurement methods we can note few points. First the perfect correspondence between the independent measurements of thermocouple and diamond sensor can be observed for the TBMF thermometry. Second the uncertainty of the SHfD method is about 3 times larger than for the TBMF regime. Third after about 25 min the TBMF regime loses calibration which is related with slowly fluctuating magnetic noise of the environment. The subsequent recalibration allows resolving the problem but just for a short period of time. The main reason for the instability of the measurement is the absence of decoupling with the magnetic field. In the TBMF regime the frequency shift of the degenerated resonance dip due to the magnetic field fluctuation in the regime of strong orthogonal field alignment is ten times smaller, as expected from Eqs.(4.12), (4.22).
Thus, our proposed method for the temperature sensing is more convenient in comparison with traditional methods, because allows one to protect the measurements from the magnetic field noise without complex protocols and technique.
In order to characterize the sensitivity of our method of temperature sensing, few traces of the lock-in output were recorded and a root-mean square amplitude spectral density was calculated using the Hanning window function. Noise contributions coming from laser, microwave excitation and electronic noise of the lock-in amplifier were estimated.

The microwaves were tuned to the center of the resonance, where the lock-in signal crossed zero and gave the highest temperature response. The square - wave modulation at 1009 Hz and modulation depth 0.25MHz were used for all recordings.

The acquisition time of an each time trace of the lock-in output was 10 min. The measurement bandwidth was limited by the lock-in time constant τ=10ms. The data of noise spectral densities are displayed in Fig. 4.2.8. Here the spectrum coloured by black corresponds to electronic noise of the lock-in amplifier and dark counts of the detector. No microwave and no laser excitation were applied. The blue line shows the data recorded without microwave excitation, while red line – to the TBMF regime. The electronic noise floor is about 2mK/Hz$^{1/2}$, the noise floor is flat and around 5mK/Hz$^{1/2}$. Microwave radiation doesn't add noise to the measurements.

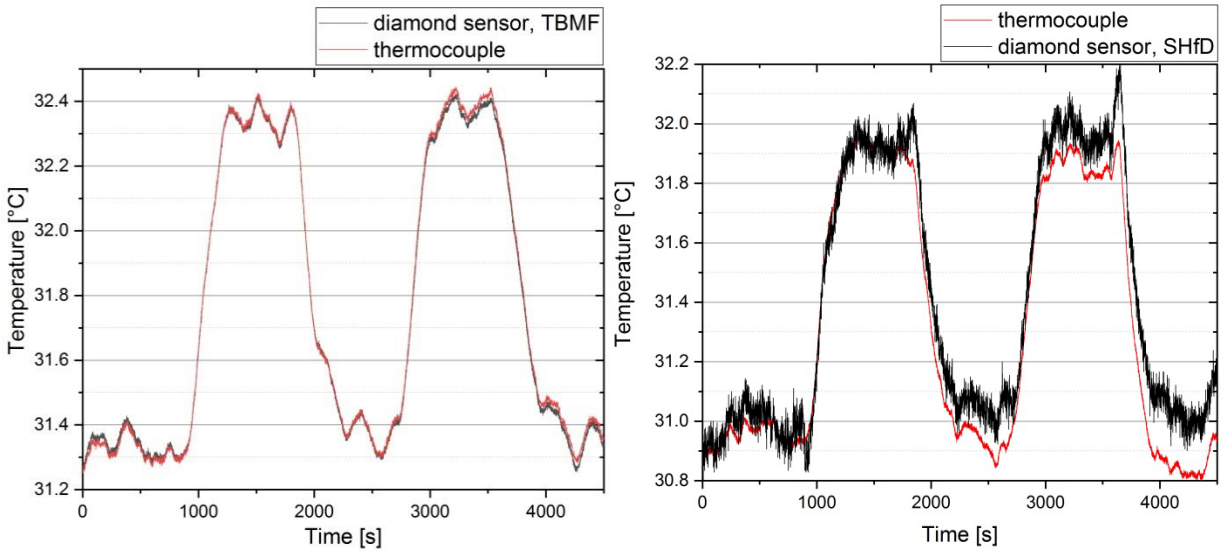

Fig.4.2.7 Recorded signals reflect cycle changes in the temperature. Red line is a thermocouple reading, black line - calibrated signal from the lock-in output. (a) Measurement of the temperature is based on registration of the frequency shift in TBMF mode. (b) Measurement of the temperature is based on registration of the frequency shift in SHfD mode.

For comparison, similar data of noise spectral densities were collected for the single frequency hyperfine driving, as well as the simultaneous frequency hyperfine driving. The corresponding data are plotted in Fig. 4.2.9. The level of the noise floor in HfD regime is 30mK/Hz$^{1/2}$ (green line). The expectation that the sensitivity of the simultaneous driving, SHfD, will be higher is confirmed by the data. One can evince from Fig. 4.2.9 (blue line) that, in contrast to single-frequency excitation, for multiple frequency modulation the level of the noise floor reduces due to the enhanced contrast of the signal on the lock-in output and a temperature sensitivity of

16mK/Hz$^{1/2}$ is achieved. However, our novel demonstrated method of sensing achieves three times better temperature sensitivity.

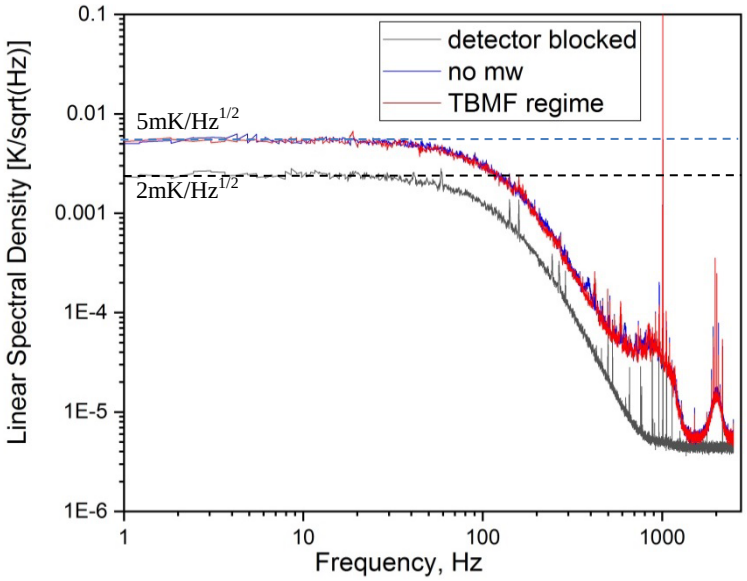

Fig. 4.2.8 Recorded noise spectral densities in temperature units, respectively, with MW tuned to TBMF mode(red line), with MW off (blue line) and electronic noise of the devices (black line). The signal roll-off around 100 Hz is due to the lock-in filtering with a 10ms time constant.

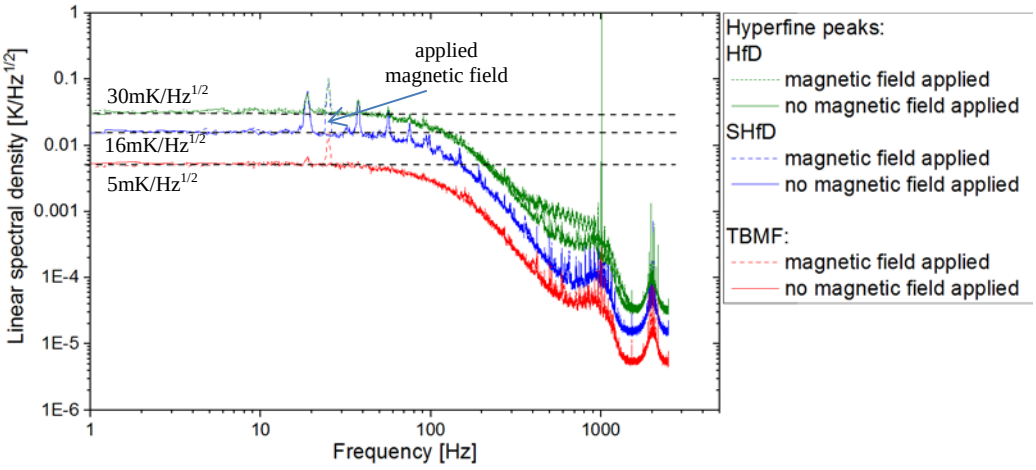

Fig.4.2.9 Recorded noise spectral densities in the units of the temperature, for three different modes of temperature sensing. Green line - with MW tuned to HfD mode, blue line - MWs tuned to SHfD mode, red line - with MW tuned to TBMF mode. Dashed lines correspond to the data, when an additional sinusoidal modulation of the magnetic field at 25 Hz is applied. The signal roll-off around 100 Hz is due to the lock-in filtering with a 10ms time constant.

As has been noted above, the resonance transition in ODMR spectrum, corresponding to the orthogonal orientation of the bias magnetic field, is protected from the magnetic field noise. To demonstrate this a very significant advantage an additional sine-wave signal, generated by coil

was applied at frequency 25 Hz for all three modes of the measurement : TBMF, HfD, SHfD. The corresponding data are plotted by dashed line in Fig. 4.2.9. The amplitude of the pick in noise protected mode TBMF is smaller than for standard modes HfD, SHfD. Also recordings in HfD, SHfD modes show a set of peaks at frequencies around (20-100) Hz, which we attribute to electronic and surround noises. All this leads to a reduction of sensitivity and to inability to separate the magnetic and temperature contributions, which induce comparable resonance shifts.

In conclusion, we have demonstrated a novel all-opticall technique for precision sensing of the temperature immunity to fluctuations in the magnetic field. The sensitivity of 5 mK/ $Hz^{1/2}$ is demonstrated. This result is comparable with state-of-the-art NV based thermometers, based on advanced pulsed protocols and complex acquisition schemes. The presented technique only requires an alignment of the bias magnetic field along the orthogonal direction of the NV axis, addition application of advanced protocols will lead to a new level of sensitivity of NV based quantum thermometers. While a simple extension of the method utilizing the degenerated resonances as a close-loop control for the other, non-degenerate ones could allow for simultaneous, independent monitoring of both the magnetic field and the temperature.

4.3 Magnetic field sensing

This chapter describes a technique for NV-diamond vector magnetometry and its experimental implementation.

4.3.1 Introduction

As described in Chapter 1, the NV center's electronic ground state has spin S=1 with the lower-energy m_s =0 level separated from the m_s=±1 levels by a zero-field splitting D =2.87 GHz. NV center has symmetry axes aligned along one of four crystallographic orientations set by the diamond lattice's tetrahedral symmetry. A bias magnetic field B_0, splits spin energy levels m_s=±1 by $\Delta\nu = 2\frac{g\mu_B}{h}B_z$ due to the Zeeman effect. By measuring the optically detected magnetic resonance (ODMR) features of an ensemble of NV centers, with NV - symmetry axes distributed along all four crystallographic orientations, the three Cartesian components of a vector magnetic field signal can be sensed using a monolithic diamond crystal.

To date, ensemble NV- vector magnetometers measure the three Cartesian magnetic field components either by sweeping a microwave (MW) frequency across the full ODMR spectrum[175], [176] or by interrogating multiple ODMR resonances individually [10], [84], [177]–[179] or in parallel[180]–[182], with near-resonant MWs. Regardless of implementation, these existing methods reconstruct the three Cartesian magnetic field components from a series of field projection measurements.

In our implementation, the projective field measurements are performed sequentially, so such magnetometer has so far only demonstrated sensing of static or slowly varying fields. To overcome these drawbacks, a simultaneous measurement of all Cartesian components of a dynamic magnetic field components using parallel addressing and readout from all four NV-orientations in a single-crystal diamond can be done.

4.3.1 Technique implementation

Figure 4.3.1(a) depicts the experimental setup, including laser excitation, MW generation, and magnetic field detection. The diamond crystal is a (3x3x0.3) mm, cut to the <100> crystal axis, was grown by Element Six Ltd. The concentration of NV $n_{NV}=3x10^{19}$ cm^{-3}. The diamond sample was mounted on a microwave planar ring antenna.

The excitation and acquisition parts of the setup is described in Chapters 1.3.2 and 4.1.3. The external magnetic field was applied by magnet which generates a ~10 mT field. The magnet was fixed on the stage in a way that all the eight ODMR frequencies were observed in ODMR spectrum. As a small magnetic field variation we used a copper wire with a diameter 30μm, extended on the top of the diamond sample (Fig.4.3.1(b)).

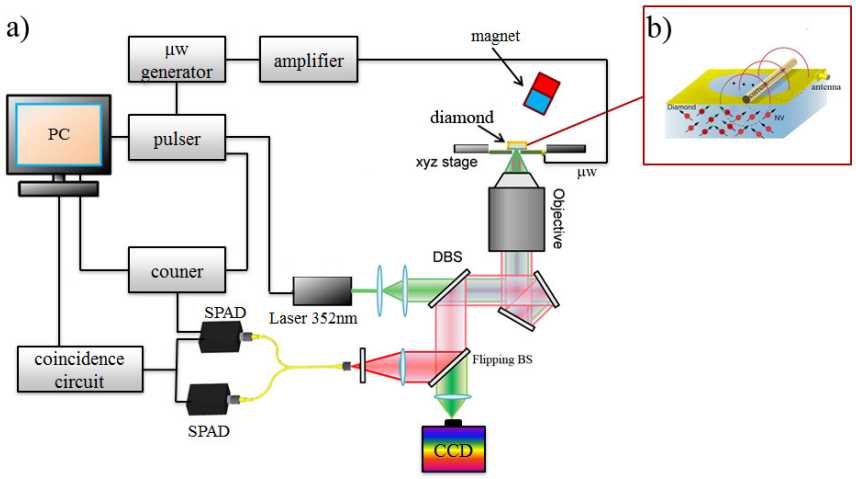

Fig. 4.3.1 (a) Experimental setup for the vector magnetometry (detailed description in Chapter 4.1.3). Insert (b) shows the position of the wire on the diamond sample and three black points, where the magnetic field was measured.

Magnetometer calibration starts from determination of the bias magnetic field B_0, the zero-field splitting D, and strain field F. This calibration procedure is separate from high-sensitivity measurements of small vector magnetic fields ΔB.

The *unambiguous definition* of the magnitude and spatial orientation of the bias magnetic field requires frequency separation of the all eight resonance dips related to all four crystallographic axes on the spectrum ODMR. For this purpose, the magnet was fixed at a distance about 4 cm from the sample and orientated in mode that all eight dips were well separated. Then the NV-diamond magnetometer measured the bias field parameters by sweeping a single MW frequecy from 2.78 to 2.96 GHz, and monitoring the PL from the diamond; this yields an ODMR spectrum as shown in Figure 4.3.2 (blue line). Using least-squares fit, we determined the line centers of the middle hyperfine levels of each of the eight m_s spin transitions. From the relation $B_0^i = \frac{\Delta\nu^i h}{g\mu_B}, i = 1,..4$, where $\Delta\nu^i$ are distances between the symmetrical dips, four projections B_0^i of the bias magnetic field can be defined.

To determine the magnetic field orientation we have considered the following vectors of four possible orientations of the NV axis in diamond lattice.

$$\vec{u}_1 = \sqrt{2/3}\left(0,1,\frac{1}{\sqrt{2}}\right);\vec{u}_2 = \sqrt{2/3}\left(0,-1,\frac{1}{\sqrt{2}}\right)$$
$$\vec{u}_3 = \sqrt{2/3}\left(1,0,-\frac{1}{\sqrt{2}}\right);\vec{u}_4 = \sqrt{2/3}\left(-1,0,-\frac{1}{\sqrt{2}}\right); \quad (4.3.1)$$

The experimental data B_0^i represent the projections of the bias magnetic field on the four above vectors (Eq.4.3.1). Therefore, we obtain a system of 4 equations with 3 unknowns, allows determining the direction of the magnetic field vector. The system has been resolved with the following conditions:

$$\begin{cases} \vec{u}_1\vec{B}_o = B_0^1 \\ \vec{u}_2\vec{B}_o = -B_0^2 \\ \vec{u}_3\vec{B}_o = -B_0^3 \\ \vec{u}_4\vec{B}_o = B_0^4 \end{cases} \quad (4.3.2)$$

In this way the components of the magnetic field were obtained and with the fourth equation in (Eq.4.3.2) the right choice of projection signs were verified. The reconstructed bias magnetic field had magnitude $B_0=(3.624\pm0.002)mT$ and orientation as shown in Fig.4.3.3(green arrow).

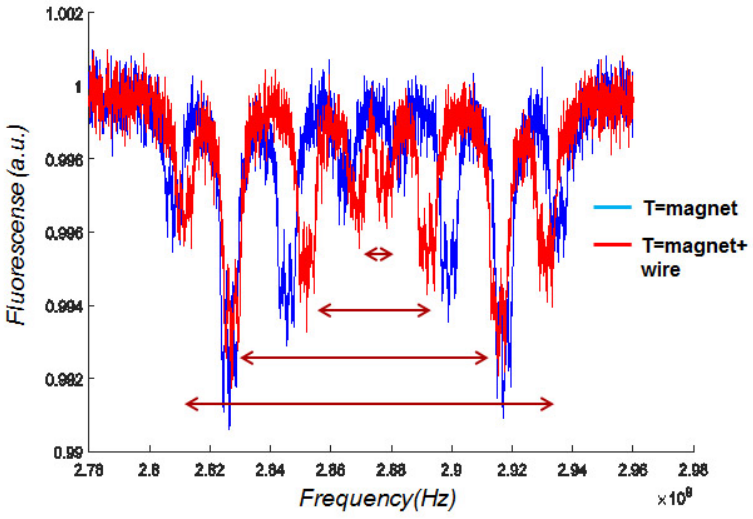

Fig.4.3.2 ODMR spectrum with a magnetic field oriented such that the projection onto each axis is different, resulting in eight separate resonances. Blue line correspond to ODMR spectrum at bias magnetic field, red – external magnetic field of the wide was added. Arrows show symmetrical couples of resonance dips.

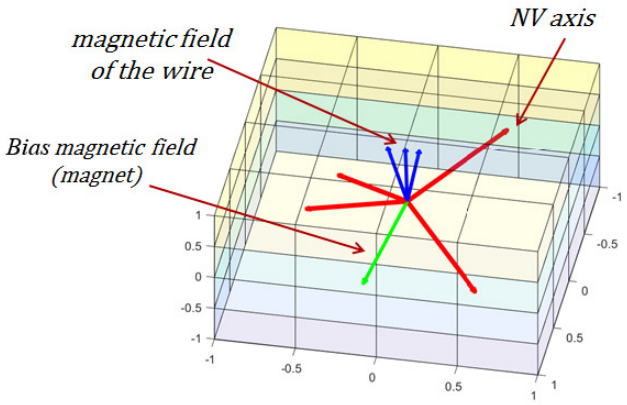

Fig 4.3.3 Diagram of the four NV orientations (red arrows), reconstructed orientations of the bias magnetic field (green arrow) and magnetic field of the fire (blue arrows) at different points of measurement.

After determination of the bias magnetic field B_o from the measured ODMR resonance dip centers, an additional constant magnetic field ΔB was applied by means of copper wire on the top of the diamond. Current passing through the wire creates a magnetic field, which can be estimated theoretically. We measured the magnetic field at three points at different distances of the wire (See Fig. 4.3.1(b)). For each point the bias B_0 and total magnetic field ($B_0 + \Delta B$) were estimated. An example of one measurement is plotted in Fig. 4.3.2. In the simple case, then an additional magnetic field quite strong and a shift of the resonance dips can be observed directly from the spectrum ODMR (as in Fig. 4.3.1), the protocol, described above, can be used for the reconstruction of the magnetic field.

The experimental results are plotted on the Fig.4.3.4. Here red line is a theoretically estimated magnetic field generated by the copper wire. Axis *x* corresponds a distance from the wire's center to point of measurement. The reconstructed orientations of the magnetic field ΔB for the three points are showed by blue arrows in Fig. 4.3.3. Statistical uncertainties in the field parameters are estimated to be ~ 5 μT.

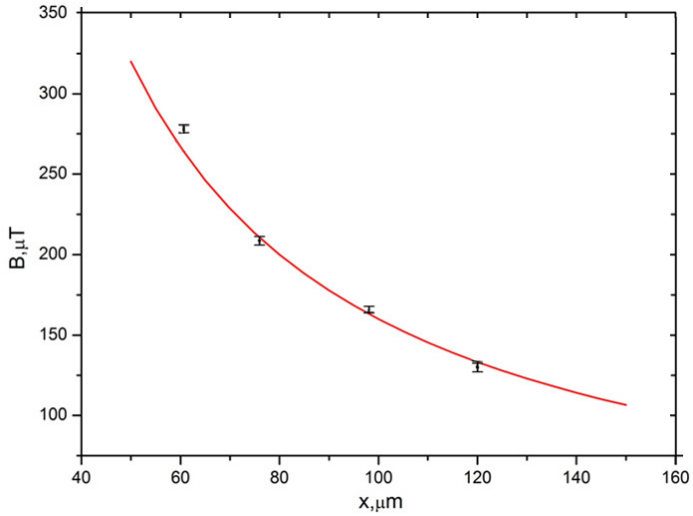

Fig.4.3.4 Theoretical curve of the magnetic field of a straight wire and experimental results.

The direct reconstruction of the external magnetic field from the ODMR spectra cannot be applied for a weak field, then a shift of the resonance frequency is much smaller the it's linewidth. To expand the effective sensitivity of the vector magnetometer, the lock-in technique can be used (see Chapter 2.2). In this case the modulated microwave frequency is tuned to the center of the resonance, where the lock-in signal crosses zero, which gives the highest magnetic response. Then even a weak shift of a resonance frequency due to magnetic field variation will be detected as a non-zero signal from the lock-in output (Fig.4.3.5 (a)). In the linear range of the lock-in spectrum, marked by red line, the shift in the frequency $\Delta\nu$ and corresponding to it component of the magnetic field (projection on the given axis) can be reconstructed. Repeat the protocol for all four resonance dips, corresponding to NV axes, the magnitude and orientation of the external magnetic field ΔB can be defined.

The magnetic field sensitivity of our magnetometer was estimated from the spectral density of the noise. A set of time traces of the lock-in output were recorded and a root-mean-square amplitude spectral density was calculated using the Hanning window function. The level of the noise floor is ~40 nT/Hz$^{1/2}$ up to the lock-in filter roll-off frequency of ~100Hz.

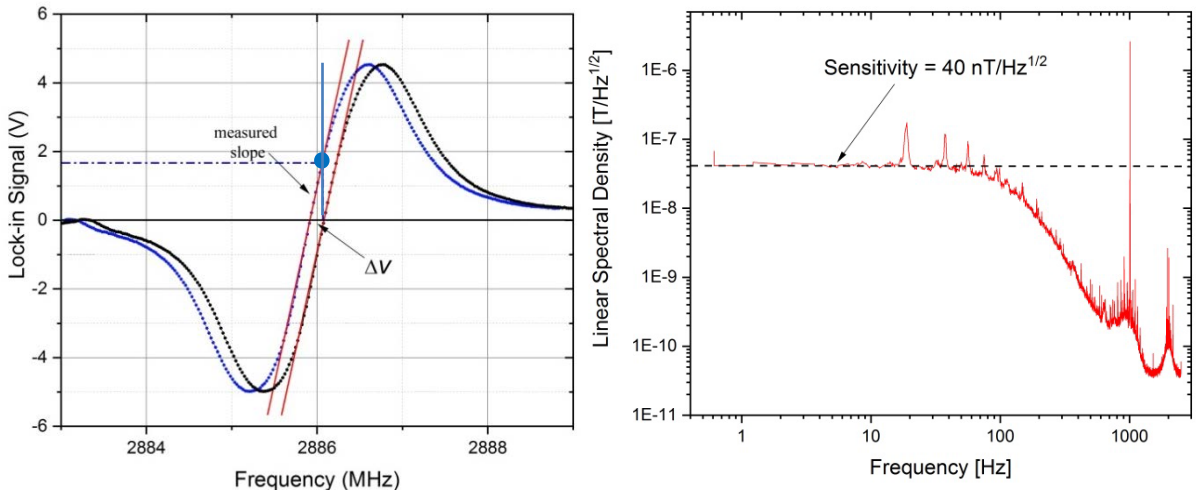

Fig.4.3.5 (a) lock-in spectrum of a single resonance. The vertical blue line is the fixed frequency of the microwave source. The black curve is the original lock-in voltage vs. frequency. With a change in magnetic field, the curve shifts by $\Delta\nu$ to the blue line and the lock-in output shifts from zero to the value at the blue dot. The value of $\Delta\nu$ is recovered by using the previously measured slope value. (b) Power spectral density of noise trace taken over 600 seconds. The time constant of the lock-in amplifier was set to 10ms.

In the present implementations, the projective field measurements can be performed only sequentially, which limited the ability of such magnetometer in terms of fast varying fields. To overcome these drawbacks, the multi-channel lock-in detection, when the four magnetic-field-dependent spin-resonance shifts are extracted simultaneously, can be used. It's just a technical challenge, that requires an availability of equipment, and we will implement a multi-channel lock-in detection in future.

Conclusion

In this chapter we have demonstrated how NV-center can be used for the precise electric, magnetic and temperature sensing.

In Section 4.1 we demonstrate that NV ensemble can be successfully exploited as a nanoscale sensor to perform direct local mapping of the internal electric-field distribution of a graphite-diamond-graphite junction. The diamond sample was investigated by means of ODMR measurement to directly measure the formation of local spatial charges predicted by the SCLC model and observed in previous works. This was achieved by performing a microscale ODMR mapping of the diamond interelectrode region and the formation of local electric fields was measured using NV– centers as local sensors. In particular this work highlited the strong persistence of long-lived charged traps in ion beam irradiated diamond. From subsequent measurements it was observed that the formation and local distribution of the spatial charge was

affected by the biasing history of the device and the associated memory effects were directly observed.

In Chapter 4.2 the temperature sensing technique based on NV sensors was demonstrated. In this Chapter we described a novel all-optical method for thermometry based on NV- centres in diamonds. Specifically, we explore the advantages of using a transverse bias magnetic field for temperature measurements. In this regime, a narrower linewidth and an enhanced ODMR appears due to the degeneracy of hyperfine transitions, this allow achieving a temperature noise floor of $5mK/Hz^{1/2}$. The method described here provides benefits in terms of its simple experimental setup and also better magnetic field noise protection.

In the last Chapter 4.3 we described a technique for NV-diamond vector magnetometry using nitrogen vacancy (NV) centers in a bulk diamond sample and its experimental implementation. A protocol for determining a vector of magnetic field was developed. Preliminary vector field measurements and estimation of the magnetometer's sensitivity were performed. Although these showed promising results, the ambient noises (magnetic, temperature fluctuation) limited the achievable sensitivity. To overcome these drawbacks, the multi-channel lock-in detection, when the four magnetic-field-dependent spin-resonance shifts are extracted simultaneously, was discussed.

Chapter 5

5.1 Detection of single-neuron action potential with NV centers: related challenges

Nitrogen-vacancy (NV) color centers in diamond are currently emerging as a practical quantum sensor, operating at ambient conditions, with very high sensitivity and spatial resolution. The spin – dependent luminescence of the NV center and all – optical initialization and read-out opens up huge avenues for the recording of weak magnetic fields occurring in various biological systems and might be particularly powerful for the neuroscience applications.

Understanding the function of the brain is one of the most significant challenges of the 21st century. Vast numbers of the human population face the prospect of neurodegenerative diseases numbers that will only get higher with ever-increasing lifespan, in-part due to success in other branches of medicine and improvements in healthy living conditions.

In-vitro recording in brain slices is a proven method for the characterization of electrical neural activity and has strongly contributed to our understanding of the mechanisms that govern neural processing. Traditional recordings methods, as electrophysiological probes (patch-clamp) are invasive and limited by the number of electrodes that can be placed in the tissue. Voltage sensitive dyes allow readout of the neuron membrane potential, but have poor signal-to-noise ratio and are toxic. Voltage sensitive fluorescent proteins are promising, but also limited temporal and spatial resolution. Alternative methods for magnetic measurements such as (superconductive quantum interference device) SQUID magnetometers are insensitive to single nerve impulses and come at great financial cost. Multi electrode arrays (MEA) systems can be used for precise parallel extracellular recording and cell stimulation but limited by the number of electrodes and designed only for *in–vitro* experiments.

The notable achievement in the field of the NV-based magnetometers promises a wide application of an incoming generation of the NV based sensors as a facile tool for use in neuroscience labs worldwide and in the clinical setting. However after the proof-of-principle experiments with a macroscopic biological objects more complex tasks, for example the imaging of planar cell activity, remains unachievable. In this chapter will discuss the major challenges that hinder these quantum sensors from reaching their full potential.

Key challenges to realize next-generation NV-based sensors suitable for neuroscience applications include:

1) ***Choice of* sensor *type*:**

   By taking advantage biotoxicity, neurons can be grown directly on the diamond surface, or nanodiamonds can be incorporated into cells, thus implying that the NV sensor can be placed extremely close to cellular magnetic fields of interest. Bulk diamond sensors can be used for wide-field electromagnetic imaging of the neural network dynamics of brain slices, but does non adapted for the nanoscale temperature measurements due to the high heat conduction. Nanodiamonds have a nanoscale size and are perfect for the intracellular temperature sensing or for a tracking, however arbitrary rotation ND crystal inside a cell and conglomeration susceptibility significantly complicate the measurements. Also linewidth broadening of the ODMR peaks in NDs respect to bulk diamond crystal limits the sensitivity. Therefore, this implies that the sensor type selection should be done for a specific target and all advantages and disadvantages should be carefully analysed.

2) **Type of measurement protocol:**

   A diverse set of experimental protocols has been conceived to precisely measure ODMR frequency shifts caused by external perturbations. The three most common approaches are the direct detection of the ODMR spectrum using continuous-wave spectroscopy, the measurement of the time evolution in pump-probe (pulsed) experiments and measurements of spin relaxation times.

   CW-ODMR scheme is more technically because avoids the difficulty facing pulsed schemes. However CW ODMR suffers from microwave and optical power broadening, degrading contrast and linewidth of the resonance peak. More sensitive approaches rely on pulsed experiments in a pump probe scheme with the laser turned off during the sensing period. The advantage of pulsed experiments is that no optical repumping occurs during the sensing period. The basic Ramsey sequence is one of these DC measurement techniques that are sensitive to static magnetic fields. CW-ODMR, pulsed ODMR and Ramsey sequence are used for the detection of static or slowly-varying magnetic fields.

Recent efforts have shown that sensitivity of NV based magnetometer can be enhanced by several orders of magnitude by moving to AC detection with signal frequencies in the kilohertz to megahertz range.

A DC magnetometer is sensitive to frequency components from DC up to the bandwidth of the sensor. An AC magnetometer, in contrast, is sensitive to synchronized magnetic fields or asynchronized magnetic noise within a narrow bandwidth around the specific frequency. AC field detection can be achieved using spin echoes and several techniques which allow one to extend the coherence time of NV centres up to milliseconds. Dynamical Decoupling (DD) is a useful technique to this purpose and it is based on long sequences applied on the NV centre in order to decouple it from the surrounding spin bath. Unfortunately, due to slow frequency processes in biological systems (<100Hz) and generally a stochastic nature of biological signals protocols designed to sense highly controllable DC and AC signal are not always compatible.

3) Bias magnetic field alignment

The principle of NV-center based magnetometer based on the registration of a shift in a resonance frequency of ODMR spectrum. NV spins in the diamond lattice may lie along four possible orientations set by the tetrahedral symmetry of the diamond lattice, which enables determination of a magnetic field's magnitude and direction from detection of the Zeeman shifts associated with each NV- orientation.Transverse crystal strain (which can be up to ~10 MHz) makes low-field magnetometry challenging, so a constant, well defined bias magnetic field is necessary for the initial "initialization" of magnetometer. Bias magnetic field helps to remove degeneration of four resonance dips and can be set up to along a single NV- axis of the diamond sensor or along a vector that equally projects onto two or more of the NV- axes. If the orientation of a weak magnetic field under study can be defined *a priori* the bias magnetic field can be aligned along the same direction. It allows one to optimize the response of the magnetometer to the shift of the resonant frequency and thus achieve maximum sensitivity. This, in turn, admits a higher resolution due to the smaller sensing volume. Hereby, both the optimal sensitivity and resolution depends on the nature, number, and spacing of magnetic sources being measured. For example, reconstructing neuronal currents of axons from acquired magnetic field maps using an NV-diamond magnetic image system requires the biomagnetic inverse problem solution. For the single axon or a simple 2D networks the inverse problem can be uniquely solved[183], [184]. 3D networks (biological tissues) are more problematic: not only are magnetic signals smaller due to greater

source-sensor standoff distance, but the problem is under-constrained, meaning that multiple reconstructions of current sources are possible from an observed magnetic field map.

4) General problems

Optimal performance of NV-based magnetometer can only be achieved with informed equipment choices for a given target application, in our case for the measurement of weak magnetic fields in the biological samples. These choices include proper selection of the diamond sensor type, optical illumination, MW field, bias magnetic field, optics, method of photoluminescence detection, sample preparation and mounting[185].

The *in vitro* imaging of biophysical processes at the molecular scale requires time-intensive sample preparation. Cells must be incubated in special sterile neurobasal medium in a humidified 5% CO2 atmosphere at 37 ºC. The same conditions are required at long-terms measurements processes.

That means a cell culture should be placed in special incubator system which often imposes restrictions on how the sample is mounted. For example, optimal photon collection efficiency requires the largest achievable numerical aperture (NA) for the microscope objective. In practice, high-NA objectives have a short working distance, sometimes shorter than the base for the cell solution (Petri dish) or diamond sensor. Usually the objective 60x for the biological imaging is used.

Increasing the illumination intensity improves the NV fluorescence intensity, the photon shot noise, and sometimes the ODMR dip lineshape. Strong microwave (MW) power improves the contrast in a CW ODMR measurement. However biological samples are very sensitive and ever low intensity, of the laser can destroy a membrane of the cell while microwave radiation heats cells composed on 75-80% of water. A strong bias magnetic field can in principle change the dynamics of ion currents, therefore additional studies are needed. Furthermore, the challenge of synchronization of biological system with the measurement apparatus should be resolved. All of this creates significant hardship for the precise measurements of biophysical processes at the molecular scale requiring phenomenal sensitivity.

5.2 Estimation of the electromagnetic fields in the nervous system

All major processes in the nervous system depend on interaction between cells and nerve fibers (axons) by means of nerve impulse transmission. In neurons, action potential (AP) plays a central role in cell-to-cell communication. It is a process when the membrane potential of a specific cell location rapidly rises and falls, creating voltage pulse with a characteristic pattern.

Figure 5.1 illustrates how a AP is created across the cell membrane of a neuron. When a neuron is at rest, layers of positive and negative charge on the outside and inside of the membrane are created. The thin membrane (10nm) separates electrically neutral fluids having differing concentrations of ions, the most important varieties being Na+, K+, and Cl^-. Although the concentrations of the different ions attempt to balance out on both sides of the membrane they cannot, because the cell membrane is semipermeable, meaning that some ions may cross it through channels (ion channels)while others cannot.

An action potential occurs when a neuron sends information down an axon. The some external event (a stimulus) causes the resting potential to move toward 0 mV. When the depolarization reaches about -55 mV, (the threshold) a neuron fires an action potential. A stimulus over the critical threshold level causes Na channels to open. Because there are many more Na+ ions on the outside, and the inside of the neuronal membrane is negative, Na+ ions rush into the neuron, so the membrane inside becomes more positive and becomes depolarized. It takes longer for K channels to open. When it happens, K^+ ions rushes out of the cell, reversing the depolarization. At the same time Na channels start to inactivate. This causes the action potential to go back toward -70 mV (a repolarization). Actually the AP goes below -70 mV (a hyperpolarization) because the K channels stay open a bit too long. Gradually, the ion concentrations go back to resting levels and the cell returns to -70 mV. Thereby AP pulse is caused by different ions cross the neuronal membrane and has duration about of 3ms.

NV-based magnetometers are aimed to measure a magnetic field generated by currents in a neuronal membrane, so the primary knowledge of currents propagation during the action potential is required. The modern techniques, as patch clamp allowing measurements of single-channel currents, while the measurement of the total current through the neuron during an action potential remains challenge. Usually the special simulators[186], [187] based on Hodgkin–Huxley model[188], [189] are used to evaluate currents in a neuronal membrane. Open ion channel cause intracellular and extracellular ionic current flows. The total current can then be described as the sum of all ionic currents, where the potassium (K) and sodium (Na) ion currents play the most significant role. Figure 5.2 shows the simulation of K^+ and Na^+ ion

currents, capacitive current and the total membrane current during an action potential. Due to the opposite direction of the K^+ and Na^+ ion currents, the pulse of the sum current is much shorter and weaker (I_{sum}~2pA/μm^2, T~1ms), however it is not an unique challenge. The method by which these electric currents are generated and transmitted is more complex than the simple movement of free charges along a conductive wire. The total current flow can be write as a sum of internal/external cellular currents (I_{trans}) of the ion channels K, Na and axial current (I_{ax}) along the axon, generated by transversal components of the intra/extra cellular currents. Only small part of the total current flow will be in longitudinal direction, parallel to the membrane. It is that axial current (I_{ax}) plays a crucial role in the formation of the magnetic field B_{ax} around the neuron. As see from the Fig.5.3(b) the internal/external currents create vortex magnetic fields B_{vor} around the ion channels on the membrane surface. The average of the $<B_{vor}>$ over some sensing volume quite unpredictable and depends on concentration, localization and type of the ion channels in the neuronal membrane. For example, near the Ranvier nodes the concertation of the ion channels is $10^4/1\mu m^2$, against the $10/1\mu m^2$ for other zones. Hereby, the magnetic field $<B_{vor}>$, generated by perpendicular ions currents, has unpredictable orientation and its magnitude does not hardly exceed of the magnetic field of the single channel.

activity of a brain or cardiac tissues.

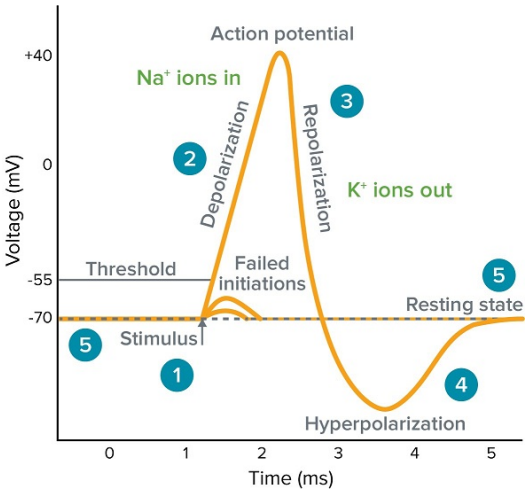

Fig.5.1 A schematic view of an idealized action potential illustrates its various phases as the action potential passes a point on a cell membrane.

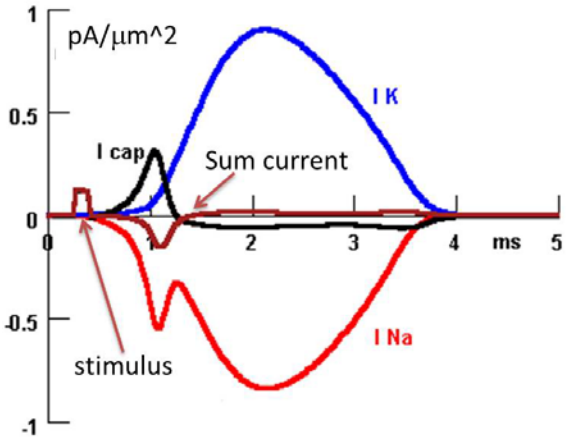

Fig. 5.2 The total membrane current (brown) and ion currents (red – sodium, K - potassium) during an action potential.

The axially oriented current I_{ax} and magnetic field distributions that occur during the action potential were estimated in [190]–[192]. In papers [191], [192] the spatiotemporal characteristics of neural magnetic fields of brain slices were estimated. The neuronal model was based on standard Hodgkin–Huxley equations and was calculated using the NEURON

software package. In this model authors considered simultaneous stimulation of neuronal cells over 500x500x300 μm sensing volume. The peak magnetic field strengths of $1.5x10^{-9}$ T for these conditions can be achieved. A more complex model was considered in work[190]. Starting from the Hodgkin–Huxley circuit representation of axon the authors transformed and significantly upgraded the model in a novel way by including spatial and temporal progression of an action potential and corresponding changes to current flows. The new model takes into account that there is no one single current, that flares up along the entire neural fiber. In fact, there are many subsequent currents. Each of them ends at the next node of Ranvier, while the next current is about to exist.If one such region is observed, the current flow through the neuron induces a time-varying circular magnetic field of localized strengths up to B= 3×10^{-12}T. The field remains homogeneous inside the myelin sheath and then starts decaying non-uniformly with distance (see Fig. 5.4). The maximum strength of the magnetic field was also calculated for the nerve composed of 100 axons. In that case the magnitude of the magnetic field was only doubled (B= 6×10^{-12}T) from the magnetic field strength for an individual axon. This is due to the current dissipation and magnetic–field–component cancellation caused by different axons within the same nerve, carrying opposing directional currents. Interestingly, the estimation of the magnetic fields in this paperare, actually, the same fields detected by magnetoencephalography (MEG). The reason why MEG detects fields of 10^{-15} T (1.000 times weaker than simple estimation gives) is not only the distance from the source but also their inhomogeneity, which this model precisely describes.

Thus, based on the *analysis,* the next parameters of magnetic field pulses from a single action potential caused by the neural activity are expected: amplitude ~3pT, duration~1mT, sensing volume~$10\mu m^3$.It applies strict requirements for the upcoming generation of NV magnetic field sensors: sensitivity ~$30fT/Hz^{-1/2}$, temporal resolution better 0.1ms, spatial resolution ~$10\mu m^3$. The fundamental sensitivity limit for spin-based magnetometers is given by the noise intrinsic to quantum projection. For a sample of *N*electronic spins with characteristic dephasing time T_2^*, the spin-projection-noise-limited sensitivity is:

$$\eta = \frac{\hbar}{g_e \mu_B} \frac{1}{\sqrt{N T_2^*}}$$

The estimation for the diamond sensor used in the work [50] (sensitivity $15pT/Hz^{1/2}$) with a density of NV centers N = $3\times10^{17}cm^{-3}$ and $T_2^* \approx$ 450 ns gives the spin projection noise of $7pT/Hz^{1/2}$for the sensing volume ~$10\mu m^3$, that in 200 times greater the required sensitivity for

the single action potential detection. This challenges that NV based magnetometers can be used for single action potential detection in neurons, they nevertheless can be applicated for the slice

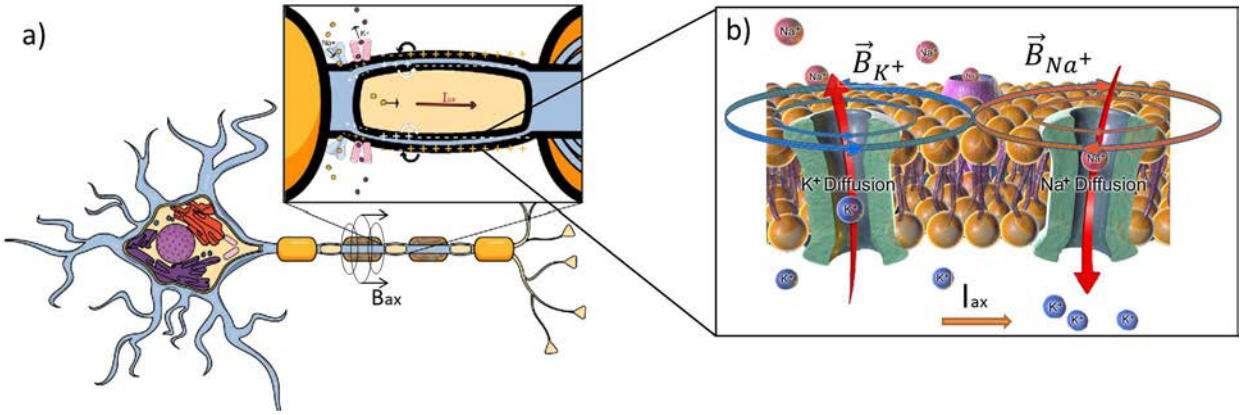

Fig.5.3 Axial and longitudinal current flows generation within a neuron. The axial current is a product of the continuous ion flow through the cell's membrane and its transversal components.

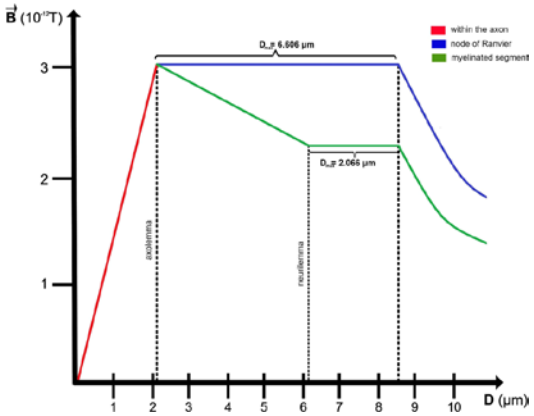

Fig.5.4 Strength of the magnetic field as a function of distance from the center of a single axon. At myelinatedsegments, the magnetic field reaches its maximum of $3.0\text{x}10^{-12}$T at axolemma, the outer membrane of the axon, then falls off to $2.3\text{x}10^{-12}$T once it reaches neurilemma, the outer layer around the myelin sheath. From neurilemma, it keeps its homogeneity for distance of 2.066μm and then it starts to decay. On the other hand, at nodes of Ranvier, the magnetic field stays homogeneous up to distances of 6.066μm away from axolemma. After this the field starts decaying non-uniformly with distance. (Data and figure were taken from the paper [190])

5.2 Interaction of nanodiamonds with neurons

Among the multitude of fairly novel materials for scientific, technological and clinical applications, diamond nanocrystals (or nanodiamonds, NDs) earned a solid reputation and vast interest due to their unique features, such as low cytotoxicity[193], the possibility of stable chemical functionalization and extreme mechanical properties (robustness, low friction coefficient)[194]. The diamond lattice can host a large number of optically active defects[195],

[196], and the most common and widely employed of which is NV center. This system is characterized by a wide excitation spectrum (500–600) nm, emission in the red range (600–800 nm) with zero phonon line (ZPL) at 638 nm. NDs incorporating NV centers provide a stable luminescent label suitable for different types of bio-imaging and bio-sensing applications[50]–[52], [83]–[86]. A significant advantage of fluorescent nanodiamond (FNDs) is related to their photostability, resistance to bleaching or quenching phenomena[88], that allows their monitoring along neuronal branches with high spatio-temporal resolution[89], as well as to perform long-term cell tracking[51], [89]. More specifically, the peculiar structure of the spin-dependent radiative transitions of the NV^- centers allows the optical detection of weak electro-magnetic fields and small temperature variations within the biological samples under exams, by means of Optically Detected Magnetic Resonance (ODMR), thus disclosing a range of new perspectives in cell sensing with unprecedented spatial resolution and sensitivity[50]–[52], [92], [197].

ND coatings represent excellent substrates for neuronal cultures, preserving intrinsic neuronal excitability as well as spontaneous synaptic transmission, even though nanoparticle size and their surface features may affect neuronal adhesion[94], [198]. However, if the bulk material is non-toxic and inert, when dealing with diamond at the nanoscale, quite heterogeneous results emerge. For example, NDs produced by detonation (DNDs) have been reported to have strong anti-bacterial properties, if not well cleaned[199]. However, aggressively cleaned FNDs do not show this behavior. Toxicity assessments, after surface preparation, have been performed on FNDs by in vitro and in vivo experiments. The most sensitive experiments were done by Cheng and coworkers[200] who conducted toxicity tests of nanodiamonds (NDs) on the zebrafish embryo model in vivo. This model is especially sensitive to toxicity at critical stages of embryo development. They found that for ND concentrations below 1 mg/ml, even in the critical stage, zebrafish embryos exhibit similar development as compared to the control groups. In a different experimental model, airway epithelial cells, functionalization may reduce ND inflammogenicity[201], while a remarkable dose-dependent decrease of neurite length of central and peripheral cultured neurons after FNDs seeding has been demonstrated[202].

In this chapter we consider howNDs, internalized in mouse hippocampal neurons, effect on the behavior of the action potential firing. As a first step the internalization of NDs in the cells was observed and measurements of the fluorescence of the NV centers contained in them were carried out. Then we combined patch-clamp and microelectrode array (MEA) recordings to evaluate their functional implications on hippocampal neurons functionality. In the end the ODMR measurement has been done in order to test the resilience of the cells to the application of the measurement protocol. The availability of the ODMR technique, alongside other type of

in vivo measurements, allows one to observe malfunctioning in the cell life processes and therefore gives access to early stage diagnosis of a wide range of neural diseases (e.g Alzheimer).

5.2.1 FND characterization and internalization

For biological applications, the geometric form and the size of NDs is a crucial parameter.The size of FNDs was estimated by means of SEM imaging, after finalizing their preparation. Figure 5.5(a) and (b) show typical SEM micrographs, where most of the nano-particles present the expected dimensions, namely below 100 nm. The powders are classified as Ib type, with a nominal substitutional N concentration of 10 - 100 ppm, and contain a low amount of native NV centers. Ion beam irradiation (Fig. 5.5c) and a subsequent thermal annealing were performed to increase the number of NV centers in each nanocrystal.The full process of FNDs preparation and cleaning is described in Section 3.1.

In follows, room temperature photoluminescence (PL) spectroscopy was performed with the purpose of assessing the spectral features of the ND emission. The spectrum in Fig. 5.5(d) is common for NV centers and confirms the effectiveness of the cleaning procedure (no features involving organic contaminants or graphite are observable).

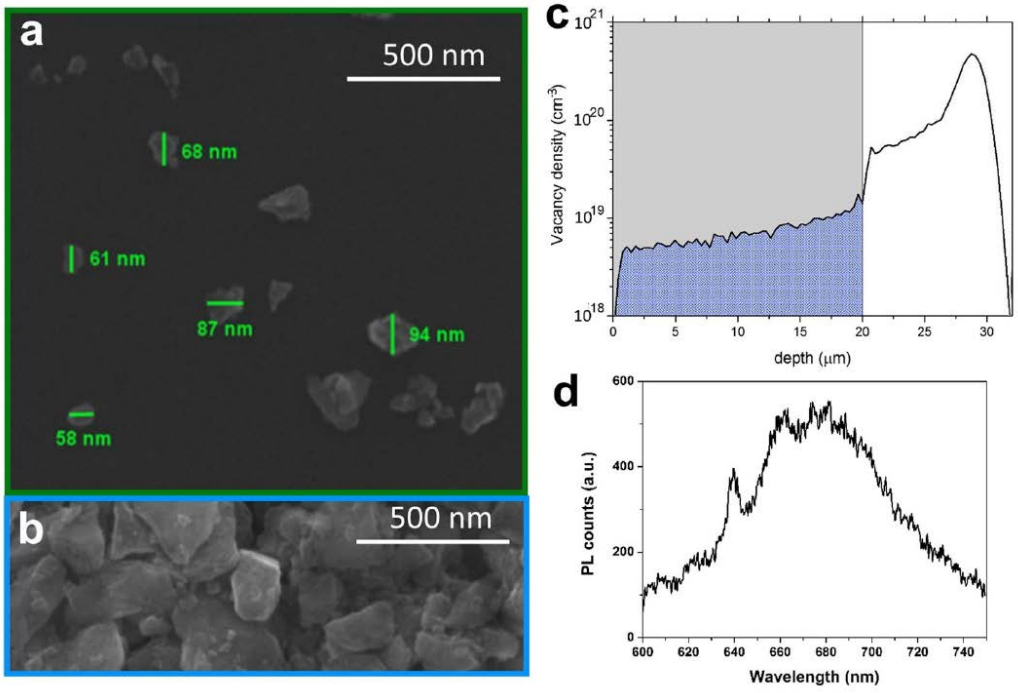

Fig.5.5 SEM imaging and SRIM simulation. a)SEM micrograph of dispersed nanodiamonds over a silicon substrate: the mean crystal dimension is smaller than 100 nm. b) SEM micrograph of a 20 μm thick nanodiamond deposition before ion irradiation. c) SRIM Monte Carlo Simulation of the damage profile induced by 2 MeV proton over the diamond deposition: the ions cross the sample creating a uniform defect concentration over the whole depth. d) confocal fluorescence spectrum of FNDs. The NV- ZPL peak is clearly visible at 638 nm, as well as the corresponding wide phonon band at larger wavelengths.

5.2.2. Cell incubation with FND and confocal imaging

The mechanisms of FNDs internalization and related motional dynamics inside cells has been previously investigated in various experimental procedures (HeLa cells, embryo hippocampal neurons, as well as lung cancer cells and embryonic fibroblasts).

In our work embryo hippocampal neurons were incubatedwith 40 μg/ml FNDs, being this concentration far below the threshold for cell toxicity (<250 μg/ml)[91]. Successively, the cytoplasmic membrane labelling dye (CellBrite™ green cytoplasmic membrane dye, Biotium) was added to the medium (24 h later). This allowed to identify the intracellular membranes (stained in green) together with the internalized FNDs, characterized by a red fluorescent emission.FNDs internalization was controlled by means of confocal microscopy.

Hippocampal neurons incubation with FND was performed at 7 or at 14 day of incubation (DIV). For both MEAs and plastic dishes, half of the culture medium (i.e. approximately 1 ml) was replaced with FND-medium to reach a final concentration of 40 μg/ml. Incubation with the cytoplasmic membrane dye was performed 24 hours later. For confocal imaging, hippocampal neurons were plated on 35 mm dishes (ibidi GmbH, Planegg/ Martinsried, Germany). Cells were analyzedusing a confocal laser scanning microscopeLeica TCS SP5, equipped with an argonion and a 561 nm DPSS laser. Cells were imaged using a HCX PL APO 63x/1.4 NA oil immersion objective at a pixel resolution of 0.08 x 0.08 x 0.3 μm.The luminescent emission from the FNDs was excited by 561 nm laser, while the emission was collected in the 650–750 nm spectral range. The same excitation wavelength was uneffective in untreated neurons. Green fluorescence for intracellular staining was obtained by 488 nm wavelength. Image analysis was performed using ImageJ software. The considered acquisition system was not destined for the detection of single FNDs and ODMR measurements. Therefore a confocal microscopy setup adopted for the wide field imaging, confocal imaging with single photon sensitive detectors (SPADs) and ODMR measurements has been implemented. The detailed description of the setup has been done in Chapter 1.3. As an example in Fig. 5.7 the comparison between the wide-field image of a sample of cultured hippocampus cells hosting FNDs and the corresponding confocal scan showing the PL signal of the hosted NV centers is presented.

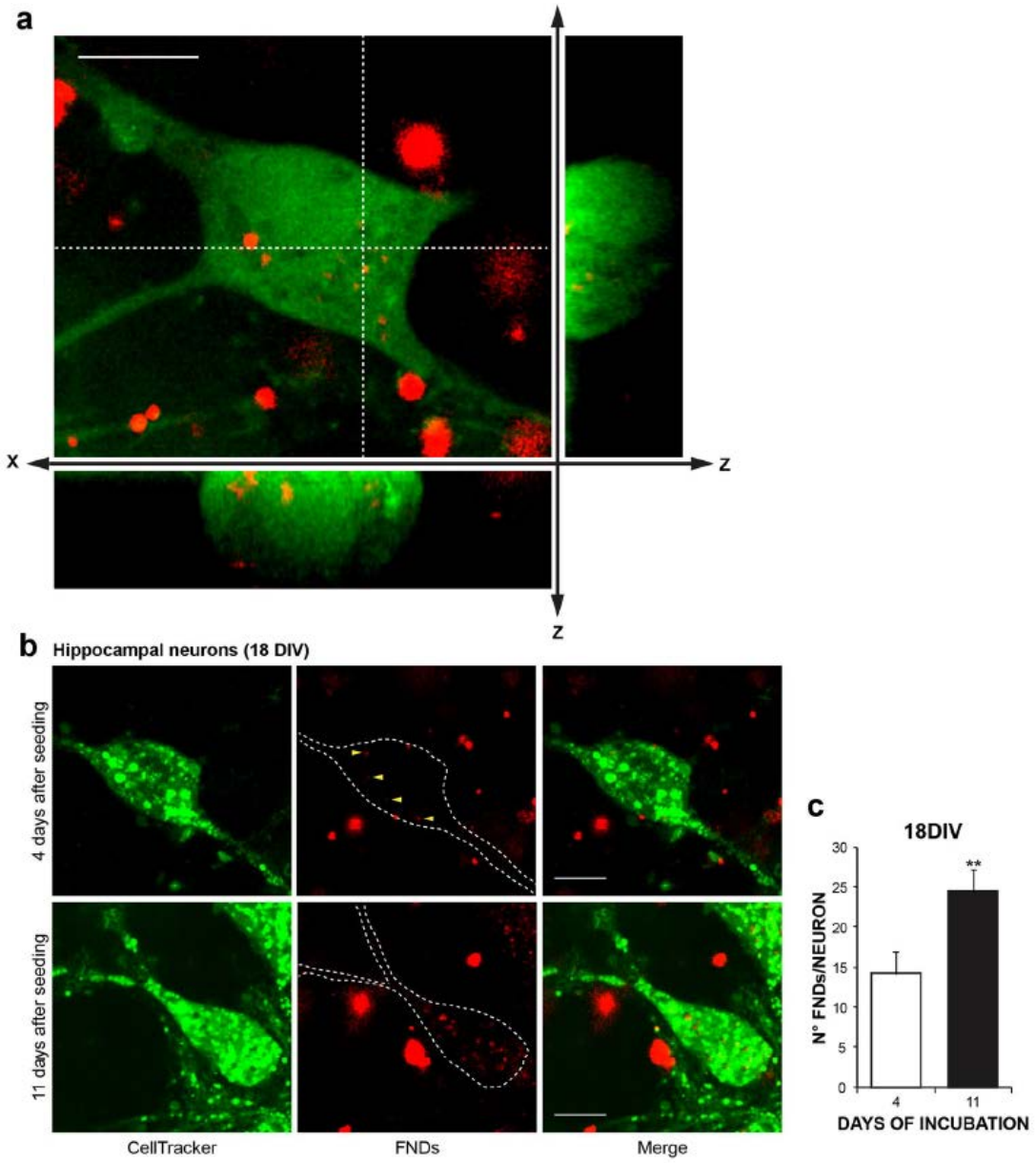

Fig.5.6 FND internalization into cultured hippocampal neurons. (**a**) Confocal fluorescence microcraph of cultured hippocampal neurons (14 DIV), exposed to 40 μg/ml FND for 2 days, and stained in green with the cytoplasmic labelling dye. Red emission is from FNDs. The entire field and cross-sections (XZ and YZ) were shown. (**b**) Hippocampal neurons were exposed to 40 μg/ml FND for 4 and 11 days and stained as in (**a**) at 18 DIV. Maximum intensity projections of confocal z-stacks are shown. (**c**) Quantification of FNDs internalized in neurons treated as in (**b**). Scale bar represents 10 μm.

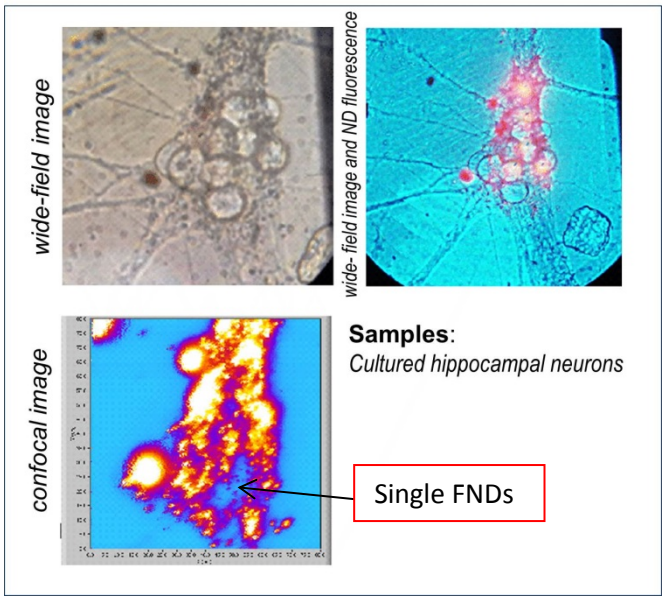

Fig 5.7 Comparison between a wide-field image (top) and confocal PL scan (bottom) of a sample of cultured hippocampal neurons hosting fluorescent nanodiamonds (diameter=0-100 nm) with NV centers.

5.2.3 Analysis of firing activity of the hippocampal network affected by FNDs.

Hippocampal neurons, when cultured on microelectrode arrays (MEAs), create a network that exhibit spontaneous firing activity which is characterized by different patterns along with culture maturation: asynchronous firing is typical of younger neurons (7–13 days *in vitro*, DIV), while in elder cultures activity becomes highly synchronized and organized into bursts (>14 DIV). We compared the firing frequency of hippocampal neurons under control conditions and after exposure to FNDs in means of microelectrode arrays (MEAs).

MEA is an arrangement of 60 or more electrodes allowing the targeting of several sites in parallel for extracellular recording and stimulation. Recorded signals are amplified by a filter amplifier and sent to the data acquisition computer. Cell can be cultivated directly on the MEA. Almost all excitable or electrogenic cells and tissues can be used for extracellular recording *in vitro*, for example, central or peripheral neurons, cardiac myocytes, whole-heart preparations, or retina. The main applications for MEAs in the fields of neurobiology and cardiac electrophysiology are: Ion channel screening, drug testing, neuroregeneration, developmental biology. It makes the MEA system a good non-invasive alternative to a standard patch-clamp method.

We found that, regardless of the exposure stage of FNDs, the number of spontaneously active neurons remained unaltered, as demonstrated by the unaltered percentage of electrodes in which the firing activity could be detected: 49 ± 7 % in control (n=26 MEAs), 41 ± 7% when

FNDs were administered at 7 DIV (n=17 MEAs) and 47 ± 8 % when FNDs were administered at 14 DIV (n=16 MEAs).

On the contrary, the firing frequency was differently affected depending on the stage of incubation with FNDs (7 versus 14 DIV). When FNDs were applied at 14 DIV (Fig. 5.8d), FNDs caused a drastic reduction of the mean frequency on 18 DIV neurons respect to controls (36%), from 1.03 ± 0.07 Hz to 0.66 ± 0.05 Hz. On the contrary, early incubation at 7 DIV preserved the firing frequency during culture maturation: in fact, mean firing frequency, measured at 14 DIV was 0.80 ± 0.20Hz (control) and remained 0.60 ± 0.04 Hz (with FND); while, at 18 DIV, mean firing frequency was 1.03 ± 0.07 Hz in control and 1.06 ± 0.07 Hz in the presence of FNDs (Fig. 5.8d and 5.8e).

Similarly, the mean number of bursts, evaluated over 120 s, decreased by 44%, from 16 ± 1 to 9 ± 1. When FNDs were applied on mature networks, but remained unaltered for early incubation (Fig. 5.8f). Burst duration was not significantly different among controls and FNDs (Fig. 5.8g).

Overall, these data suggest that spontaneous firing is significantly impaired only if the exposure occurs at later stages. Since early incubation (7 DIV) did not induce any significant effect, all other experiments were carried out by adding the FNDs at 14 DIV and recording the firing activity at 18 DIV.

The Analysis of miniature inhibitory and excitatory postsynaptic currents (mIPSCs and mEPSCs) also showed drastically reduction of the mean frequency of spontaneous GABAergic and glutamatergic transmissions[1]. Representative traces are shown in Fig. 5.9(a and b). Experiments were performed at 18 DIV. Other parameters such as amplitude, the time-to-peak and the half-width of mPSCs remained unaltered upon FNDs application (Fig. 5.9c). Overall, these findings suggest that, despite the marked frequency changes, GABAergic and glutamatergic transmission was equally affected during exposure to FNDs and thus likely preserving their balance.

[1]Glutamate and gamma-aminobutyric acid (GABA) are the major neurotransmitters in the mammalian brain. Inhibitory GABA and excitatory glutamate work together to control many processes, including the brain's overall level of excitation.

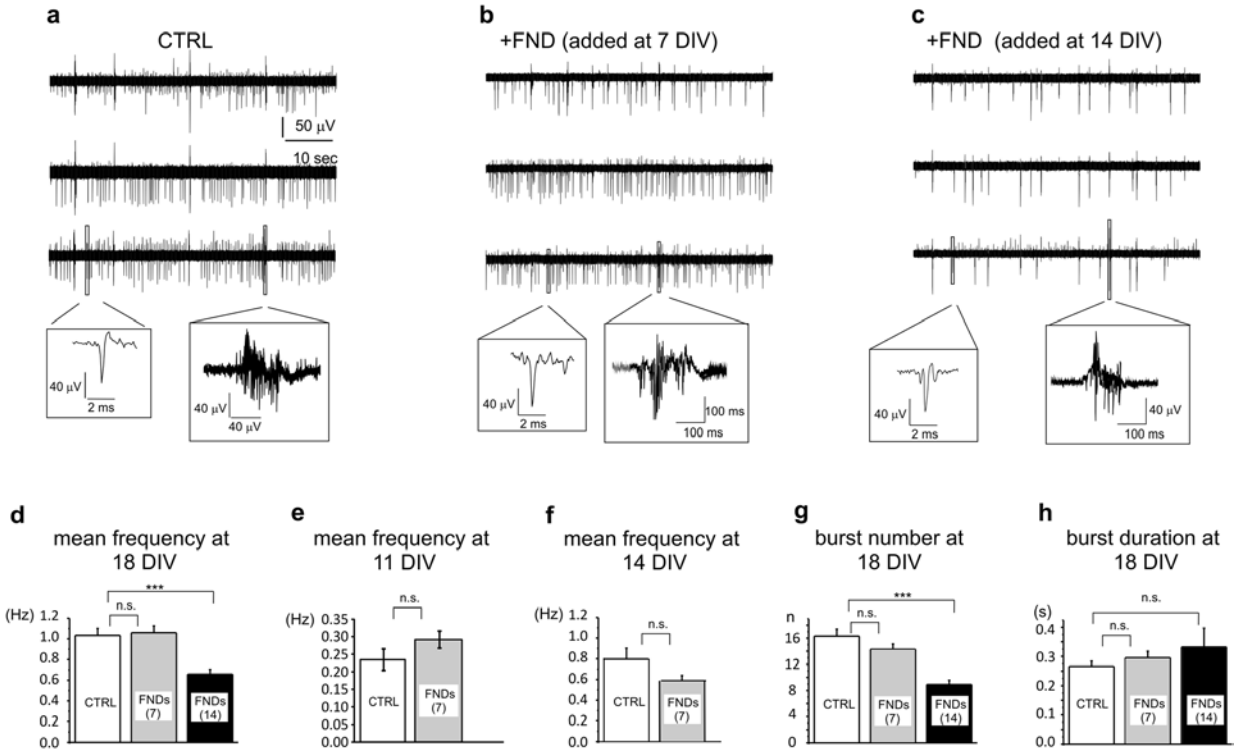

Fig. 5.8 MEA recordings of hippocampal neurons activity without FNDs and after FNDs seeding. (**a**–**c**) Representative traces of spontaneous firing at 18 DIV (data from 3 representative MEA channels) under control conditions (CTRL), without FNDs (**a**), with FNDs seeded at 7 DIV (b) and at 14 DIV (**c**). Insets: higher magnification of single spikes and bursts. (**d**) Bar graphs of the mean frequency measured at 18 DIV without FNDs (CTRL, white) and after FNDs administration at 7 DIV (grey) and 14 DIV (black). (**e**) Bar graphs of mean frequency of the spontaneous activity measured at 11 DIV without FNDs (CTRL) and after FNDs administration at 7 DIV. (**f)** Bar graphs of mean frequency of the spontaneous activity measured at 14 DIV without FNDs (CTRL) and after FNDs administration at 7 DIV. (**g**) Bar graphs of mean number of bursts and mean burst duration without FNDs (CTRL), and after FNDs administration at 7 and 14 DIV. (**h**) Bar graphs of mean burst duration (s) without (CTRL) and after FND seeding at 7 and 14 DIV.

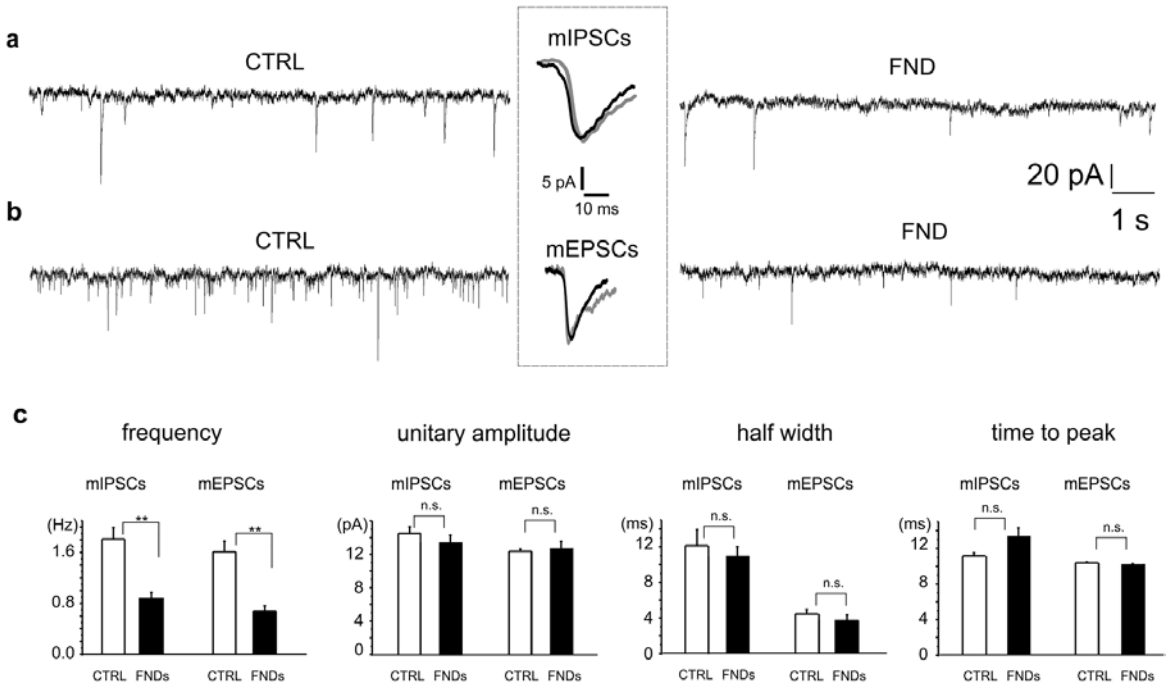

Fig. 5.9 Frequency of miniature inhibitory and excitatory currents is reduced by FNDs. (**a**) Occurrence of miniature inhibitory and (**b**) excitatory post synaptic currents is reduced by FNDs with respect to controls. Inset: averaged miniature currents in control (black) and after FND seeding (grey). (**c**) Bar graphs showing the mean values of the following mPSCs parameters: frequency, unitary amplitude, half width and time to peak, for control (white bars) and FNDs-treated neurons (black bars).

5.2.4 ODMR: towards bio-sensing applications

We applied the Optically Detected Magnetic Resonance (ODMR) technique to detect signals from FNDs incorporating NV centers that were internalized into hippocampal neurons. Negatively charged nitrogen-vacancy (NV) colorcenters in diamond can be regarded as an atomic-sized magnetic field sensor that can be optically read-out optically using ODMR. We successfully performed a demonstrative ODMR measurement in a sample of hippocampal neurons hosting NV centers in nanodiamonds (Fig. 5.10). During an ODMR experiment, the sample was continuously illuminated and irradiated by microwave field of-20 dBm power at variable frequency in the 2.80-2.96 GHz range, by positioning a micro strip antenna in close proximity of the investigated sample. This enabled the observation of a local minimum in the PL emission intensity corresponding to the resonance frequency (2.88 GHz) of the ground-state zero-field splitting between the $|0\rangle$ and $|\pm1\rangle$ states. In this way we had exposed the cells to a measurement protocol that in perspective would enable detecting in a non-destructive way the weak magnetic field associated to the action potential firing. Under these experimental conditions, spontaneous firing was preserved, as shown in Fig. 5.10(c) for two representative cells, respectively without (CTRL) and after the FND treatment, suggesting that cell functionality was maintained after the implementation of the ODMR measurement protocol (ND hosting, mW-regime laser exposure, microwave excitation).

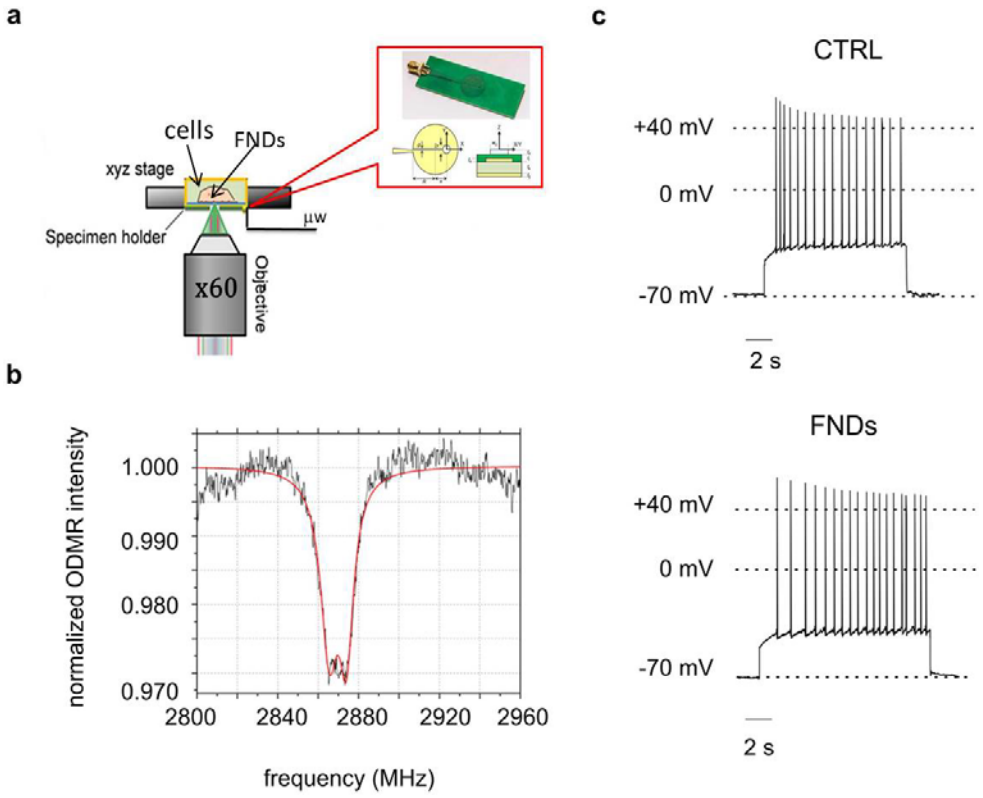

Fig 5.10 ODMR measurement. (**a**) Schematics of the confocal setup for ODMR measurements. The sample was observed via a single-photon-sensitive confocal microscope integrated to the Olimpus IX73, the excitation light being provided by a solid state laser at 532 nm. A dichroic beamsplitter (long-pass at 570 nm) reflected the excitation light inside the air objective (Olympus, 60x, NA = 0.9) focusing inside the sample and transmitted the photoluminescence towards the detecting apparatus. A microwave field with power Pmw = −20 dBm was transmitted via a micro-strip antenna. (**b**) ODMR signal detected from NV centers in nanodiamonds internalized in a neural cell. (**c**) Spontaneous firing of hippocampal neurons, without and with FNDs, is preserved by the application of the ODMR protocol.

Conclusion

In this Chapter the discussed the current challenges related with application of NV based magnetometer for the biological systems. Major constraints for diamond sensor type as optical illumination, MW field, bias magnetic field, optics, method of photoluminescence detection and sample preparation have been analysed. Special attention was paid to estimation of the electromagnetic fields in the nervous system. The nature of biological currents in neurons and generated by them magnetic fields were estimated. It was shown that sensitivity of upcoming generation of NV magnetic field sensors may not be enough for the measurement single neuron action potential but measurement of the magnetic field of the slice activity of the brain, cardiac tissues or intracellular temperature measurements seem very promising. Also the functional effects of fluorescent diamond nanocrystals on primary cultures of hippocampal neurons were investigated. Fluorescent nanodiamonds were internalized in living neuronal cells dissociated from an embryo mice's hippocampi. ODMR measurements were successfully carried out as a

proof of feasibility of this type of measurement without affecting the cells physiological functions. The possibility of implementing ODMR protocols inside living cells is of high relevance for applied neurophysiology and bio-chemistry researches since the ODMR technique allows high sensitivity measurements of the temperature and low intensity electrical currents that characterizes biological systems.

Summary

The common thread running through all the chapters of this dissertation was the sequential analysis and practical implementation of the possible applications of color centers in diamonds. The above studies show the enormous potential of defects in diamond structure (especially NV - center) not only as robust single photon sources, but also as high sensitivity, nanoscale sensors operating under ambient conditions for quantum metrology applications and biosensing.

The reported results were summarized in five chapters. Background regarding the properties of colour centers in diamond and applied techniques for manipulation, initialization and read-out of quantum state of the NV center were described in **Chapters 1, 2.** Sensing with NV centers and a comparison of state of the art measurement techniques for magnetometry and thermometry has been reported in **Chapter 2**. It was shown that NVs as magnetic/temperature sensors potentially reach unprecedented sensitivity over a large spatial resolution range.

The fabrication process of fluorescent nanodiamonds, its characterization and application were reported in **Chapter 3**. The produced samples were used to implement measurement protocols for the experimental demonstration of a new non-classicality criterion, in comparison with the characterization carried with the conventional second-order autocorrelation function. This technique has the drawback that the value of the new quantifier depends from several experimental parameters (optical and coupling losses, detection efficiency, detector-tree splitting ratio). On the other hand, if the measurement apparatus is previously characterized, it allows identifying the number of single-photon emitters in ensembles in presence of significant background luminescence. Another important advantage of the new criterion is that the resulting quantifier gets more “non-classical” in its numerical value for increasing number of emitters, while the value of the second order autocorrelation function approaches the classical value in these cases. The technique is of high interest in quantum technology because, in principle, the information gained by its implementation can be used together with other multicoincidence techniques, leading to an improvement of the latter applications.

Fluorescent nanodiamonds were also used as a single photons source for the pilot comparison of the $g^{(2)}(0)$ parameter among three metrological institutes INRIM, NPL and PTB. This comparison has been conducted by each partner individually by means of their own equipment at INRIM laboratories, which were responsible for the operation of the source.

Using a Hanbury Brown and Twiss interferometer, the coincidence and click probabilities from single photons emitted from a nitrogen–vacancy centre in diamond were measured, which allows estimating the second-order correlation function — a parameter commonly used to describe single-photon sources. The independent results agree within uncertainty and mark the first step towards to develop the first standardized technique to characterize single-photon sources and to provide common uncertainty estimation procedures.

In **Chapter 4** we present three protocols of quantum sensing based on NV centres in diamonds. The electric, magnetic field and temperature sensing, demonstrated in this work by means of ODMR measurements, pave the way for the application of quantum metrology in material sciences as well as in life sciences.

It was shown that NV ensembles can be successfully exploited as nanoscale sensors to perform local mapping of the internal electric-field distribution of a graphite-diamond-graphite junction exhibiting electrical properties dominated by trap- and space-charge related conduction mechanisms. In this novel "self-diagnostic" approach, NV centers represent not only the source of detrimental spatial charge but also a unique tool for their direct investigation.

A novel optical method for thermometry based on NV centres in diamonds was demonstrated in the second part of the chapter. In the experiment employing CW-ODMR magnetometry and special regime of transverse bias magnetic field was illustrated a narrower linewidth and an enhanced ODMR appears due to the degeneracy of hyperfine transitions, this allow achieving a temperature noise floor of $5mK/Hz^{1/2}$. The demonstrated method provides benefits in terms of its simple experimental setup and also better magnetic field noise protection.

With the same diamond sensor a technique of vector magnetometry was demonstrated. A magnitude and orientation of the magnetic field, generated by copper wire, were reconstructed by means of developed protocol. The magnetic field sensitivity of our magnetometer was 40 $nT/Hz^{1/2}$ up to the lock-in filter roll-off frequency of 100Hz. The higher sensitivity could be achieved be meand of sophisticated ODMR protocols (Ramsey, multi-frequency MW modulation withlock-in detection).

The sensing of magnetic fields has important applications, especially in the fields of biology and biomedicine as it can be used noninvasively for diagnoses. However, current challenges, discussed in **Chapter 5**, hinder these quantum sensors from reaching their full potential. Major constraints for diamond sensor type as optical illumination, MW field, bias magnetic field, optics, method of photoluminescence detection and sample preparation have been analysed in this thesis. Special attention was paid to estimation of the electromagnetic fields in the nervous system. It was shown that sensitivity of upcoming generation of NV magnetic field sensors may not be enough for the measurement single neuron action potential but measurement of the

magnetic field of the slice activity of the brain, cardiac tissues or intracellular temperature measurements seem very promising.

Also the biocompability of fluorescent diamond nanocrystals on primary cultures of hippocampal neurons were investigated. ODMR measurements were successfully carried out as a proof of feasibility of this type of measurement without affecting the cells physiological functions. The possibility of implementing ODMR protocols inside living cells is of high relevance for applied neurophysiology and bio-chemistry researches since the ODMR technique allows high sensitivity measurements of the temperature and low intensity electrical bio-currents that characterizes biological systems.

Acknowledgments

The performed work would have not been possible without the constant support of my colleagues. Here I would like to acknowledge the whole Quantum Optics Group of the National Institute of Metrological Research (INRiM): during the years spent working together I had the chance to learn a lot, also thanks to the many challenges faced. I feel included in a very united group with a very pleasant climate to work in.

I want to thank Prof. Marco Genovese, my supervisor and head of our Quantum Optics Group for giving me this amazing opportunity to work under his direction at this institute and topic. Last but not least, for the correction of the drafts of this manuscript.
A special thanks goes to Dr. Ivo Degiovanni, Dr. Paolo Traina and Dr. Ettore Bernardi for all the valuable discussions, ideas and a great work environment.

Many other people supported me and I am grateful to all of them, in particular:
-Solid State Physics group of the University of Turin coordinated by Prof. Paolo Olivero: special thanks to Dr. Jacopo Forneris, Dr. Sviatoslav Ditalia Tchernij, and Federico Picollo for the support in sample preparation and the implantation of NV centers. Without them, there would be no samples and therefore no new and exciting experiments.
-Expert help of collaborators Prof. Valentina Carabelli, Dott. Laura Guarina, Dott. Claudio Franchino.
-My family, for always being at my side and supporting me in everything I do.

Also I would like to go special thanks to bureaucratic system in Italy, which motivated me to take my second PhD.

Bibliography

[1] V. S. Vavilov, “The properties of natural and synthetic diamond,” *Uspekhi Fiz. Nauk*, 1993.

[2] P. Pavone *et al.*, “Ab initio lattice dynamics of diamond,” *Phys. Rev. B*, 1993.

[3] O. A. Williams *et al.*, “Growth, electronic properties and applications of nanodiamond,” *Diam. Relat. Mater.*, 2008.

[4] H. P. Bovenkerk, F. P. Bundy, H. M. Strong, R. H. Wentorf, and H. T. Hall, “Preparation of diamond,” *Nature*, 1959.

[5] M. W. Doherty, N. B. Manson, P. Delaney, F. Jelezko, J. Wrachtrup, and L. C. L. Hollenberg, “The nitrogen-vacancy colour centre in diamond,” *Physics Reports*. 2013.

[6] E. Bourgeois *et al.*, “Photoelectric detection of electron spin resonance of nitrogen-vacancy centres in diamond,” *Nat. Commun.*, 2015.

[7] J. Wrachtrup and F. Jelezko, “Processing quantum information in diamond,” *J. Phys. Condens. Matter*, 2006.

[8] M. W. Doherty *et al.*, “Temperature shifts of the resonances of the NV-center in diamond,” *Phys. Rev. B - Condens. Matter Mater. Phys.*, 2014.

[9] F. M. Hrubesch, G. Braunbeck, M. Stutzmann, F. Reinhard, and M. S. Brandt, “Efficient Electrical Spin Readout of NV- Centers in Diamond,” *Phys. Rev. Lett.*, 2017.

[10] J. M. Taylor *et al.*, “High-sensitivity diamond magnetometer with nanoscale resolution,” *Nat. Phys.*, 2008.

[11] A. Lenef, S. Brown, D. Redman, S. Rand, J. Shigley, and E. Fritsch, “Electronic structure of the N-V center in diamond: Experiments,” *Phys. Rev. B - Condens. Matter Mater. Phys.*, 1996.

[12] A. Gali, M. Fyta, and E. Kaxiras, “Ab initio supercell calculations on nitrogen-vacancy center in diamond: Electronic structure and hyperfine tensors,” *Phys. Rev. B - Condens. Matter Mater. Phys.*, 2008.

[13] A. A. Cottey, “Group Theory and Quantum Mechanics,” *Phys. Bull.*, 1975.

[14] M. W. Doherty *et al.*, “Theory of the ground-state spin of the NV - center in diamond,” *Phys. Rev. B - Condens. Matter Mater. Phys.*, 2012.

[15] A. Beveratos, R. Brouri, T. Gacoin, J. P. Poizat, and P. Grangier, “Nonclassical radiation from diamond nanocrystals,” *Phys. Rev. A - At. Mol. Opt. Phys.*, 2001.

[16] E. M. Purcell, H. C. Torrey, and R. V. Pound, “Resonance absorption by nuclear magnetic moments in a solid [7],” *Physical Review*. 1946.

[17] L. J. Rogers, S. Armstrong, M. J. Sellars, and N. B. Manson, “Infrared emission of the NV centre in diamond: Zeeman and uniaxial stress studies,” *New J. Phys.*, 2008.

[18] F. Jelezko and J. Wrachtrup, “Single defect centres in diamond: A review,” *Physica Status Solidi (A) Applications and Materials Science*. 2006.

[19] V. M. Acosta, A. Jarmola, E. Bauch, and D. Budker, “Optical properties of the nitrogen-vacancy singlet levels in diamond,” *Phys. Rev. B - Condens. Matter Mater. Phys.*, 2010.

[20] J. Harrison, M. J. Sellars, and N. B. Manson, “Optical spin polarisation of the N-V centre in diamond,” in *Journal of Luminescence*, 2004.

[21] N. B. Manson, X. F. He, and P. T. H. Fisk, “Raman heterodyne studies of the nitrogen-vacancy centre in diamond,” *J. Lumin.*, 1992.

[22] N. B. Manson, X.-F. He, and P. T. H. Fisk, “Raman heterodyne detected electron-nuclear-double-resonance measurements of the nitrogen-vacancy center in diamond,” *Opt. Lett.*, 1990.

[23] A. Gupta, L. Hacquebard, and L. Childress, “Efficient signal processing for time-resolved fluorescence detection of nitrogen-vacancy spins in diamond,” *J. Opt. Soc. Am. B*, 2016.

[24] J. H. N. Loubser and J. A. Van Wyk, “Electron spin resonance in the study of diamond,” *Reports Prog. Phys.*, 1978.

[25] J. H. N. Loubser and J. A. Van Wyk, “OPTICAL SPIN-POLARISATION IN A TRIPLET STATE IN IRRDIATED AND ANNEALED TYPE 1B DIAMONDS.,” *Diam. Res*, 1977.

[26] V. K. A. Sreenivasan, A. V. Zvyagin, and E. M. Goldys, “Luminescent nanoparticles and their applications in the life sciences,” *J. Phys. Condens. Matter*, 2013.

[27] L. M. Pham *et al.*, “Magnetic field imaging with nitrogen-vacancy ensembles,” *New J. Phys.*, 2011.

[28] F. Dolde *et al.*, “Electric-field sensing using single diamond spins,” *Nat. Phys.*, 2011.

[29] G. Davies and M. F. Hamer, “Optical Studies of the 1.945 eV Vibronic Band in Diamond,” *Proc. R. Soc. A Math. Phys. Eng. Sci.*, 1976.

[30] J. Meijer *et al.*, “Generation of single color centers by focused nitrogen implantation,” *Appl. Phys. Lett.*, 2005.

[31] I. Aharonovich and E. Neu, “Diamond nanophotonics,” *Adv. Opt. Mater.*, 2014.

[32] R. H. Webb, “Confocal optical microscopy,” *Reports Prog. Phys.*, 1996.

[33] M. O. Scully and M. S. Zubairy, “Quantum Optics,” *Cambridge University Press*. 1997.

[34] D. F. Walls, G. J. Milburn, D. F. Walls, and G. J. Milburn, “Coherence Properties of the Electromagnetic Field,” in *Quantum Optics*, 1994.

[35] L. Fleury, J. M. Segura, G. Zumofen, B. Hecht, and U. P. Wild, “Nonclassical photon statistics in single-molecule fluorescence at room temperature,” *Phys. Rev. Lett.*, 2000.

[36] A. Beveratos, R. Brouri, J.-P. Poizat, and P. Grangier, “Bunching and Antibunching from Single NV Color Centers in Diamond,” in *Quantum Communication, Computing, and Measurement 3*, 2006.

[37] L. Rondin, J. P. Tetienne, T. Hingant, J. F. Roch, P. Maletinsky, and V. Jacques, “Magnetometry with nitrogen-vacancy defects in diamond,” *Reports on Progress in Physics*. 2014.

[38] E. O. Göbel and U. Siegner, *Quantum Metrology: Foundation of Units and Measurements*. 2015.

[39] L. Childress and R. Hanson, “Diamond NV centers for quantum computing and quantum networks,” *MRS Bulletin*. 2013.

[40] R. Schirhagl, K. Chang, M. Loretz, and C. L. Degen, “Nitrogen-Vacancy Centers in Diamond: Nanoscale Sensors for Physics and Biology,” *Annu. Rev. Phys. Chem.*, 2014.

[41] E. Bernardi, R. Nelz, S. Sonusen, and E. Neu, “Nanoscale sensing using point defects in single-crystal diamond: Recent progress on nitrogen vacancy center-based sensors,” *Crystals*, 2017.

[42] S. Zhao *et al.*, “Single photon emission from graphene quantum dots at room temperature,” *Nat. Commun.*, 2018.

[43] J. Y. Cheung *et al.*, “The quantum candela: A re-definition of the standard units for optical radiation,” in *Journal of Modern Optics*, 2007.

[44] G. Balasubramanian *et al.*, “Nanoscale imaging magnetometry with diamond spins under ambient conditions,” *Nature*, 2008.

[45] J. Forneris *et al.*, “Mapping the Local Spatial Charge in Defective Diamond by Means of N- v Sensors - A Self-Diagnostic Concept,” *Phys. Rev. Appl.*, 2018.

[46] M. W. Doherty *et al.*, “Electronic properties and metrology applications of the diamond NV - Center under pressure,” *Phys. Rev. Lett.*, 2014.

[47] Y. K. Tzeng *et al.*, “Time-Resolved Luminescence Nanothermometry with Nitrogen-Vacancy Centers in Nanodiamonds,” *Nano Lett.*, 2015.

[48] J. Wang *et al.*, “High-sensitivity temperature sensing using an implanted single nitrogen-vacancy center array in diamond,” *Phys. Rev. B - Condens. Matter Mater. Phys.*, 2015.

[49] P. Neumann *et al.*, “High-precision nanoscale temperature sensing using single defects in diamond,” *Nano Lett.*, 2013.

[50] J. F. Barry *et al.*, “Optical magnetic detection of single-neuron action potentials using quantum defects in diamond.,” *Proc. Natl. Acad. Sci. U. S. A.*, vol. 113, no. 49, pp.

14133–14138, Dec. 2016.

[51] L. P. McGuinness *et al.*, "Quantum measurement and orientation tracking of fluorescent nanodiamonds inside living cells," *Nat. Nanotechnol.*, 2011.

[52] G. Kucsko *et al.*, "Nanometre-scale thermometry in a living cell," *Nature*, 2013.

[53] D. Robbes, "Highly sensitive magnetometers-a review," *Sensors Actuators, A Phys.*, 2006.

[54] D. Sheng, S. Li, N. Dural, and M. V. Romalis, "Subfemtotesla scalar atomic magnetometry using multipass cells," *Phys. Rev. Lett.*, 2013.

[55] I. K. Kominis, T. W. Kornack, J. C. Allred, and M. V. Romalis, "A subfemtotesla multichannel atomic magnetometer," *Nature*, 2003.

[56] S. Knappe, T. H. Sander, O. Kosch, F. Wiekhorst, J. Kitching, and L. Trahms, "Cross-validation of microfabricated atomic magnetometers with superconducting quantum interference devices for biomagnetic applications," *Appl. Phys. Lett.*, 2010.

[57] C. L. Degen, "Scanning magnetic field microscope with a diamond single-spin sensor," *Appl. Phys. Lett.*, 2008.

[58] J. R. Maze *et al.*, "Nanoscale magnetic sensing with an individual electronic spin in diamond," *Nature*, 2008.

[59] V. M. Acosta *et al.*, "Diamonds with a high density of nitrogen-vacancy centers for magnetometry applications," *Phys. Rev. B - Condens. Matter Mater. Phys.*, 2009.

[60] M. Vengalattore, J. M. Higbie, S. R. Leslie, J. Guzman, L. E. Sadler, and D. M. Stamper-Kurn, "High-resolution magnetometry with a spinor bose-einstein condensate," *Phys. Rev. Lett.*, 2007.

[61] M. I. Faley, U. Poppe, K. Urban, D. N. Paulson, and R. L. Fagaly, "A new generation of the HTS multilayer DC-SQUID magnetometers and gradiometers," *J. Phys. Conf. Ser.*, 2006.

[62] F. Baudenbacher, L. E. Fong, J. R. Holzer, and M. Radparvar, "Monolithic low-transition-temperature superconducting magnetometers for high resolution imaging magnetic fields of room temperature samples," *Appl. Phys. Lett.*, 2003.

[63] K. Fang *et al.*, "High-sensitivity magnetometry based on quantum beats in diamond nitrogen-vacancy centers," *Phys. Rev. Lett.*, 2013.

[64] G. Chatzidrosos *et al.*, "Miniature Cavity-Enhanced Diamond Magnetometer," *Phys. Rev. Appl.*, 2017.

[65] H. Clevenson, M. E. Trusheim, C. Teale, T. Schröder, D. Braje, and D. Englund, "Broadband magnetometry and temperature sensing with a light-trapping diamond waveguide," *Nat. Phys.*, vol. 11, no. 5, pp. 393–397, Apr. 2015.

[66] Y. Yue and X. Wang, “Nanoscale thermal probing,” *Nano Rev.*, 2012.

[67] T. D. Vreugdenburg, C. D. Willis, L. Mundy, and J. E. Hiller, “A systematic review of elastography, electrical impedance scanning, and digital infrared thermography for breast cancer screening and diagnosis,” *Breast Cancer Research and Treatment*. 2013.

[68] S. Gomès and A. Assy, “Scanning thermal microscopy,” in *Nanostructured Semiconductors: Amorphization and Thermal Properties*, 2017.

[69] J. M. Yang, H. Yang, and L. Lin, “Quantum dot nano thermometers reveal heterogeneous local thermogenesis in living cells,” *ACS Nano*, 2011.

[70] S. H. Kim, J. Noh, M. K. Jeon, K. W. Kim, L. P. Lee, and S. I. Woo, “Micro-Raman thermometry for measuring the temperature distribution inside the microchannel of a polymerase chain reaction chip,” *J. Micromechanics Microengineering*, 2006.

[71] F. Vetrone *et al.*, “Temperature sensing using fluorescent nanothermometers,” *ACS Nano*, 2010.

[72] S. J. Yu, M. W. Kang, H. C. Chang, K. M. Chen, and Y. C. Yu, “Bright fluorescent nanodiamonds: No photobleaching and low cytotoxicity,” *J. Am. Chem. Soc.*, 2005.

[73] C. G. Specht, O. A. Williams, R. B. Jackman, and R. Schoepfer, “Ordered growth of neurons on diamond,” *Biomaterials*, 2004.

[74] V. M. Acosta, E. Bauch, M. P. Ledbetter, A. Waxman, L. S. Bouchard, and D. Budker, “Temperature dependence of the nitrogen-vacancy magnetic resonance in diamond,” *Phys. Rev. Lett.*, 2010.

[75] X. D. Chen *et al.*, “Temperature dependent energy level shifts of nitrogen-vacancy centers in diamond,” *Appl. Phys. Lett.*, 2011.

[76] L. Gao, L. Shao, B. C. Chen, and E. Betzig, “3D live fluorescence imaging of cellular dynamics using Bessel beam plane illumination microscopy,” *Nat. Protoc.*, 2014.

[77] L. Gu *et al.*, “In vivo time-gated fluorescence imaging with biodegradable luminescent porous silicon nanoparticles,” *Nat. Commun.*, 2013.

[78] M. F. Juette *et al.*, “The bright future of single-molecule fluorescence imaging,” *Current Opinion in Chemical Biology*. 2014.

[79] P. J. Keller, “Imaging morphogenesis: Technological advances and biological insights,” *Science*. 2013.

[80] A. Kusumi, T. A. Tsunoyama, K. M. Hirosawa, R. S. Kasai, and T. K. Fujiwara, “Tracking single molecules at work in living cells,” *Nature Chemical Biology*. 2014.

[81] T. Iwasaki *et al.*, “Germanium-Vacancy Single Color Centers in Diamond,” *Sci. Rep.*, 2015.

[82] C. Hepp *et al.*, “Electronic structure of the silicon vacancy color center in diamond,”

Phys. Rev. Lett., 2014.

[83] Y. Y. Hui, L. J. Su, O. Y. Chen, Y. T. Chen, T. M. Liu, and H. C. Chang, "Wide-field imaging and flow cytometric analysis of cancer cells in blood by fluorescent nanodiamond labeling and time gating," *Sci. Rep.*, 2014.

[84] D. Le Sage *et al.*, "Optical magnetic imaging of living cells," *Nature*, 2013.

[85] L. T. Hall *et al.*, "Monitoring ion-channel function in real time through quantum decoherence," *Proc. Natl. Acad. Sci. U. S. A.*, 2010.

[86] D. R. Glenn *et al.*, "Single-cell magnetic imaging using a quantum diamond microscope," *Nat. Methods*, 2015.

[87] P. Reineck *et al.*, "Brightness and Photostability of Emerging Red and Near-IR Fluorescent Nanomaterials for Bioimaging," *Adv. Opt. Mater.*, 2016.

[88] G. Balasubramanian, A. Lazariev, S. R. Arumugam, and D. wen Duan, "Nitrogen-Vacancy color center in diamond-emerging nanoscale applications in bioimaging and biosensing," *Current Opinion in Chemical Biology*. 2014.

[89] S. Haziza *et al.*, "Fluorescent nanodiamond tracking reveals intraneuronal transport abnormalities induced by brain-disease-related genetic risk factors," *Nat. Nanotechnol.*, 2017.

[90] I. Rehor *et al.*, "Fluorescent nanodiamonds embedded in biocompatible translucent shells," *Small*, 2014.

[91] T. C. Hsu, K. K. Liu, H. C. Chang, E. Hwang, and J. I. Chao, "Labeling of neuronal differentiation and neuron cells with biocompatible fluorescent nanodiamonds," *Sci. Rep.*, 2014.

[92] S. R. Hemelaar *et al.*, "The interaction of fluorescent nanodiamond probes with cellular media," *Microchim. Acta*, 2017.

[93] S. R. Hemelaar *et al.*, "Nanodiamonds as multi-purpose labels for microscopy," *Sci. Rep.*, 2017.

[94] N. Mohan, C. S. Chen, H. H. Hsieh, Y. C. Wu, and H. C. Chang, "In vivo imaging and toxicity assessments of fluorescent nanodiamonds in caenorhabditis elegans," *Nano Lett.*, 2010.

[95] C. J. Chunnilall, I. Pietro Degiovanni, S. Kück, I. Müller, and A. G. Sinclair, "Errata: Metrology of single-photon sources and detectors: a review," *Opt. Eng.*, 2014.

[96] M. D. Eisaman, J. Fan, A. Migdall, and S. V. Polyakov, "Invited Review Article: Single-photon sources and detectors," *Review of Scientific Instruments*. 2011.

[97] E. Wu, V. Jacques, H. Zeng, P. Grangier, F. Treussart, and J.-F. Roch, "Narrow-band single-photon emission in the near infrared for quantum key distribution," *Opt. Express*,

vol. 14, no. 3, p. 1296, Feb. 2006.

[98] L. Rondin *et al.*, "Stray-field imaging of magnetic vortices with a single diamond spin," *Nat. Commun.*, 2013.

[99] E. Ampem-Lassen *et al.*, "Nano-manipulation of diamond-based single photon sources," *Opt. Express*, vol. 17, no. 14, p. 11287, Jul. 2009.

[100] T. Schröder *et al.*, "Quantum nanophotonics in diamond [Invited]," *J. Opt. Soc. Am. B*, 2016.

[101] A. Härtl *et al.*, "Protein-modified nanocrystalline diamond thin films for biosensor applications," *Nat. Mater.*, 2004.

[102] Y. R. Chang *et al.*, "Mass production and dynamic imaging of fluorescent nanodiamonds," *Nat. Nanotechnol.*, 2008.

[103] T. Gaebel *et al.*, "Size-reduction of nanodiamonds via air oxidation," *Diam. Relat. Mater.*, 2012.

[104] A. Quaranta, G. Valotto, A. De Lorenzi Pezzolo, and G. A. Mazzocchin, "Ion Beam Induced Luminescence capabilities for the analysis of coarse-grained river sediments," *Spectrochim. Acta - Part A Mol. Biomol. Spectrosc.*, 2014.

[105] A. Re *et al.*, "Ion Beam Analysis for the provenance attribution of lapis lazuli used in glyptic art: The case of the 'collezione Medicea,'" *Nucl. Instruments Methods Phys. Res. Sect. B Beam Interact. with Mater. Atoms*, 2015.

[106] J. F. Ziegler, M. D. Ziegler, and J. P. Biersack, "SRIM - The stopping and range of ions in matter (2010)," *Nucl. Instruments Methods Phys. Res. Sect. B Beam Interact. with Mater. Atoms*, 2010.

[107] D. Saada, J. Adler, and R. Kalish, "Transformation of diamond (sp 3) to graphite (sp 2) bonds by ion-impact," *Int. J. Mod. Phys. C*, 1998.

[108] S. Pezzagna, B. Naydenov, F. Jelezko, J. Wrachtrup, and J. Meijer, "Creation efficiency of nitrogen-vacancy centres in diamond," *New J. Phys.*, 2010.

[109] J. Forneris *et al.*, "Electrical stimulation of non-classical photon emission from diamond color centers by means of sub-superficial graphitic electrodes," *Sci. Rep.*, 2015.

[110] D. Gatto Monticone *et al.*, "Native NIR-emitting single colour centres in CVD diamond," *New J. Phys.*, 2014.

[111] C. Kurtsiefer, P. Zarda, S. Mayer, and H. Weinfurter, "The breakdown flash of silicon avalanche photodiodes-back door for eavesdropper attacks?," *J. Mod. Opt.*, 2001.

[112] A. Meda, I. Pietro Degiovanni, A. Tosi, Z. Yuan, G. Brida, and M. Genovese, "Quantifying backflash radiation to prevent zero-error attacks in quantum key distribution," *Light Sci. Appl.*, 2017.

[113] R. Brouri, A. Beveratos, J.-P. Poizat, and P. Grangier, “Photon antibunching in the fluorescence of individual color centers in diamond,” *Opt. Lett.*, 2000.

[114] J. Storteboom, P. Dolan, S. Castelletto, X. Li, and M. Gu, “Lifetime investigation of single nitrogen vacancy centres in nanodiamonds,” *Opt. Express*, 2015.

[115] M. Berthel, O. Mollet, G. Dantelle, T. Gacoin, S. Huant, and A. Drezet, “Photophysics of single nitrogen-vacancy centers in diamond nanocrystals,” *Phys. Rev. B - Condens. Matter Mater. Phys.*, 2015.

[116] X. Liu *et al.*, “Fiber-integrated diamond-based magnetometer,” *Appl. Phys. Lett.*, 2013.

[117] S. Ramelow *et al.*, “Highly efficient heralding of entangled single photons,” *Opt. Express*, 2013.

[118] S. Krapick, H. Herrmann, V. Quiring, B. Brecht, H. Suche, and C. Silberhorn, “An efficient integrated two-color source for heralded single photons,” *New J. Phys.*, vol. 15, no. 3, p. 033010, Mar. 2013.

[119] M. Förtsch *et al.*, “A versatile source of single photons for quantum information processing,” *Nat. Commun.*, 2013.

[120] N. Montaut *et al.*, “High-efficiency plug-and-play source of heralded single photons,” *Phys. Rev. Appl.*, 2017.

[121] A. J. Shields, “Semiconductor quantum light sources,” in *Nanoscience and Technology: A Collection of Reviews from Nature Journals*, 2009.

[122] M. Arita, F. Le Roux, M. J. Holmes, S. Kako, and Y. Arakawa, “Ultraclean Single Photon Emission from a GaN Quantum Dot,” *Nano Lett.*, 2017.

[123] F. Diedrich and H. Walther, “Nonclassical radiation of a single stored ion,” *Phys. Rev. Lett.*, 1987.

[124] B. Lounis and W. E. Moerner, “Single photons on demand from a single molecule at room temperature,” *Nature*, 2000.

[125] M. Genovese, “Real applications of quantum imaging,” *Journal of Optics (United Kingdom)*. 2016.

[126] I. I. Arkhipov, J. Peřina, O. Haderka, and V. Michálek, “Experimental detection of nonclassicality of single-mode fields via intensity moments,” *Opt. Express*, 2016.

[127] P. Grangier, G. Roger, and A. Aspect, “Experimental Evidence for a Photon Anticorrelation Effect...,” *Europhys. Lett.*, 1986.

[128] R. Q. Twiss and R. H. Brown, “The question of correlation between photons in coherent beams of light [2],” *Nature*. 1957.

[129] E. A. Goldschmidt *et al.*, “Mode reconstruction of a light field by multiphoton statistics,” *Phys. Rev. A - At. Mol. Opt. Phys.*, 2013.

[130] D. Gatto Monticone *et al.*, "Beating the abbe diffraction limit in confocal microscopy via nonclassical photon statistics," *Phys. Rev. Lett.*, 2014.

[131] S. Oppel, T. Büttner, P. Kok, and J. Von Zanthier, "Superresolving multiphoton interferences with independent light sources," *Phys. Rev. Lett.*, 2012.

[132] A. Classen *et al.*, "Superresolving Imaging of Arbitrary One-Dimensional Arrays of Thermal Light Sources Using Multiphoton Interference," *Phys. Rev. Lett.*, 2016.

[133] L. Lachman, L. Slodička, and R. Filip, "Nonclassical light from a large number of independent single-photon emitters," *Sci. Rep.*, 2016.

[134] J. C. F. G. I. M. Jcgm, "Evaluation of measurement data — Guide to the expression of uncertainty in measurement," *Int. Organ. Stand. Geneva ISBN*, 2008.

[135] J. Tisler *et al.*, "Fluorescence and spin properties of defects in single digit nanodiamonds," *ACS Nano*, 2009.

[136] H. Paul, P. Törmä, T. Kiss, and I. Jex, "Photon chopping: New way to measure the quantum state of light," *Phys. Rev. Lett.*, 1996.

[137] A. Divochiy *et al.*, "Superconducting nanowire photon-number-resolving detector at telecommunication wavelengths," *Nat. Photonics*, 2008.

[138] O. A. Shcherbina *et al.*, "Photon correlations for colloidal nanocrystals and their clusters," *Opt. Lett.*, 2014.

[139] G. B. Lemos, V. Borish, G. D. Cole, S. Ramelow, R. Lapkiewicz, and A. Zeilinger, "Quantum imaging with undetected photons," *Nature*, 2014.

[140] M. Avenhaus, K. Laiho, M. V. Chekhova, and C. Silberhorn, "Accessing higher order correlations in quantum optical states by time multiplexing," *Phys. Rev. Lett.*, 2010.

[141] M. J. Stevens, S. Glancy, S. W. Nam, and R. P. Mirin, "Third-order antibunching from an imperfect single-photon source," in *Optics InfoBase Conference Papers*, 2011.

[142] A. H. and K. H. R. Nemanich, J.Carlisle, "CVD diamond - research, applications and challenges," *MRS Bull*, vol. 39, p. 490, 2014.

[143] C. E. Nebel, "Electronic properties of CVD diamond," *Semiconductor Science and Technology*. 2003.

[144] J. W. Liu, M. Y. Liao, M. Imura, E. Watanabe, H. Oosato, and Y. Koide, "Diamond logic inverter with enhancement-mode metal-insulator-semiconductor field effect transistor," *Appl. Phys. Lett.*, 2014.

[145] S. Lagomarsino *et al.*, "Radiation hardness of three-dimensional polycrystalline diamond detectors," *Appl. Phys. Lett.*, 2015.

[146] J. B. S. Abraham, B. A. Aguirre, J. L. Pacheco, G. Vizkelethy, and E. Bielejec, "Fabrication and characterization of a co-planar detector in diamond for low energy

single ion implantation," *Appl. Phys. Lett.*, 2016.

[147] F. Picollo *et al.*, "Development and characterization of a diamond-insulated graphitic multi electrode array realized with ion beam lithography," *Sensors (Switzerland)*, 2015.

[148] M. Gulka *et al.*, "Pulsed Photoelectric Coherent Manipulation and Detection of N-V Center Spins in Diamond," *Phys. Rev. Appl.*, 2017.

[149] A. Bendali *et al.*, "Distinctive glial and neuronal interfacing on nanocrystalline diamond," *PLoS One*, 2014.

[150] Y. Doi *et al.*, "Deterministic electrical charge-state initialization of single nitrogen-vacancy center in diamond," *Phys. Rev. X*, 2014.

[151] L. C. Bassett, F. J. Heremans, C. G. Yale, B. B. Buckley, and D. D. Awschalom, "Electrical tuning of single nitrogen-vacancy center optical transitions enhanced by photoinduced fields," *Phys. Rev. Lett.*, 2011.

[152] A. Lohrmann *et al.*, "Diamond based light-emitting diode for visible single-photon emission at room temperature," *Appl. Phys. Lett.*, 2011.

[153] A. Lohstroh, P. J. Sellin, S. G. Wang, A. W. Davies, and J. M. Parkin, "Mapping of polarization and detrapping effects in synthetic single crystal chemical vapor deposited diamond by ion beam induced charge imaging," *J. Appl. Phys.*, 2007.

[154] P. Olivero *et al.*, "Investigation of chemical vapour deposition diamond detectors by X-ray micro-beam induced current and X-ray micro-beam induced luminescence techniques," in *Spectrochimica Acta - Part B Atomic Spectroscopy*, 2004.

[155] E. Vittone *et al.*, "Semiconductor characterization by scanning ion beam induced charge (IBIC) microscopy," *Nucl. Instruments Methods Phys. Res. Sect. B Beam Interact. with Mater. Atoms*, 2008.

[156] T. Sekiguchi, S. Koizumi, and T. Taniguchi, "Characterization of p-n junctions of diamond and c-BN by cathodoluminescence and electron-beam-induced current," in *Journal of Physics Condensed Matter*, 2004.

[157] J. Forneris *et al.*, "Electrical control of deep NV centers in diamond by means of sub-superficial graphitic micro-electrodes," *Carbon N. Y.*, 2017.

[158] M. Lesik *et al.*, "Production of bulk NV centre arrays by shallow implantation and diamond CVD overgrowth," *Phys. Status Solidi Appl. Mater. Sci.*, 2016.

[159] S. Ditalia Tchernij *et al.*, "Electrical characterization of a graphite-diamond-graphite junction fabricated by MeV carbon implantation," *Diam. Relat. Mater.*, 2017.

[160] T. Iwasaki *et al.*, "Direct Nanoscale Sensing of the Internal Electric Field in Operating Semiconductor Devices Using Single Electron Spins," *ACS Nano*, 2017.

[161] T. Lühmann *et al.*, "Investigation of the graphitization process of ion-beam irradiated

diamond using ellipsometry, Raman spectroscopy and electrical transport measurements," *Carbon N. Y.*, 2017.

[162] F. C. Chiu, "A review on conduction mechanisms in dielectric films," *Advances in Materials Science and Engineering*. 2014.

[163] M. A. Lampert, "Simplified theory of space-charge-limited currents in an insulator with traps," *Phys. Rev.*, 1956.

[164] P. Olivero *et al.*, "Focused ion beam fabrication and IBIC characterization of a diamond detector with buried electrodes," *Nucl. Instruments Methods Phys. Res. Sect. B Beam Interact. with Mater. Atoms*, 2011.

[165] F. Bosia *et al.*, "Direct measurement and modelling of internal strains in ion-implanted diamond," *J. Phys. Condens. Matter*, 2013.

[166] A. Battiato *et al.*, "Softening the ultra-stiff: Controlled variation of Young's modulus in single-crystal diamond by ion implantation," *Acta Mater.*, 2016.

[167] C. E. Nebel, M. Stutzmann, F. Lacher, P. Koidl, and R. Zachai, "Carrier trapping and release in CVD-diamond films," *Diam. Relat. Mater.*, 1998.

[168] E. Gaubas, T. Ceponis, D. Meskauskaite, and N. Kazuchits, "Profiling of current transients in capacitor type diamond sensors," *Sensors (Switzerland)*, 2015.

[169] N. Mizuochi *et al.*, "Electrically driven single-photon source at room temperature in diamond," *Nat. Photonics*, 2012.

[170] H. Kato *et al.*, "Tunable light emission from nitrogen-vacancy centers in single crystal diamond PIN diodes," *Appl. Phys. Lett.*, 2013.

[171] K. Sasaki *et al.*, "Broadband, large-area microwave antenna for optically detected magnetic resonance of nitrogen-vacancy centers in diamond," *Rev. Sci. Instrum.*, 2016.

[172] D. M. Toyli, C. F. De Las Casas, D. J. Christle, V. V. Dobrovitski, and D. D. Awschalom, "Fluorescence thermometry enhanced by the quantum coherence of single spins in diamond," *Proc. Natl. Acad. Sci. U. S. A.*, 2013.

[173] A. M. Wojciechowski *et al.*, "Precision temperature sensing in the presence of magnetic field noise and vice-versa using nitrogen-vacancy centers in diamond," *Appl. Phys. Lett.*, 2018.

[174] H. A. R. El-Ella, S. Ahmadi, A. M. Wojciechowski, A. Huck, and U. L. Andersen, "Optimised frequency modulation for continuous-wave optical magnetic resonance sensing using nitrogen-vacancy ensembles," *Opt. Express*, 2017.

[175] S. Steinert *et al.*, "High sensitivity magnetic imaging using an array of spins in diamond," *Rev. Sci. Instrum.*, 2010.

[176] B. J. Maertz, A. P. Wijnheijmer, G. D. Fuchs, M. E. Nowakowski, and D. D.

Awschalom, “Vector magnetic field microscopy using nitrogen vacancy centers in diamond,” *Appl. Phys. Lett.*, 2010.

[177] P. Wang *et al.*, “High-resolution vector microwave magnetometry based on solid-state spins in diamond,” *Nat. Commun.*, 2015.

[178] A. K. Dmitriev and A. K. Vershovskii, “Concept of a microscale vector magnetic field sensor based on nitrogen-vacancy centers in diamond,” *J. Opt. Soc. Am. B*, 2016.

[179] S. M. Blakley *et al.*, “Fiber-optic vectorial magnetic-field gradiometry by a spatiotemporal differential optical detection of magnetic resonance in nitrogen–vacancy centers in diamond,” *Opt. Lett.*, 2016.

[180] S. Kitazawa, Y. Matsuzaki, S. Saijo, K. Kakuyanagi, S. Saito, and J. Ishi-Hayase, “Vector-magnetic-field sensing via multifrequency control of nitrogen-vacancy centers in diamond,” *Phys. Rev. A*, 2017.

[181] C. Zhang *et al.*, “Vector magnetometer based on synchronous manipulation of nitrogen-vacancy centers in all crystal directions,” *J. Phys. D. Appl. Phys.*, 2018.

[182] H. Clevenson, L. M. Pham, C. Teale, K. Johnson, D. Englund, and D. Braje, “Robust high-dynamic-range vector magnetometry with nitrogen-vacancy centers in diamond,” *Appl. Phys. Lett.*, 2018.

[183] J. Sarvas, “Basic mathematical and electromagnetic concepts of the biomagnetic inverse problem,” *Phys. Med. Biol.*, 1987.

[184] C. M. Michel, M. M. Murray, G. Lantz, S. Gonzalez, L. Spinelli, and R. Grave De Peralta, “EEG source imaging,” *Clinical Neurophysiology*. 2004.

[185] E. V. Levine *et al.*, “Principles and techniques of the quantum diamond microscope,” *Nanophotonics*, 2019.

[186] M. Hines, “NEURON — A Program for Simulation of Nerve Equations,” in *Neural Systems: Analysis and Modeling*, 1993.

[187] M. L. Hines and N. T. Carnevale, “The NEURON Simulation Environment,” *Neural Computation*. 1997.

[188] F. Santamaria and J. M. Bower, “Hodgkin-Huxley Models,” in *Encyclopedia of Neuroscience*, 2009.

[189] B. Agüera y Arcas, A. L. Fairhall, and W. Bialek, “Computation in a single neuron: Hodgkin and Huxley revisited,” *Neural Computation*. 2003.

[190] J. Isakovic, I. Dobbs-Dixon, D. Chaudhury, and D. Mitrecic, “Modeling of inhomogeneous electromagnetic fields in the nervous system: a novel paradigm in understanding cell interactions, disease etiology and therapy,” *Sci. Rep.*, 2018.

[191] M. Karadas, A. M. Wojciechowski, A. Huck, N. O. Dalby, U. L. Andersen, and A.

Thielscher, “Feasibility and resolution limits of opto-magnetic imaging of neural network activity in brain slices using color centers in diamond,” *Sci. Rep.*, 2018.

[192] L. T. Hall *et al.*, “High spatial and temporal resolution wide-field imaging of neuron activity using quantum NV-diamond,” *Sci. Rep.*, 2012.

[193] G. Xi *et al.*, “Convection-enhanced delivery of nanodiamond drug delivery platforms for intracranial tumor treatment,” *Nanomedicine Nanotechnology, Biol. Med.*, 2014.

[194] R. Kaur and I. Badea, “Nanodiamonds as novel nanomaterials for biomedical applications: Drug delivery and imaging systems,” *International Journal of Nanomedicine*. 2013.

[195] B. Dischler, *Handbook of Spectral Lines in Diamond*. 2012.

[196] R. M. Wood, “Optical properties of diamond: a data handbook,” *Opt. Lasers Eng.*, 2004.

[197] R. J. Edgington *et al.*, “Patterned neuronal networks using nanodiamonds and the effect of varying nanodiamond properties on neuronal adhesion and outgrowth,” *J. Neural Eng.*, 2013.

[198] A. Thalhammer, R. J. Edgington, L. A. Cingolani, R. Schoepfer, and R. B. Jackman, “The use of nanodiamond monolayer coatings to promote the formation of functional neuronal networks,” *Biomaterials*, 2010.

[199] J. Wehling, R. Dringen, R. N. Zare, M. Maas, and K. Rezwan, “Bactericidal activity of partially oxidized nanodiamonds,” *ACS Nano*, 2014.

[200] Y. C. Lin *et al.*, “Nanodiamond for biolabelling and toxicity evaluation in the zebrafish embryo in vivo,” *J. Biophotonics*, 2016.

[201] Y. A. Huang *et al.*, “The effect of fluorescent nanodiamonds on neuronal survival and morphogenesis,” *Sci. Rep.*, 2014.

[202] J. R. Rabeau *et al.*, “Single nitrogen vacancy centers in chemical vapor deposited diamond nanocrystals,” *Nano Lett.*, 2007.